Utilising Mantle Seismic Structure to Constrain Mantle Circulation

Gwynfor Thomas Morgan

A thesis submitted for the degree of

Doctor of Philosophy

Cardiff University

July 2025

Abstract

Earth's mantle's sub-solidus convection is studied with numerical models. The impact of major phase transformations in the mantle transition zone (MTZ) on flow is already well understood. Phase transformations are associated with 'discontinuities' in 1D seismic structure (d410 and d660) whose topography is observed globally using SS-precursors.

Recently, advances in computational and experimental mineral physics have improved knowledge of mantle phase relations, revealing a patchwork of stability fields with 'branching' and 'curving' boundaries in pressure-temperature space. Using parametrisations of physics that relates mineral physics to geodynamics, and both of these to seismological observations, this thesis evaluates the impact more complex phase boundaries have on mantle dynamics and how mantle models might be evaluated with reference to observations of d410 and d660.

Others suggest 'non-linear' phase boundaries in pressure-temperature space could have distinct dynamic impacts. Chapter 2 investigates this for the ringwoodite-out via akimotoite and garnet-out reactions, 'branching' and 'curving' phase boundaries respectively. In 3D spherical shell mantle convection and circulation models, impacts are found to be negligible.

Chapter 3 introduces methods for predicting topography on d410 and d660 from mantle circulation models and simply filtering for SS-precursors' sensitivity. A mantle circulation model (MCM) is evaluated and does not satisfy observations, overpredicting MTZ temperature range and underpredicting the recycled chemical heterogeneity.

MCMs where viscosity structure, compositional initial condition, and core-mantle boundary temperature are presented in Chapter 4. d410-d660 structure are predicted and the models are assessed against published observations. Viscosity structure dominantly controls the variation of the discontinuity topographies, but no simulation provided a satisfactory fit to d410 and d660. Specifically, the reported positive correlation of the discontinuities was elusive. Various explanations for this correlation are found insufficient. Although synthetic discontinuity structure does not yet seem to be a simple constraint on MCMs, they show promise for understanding Earth observations.

Contents

List of Figures

List of Tables

Acknowledgements

Firstly I thank my lead supervisor Prof. J. Huw Davies, who has been the most supportive mentor that a student could ask for. Thank you for being so generous with your time, securing my funding and supporting me as I have learnt to teach and research (even when I've gone on detours and diversions from what you initially hoped!). Dr James Panton's (who is now at Universität zu Köln) support was invaluable at every step of this process. The support and patience of Dr Robert Myhill and Prof. James Wookey (both University of Bristol) made a thesis that trespasses quite so freely into seismology and mineral physics possible. I also thank Huw Davies, James Panton, James Wookey, Robert Myhill and many others corporately as the *Mantle Circulation Constrained* ('MC2') NERC large grant team. MC2 have been very generous in allowing me access to the large suite of mantle circulation models run for that project – which allowed me to experiment with the workflow and ideas in Chapters 3 and 4 with much shorter lead times than otherwise. I also benefited from participating in the meetings of the large grant and the ECRs on the grant, and I want to thank everyone involved in helping shape my understanding of the Earth and how to use mantle circulation models to improve our knowledge of it.

This work was funded by the College of Physical Sciences and Engineering of Cardiff University, and I am grateful for their support. I have benefited from the supportive environment in the school of Earth and Environmental Sciences at Cardiff, and in particular wish to thank Jo Poynter for her support all the times when I seem to have ended up being an edge case in various systems! The computational resource used in this project was ARCHER2, the UK's national supercomputer. I am grateful for the generous allocations of compute time and storage I received and in particular to Prof. John Brodholt (UCL) for managing the n03 account this was granted through.

I have been fortunate to have received the feedback, formal and informal, of many world-leading scientists on the work that is present in this thesis. Firstly thank you to my examiners Prof. Saskia Goes (Imperial College London) and Dr Glenn Jones (Cardiff University) for an enjoyable *viva* and the constructive comments throughout the text of the thesis that have improved it. Thank you

also to Dr Shasta Marrero who helped the *viva* run smoothly as chair. Specifically for Chapter 2, I thank Prof. Scott King (Virginia Tech) and Lior Suchoy (Imperial College London) whose feedback improved this work when I submitted a version of it for publication in *Solid Earth*. Specifically for Chapter 3, I thank Prof. Christine Houser (Tokyo Earth-Life Science Institute, Tokyo) and an anonymous reviewer whose feedback improved this work when I submitted a version of it for publication in *Geophysical Journal International*. I would also like to thank all the members of the geophysical community that I've met at conferences in the UK and abroad for their thoughtful conversation. In particular I would like to thank Prof. Ying Zhou (Virginia Tech) and Prof. Christine Houser (Earth-Life Science Institute, Tokyo) who shared with me their MTZ discontinuity topography models that were not publicly available – this has been very useful to the work in the latter part of this thesis.

I also thank everyone who has supported me along the way; the postdocs and PhD students at Cardiff for their company, and particularly the Geody lab PhD students (Lei, Duo, Nico and Abi) who have put up with obscene number of times in a day I boil the kettle for tea!

Simultaneous to this research, I have learnt to teach and I would like to thank the staff and students who have helped me improve; Prof. J. Huw Davies, Prof. Sammie Buzzard (now at Northumbria University), Gianluca Bianchi, Nicolas Récalde, many other staff in the school, and Dr Huw Pritchard (School of Law and Politics), as well as all the students I've confused over the last four years.

The path to me submitting the PhD today began long before I applied. I thank my parents for fighting for my education and showing me and my sibling how to think on the back of an envelope and giving us an appreciation and curiosity for the natural world. Without your support, Dad, Mum, GJ, this wouldn't be possible. I also thank Susan Brown and Rockwatch for formative experiences hunting for fossils when I was young and giving me the rock-bug that hasn't quite left me. David Boon at the BGS and Dr Jana Horák at the National Museum of Wales gave me early experiences of scientific research that set me on this road – thank you. Prof. Karin Sigloch and Prof. Conall Mac Niocaill encouraged my aspirations of studying the deep Earth further and I remain grateful for their support of me as an undergraduate.

And to all my friends, many of whom I do not show my appreciation of very well – thank you for your camaraderie and care of me over the years. I will try to do better. Finally, thank you Laura for all that you do for me. You are more wonderful than any words.

Chapter 1

Introduction

1.1 The Earth as a Heat Engine: Whole Mantle Convection

At a high level of abstraction, it is possible to view the Earth as giant heat engine (e.g., Lay *et al.*, 2008), heat flowing from the Earth's interior (the remnant of that generated during accretion and supported by that generated by the crystallisation of the inner core and radioactive decay) to the surface, and through processes in the crust, oceans, and atmosphere, to the void, at absolute zero. This thermal anomaly has decayed only very slowly over billions of years since its formation when the Earth accreted 4.56Ga ago (e.g., Patterson, 1956). In the early Earth, most of the heat was generated due to the decay of radioactive nuclides with short half-lives. However, these have now decayed to the point where the enthalpy of crystallisation of the inner core provides a similar amount of heat (e.g., Lay *et al.*, 2008) across the Core Mantle Boundary (CMB). See Figure 1a. Through the Earth's mantle, this heat flow is achieved principally through the advection of heat by mantle convection. The ratio of conductive and convective timescales is assessed with the Rayleigh number.

$$Ra = \frac{\alpha \rho g \Delta T D^3}{\kappa \eta} \tag{1.1}$$

where α is the thermal expansivity ($\sim 2.5 \times 10^{-5}$ K^{-1}), ρ is the density of the mantle (take 4500 kg.m^{-3}), ΔT is the non-adiabatic temperature drop across the convecting layer ($\sim$ 2800 K), D is the thickness of the convecting layer (the CMB is 2891 km deep), κ is thermal diffusivity ($\sim 8 \times 10^{-7}$ m^{2}s^{-1}), and η is the viscosity ($\sim 10^{21}$ Pa.s). The Rayleigh number for the Earth then is estimated as $O(10^8)$, suggesting that convection is much faster than conduction and therefore the Earth's mantle vigorously convects. This convection maintains a geotherm

between the Earth's surface temperature and its CMB temperature. As the convection is vigourous we can assume that this is adiabatic (i.e. that a convecting parcel does not exchange energy with its surroundings) in the manlte interior. Using values for the potential temperature of the mantle beneath mid-ocean ridges and plumes calculated from estimates of the crystallisation temperature of olivine from Li *et al.* (2025), and taking the same values for α, and g as in (1.1), and $C_P = 1100$ Jkg^{-1}K^{-1}, using the expression for adiabatic compression (e.g. Poirier, 2000, p. 204, eq. 7.21), I plot adiabats for the Earth in Figure 1a. These adiabats are deformed by the enthalpy of phase transformation of mantle minerals, shown here for a simple harzburgitic (i.e. fully olivine upper mantle) mantle of $MgSiO_4$, where there is a phase transformation from olivine to wadsleyite at 410 km depth, wadsleyite to ringwoodite at 520 km depth, ringwoodite to bridgmanite and periclase at 670 km depth, and bridgmanite to post-perovskite at 2700 km depth[1] (Figure 1a). However, we know from daily experience that the surface of the silicate of the Earth is not a searing 1600 K! Like all convecting systems, the silicate Earth has thermal boundary layers, where conduction dominates its interface to other thermodynamic systems (atmosphere and core), which also convect, but on much shorter timescales than the mantle. For these purposes then, we can seek to take T_{surf} as a constant 300 K, and T_{CMB} as a constant 3740 K (Deschamps and Cobden, 2022, although with significant uncertainty). If the thermal boundary layers have reached equilibrium, then the temperature distribution through them is a straight line from the adiabat to the boundary condition[2].

At the CMB, a hot thermal boundary layer in the mantle is formed from the heating below, from which plumes rise into the mantle and to the surface if sufficiently buoyant, where they create localised volcanism at so-called 'hotspots' (Morgan, 1971) (see red geotherm in Figure 1a). At the surface, the uppermost layer of the mantle cools conductively, forming rigid plates that shift around the surface due to the processes of plate tectonics (e.g. McKenzie and Parker, 1967). These motions are ultimately controlled by the broader mantle circulation effecting the subducted slabs (which in turn tug on the surface plates (Forsyth and Uyeda, 1975)). Plate tectonic motions ultimately control much of surface geology, geomorphology and geography, from the deformation of continents, to the distribution of melt in the crust - all controlled by and

[1]The temperature changes were calculated using the parameters listed in Table 1 for the olivine- and ringwoodite-out reactions, $\gamma_{Wd-out} = 4$ MPa.K^{-1}, $\Delta\rho_{Wd-out}/\rho = 1.86\%$, $\gamma_{PPv-in} = 8$ MPa.K^{-1}, $\Delta\rho_{PPv-in}/\rho = 1.48\%$, the enthalpy release stated in (1.27), and the relation $\Delta T = H^P/C_P$ (Turcotte and Schubert, 2014, p. 221).

[2]The thickness of this conductive thermal boundary layer is assessed here using the relation $\delta \sim D(Ra_c/Ra)^{0.3}$(e.g Schubert *et al.*, 2009, p. 589), where Ra_c is the critical Rayleigh number for convection, $\sim 10^3$

influencing the circulation of material in the deep mantle. As plates are subducted and descend to depth, new material is formed from uppermost mantle melts at Mid Ocean Ridges (MORs) - shallow features fed by distributed upwellings from the mid mantle.

These convective upwellings (plumes) and downwellings (slabs) together cool the deep Earth, bringing heat up from core and bringing cold material to the lower mantle. Unlike some other convecting systems, the mantle's convection happens as a viscous, heterogenous, fluid.

Firstly, whilst the mantle flows, it does so whilst remaining beneath the solidus, as a fluid with a viscosity of $\sim 10^{21}$ Pa.s (e.g. Haskell, 1935). For comparison the infamous bitumen of the Queensland pitch-drop experiment has a viscosity of 10^8 Pa.s (Edgeworth *et al.*, 1984). This makes it more difficult for humans to study observationally, and requires that we use modelling techniques (analytical (e.g. Ribe *et al.*, 2007), numerical (e.g. Baumgardner, 1983) and physical (e.g. Fourel *et al.*, 2017)) to relate those observations we are able to make of today's system and of the past in geological materials. These models are non-unique, have a broad span of potential values of parameters and so a large range of possible dynamics can be accommodated when looking at select Earth observables. This then necessitates the simultaneous consideration of various datasets from multiple geoscientific disciplines, which is challenging (Davies *et al.*, 2025).

Secondly, unlike most convecting systems we commonly think of, the mantle is extremely rheologically, chemically and mineralogically heterogeneous. Rigid slabs, fractionated from the material below, plunge into a comparatively runny mantle interior and experience a complex series of phase changes (Figure 1) in two parallel mineralogical systems (see below section 1.2). However, it is generally thought that despite these complexities, Earth's mantle undergoes whole-mantle convection. This was not the predominant view of early workers grappling with the deep-Earth consequences of the plate tectonics revolution, who tended to favour a multi-layered system (e.g., Hess 1966), with radiative heat flow in the lower mantle. Later, ideas of whole mantle convection (e.g. Schubert *et al.* 1975) and layered convection due to chemical differentiation in the lower mantle (e.g. Christensen and Yuen 1984) became more popular. Whilst today layered mantle convection seems unlikely, the advection of heat through the whole mantle is not simple with uniform behaviours from surface to CMB.

Here I introduce the mantle's mineralogical composition (section 1.2), its viscous convection (section 1.3), and our observation of it with elastic waves (section 1.4) and introduce the problems considered in this thesis.

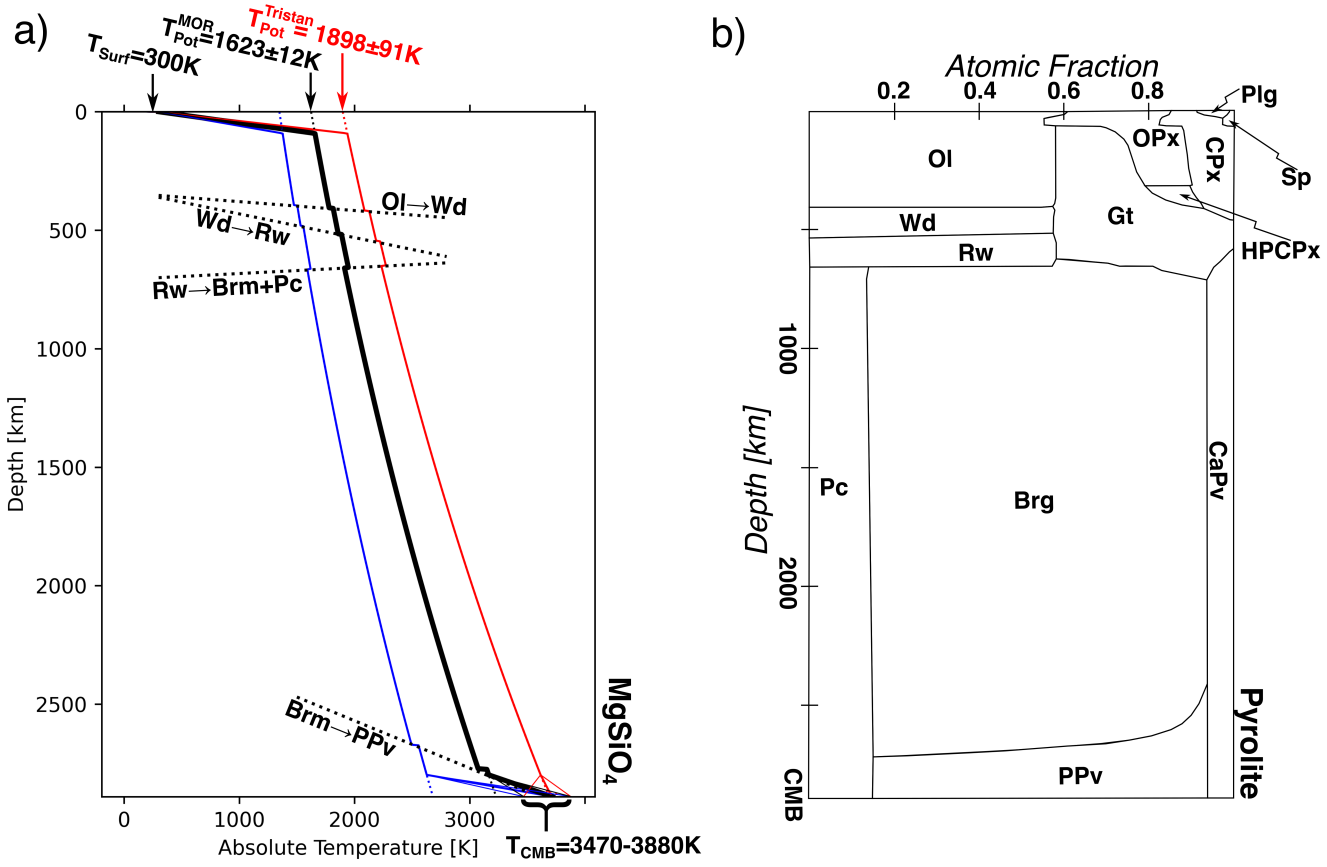

Figure 1: A summary of subsolidus convection in the Earth *a)* Convection within the mantle maintains an adiabat between the surface temperature (T_{surf} = 300 K) and the CMB Temperature ($T_{CMB} \sim$ 3740 K, Deschamps and Cobden 2022). Potential temperature beneath mid-ocean ridges (taken as indicative of the average mantle) and beneath ocean islands (taken as indicative of upwelling plumes) are estimated from olivine crystallisation temperatures (e.g. Li *et al.*, 2025), and used here to plot adiabats for the mean mantle (black dotted line), upwelling mantle (red dotted line), and downwelling mantle (naïvely assuming that the downwelling potential temperature is as cold against the ambient mantle potential temperature as the upwelling's is hot). These adiabats are deformed by the enthalpy of transformation of the mantle phase transformations, with a simplified phase diagram for $MgSiO_3$ used here. *b)* Phase proportions through the Earth's mantle (along a 1600; K adiabat for a pyrolytic mantle) adapted from Stixrude and Lithgow-Bertelloni (2024), their Figure 13. $(Mg, Fe)SiO_4$ polymorphs ('Ol' – olivine, 'Wd' – wadsleyite, 'Rw' – ringwoodite), Pyroxenes ($(Mg, Fe)SiO_3$) and Garnets ($(Mg, Fe)_3Al_2(SiO_4)_3$), ('Plg' – plagioclase, 'Sp' – spinel, 'Cpx' – clinopyroxene, 'Opx' – orthopyroxene, 'Gt' – Garnet, 'HPCpx' – high-pressure clinopyroxene), lower-mantle minerals ('Pc' – ferro-periclase, 'Brg' – bridgmanite, 'CaPv' – calcium-perovskite), and post-perovskite ('PPv').

1.2 Mantle Mineralogy

The bulk composition of the Earth is well known from the composition of rocks formed by mantle melts (e.g. Ringwood, 1962*b*) and by the composition of chondritic meteorites (e.g. Allègre *et al.*, 2001). From experimental (diamond anvil cell (e.g. Ye *et al.*, 2014)) and computational (*ab initio* calculations that use models of the fundamental physics of how mineral structure deform to determine their stability (e.g. Yu *et al.*, 2008)) studies the stability of materials under mantle conditions has been studied. This has allowed mineral physicists and petrologists to study the stability of different phases through the mantle for different compositions.

Xenoliths and ophiolites reveal that the uppermost mantle is dominantly ($\sim 60\%$, e.g. Ringwood 1962*b*) Olivine ($(Mg, Fe)SiO_4$), the remainder formed of pyroxenes and garnets. Like any mineralogical structure olivine has a limited stable range, and at increasing pressure transforms to the polymorphs Wadsleyite and Ringwoodite (Figure 1). Ringwoodite decomposes to Bridgmanite ($(Mg, Fe)SiO_3$) and Ferro-periclase ($(Mg, Fe)O$) at the top of the lower mantle. Recently the further decomposition of this perovskite structured bridgmanite has been discovered (Murakami *et al.*, 2004; Oganov and Ono, 2004) (see below section 1.4.4), where bridgmanite transforms into a 'post-perovskite' polymorph in the lowermost mantle.

The non-Olivine components of the upper mantle have a higher silica content than olivine, and are concentrated in basaltic material formed in melting at mid-ocean ridges, with a lower "magnesium number" (ratio of magnesium to iron) than the whole mantle. In the uppermost mantle, basalt is converted to eclogite, forming an assemblage of pyroxenes ($(Mg, Fe)SiO_3$) and garnets ($(Mg, Fe)_3Al_2(SiO_4)_3$). The orthopyroxene converts to a form of clino-pyroxene around 340 km depth (e.g. Xu *et al.*, 2008) and the clinopyroxene reacts to form garnet around 400 km depth. Garnet decomposes to perovskites (bridgmanite and calcium perovskite) (e.g. Stixrude and Lithgow-Bertelloni, 2022) at the base of the upper mantle. The resulting phase proportions with depth are summarised in Figure 1b for a pyrolitic mantle, which highlights the transformations with increasing depth. These phase transformations can significantly affect the dynamics and seismology, as discussed below in sections 1.3.6 and 1.4.4.

The stability of mineral phases is not just understood from an *ad hoc* empirical basis, but also from the fundamental thermodynamics (e.g. Connolly, 2005). For a particular composition, the stable assemblage is determined in nature by that assemblage that has the lowest internal energy across the

constituent phases. Using this logic codes like THERMOCALC (Powell and Holland, 1988), PerpleX (Connolly, 2005), HeFESTo (Stixrude and Lithgow-Bertelloni, 2005), Theriak/Domino (Capitani and Petrakakis, 2010), or MMA-EoS (Chust *et al.*, 2017) use our knowledge of mineral structures to find the Gibbs' free energy of every possible mineral phase at all P-T conditions, and find the assemblage of phases with the lowest Gibbs Free Energy (i.e. the stable assemblage). These same codes can produce forward models of V_S, V_P and ρ (S-wave & P-wave velocity (see Section 1.4) and density respectively) that geodynamicists can use to predict seismological structures from their thermochemical structures.

1.3 Mantle Convection

1.3.1 Equations of the Conservation of Mass, Momentum and Energy

It has been understood since the 1940s that some form of mantle convection is required, and that this convection would take the form of viscous sub-solidus convection (e.g. Holmes, 1931; Bull, 1931). Since the viscosity of the Earth's mantle is very large ($\sim 10^{21}$ Pa.s Haskell e.g. 1935) the Prandtl number

$$Pr = \frac{\eta C_P}{\kappa} \tag{1.2}$$

(which is the ratio of 'viscous diffusion' to thermal diffusion where η is the viscosity, C_P is the isobaric specific heat, and κ is thermal diffusivity (Schubert *et al.*, 2009, p266)) is very large also. This allows us to assume that inertial component of the momentum balance is negligible. As we are interested in the creeping flow problem here not the propagation of seismic waves, we also take the anelastic approximation, which will neglect a $\frac{\partial \rho}{\partial t}$ term in the mass conservation (e.g. Schubert *et al.*, 2009, p. 267) This leads to a description of the mass, momentum and energy conservation in the Earth's mantle (Schubert *et al.*, 2009, p272).

$$\frac{\partial \rho \dot{u}_i}{\partial x_i} = 0 \tag{1.3}$$

$$0 = \frac{\partial P}{\partial x_i} + \frac{\partial}{\partial x_j}\left[\eta\left(\frac{\partial \dot{u}_i}{\partial x_j} + \frac{\partial \dot{u}_j}{\partial x_i} - \frac{2}{3}\delta_{ij}\frac{\partial \dot{u}_k}{\partial x_k}\right)\right] + F_i^B \tag{1.4}$$

$$\rho C_P \frac{DT}{Dt} - \alpha T \dot{u}_i \frac{\partial P}{\partial x_i} = \frac{\partial}{\partial x_i}\left(k\frac{\partial T}{\partial x_i}\right) + \Phi + H^R + H^P \tag{1.5}$$

Where ρ is density, t is time, $\dot{u}$ is velocity of the convecting fluid, P is pressure, x is position, η is the viscosity which can vary based on most local parameters (see section 1.3.5), F^B denotes body forces - dominantly thermal - applied within the mantle (see section 1.3.6), C_P denotes the isobaric specific heat, T is temperature, α is the coefficient of thermal expansion, k is thermal conductivity, Φ is the viscous dissipation (see section 1.3.7), and internal heating is denoted by H (see section 1.3.7), split into radiogenic heating H^R and the heating due to the enthalpy of phase transformation H^P. The Einstein summation convention is used here, i, j, and k are indexes in 3D space, and δ_{ij} is the Kronecker Delta.

By the simultaneous solution of the equations above, it is possible to describe the evolution of the mantle interior. In this thesis the finite element code TERRA (Baumgardner, 1983) is used to solve these equations within a spherical shell (see section 1.5). In addition to the constitutive equations above, we require boundary conditions to solve them for an 'Earth-like' scenario.

1.3.2 Boundary Conditions

Here I describe the boundary conditions used for the simulations in this thesis that have a spherical shell geometry. For other geodynamic problems set up in different geometries different boundary conditions are required, and they can have a significant impact (e.g. van Zelst *et al.*, 2021, p607).

To solve the governing equations (1.3-1.5), we require boundary conditions on the flow and temperature. Since the surface has remained at a constant temperature over geological time (within 50 K, Judd *et al.* 2024), a fixed surface temperature is usually used. The boundary condition at the CMB is less clear - workers use either a constant temperature CMB, constant heat-flux CMB, or a CMB that has a parametrised core-cooling boundary condition (e.g. Davies, 2015). Most of the simulations here have a fixed CMB temperature boundary condition (a varied parameter as it is poorly known in the real Earth, but for compressible simulations it is around $3200 - 4000$ K (e.g. Boehler, 2000)).

The boundary condition on flow however are less trivial. Since the mantle cannot transmit stresses from itself to the atmosphere or outer core, this requires that the surface and the CMB act as free surfaces. This then requires that the surface normal traction vector (t_i) goes to 0 (e.g. Kennett and Bunge, 2008, p. 134), so

$$t_i = \sigma_{ij} \cdot \hat{n_i} = 0 \tag{1.6}$$

where σ_{ij} is the full stress tensor and $\hat{n_i}$ is the unit normal vector. This then implies 0 radial stress at the surface. This is then approximated as a free-slip

condition,

$$\hat{n_i} \cdot \hat{\dot{u}_i} = 0 \tag{1.7}$$

where $\dot{u}_i$ as above is velocity. This implies no-mass flux across the Earth's surface and CMB. Whilst not strictly true (for instance, ocean water is entrained into subducted slabs and can have an important role in the dynamics, geochemistry and seismology of the mantle wedge (e.g. Ohtani, 2021)), as a first order assumption for the whole mass of mantle material this assumption holds.

However, at the surface we have a good knowledge of the current and historic plate motion histories (e.g. Müller *et al.*, 2022). Imposing these as a surface boundary condition allows us instead to simulate the historic *circulation* of the Earth's interior – this boundary condition to TERRA was introduced by Bunge *et al.* (1998). We then require instead the plate-motion velocities ($\dot{u_i}^{p(t)}$)

$$\dot{u_i} = \dot{u_i}^{p(t)} \tag{1.8}$$

at the surface of the simulated mantle. The great advantage of these Mantle Circulation Models (MCMs) is that they allow models to assimilate our knowledge of the Earth's surface motions as a constraint on the model evolution and to simulate the impact of these surface motion patterns on the interior dynamics (e.g. Bunge *et al.*, 2002).

1.3.3 Compressibility and the Equation of State

Thermodynamic state is described using "variables of state". For the mantle convection problem (1.3-1.5) these are P, T, and V (as density, ρ) (e.g. Poirier, 2000, p. 56), and as we solve the convection problem we require a relation between them.

If we take the Boussinesq approximation that only lateral density anomalies need be considered, then we also assume an *incompressible* equation of state. (1.3) becomes

$$\frac{\partial \dot{u}_i}{\partial x_i} = 0 \tag{1.9}$$

(i.e. we conserve volume not mass). The first term in the momentum equation (1.4) becomes the gradient in non-hydrostatic pressure, $P' = P - \rho_0 g z$, where z is the radial depth (Kennett and Bunge, 2008, p. 122). Therefore, the momentum conservation equation (1.4) becomes

$$0 = \frac{\partial P'}{\partial x_i} + \frac{\partial}{\partial x_j}\left[\eta\left(\frac{\partial \dot{u}_i}{\partial x_j} + \frac{\partial \dot{u}_j}{\partial x_i} - \frac{2}{3}\delta_{ij}\frac{\partial \dot{u}_k}{\partial x_k}\right)\right] + F_i^B \tag{1.10}$$

We must also drop the adiabatic heat change term $\left(\alpha T\dot{u}_i \cdot {}^{\partial P}/_{\partial x_i}\right)$ from the heat conservation equation (1.5), as well as Φ and heat generated non-radiogenically (see section 1.3.7 below), so the energy conservation equation becomes

$$\rho C_P \frac{DT}{Dt} = \frac{\partial}{\partial x_i}\left(k\frac{\partial T}{\partial x_i}\right) + H^R \tag{1.11}$$

The Boussinesq approximation has the advantage that it makes the convection problem much simpler and computationally cheaper to solve, but its validity shouldn't be taken for granted. The validity of the Boussinesq approximation is evaluated by considering the length scale of variations of density ($\bar{h_d}$) compared to the thickness of the convecting layer (Ricard, 2007, p. 52). The approximation is valid when

$$\frac{D}{\bar{h_d}} \ll 1$$

This ratio is known as the Dissipation number,

$$D_i = \frac{\alpha g D}{C_P} \tag{1.12}$$

which for the mantle works out to be around 0.6. Since the Boussinesq approximation assumes $D_i \to 0$, it is only approximately valid for the Earth's mantle (e.g. Ricard, 2007). If instead we allow the mantle to be compressible we require values for ${}^{\partial P}/_{\partial x_i}$. The compressible simulations in this simulation use a *Murnaghan* equation of state. If we consider the compression from an initial pressure P_0 to some other pressure P, this is written in terms of the bulk modulus K, the initial gradient of the bulk modulus $K_0' = {}^{dK}/_{dP})_{P_0}$ and the initial density at ρ_0 (e.g. Poirier, 2000, pp. 56-58).

$$P = \frac{K_0}{K_0'}\left[\left(\frac{\rho}{\rho_0}\right)^{K_0'} - 1\right] \tag{1.13}$$

which is readily differentiable to yield ${}^{\partial P}/_{\partial x_i}$, where

$$K_0 = \frac{1}{3}(3\lambda_0 + 2\mu_0) \tag{1.14}$$

and ρ is the density at the pressure of interest, λ_0 and μ_0 are the Lamé constants before compression (μ is also known as the shear modulus). The most significant impact of including the compressibility is in the radial temperature profile. Since for gentle pressure-temperature profiles ${}^{\partial P}/_{\partial x_i}$ is small, this does not effect the dynamics dramatically (e.g. Ita and King, 1994), but captures the fundamental fluid dynamics better. The Boussinesq approximation, however,

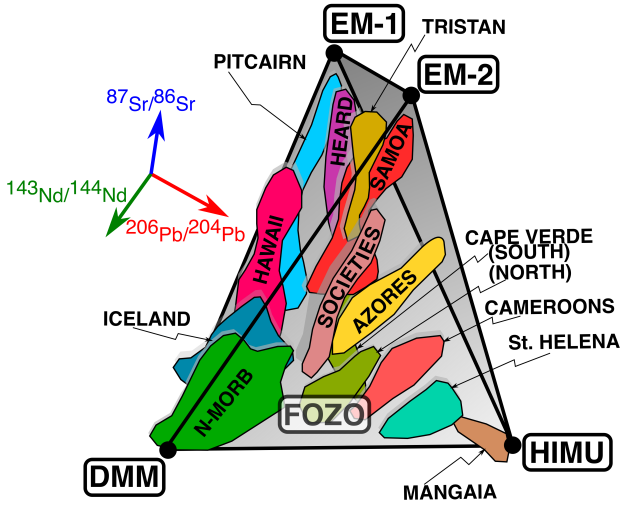

Figure 2: Compositional trends of oceanic basalts after Hart *et al.* (1992), plotted in $^{87}Sr/^{86}Sr$, $^{206}Pb/^{204}Pb$, and $^{143}Nd/^{144}Nd$ space. Interpreted endmembers DMM (depleted mantle), EM-1 and EM-2 (Enriched Mantle sources), HIMU (high field strength abundance) and FOZO (Focal Zone composition). Clusters are labelled according to ocean island or as N-MORB ("Normal" variety of MORB). This figure is traced from the figure in the original paper, with sketched shadows to aid the perception of the third dimension.

allows for simpler models that focus on the effects of the forces that drive the global convection. Various simulations in this thesis use compressible and incompressible equations of state, as appropriate to the motivation of the simulation.

1.3.4 Variation in Composition

It is well known that the silicate Earth – surface and interior – is compositionally heterogenous. Fertile lherzolitic upper mantle melts at mid-ocean ridges (e.g. Hess, 1966), producing 'enriched' (in incompatible elements and isotopes) basaltic crust and a 'depleted' refractory reservoir of harzburgite beneath. These are moved together to the oceanic trench before being subducted (along with sediments and water hosted within them (e.g. Pons *et al.*, 2022)) into the mantle interior. Whilst a series of complex fluid-mediated reactions take place in the mantle wedge, the bulk compositional heterogeneity being of fertile, enriched, and refractory, depleted, material sinks deep into the mantle. The ocean-ridge derived melts described above are known as mid-ocean ridge basalts (MORB). As well as at mid ocean ridges the mantle melts at 'hotspots' created due to hot thermal plumes (Morgan, 1971) beneath the plate interiors forming ocean island basalts (OIB) (e.g. Wilson, 1965). These are generally thought to be associated with plume upwellings from the CMB.

Whilst MORB basalts tend to fall in a tight geochemical space, for many trace element concentrations and isotopic ratios, Ocean Island Basalts, on the other hand, have diverse compositions often plotting away from the MORB trend (e.g. Hart *et al.*, 1992, see Figure 2).

The focus of this thesis is not the geochemical evolution of the mantle, but the point of this discussion is to highlight that whilst the details of the compositions are complex, bulk composition can be simplified into four end-members; 'fertile' Lherzolite that melts to form 'Enriched' basalt leaving behind a 'depleted' harzburgitic residue. Additionally, a plume-feeding 'primordial' reservoir may also be present.

Details of the implementation of particles and melting in TERRA are included in section 1.5. In many geodynamic codes, compositional variation is described using a scalar C. In TERRA this value ranges between 0 and 2. Depleted material has a 'C-Value' of 0, Lherzolite of 0.2, Basalt of 1 and any primordial material in a simulation is treated as having a C-Value of 2 (Van Heck *et al.*, 2016). The advection of composition is governed by the conservation law that is solved simultaneously with (1.3-1.5)(e.g. Zhong *et al.*, 2007)

$$\frac{\partial C}{\partial t} - \dot{u}_i \frac{\partial C}{\partial x_i} = 0 \tag{1.15}$$

to prevent the bulk composition of the Earth changing as there are no significant mass fluxes to effect this (Equation 1.7). If melting happens in a scheme like TERRA's that allows it, the amount of depletion according to the applied solidus is calculated, the C-value of the particle that is undergoing melting is reduced by that amount, and this C-value is transmitted to a particle that can receive it (i.e. has a C-value less than 1) near the surface, neither creating nor destroying composition.

The implementation of composition is discussed in section 1.5.3

1.3.5 Viscosity

The development of isostatic theory to explain gravity anomaly data in the late 19th Century, combined with the propagation of longitudinal waves through the mantle established that the Earth's mantle was a viscously deformable solid (e.g. Gilbert, 1890, pp. 377-383). Haskell (1935) used the then-recently dated elevated paleo-beaches in Scandinavia to estimate the uplift history of the Fenno-Scandinavian shield after the last glaciation. This allowed him to estimate the viscosity of the mantle under the shield as 3×10^{21} Pa.s. Whilst a "classic and enduring constraint on the Earth's interior" (Mitrovica, 1996) – to understand its significance a couple of caveats must be applied. Firstly, that the

constraint is on the *mean* viscosity beneath the rebounding continent, and secondly that the sensitivity is not uniform - but rather focused in the upper mantle and transition zone and extends down to $\sim$ 1400 km depth, decaying with depth (Mitrovica, 1996). Together, this means the strong 'Haskell constraint' on upper mantle rheology leaves room for a broad suite of different radial mean viscosity structures that still satisfy it (e.g. Steinberger and Calderwood, 2006). The radial viscosity structure and the rheology more broadly are therefore a key modifiable parameter in current geodynamic modelling (e.g. Gülcher *et al.*, 2022; Desiderio and Ballmer, 2024). Further, lateral variations in viscosity controlled by temperature, composition, and strain rate may be as significant as radial viscosity variations, although TERRA is not as effective as other codes at resolving these strong lateral variations.

Asthenosphere

In the upper mantle the primary region of interest lies directly beneath the lithosphere – coincident with the low velocity layer where V_S and V_P drop (e.g. Rychert and Shearer, 2009). A weak thin aesthenosphere is argued for from the relaxation-time structure of post-glacial rebound. Short wavelength lateral distribution of the decay time of the rebound suggests a slower lateral isostatic adjustment – i.e. a more viscous aesthenosphere (e.g. Paulson and Richards, 2009). From this decay-time data there exists a strong trade-off between the viscosity reduction in this layer and its thickness. A weak aesthenosphere could prove useful in explaining a broad suite of data. Sitting as it would on the interface between the convecting mantle and the cold thermal boundary layer, the aesthenosphere potentially has complex dynamics (e.g. Wang *et al.*, 2023) and a significant impact on the dynamics of slabs (Cerpa *et al.*, 2022), plumes and the broader circulation. In the class of models considered in this thesis, however, it is often difficult to resolve the aesthenosphere.

Lower Mantle Viscosity Structure

Going into the mid- and lower-mantle the glacial isostatic adjustment (GIA) data discussed above is insufficient to recover many details about the viscosity structure. Instead, other constraints must be used. Mitrovica and Forte (2004) showed that inverting GIA data alone leads to a simple viscosity structure $log(\eta) \propto z$ in the lower mantle. Authors generally consider a combination of geophysical observables (Geoid (e.g. King, 2016), CMB ellipticity (e.g. Mitrovica and Forte, 2004), surface motions, and dynamic topography (e.g. Panasyuk and Hager, 2000)) or make *a priori* assumptions about the physics of

grain deformation to predict the viscosity structure with depth (e.g. Steinberger and Calderwood, 2006; King, 2016).

The simplest intuition from mineral physics is that the viscosity should change at the 670 km deep seismic discontinuity (see section 1.4.2) where the mineralogy changes from Ringwoodite to Bridgmanite (which is experimentally quite rigid (e.g. Girard *et al.*, 2016)) and periclase (experimentally weaker but less abundant so cannot form interconnected weak layers (e.g. Thielmann *et al.*, 2020)). The assumption historically has been that this should lead to an increase of viscosity by a factor of $10 < \Delta\eta < 100$. Garel *et al.* (2014) showed that a viscosity jump in this range produces a variety of downwelling morphologies comparable to those of seismically fast regions imaged by seismic tomography. However a simple 'jump' at 660km is but one of the many mid-mantle radial viscosity structures that have been proposed in the literature, including multiple jumps, viscosity hills or a jump at a deeper depth than 660km.

Temperature Dependent rheology

Ultimately, the viscous flow of the mantle requires the grains that make up mantle rocks to deform. Two key deformation mechanisms were first highlighted by Gordon (1967, Schubert *et al.* 2009, p. 240) to be relevant in the mantle; diffusion creep and dislocation creep.

In diffusion creep vacancies 'diffuse' through the lattice, with atoms swapping into the space of the vacancy, forming a new vacancy, thus achieving the deformation of the grain. Herring's (1950) formulation of diffusion creep was demonstrated as correct by experiments in alkali metals (e.g. Jones, 1965) and oxides (including periclase, e.g. Vasilos *et al.*, 1964) where the strain rate ($\dot{\varepsilon}$) is dependent on deviatoric stress (τ), grain size (d), and temperature (T),

$$\dot{\varepsilon} \propto \frac{\tau}{d^2 T} \tag{1.16}$$

(Gordon 1967, Poirier 2000, p. 153). The linear dependence on stress means that diffusion creep is a Newtonian viscosity law.

The other major mode of deformation is dislocation creep where linear defects move the volume of the mineral. Unlike diffusion creep, dislocation creep has a non-Newtonian dependence

$$\dot{\varepsilon} \propto \tau^n e^{\frac{-(E_A + pV_A)}{RT}} \tag{1.17}$$

where n is usually around 3.5 (e.g. Schubert *et al.*, 2009, p. 243). Both diffusion

and dislocation creep happen within mantle materials, but the strain rate is controlled by the faster of the two mechanisms, and this varies on temperature, pressure, shear stress and grain size, and therefore in different regions of the mantle different creep regimes dominate (e.g., Figure 1 in Dannberg *et al.*, 2017), with diffusion creep usually expected to dominate in the lower mantle, and dislocation creep in the upper mantle. The simulations in this thesis use a linear, Newtonian rheology that is physically motivated by diffusion creep, perhaps acceptable if it dominates in the deep mantle (e.g. Karato *et al.*, 1995), but principally for computational reasons.

As both creep laws are dependent on temperature (Poirier, 2000, pp. 152 – 157) the viscosity is also expected to be temperature dependent (e.g. Yang, 1997). Whilst many formulations for the temperature dependence of viscosity exist, the simulations in this thesis use the relation (Davies *et al.*, 2012)

$$\eta(z, T) = \eta_0 f(z) e^{V_a Z' - E_a T'} \tag{1.18}$$

where V_a and E_a are the non-dimensionalized activation volumes and energies respectively, η_0 is the reference viscosity, and $f(z)$ are depth-dependent factors that capture the radial control on rheology. T' and Z' are non-dimensionalized temperature (against the temperature range in the mantle $T' = 0.5 - \frac{T - T_{CMB}}{T_{surf} - T_{CMB}}$) and depth (against the depth of the mantle $Z' = \frac{z}{D}$) respectively. V_a is usually assumed to be 1 in the models in this thesis so that the depth-dependence comes predominantly from the pre-exponential term. E_a is usually set at 1.75, a moderate temperature dependence compared to other recent studies using TERRA (e.g. Plimmer *et al.*, 2024; Davies *et al.*, 2025), although when dimensionalized (e.g. Javaheri *et al.*, 2024) to $E_a^* \simeq 5 \times 10^4$ J.mol^{-1}, this is an order of magnitude less than those used in other studies of mantle dynamics (e.g. Agrusta *et al.*, 2017), and reflects the challenges of resolving strong lateral viscosity variations in TERRA.

1.3.6 Body Forces

Above in Equation 1.4 I described the term F_i^B as 'body forces'. I enunciate them here such that F_i^B is the sum of the thermal, compositional and phase boundary buoyancy forces.

$$F_i^B = \rho_0(z)(1 + \alpha \Delta T) \cdot g_i + C \Delta \rho_C(z) \cdot g_i + F_i^P \tag{1.19}$$

where $\rho_0(z)$ is the depth-dependent reference density, g is gravitational acceleration, C is the C-value discussed in section 1.3.4, $\Delta \rho_C(z)$ describes the

density anomaly for the composition at that depth. F^P denotes the buoyancy force due to topography on phase transitions (below and Chapter 2).

Thermal Buoyancy

The first term defines the buoyancy anomalies due to temperature variations. These are the main driver of the convection, but it is worth verifying this briefly. We can consider the buoyancy number (e.g. Tackley, 2007) of a material in a convecting mantle as

$$B = \frac{\Delta\rho_C}{\rho\alpha\Delta T} \tag{1.20}$$

i.e. the ratio of compositional and thermal buoyancies.

For the density variations predicted for enriched compositions in the mid-mantle, ($\Delta\rho_C/\rho \sim 3\%$, see Figure 3, and assuming a temperature range of 500 K) B is typically ~ 0.5, that is the compositional density anomalies are half that produced by the thermal convection, so are able to modulate the convection to some degree.

Phase Transitions

Whilst the whole mantle convects as one system, the phases that make up mantle rocks change through the depth of the mantle. These "phase transitions" are chemical reactions where some mineral assemblage $A + B$ transforms to denser phases $C + D$ with increasing pressure. For an exothermic reaction (where the entropy change is positive, i.e. $\Delta S > 0$) the equilibrium pressure moves to lower values at cooler temperatures and *vice versa* at warmer temperatures. This results in density anomalies *due to the change in phase* in regions hotter or cooler than average, and therefore body forces F_P. For exothermic reactions the resulting buoyancy forces are in the same sense as the thermal buoyancy force and are so called 'pro-convective'. For endothermic reactions (i.e. $\Delta S < 0$), however, the body forces work against thermal buoyancy. If the reaction parameters are suitable this can result in a "layered" convection. This phase buoyancy effect is the dominant effect of phase transitions on the convection, but the heat released by the reaction does change the local temperature field (Verhoogen, 1965), but this effect is smaller than the topography effect. Christensen (1998) quantified the impact globally of the latent-heat effect as causing a topography of ~ 4 km on the discontinuity (the buoyancy effect of this would be stronger than the variations due to thermal expansion). For comparison, for a temperature range of 500 K, a mid-mantle pressure gradient of 40MPa.km^{-1}, and using the same Clapeyron slope as

Christensen (1998) of -2.8MPa.K^{-1}, the global variation in the phase transformation depth not accounting for the latent heat is about 35 km. This can visually be verified by considering Figure 1a. The distortion of the temperature field by the endothermic ringwoodite-out reaction makes the mantle directly beneath a downwelling slightly cooler, favouring the downwelling's penetration of the boundary, but this thermal buoyancy difference is much smaller than that due to the $O(10\%)$ density difference across the phase transformation, which the topography on the transformation causes to exert a counter-convective forcing. I discuss the effects of phase transitions on the dynamics of the Earth's mantle at length in Chapter 2.

Melting-Derived Chemical Heterogeneity Density Anomalies

Pyroxenite, formed from basalt as it enters the mantle, is generally denser than harzburgite or lherzolite, and so regions with a lot of basaltic composition material have a different buoyancy field. When this melting-derived heterogeneity is tracked in simulations depending on the size of the compositional density anomaly it can form "ribbons" of compositional heterogeneity in the mid-mantle (e.g. Van Heck *et al.*, 2016) or can accumulate to form large piles at the base of the mantle (e.g. Jones *et al.*, 2021). The dynamic significance of compositionally distinct material is described with the 'buoyancy number' above (Equation 1.20).

The "Basalt Barrier Effect"

There are two major groups of mantle materials, which undergo two distinct sets of reactions. The reactions in the olivine group are $Ol \rightarrow Wd(410)$, $Wd \rightarrow Rw(520)$, $Rw \rightarrow Brm + Pc(660)$, and for the pyroxene group of minerals they are $OPx \rightarrow Gt(60)$, $Cpx \rightarrow Gt(400)$, $Gt - Brm(720)$ (e.g. Ono *et al.*, 2001). Through the upper mantle the difference in depths of the reactions are small or the magnitude of the pyroxene-series reaction density jumps are small enough that they do not exceed the density of pyrolite (e.g. Yan *et al.*, 2020). However, at most temperatures, the post-garnet reaction is much deeper than the post-spinel reaction, meaning that garnet-rich material (such as might be formed from subducted oceanic crust) is more buoyant than pyrolite in the mantle between the post-spinel and post-garnet reactions (between around 670 and 720 km depth), see Figure 3. Davies ($2008a$) named this the "basalt barrier", which in numerical models results in an accumulation of basaltic material between the post-spinel and post-garnet reactions, potentially producing sheets of basaltic composition material in the mid-mantle, which are

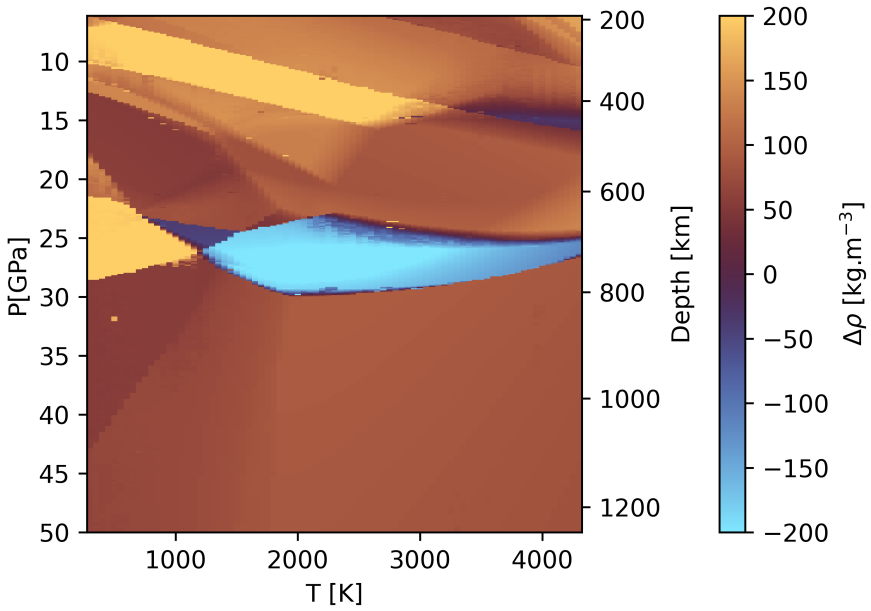

Figure 3: Difference in density between Basaltic material and Lherzolite in P-T space in the mid-mantle, calculated from tables found using (Stixrude and Lithgow-Bertelloni, 2005, 2011, 2022) data and the PerpleX (Connolly, 2005) Gibbs free energy minimisation software. Note that in most of the mid-mantle, basalt is denser than lherzolite, but in the basalt density filter around 700 km depth, since the post-garnet reaction is deeper than the post-spinel reaction, the basaltic material is less dense than lherzolite.

emplaced by hot plumes, before the basaltic material cools and descends into the interior. This could produce an enriched reservoir in the mid-mantle as well as in the thermal boundary layers (e.g. Yan *et al.*, 2020).

Primordial Material

As discussed above (section 1.3.4) there has been an expectation from some geochemical systems (e.g. Hart *et al.*, 1992; Hofmann, 2014) for distinct reservoirs in the lower mantle that feed plumes and OIB-source rocks (although not all systematics require it (e.g. Panton, 2020)). Additionally observations of the large low velocity provinces (LLSVPs – see section 1.4.3) in the lowermost mantle, which have an elevated $^{V_S}/_{V_P}$ ratio have been explained with distinct material at the CMB although the post-perovskite phase transition may make this unnecessary (Davies *et al.*, 2012). Primordial material, enriched in the incompatible elements concentrated in OIBs have long been suggested as a candidate reservoir, but remain hotly debated. Situated at the base of the mantle at the start of geodynamic simulations, they are swept by the circulation (constrained by plate motion histories) into piles resembling LLSVPs (e.g. Bull *et al.*, 2014), the significance of LLSVPs is discussed further in Section 1.4.3,

but here it is important to note that the LLSVPs need not be and probably are not primordial piles (e.g. Davies *et al.*, 2015*b*). Properly, such simulated structures should not be referred to as LLSVPs, or variants there on, but rather as piles to distinguish them from the observation. To remain at the CMB they must remain denser than the surrounding downwelling material, even when heated from below (and within – see section 1.3.7), so are usually simulated with a higher excess density than basalt. Although they are controversial within the geodynamic community, primordial materials (particularly when swept into piles) do change the pattern of convection so are considered in this thesis as an hypothesis of interest.

1.3.7 Energy Balance

Turning from the 'momentum' equation (1.4) to the advection-diffusion equation (1.5). As well as the terms relating to change in thermal energy, adiabatic temperature changes and thermal diffusion, the thermal balance is controlled by the terms Φ and H.

Shear Heating or Viscous Dissipation

Φ represents the "viscous dissipation" or "shear heating" within the convecting solid – essentially indicative of the work done ($W = F\Delta x$) against the rheology of the mantle's interior (e.g. Schubert *et al.*, 2009, p. 262).

$$\Phi = \tau_{ij}\frac{\partial \dot{u}_i}{\partial x_j} \tag{1.21}$$

where τ is the deviatoric stress tensor. If incompressibility is assumed, Φ is neglected, since viscous dispersion implicitly requires the material to be compressible in order for work to be done against and generate heat (Kennett and Bunge, 2008, p. 122).

Internal Heating

As well as heat from the base of the mantle, energy to drive the convection comes from heat sources within the mantle interior, referred to as H.

I have already mentioned that phase transitions release and consume heat as material passes through them, and this affects the energy balance in the term H^P in (1.5), either as a positive source or a negative sink, depending on the direction of the reaction and the endothermic/exothermic nature of the reaction. This is included in the simulations in this thesis, except where explicitly mentioned in Chapter 2.

Additionally, the decay of heat producing elements (HPEs) in rocks produces heat (H^R in (1.5)). As HPEs tend to be large, heavy isotopes they tend to strongly segregate into melts (e.g. Davies, 1999, p193) and are consequently most concentrated in the continents. However, since this heating is near the surface it does not have a driving effect on the flow in the mantle below. The decay of HPEs within the interior of the mantle provides just over half the heat budget of the Earth (e.g. Lay *et al.*, 2008). Due to their relative (in)compatibility, the distribution of HPEs can create non-uniform internal heating. This can counteract the excess density of enriched or primordial material, eventually destroying piles if the concentration of HPEs is sufficiently high or the excess density of enriched/primordial material is not sufficiently high (e.g. Huang *et al.*, 2022). Both of these effects will be included in the simulations presented in this thesis where appropriate. Where H^R is assumed to be uniform, such as in the initial convection phase of the simulations in Chapter 4, a globally uniform but time-dependent (based on the decay of radiogenic elements in the bulk-silicate Earth) value is used. Where the distribution of internal heating varies through the model interior, the abundance of individual heat producing isotopes are tracked on each particle, fractionating according to their relative partition coefficients (e.g. Van Heck *et al.*, 2016), which then decay according to their decay constants (Panton *et al.*, 2022, 2025; Davies *et al.*, 2025).

1.4 Mantle Seismology

1.4.1 The Seismic Wave Equation

As well as being a viscous fluid on the time scale of mantle convection (~ 10 Ma), on much shorter timescales (~ 1 s) the Earth's mantle behaves elastically. Large energy releases in the interior of a body creates waves that travel large distances ("teleseismic waves") – first observed at Potsdam in Germany from a Japanese earthquake in 1889 (Rebeur-Paschwitz, 1889). The traveltimes and amplitudes of waves from earthquakes and large (nuclear) explosions allow us to study the bulk-mechanical properties of the mantle's interior. This behaviour can be described with the seismic wave equation (Aki and Richards, 1980, p64).

$$\rho \cdot \ddot{u}_i = f_i + (\lambda + 2\mu)\frac{\partial}{\partial x_j}\frac{\partial u_j}{\partial x_i} - \mu\frac{\partial}{\partial x_i}\frac{\partial u_j}{\partial x_j} \tag{1.22}$$

where $\ddot{u}_i$ is acceleration, u_i is displacement (that is the motion of elements of

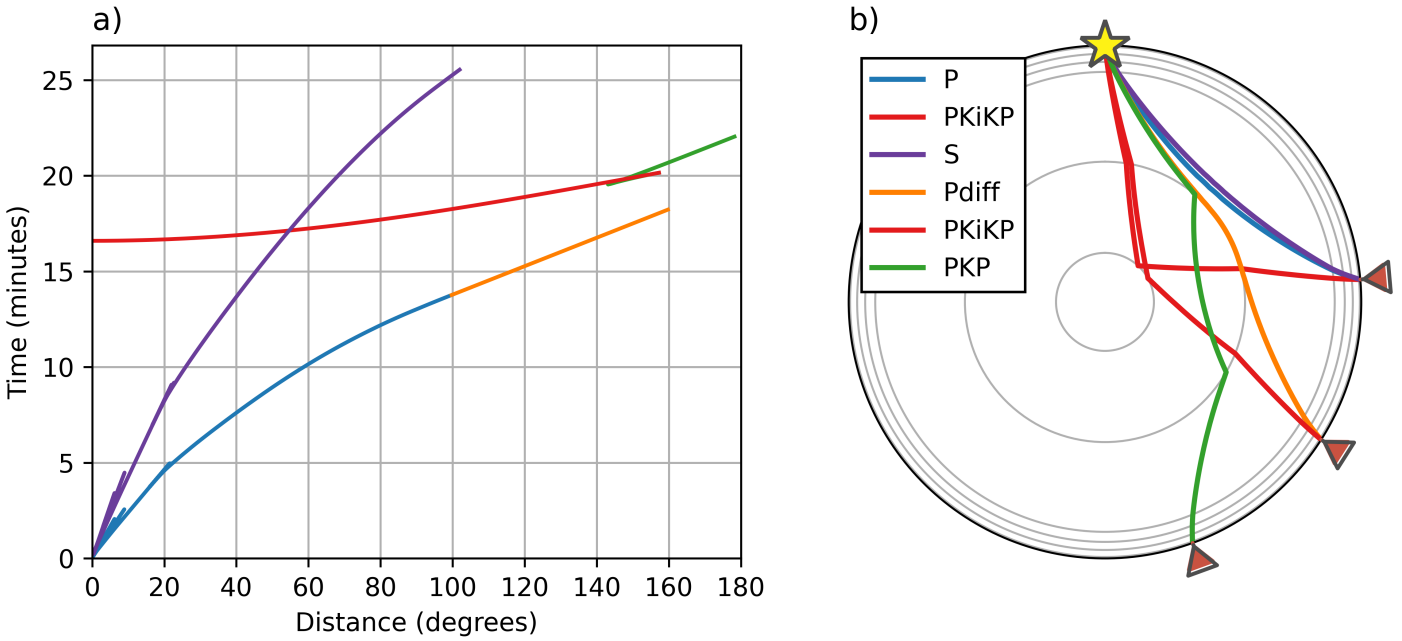

Figure 4: *a)* travel time curves and *b)* ray geometries for select phases *P*, *S*, *Pdiff*, *PKiKP*, *PKP*. Plotted using *ObsPy* (Krischer *et al.*, 2015) for Jeffreys and Bullen (1940) tables.

the Earth away from their elastic equilibrium), f_i is a source term, λ and μ are again the Lamé constants.

Qualitatively this equation of motion has three terms. First, the source term f_i drives the propagation of waves through the volume. Away from the source, we are left with a term where the motion is dependent on the divergence gradient of displacement ($\frac{\partial}{\partial x_j}\frac{\partial u_j}{\partial x_i}$) and a term where the motion is dependent on the second curl ($\frac{\partial}{\partial x_i}\frac{\partial u_j}{\partial x_j}$) of the displacement field. These terms describe the two body waves that can penetrate through elastic volumes – P waves and S waves with velocities $V_P = \sqrt{\frac{\lambda+2\mu}{\rho}}$ and $V_S = \sqrt{\frac{\mu}{\rho}}$, (e.g. Shearer, 2009, p45).

1.4.2 Traveltime Curves and 1D Profiles

The most fundamental data from global seismology about the Earth's mantle is the teleseismic-traveltime curves. These were constructed for individual earthquakes in the earliest 20th century (e.g. Mohorovicic, 1992; Byerly, 1926) but by the the mid-century global travel-time tables were being used to locate earthquakes and nuclear explosions from teleseismic arrivals (e.g. Kennett and Engdahl, 1991). These are constructed by recording the traveltimes of phases to seismic stations at different offsets from Earthquakes. The gradient of the travel-time offset curve represents the ray parameter $\left(p = \frac{sin(i)}{V_\Psi}\right.$, where i is the

angle of incidence of the ray$\Big)$ of the wave, that suggests that these may be inverted for velocity structure.

As well as direct S or P wave arrivals other seismic phases exist, generated from the interaction of a seismic wave with Earth structure. For instance, Mohorovicic found distinct 'direct' (surface), (topside) 'reflected', and 'head' (refracted) phases from the interaction of S and P waves with the crust-mantle boundary - now named in his honour the Moho discontinuity. Similarly, Byerly (1926) interpreted a shallowing of the travel-time curves at 20° source-receiver separation as a jump in seismic velocity – this "20° discontinuity" (see Figure 4 a) is now known as the 410 km discontinuity.

A casual glance at travel-time curves also highlights that most phases are not present out to antipodal source-receiver separations – requiring specific ray-paths through the Earth's interior. The presence of the liquid outer core creates "shadow zones" such that S-waves cannot propagate and P-waves only at a much reduced velocity compared to the surrounding mantle. Gutenberg (1913) used phases P and *Pdiff* (see Figure 4 a) to estimate the depth of the core-mantle boundary to within 10 km of current estimates, and produced a first estimate on V_P and V_S structure of the core (it was not until 1926 Jeffreys (1926) showed that the outer core was fluid). Lehmann (1936) used arrivals within this shadow zone to argue for the existence of so-called 'P'' arrivals (now known as *PKiKP* – see Figure 4 a) due to reflections off an inner core boundary. When a seismic wavefront interacts with an interface within the volume of the Earth, as well as reflecting or refracting, the mode of propagation can change, for instance *Ps* which are S arrivals formed at an interface by the interaction of an incident P-wave (e.g. Vinnik, 1977). These arrivals are usually very low amplitude, and the seismogram must be post-processed for the arrivals to be 'picked', usually using receiver-function processing methods (e.g. Vinnik, 1977), for inferences about mid-mantle structure to be drawn (e.g. Chevrot *et al.*, 1999; Glasgow *et al.*, 2024). Conversions also happen at interfaces like the CMB, where *PKS* arrivals have a sufficiently high amplitude that it is possible to investigate the anisotropy in the mantle and lithosphere from S-waves formed and polarised perpendicular to each other during the interaction (e.g. Wolf *et al.*, 2025).

The slope of the travel time curves (Figure 4a) imply a slowness $\left(\delta{}^{1}\!/\!_{\dot{u}}\right)$, which we might naïvely attempt to invert for $\dot{u}$. However, many different velocity structures will produce the same traveltime curve (e.g. Shearer, 2019, Figure 5.3), to resolve this, additional arrivals that may form triplications from layers in velocity must be considered (e.g. Shearer, 2019, p. 102). The methods

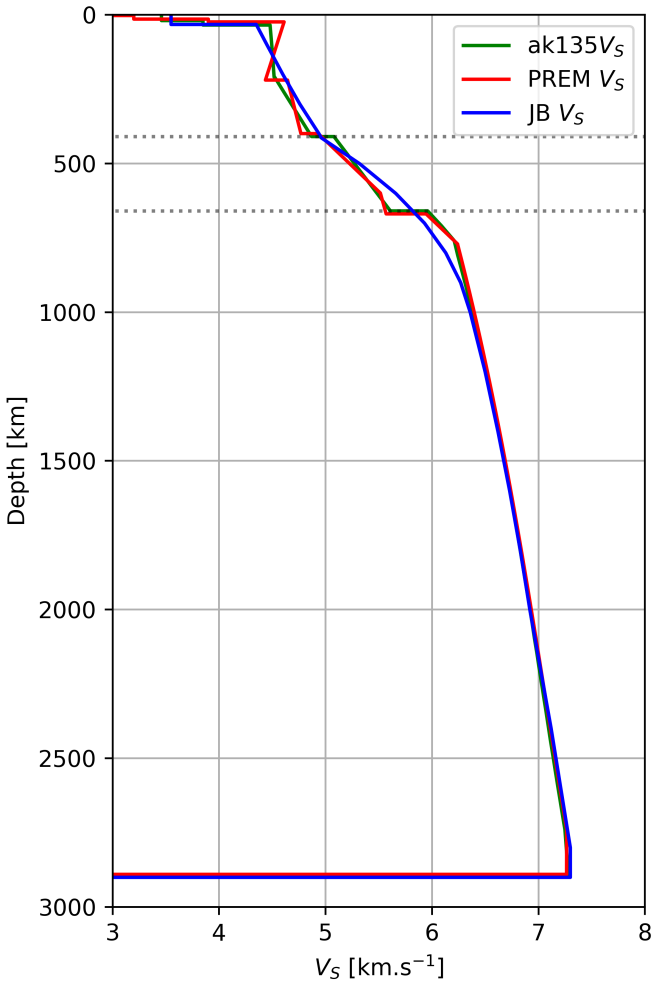

Figure 5: Comparison of radial V_S structure of 1D global models in the mantle. Jeffreys and Bullen (1940) (JB – blue line) are compared to PREM (red line) (Dziewonski and Anderson, 1981) and ak135 (green line) (Kennett *et al.*, 1995). Note that throughout the lower mantle, the inverted V_S structures are extremely similar, and that elsewhere, the models (particularly PREM and ak135) are so close to each other that they cannot be distinguished, suggesting the 1D structure of the lower mantle is well known. Dotted lines indicate the depths of 410 and 660 km, associated with discontinuities in V_S and V_P in modern models of seismic velocity.

used to invert traveltime data for modern 1D radial velocity profiles is beyond the scope of this discussion (e.g. Dziewonski and Anderson, 1981; Kennett and Engdahl, 1991; Kennett *et al.*, 1995). Whilst authors such as Gutenberg (1913) had produced velocity-depth tables, the classic traveltime tables and velocity inversion were the "JB" tables (Jeffreys and Bullen, 1940) which were widely used into the late 20th century for the location of Earthquakes, when newer tables (e.g. PREM (Dziewonski and Anderson, 1981), ak135 (Kennett *et al.*, 1995), iasp91 (Kennett and Engdahl, 1991)) were produced and superseded JB. The JB tables were calculated by hand, with much more limited data than modern velocity inversions, are not that dissimilar through most of the mantle from these newer tables (see Figure 5). Birch (1952) used the JB tables to demonstrate that the seismic discontinuities had to be due to a chemical or mineralogical change (although Bernal (1936) had already suggested an Ol-out reaction to explain the 20° discontinuity). Ringwood (1962*a*) associated the 660 km discontinuity with the spinel-out reaction, and this was later demonstrated experimentally to occur at appropriate $P-T$ conditions by Liu (1974).

1.4.3 Tomography

Whilst the travel time curves demonstrated the radial structure of the Earth's structure well they could not illuminate 3D mantle V_S, V_P, or ρ structure. Dziewonski *et al.* (1977) used the perturbations δt in travel time of the direct phases P and S to develop the first 3D global tomography model. δt is the integral of slowness perturbations $\left(\delta 1/\dot{u}\right)$ along a ray path s

$$\delta t = \int \delta 1/\dot{u}(s)\, ds \tag{1.23}$$

for rays (indexed in i) and regions (j) (1.23) becomes

$$\Delta t_i = \sum_{j=1} G_{ij} \Delta 1/\dot{u}_j$$

$$\underline{d} = \underline{\underline{G}} \cdot \underline{m} \tag{1.24}$$

this is the fundamental equation (where $\underline{\underline{G}}$ is a matrix of coefficients) between the travel-time data vector $\underline{d}$ and velocity model vector $\underline{m}$ allowed Dziewonski *et al.* (1977) to produce a model for mantle seismic structure. Modern seismic inversion uses many more parts of the waveform the just the direct-ray travel time. These images have proved an enduring constraint and motivation for mantle geodynamics. As V_S in particular is dependent on temperature

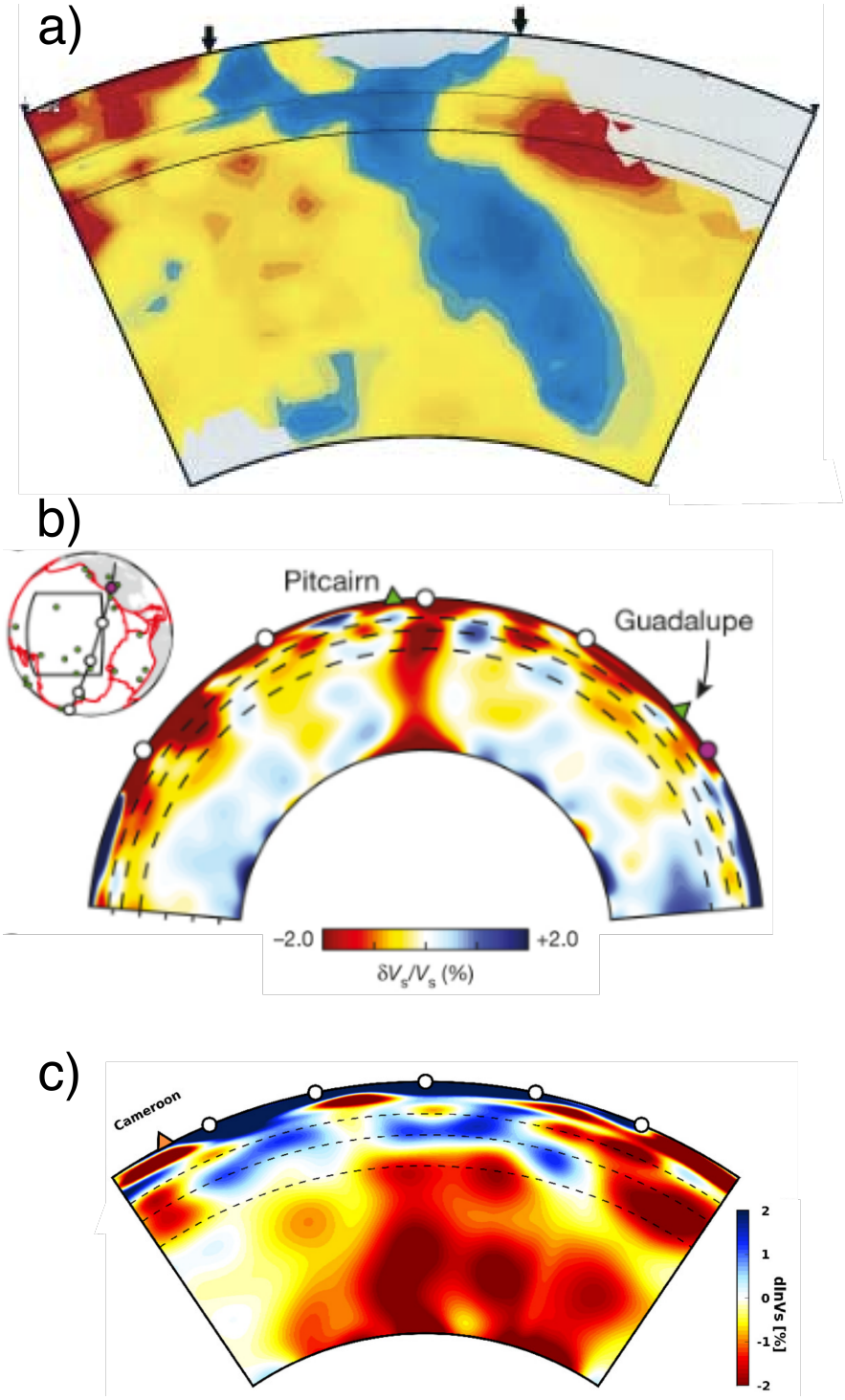

Figure 6: Classic images of mantle seismic tomography. *a)* downwelling slab as imaged by Grand *et al.* (1997) (their Figure 1b), *b)* Pitcairn plume as imaged by French and Romanowicz (2015) (their Figure 1c), *c)* Plume clusters as imaged by Munch *et al.* (2024) (their Figure 5, line CC′)

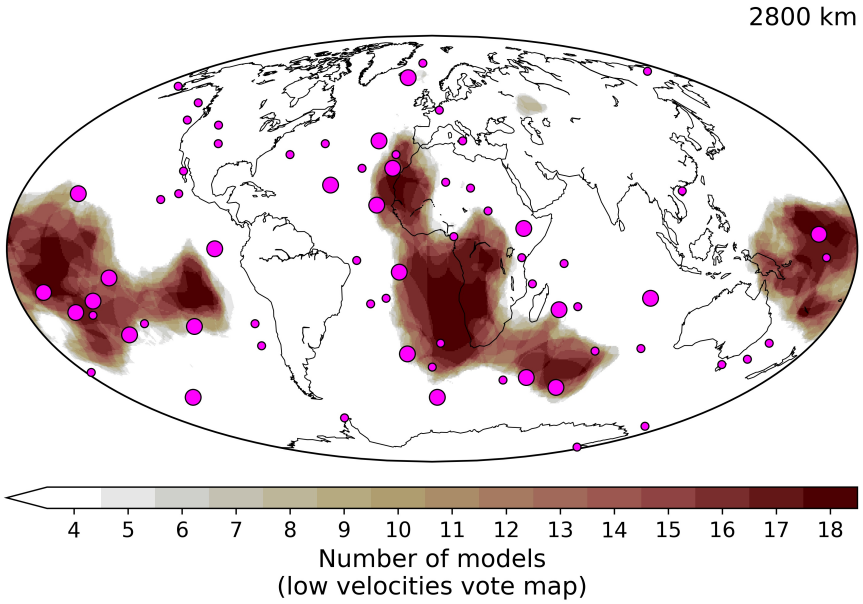

Figure 7: Votemap (Shephard *et al.*, 2017) of S-wave tomography models in the lowermost mantle (2800 km depth), showing the agreement of S-wave tomography models on two LLSVPs beneath Africa and the Pacific ocean. Pink circles show hotspots locations, and their radius is indicative of buoyancy flux (Whittaker *et al.*, 2015). Generated using *Submachine* (Hosseini *et al.*, 2018).

variations, which also drive the convection, modern tomographic images promised to provide images of mantle downwellings (e.g. Grand *et al.*, 1997) (see Figure 6 a) and upwellings (e.g. French and Romanowicz, 2015) (see Figure 6 b) and in doing so have helped bring debates around terrestrial layered mantle convection and the existence of deep-originating mantle plumes towards a conclusion.

LLSVPs

In the lower mantle the dominant feature of every tomographic inversion since Dziewonski *et al.* (1977) has been the low-velocity degree 2 structure that forms two large regions of low seismic velocity centred beneath Africa and the Southern Pacific (see Figure 7). Whilst tomography models vary considerably in the details of recovered structure, the Large Low Shear Velocity Provinces (LLSVPs) are a robust result of modern seismology (e.g. Hosseini *et al.*, 2018).

What these regions represent is considerably more controversial than their existence. Dziewonski *et al.* (1977) outline two of the popular explanations since then; that either the LLSVPs represent recycled lithosphere accumulating at the CMB, or that they are comparatively static heterogeneities formed of intrinsically dense material. Alternatively, they might be purely thermal anomalies constrained by the Earth's history of subduction.

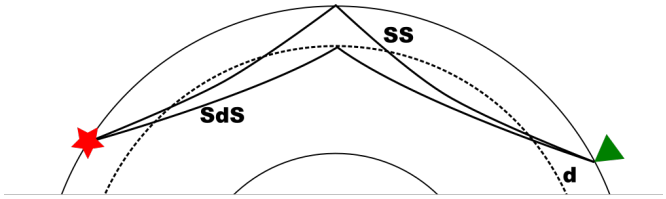

Figure 8: Acquisition geometry of seismic phase *SdS*. Source is shown with red star, and receiver with down-pointing green triangle. Topography is derived from the differential travel time of the *SS* phase that makes an underside reflection off the Earth's surface, and *SdS* which reflects off the underside of the discontinuity.

For a long time the elevated ratio of $^{V_S}/_{V_P}$ in the LLSVPs was interpreted as evidence for a compositionally distinct origin. Davies *et al.* (2012) showed that dense lenses of post-perovskite can have a similar effect without compositionally distinct material in the LLSVPs, and that when filtered for the sensitivity of the tomographic model, purely thermal plume clusters provided an acceptable fit to the tomography. Munch *et al.* (2024) has recently shown high resolution tomography models of the lowermost mantle where distinct plume-roots are visible, even within the African LLSVP (see Figure 6 c).

Some have argued that the LLSVPs are long lived stable features at the base of the mantle based on correlations (Torsvik *et al.*, 2006; Doubrovine *et al.*, 2016) between reconstructed Large Igneous Province locations (which are associated with the interaction of the head of plumes with the surface) and the edges of LLSVPs (see Figure 7). Thermochemical piles, favoured by these authors, help to 'seed' plumes in numerical models (Torsvik *et al.*, 2006). The underlying correlations have, however, been shown by other workers not to be statistically significant (Davies *et al.*, 2015*b*).

1.4.4 Discontinuity Topography

Birch's 1952 assessment that the mid-mantle discontinuities represented chemical reactions within the Earth's interior led some others (e.g. Verhoogen, 1965) to predict that seismically observable topography on these surfaces might be produced. Whilst sometimes observed using *ScS* precursors (Revenaugh and Jordan, 1991*a*; Waszek *et al.*, 2024), the topography of the 410- and 660-deep discontinuities are usually observed using *SS* precursors (e.g. Shearer and Masters, 1992) and Receiver Functions (e.g. Chevrot *et al.*, 1999).

SS Precursors for Mantle Transition Zone (MTZ) Topography

Here I aim to provide a brief overview of what has been learnt in the 30-odd years since Shearer and Masters (1992) – the first global *SS*-precursor study of

d660, but will leave the discussion of the geodynamic significance of these observations to chapter 3 and chapter 4 where I consider this in depth.

The seismic phase *SS* occurs as an underside reflection on the Earth's surface, (see Figure 8), and precursors (*SdS*) occur since any energy reflected within the mantle travels a shorter path through material of higher seismic velocity than the main *SS* phase. The depth of the reflector is then recovered by translating the travel-time difference $SS-SdS$ into a depth, although Mantle Transition Zone (MTZ) thickness may be obtained directly from the travel-time difference between *S660S* and *S410S* (Waszek *et al.*, 2021).

Following the Shearer and Masters (1992) model for d660, producing models for d410 and d660 topography has become one of the standard seismological products about the Earth's mantle, alongside 3D seismic tomography inversions (section 1.4.3) and 1D velocity structures (section 1.4.2). The sensitivity of these models to the discontinuity structure is limited by the highly uneven distribution of bounce-points (due to the uneven distribution of sources and receivers), and the sensitivity of the SS-precursor to the discontinuity topography. The Fresnel zone of *SS*-*SdS* extends 1000s of kilometres away from the ray-theory bounce-point (e.g. Guo and Zhou, 2020, figure 4). There have been two approaches to handle this sensitivity problem; either to approximate the χ-shaped Fresnel zone as a circular cap of radius $\sim 5^\circ$ (e.g. Gu *et al.*, 1998, 2003; Houser, 2016; Huang *et al.*, 2019), or by taking account of the full finite-frequency sensitivity kernel (e.g. Lawrence and Shearer, 2008; Guo and Zhou, 2020). Finite frequency models appear to recover a shorter-wavelength topography variation from the *SS* precursor travel-times than those stacked using spherical caps, although the peak-to-peak topography of these models is not significantly larger than spherical cap models recover.

There is a lot of disagreement between the global d410 and d660 topography models on the regional distribution of topography deflections (Figure 9). As a whole, however, there is some concensus on the amplitude of recovered topographies and their relationship to each other; the peak-to-peak topography on both d410 (e.g. Chambers *et al.*, 2005*b*) and d660 (e.g. Shearer and Masters, 1992) is on order 30 ± 10 km and that d410 and d660 are globally positively correlated (e.g. Gu *et al.*, 1998; Houser, 2016; Guo and Zhou, 2020; Waszek *et al.*, 2021).

This last result is somewhat surprising. Given the understanding that d410 is controlled by the exothermic olivine-out reaction, and d660 by the endothermic ringwoodite-out reaction, and the expectation that thermal structure should be strongly radially correlated in the mid-mantle, d410 and d660 should be strongly anticorrelated. Many solutions to this problem have

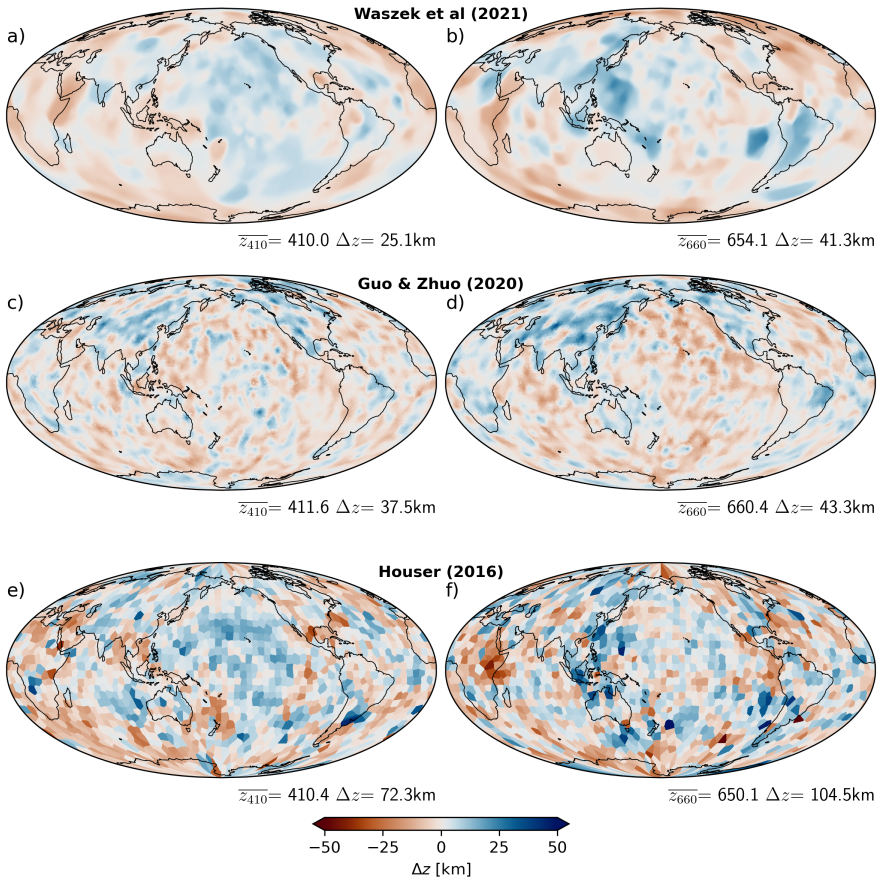

Figure 9: Maps of d410 and d660 topography acquired using SS precursors. *a)* d410 topography and *b)* d660 topography model of Waszek *et al.* (2021). *c)* d410 topography and *d)* d660 topography model of Guo and Zhou (2020). *e)* d410 topography and *f)* d660 topography model of Houser (2016).

been suggested; (i) that thermal structure is offset in the mid-mantle (e.g. Shearer and Masters, 1992; Goes *et al.*, 2022), (ii) compositional variations (e.g. Houser *et al.*, 2008), (iii) a positive Clapeyron slope at high temperatures controlling d660 (e.g. Houser and Williams, 2010; Waszek *et al.*, 2021), (iv) the presence of water changing phase diagrams (although this is considered unlikely by seismologists and mineral physicists alike(Houser, 2016; Muir *et al.*, 2021)), (v) uncorrected crustal and upper mantle structure (Tauzin *et al.*, 2022) (although this is usually corrected for in *SS* precursor studies, and more sophisticated picking methods that can more accurately pick the true surface-underside reflection still find the strong positive correlation (Dai, 2024)), or (vi) that the travel time of *S410S* is strongly sensitive to d660 topography structure (Koroni *et al.*, 2017). At present there is no concensus in the seismological, mineral physical, or geodynamical communities about how to resolve this – I will discuss this problem further in Chapter 4.

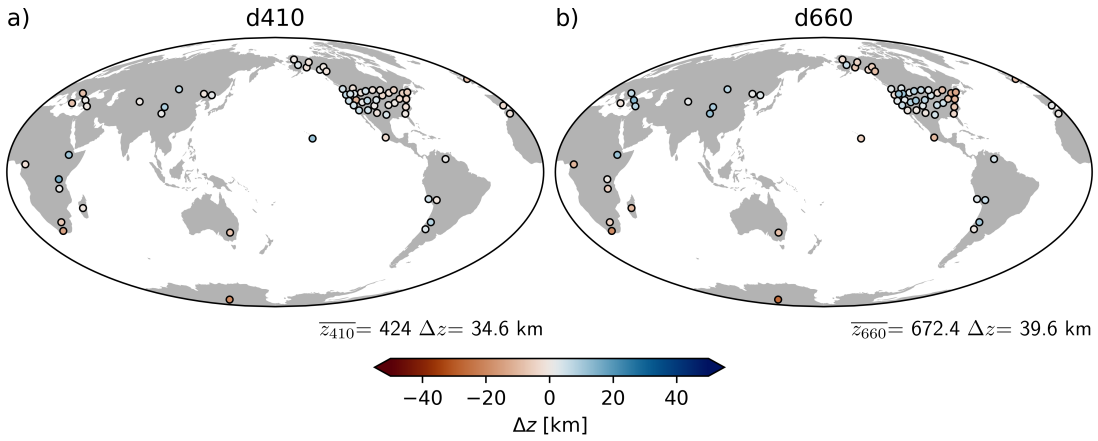

Figure 10: Global summary of receiver-function derived d410-d660 topography, compiled by Glasgow *et al.* (2024). *a)* d410 topography, *b)* d660 topography. Each point represents a single array's average discontinuity depths.

Receiver Functions for MTZ Topography

As well as a reflected phase, at a jump in V_S and ρ, an incident wavefront can create converted phases. Most commonly in mantle seismology the conversion from a P wave to S (Pds) is found by the deconvolution of the vertical from the horizontal component of the arriving wave (e.g. Vinnik, 1977), which produces the receiver function. This is often interpreted as a 'direct' representation of Earth structure back along the incident ray-path, which is sub-vertical (e.g. Jenkins *et al.*, 2016). This last point means that the data from receiver functions illuminates Earth structure only directly beneath the receivers. Historically this has led to studies that are regional in scope (e.g. Maguire *et al.*, 2018), and as a result constraints on global geodynamics are more difficult to gleam, although there have been recent efforts to integrate receiver functions from seismic arrays to provide a global picture (Glasgow *et al.*, 2024, see Figure 10 here). Although the data coverage for receiver functions is extremely poor, even compared to *SS*-precursors, the higher frequency of waves used (< 0.2 vs 0.05 Hz for *SdS*) means the Fresnel zone is much smaller; 200 km (e.g. Chevrot *et al.*, 1999) across instead of $\sim$ 1000 km. This allows much narrower features to be resolved, however no arrays span a full suite of geodynamic environments so it is difficult to estimate what a peak-to-peak topography value is globally, but deflections in some studies appear higher than those recovered from *SS* precursor studies. For instance Jenkins *et al.* (2016) recovered $\sim$ 40 km deflection on d410 beneath the Iceland plume $\sim$ 1000 km across compared to recovered 'hills/valleys' on d410 peaking around $\pm$20 km from the average discontinuity depth (e.g. Houser *et al.*, 2008; Waszek *et al.*, 2021)

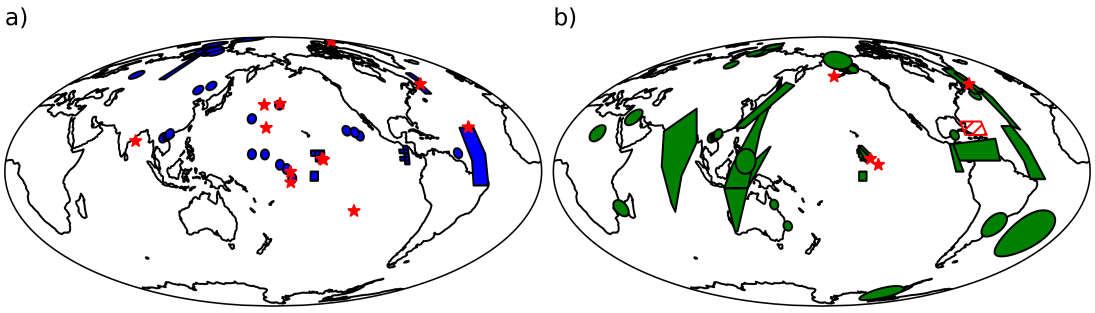

Figure 11: Observations of D″ using *a)* P-waves and *b)* S-waves, after similar figures in Wysession *et al.* (1998); Cobden *et al.* (2015); Jackson and Thomas (2021). Sources are listed in Table 9 in Appendix A.

MTZ Topography and Thermochemical Structure

Given the understanding that the d410 and d660 can be linked to specific phase transitions, there has always been an understanding that in principle the discontinuity topography from *SS* precursors or from receiver functions could be inverted for thermochemical structure (e.g. Verhoogen, 1965; Shearer and Masters, 1992). Recently, a few groups have inverted global *SdS* (Waszek *et al.*, 2021; Tauzin *et al.*, 2022), receiver function (Glasgow *et al.*, 2024), and *ScS* reverberation (Waszek *et al.*, 2024) derived topography maps and reflectivity data for thermal and chemical variations in the mid-mantle. These authors generally assume that inverted thermal structure is reliably obtained from their datasets. Waszek *et al.* (2021) and Tauzin *et al.* (2022) find a thermal variation of ~ 300 K, similar to values proposed by Shearer and Masters (1992) from contemporary mineral physical estimates for the Clapeyron slopes. Glasgow *et al.* (2024) estimate a similar range of thermal anomalies using a global distribution of receiver functions, but with a significantly different distribution of warm and cool regions than found by Tauzin *et al.* (2022). Waszek *et al.* (2024) found a much larger range of temperature values (~ 600 K), but the *ScS* reverberation data this is inverted from is not significantly higher frequency than *SS* precursors, so has a similar lateral sensitivity. The lateral distributions of these inverted temperatures is not convincingly similar. I will discuss further the geodynamic significance of these inversions of thermochemical structure in Chapter 4.

ScS Precursors and D″

That the lowermost mantle has strong seismic velocity gradients was well established early in the history of seismology (e.g. Jackson and Thomas, 2021), with the region gaining the name 'D″' by the early 1950s. Whilst from travel-time curves, a discontinuity in $\frac{dV_S}{dr}$ for the lowermost mantle, was known (e.g. Jeffreys and Bullen, 1940, see Figure 5), a triplication between ScS and S arrivals was first observed by Lay and Helmberger (1983), which they associated with a jump in V_S at the top of the D" beneath the North Pacific, the Arctic and Central America.

In the following 40 years, the observation of a D″ "*SdS*" arrival has become common in many regions around the Earth (e.g. Jackson and Thomas, 2021) – see Figure 11. However, in a handful of locations, a triplication has been looked for and is not found. Some of these non-observations are at small source-receiver separations so the amplitude of the returned phase would be quite small, but others are at similar source-receiver separations to where there are observed D″ arrivals in other regions.

Following the observation by Lay and Helmberger (1983) of this lower-most mantle velocity discontinuity, it was uncertain whether this jump in seismic properties was due to an accumulation of cool downwellings above the thermal boundary layer, a phase transition, or a dense layer in the lowermost mantle (e.g. Wysession *et al.*, 1998). Sidorin *et al.* (1998, 1999), using 2D convection models and temperature structures predicted from tomography models of the lowermost mantle favoured a phase transition, and estimated a Clapeyron slope of ~ 6 MPa.K^{-1}. It was not until 2004 that several groups successfully formed a new polymorph of $MgSiO_3$ at CMB pressures – aka 'post-perovskite' (Murakami *et al.*, 2004; Oganov and Ono, 2004). The phase transition Clapeyron slope found by these workers agreed well with the Clapeyron slope Sidorin *et al.* (1999) suggested for a lowermost mantle phase transition.

Motivated by these constraints on the post-perovskite reaction, there has been some interest in observing (e.g. Whittaker *et al.*, 2016) and explaining topography on the D″ discontinuities (Bower *et al.*, 2013).

1.5 TERRA – a 'Geodynamic Laboratory'

Here I will briefly introduce TERRA; some aspects of the code and general methods employed in all the chapters of this thesis. I will highlight elements that make TERRA distinct among peer geodynamic codes, but will not discuss the numerical methods used to solve the conservation equations at length since I

did not amend these beyond the state described by Davies (2008*b*, pp. 256 - 286)

1.5.1 History

TERRA was initially developed by John Baumgardner to solve the conservation equations (1.4-1.5) on a finite element grid describing a 3D spherical shell (i.e. the Earth-mantle's actual morphology). Bunge and Baumgardner (1995) parallelised the code, allowing it to take advantage of more computing power and memory for higher-resolution simulations. Yang (1997) introduced depth- and temperature-dependent viscosity and Bunge *et al.* (1998) introduced mantle circulation modelling using TERRA. Stegman (2003) introduced particles into the code, allowing some geochemical problems to be addressed in TERRA (e.g. Gottschaldt *et al.*, 2006). Davies (2008*b*) introduced radial grid refinement to allow a computationally efficient handling of low viscosities in the upper mantle and high thermal gradients in the thermal boundary layers. Whilst used by some authors (Davies *et al.*, 2009, 2013; Wolstencroft, 2008), the grid refinement has not been used recently, and is not used in this thesis. Van Heck *et al.* (2016) improved the implementation of particles in TERRA, and introduced a method to simulate shallow melting - enunciated below.

1.5.2 Discretisation

TERRA's dyadic refinement of the icosahedral grid produces an even distribution of points across the Earth's surface – and this has allowed the code to remain efficient and competitive over 40 years of science. This discretisation scheme is illustrated in Figure 12. The sphere is treated as an icosahedron, formed of 20 triangles. For parallelization reasons the triangles are grouped into 10 diamonds, centred at the North and South poles (Bunge and Baumgardner, 1995). The grade of grid-refinement is described by the parameter mt, which is described by

$$mt = 2^k \tag{1.25}$$

where k is an index.

At $mt = 1$, the sphere is discretised into the 20 triangles. As mt is increased, the sides of the triangle are split mt times, so that, for instance at $mt = 4$, the initial triangle's sides have been split into four segments (orange triangle in Figure 12). This is repeated until a grid with a desired resolution is formed, with an even distribution of points across the surface (Baumgardner and Frederickson, 1985). Most of the models presented in this thesis have a

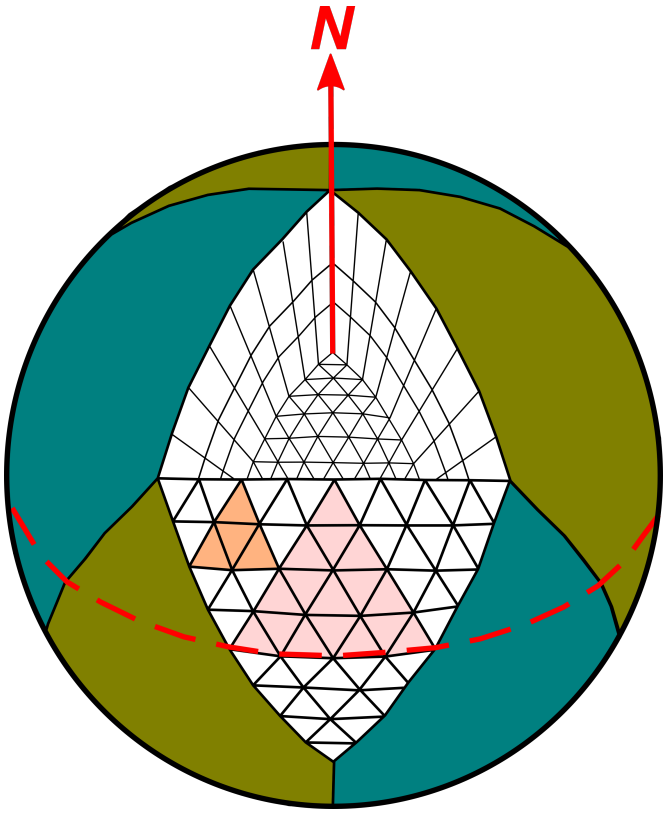

Figure 12: Icosahedral discretisation of the sphere as implemented by Baumgardner (1983); Baumgardner and Frederickson (1985) for TERRA. Initially the Earth's surface is divided into 10 diamonds (shown as teal and khaki regions on surface) centred on the poles. Next, these diamonds are divided into the icosahedral triangles ($mt = 1$), this is shown for the central diamond of the sphere shown. This grid then undergoes dyadic grid refinement – this is shown as the pink ($mt = 2$), orange ($mt = 4$), and white ($mt = 8$) triangles on the southern half of the central diamond of the sphere. The grid is applied at radial discretisations $nr = {}^{mt}/_{2}$ through the spherical shell, which is revealed by the removed northern triangle of the central diamond. This results in a equal area grid which as an approximately square aspect ratio in the third dimension.

resolution of $mt = 128^3$. For the geodynamic problem, it is advantageous to have equant element volumes, which then requires that $nr = {}^{mt}/_{2}$ (Yang, 1997, p 15)[4].

1.5.3 Particles and Melting

Stegman (2003) introduced particles to TERRA to allow him to quantify the mixing of heterogeneity from the surface into the mantle interior. The particles are advected according to a second order Runge-Kutta scheme using the velocities calculated on the nodes interpolated onto the particles (Stegman, 2003). The particle routines were substantially extended and altered by Van Heck *et al.* (2016) to allow for the modelling of melting in the uppermost mantles of TERRA simulations.

Particles are initialised so that around each node there are 10 particles. Then their bulk composition (described by the C-value described above in section 1.3.4) is initialised so that of these 10 particles on each node, 1 has a basaltic composition, 5 lherzolitic, and 4 has a harzburgitic composition, representing a partially processed mantle (Davies *et al.*, 2025) with a bulk composition of lherzolite, $C = 0.2$. The particles are then advected in the flow using the methods implemented by Stegman, adding a chemical buoyancy to their nearest nodes and so influencing the flow. This then means that there is nothing to stop the "bunching" of particles around particular nodes, leaving few or none around others (Van Heck *et al.*, 2016). Particles are therefore "split" if there are less than two on a single node, and similarly must be "merged" if there are many (35) on a single node. These processes are done such that the mass and compositions tracked on the particles are conserved.

To model the melting, the routines of Van Heck *et al.* (2016) use a simple 'planar' solidus in P-T-C space. Where particles sit above the solidus, they undergo melting (if they are in the upper 300km where melting is considered in these simulations). The composition of the residue formed by this melting is found by projecting from the particle's current P-T-C position to where it would meet the solidus plane at the same P-T conditions. This allows the degree of melting to be determined and the amount of enriched melt extracted from the source particle to be calculated as well. This extracted 'melt' is then moved to the surface, where it is distributed among the particles at the surface until they are fully enriched (i.e. their C-Value is 1). In the melting scheme in TERRA, primordial particles ($C = 2$) are not allowed to melt or receive melt,

[3]This grid spacing is about 45 km laterally on average, but this varies with depth so that at the surface the grid spacing is only $\sim$ 60km, but at the CMB it is 32 km. This represents a balance of being able to resolve more vigorous convection with computational cost.

[4]So for a resolution of $mt = 128$, $nr = 64$, and the radial grid spacing is $\sim$ 45 km

and are simply advected. Then, melt is distributed to particles further away from the Earth's surface. As well as conserving composition, this is done so that the mass tracked on the particles is conserved. As well as the bulk chemistry, trace elements, and the concentration of radiogenic elements is also tracked and evolves in melting according to the partition coefficients of the elements. Since radiogenic element abundance is tracked on the particles, this allows internal heating to vary according to the abundance of mother nucleotides.

1.5.4 Outline Solution Scheme

I now offer a sketch of the solution scheme used in TERRA. The fundamental solution strategy of TERRA was not modified in anyway for the work in this thesis, and the reader is referred to Davies (2008*b*), Appendix E, who provides a thorough account of the numerical methods and underlying mathematics used by TERRA to solve the governing equations (1.3-1.5) of the thermal convection problem. First TERRA is initiated and reads in its input parameters and opens various files to write output to. If the simulation is restarted, the thermal structure and particle data (position, mass tracked, composition, species abundance etc.) from the previous output file are imported, otherwise they are initialised.

The code then begins to advance through the simulated time. At each time step it advances the solution by:

1. Adjusting the viscosity structure if temperature-dependent viscosity has been employed.

2. Advecting particles according to the velocity field of the previous time step.

3. Calculating the distribution of shear heating from the previous time-step's velocity field.

4. The conservation equations (1.3-1.5) are solved within a second-order Runge-Kutta time-stepping scheme. First, the velocity ($\underline{\dot{u}}$) structure is solved through the coupled solution of (1.3) and (1.4) using the finite element method (which solves a discretised version of the mass and momentum conservation equations, minimising the error in pressure, see Davies, 2008*b*, pp. 265-276), computationally implemented with the aid of the geometric multigrid method (which calculates an approximate solution on a coarse grid, and then considers a solution on a finer grid, before resolving the solution on the coarse grid, see Davies, 2008*b*, pp. 276-280,

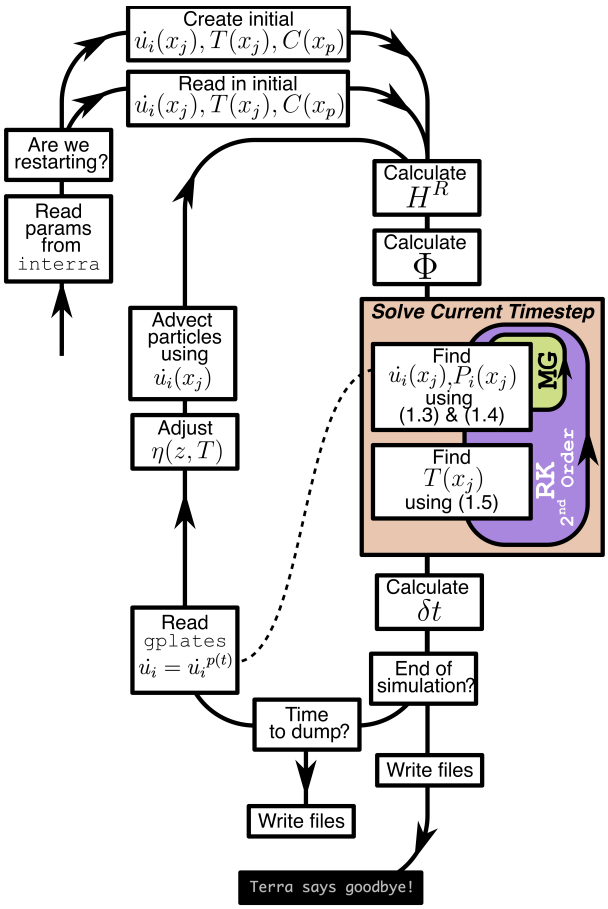

Figure 13: Sketch flow diagram for TERRA, sketching how the numerical solution of (1.3-1.5) is accomplished. Symbols and equation numbers as per the text. 'MG' stands for 'Multigrid', indicating that the simultaneous solution of (1.3) and (1.4) is accomplished first on a coarse grid, then on the refined grid, before being calculated on a coarse grid again, a 'V'-cycling multigrid scheme (Davies, 2008*b*, p. 277, p. 292). 'RK 2nd Order' refers to the second-order Runge-Kutta time stepping scheme used, where the solution is found based on the gradient at the start of the timestep and at the end of the timestep (based on the slope at the start of the timestep). The boundary conditions are applied during the numerical solution of (1.3-1.5), including using the surface motions constrained by the plate motion histories in 'gplates' files (Müller *et al.*, 2018) in a circulation model. Minor modifications are made to (1.4) in Chapter 2 (specifically the term F_i^P of F_i^B in 1.19), and a modification to 1.5 (specifically to H^P) is neglected for argumentative reasons. These modifications are not used in the later simulations in this thesis, and are not commended for further use by users of TERRA based on the results of Chapter 2. Elsewhere, I principally use TERRA in the format described by Panton (2020); Panton *et al.* (2022).

pp. 287-295). Using the calculated velocity field, the advection-diffusion equation (1.5) is solved to yield the temperature field on a finite volume scheme (see Davies, 2008*b*, pp. 280-283) which considers the energy advected and diffused into (or out of) a grid volume through its faces.

5. The parameters for adaptive time stepping are then calculated.

6. If the time since the last dump of data from the nodes (and particles if they are included) has exceeded a certain amount of time, this data is then written as netcdf files.

Additionally, data is dumped at the end of the simulation. This is sketched in Figure 13.

1.6 Bringing it Together

Having discussed a simplified account of the mineralogical composition of the mantle (Section 1.2), the essential aspects of its convective physics (Section 1.3), the physics of seismic waves and the key observational results of mantle seismology (Section 1.4), and a sketch account of the numerical tools used in this thesis (Section 1.5), I now address previous key results that have addressed the intersection of these.

1.6.1 The Mantle Transition Zone, Phase Transformations and Mantle Convection

The region between c. 400 and 1000 km depth was first identified as a region where the properties of mantle materials changed as the region 'C' in Bullen's annotation of the Jeffreys and Bullen (1940) tables and, as mentioned above, Birch (1952) demonstrated this required a change in chemistry or of mineral phase. By the 1960s, it was clear that there were some phase transformations in mantle rock-forming minerals that took place in the mid-mantle, and it was a subject of debate what role they might play in mantle dynamics (e.g. Verhoogen, 1965). Verhoogen (1965) examined the potential role of phase transformations (particularly exothermic transformations) on the temperature and density profiles of upwellings and downwellings, finding it unlikely that they posed a significant barrier to convection. During the 1970s and early 1980s, much more sophisticated models of mantle convection and flow began to be considered. These included work using linear stability analyses, analytical solutions for steady state cases and time-dependent numerical models as

scientists gained access to the required electronic computational resource. One of the critical results from this era of modelling is that of Christensen and Yuen (1985), which used 2D box models to explore the impact of an endothermic phase transformation on mantle convection, finding that the convective regime changed from whole- to layered-mantle convection around $\gamma = -6 \pm 2$ MPa.K^{-1} for the density changes associated with the ringwoodite to bridgmanite and periclase reaction. This was slightly more negative than contemporary measurements of the post-spinel reaction. As well as the transition to layered convection, Christensen and Yuen also reported that around the critical Clapeyron slope, they produced 'leaky' layered convection with occasional 'heavy mass flux' across the phase boundary, which later authors would refer to as 'avalanching' (e.g. Tackley *et al.*, 1994). Christensen and Yuen used a phase-function Γ to represent the phase fraction, and introduced the scheme

$$\Gamma(z,T) = \frac{1}{2}\tanh(\frac{z - z_t(T)}{d_t}) \tag{1.26}$$

where z is the depth, d_t is the width of the transformation, z_t is the equilibrium depth of the transformation at temperature T, calculated as $z_t(T) = z_{ref} + \gamma \Delta T^t$ where z_{ref} is the depth of the transformation at a reference temperature (T^t_{ref}), ΔT^t is here the temperature anomaly away from this, and γ is the Clapeyron slope. In this scheme then, the body forces (F_i^B, 1.19) in the momentum equation (1.4) are written

$$F_i^B = \rho_0(\alpha \Delta T + \Gamma(z,T)\frac{\Delta \rho}{\rho})$$

where ΔT is here the temperature anomaly against the radial average. Similarly, the heat released or adsorbed due to the phase transition is given by

$$H^P = \frac{\gamma T \Delta \rho}{\rho_0^2 C_P}\frac{D\Gamma}{Dt} \tag{1.27}$$

With the advent of more extensive computational resource in the 1980s and 1990s, numerical modelling of mantle convection began to happen using 3D models (e.g. Baumgardner, 1983; Bercovici *et al.*, 1989), although at this stage with a reduced resolution compared to 2D models. This motivated the introduction of the 'sheet mass anomaly' approximation by Tackley *et al.* (1993), which is of particular interest to this thesis since it was introduced to TERRA by Bunge *et al.* (1997) and remains the implementation of phase transformations used in models produced using the TERRA code. In it, the phase transformation is assumed to happen at a singular depth in the model,

and a buoyancy force is applied such that F_i^P in (1.19) is

$$F_i^P = \gamma \frac{\Delta\rho}{\rho}(T - T_{ref}) \tag{1.28}$$

and the phase transformation heat term is

$$H^P = \gamma T J_r \tag{1.29}$$

where J_r is the radial volume flux through the phase transformation. Tackley *et al.* (1993) showed a mode of convection where downwellings were restricted to the lower mantle apart from where downwelling sheets met, allowing cylinders of cool material to descend to the mantle interior, although with similar parameters Bunge *et al.* (1997) did not produce similar localised lower mantle downwellings but instead downwellings stagnated and were deflected in the transition zone.

As well as advancing the complexity of geodynamic modelling the sudden increase in computing resource in the last quarter of the 20th Century spurred the development of tables of thermodynamic properties at many pressure-temperature pairs using Gibbs-Free-Energy minimisation codes such as THERMOCALC (Powell and Holland, 1988). These revealed a much more complex set of phase relations and so suggested that the dynamic impact of these might be captured by integrating these tables into the convection simulation. Whilst this has been done in some form since the 1990s (e.g. Ita and King, 1994), larger, more Earth-like implementations of this were not possible until the 2000s (e.g. Nakagawa *et al.*, 2009) due to the high computational cost of performing the look-up for density at every grid-point. This requires, however, the calculation of the latent heat term explicitly using an 'effective thermal expansion' coefficient (Nakagawa *et al.*, 2009). More recently, Dannberg *et al.* (2022) have re-cast the governing equations of the convection problem in terms of entropy using the projected density approximation compressibility assumption (Gassmöller *et al.*, 2020), so instead interrogates tables at regular entropy and pressure intervals, meaning the latent heat term does not need to be explicitly calculated (Gassmöller *et al.*, 2020). Whilst these table-based implementations of phase boundaries implicitly have more complex phase boundaries than those implemented using the explicit parametrisations described above, it is not possible to vary the geodynamic parameters of the phase transformations (i.e. the Clapeyron slope and the density change), although the cooling mantle adiabat through geological history may result in interesting evolving dynamics (Li *et al.*, 2024).

Changing the Clapeyron slope in particular has been motivated by the spread of phase boundaries that mineral physicists have produced in experimental and computational work, which in particular for the ringwoodite-out reaction have spanned a large range of Clapeyron slopes (which requires an assessment of the stability of samples of materials of mantle compositions at different pressure-temperature conditions, so is more uncertain than the density change). Prominent early examples included Ito and Takahashi (1989), who estimated a slope of -2.5 MPa.K^{-1}, and Ito *et al.* (1990) who estimated a slope of -4 MPa.K^{-1} (e.g. Bunge *et al.*, 1997). More recent evaluations have tended to find more moderate (e.g. Ishii *et al.* (2011) report a slope of -1MPa.K^{-1} in pyrolite) or even null (e.g. Chanyshev *et al.* (2022) report a slope of -0.1 below 1700 K, although with increasing temperature this becomes slightly more negative to $-0.9;$ MPa.K^{-1} at 2000 K) slopes. As such, varying the phase transformation parameters is still motivated by the considerable uncertainty in the phase transition parameters for the simulation of Earth-like mantle convection.

In the absence of robust constraints on the value of the ringwoodite-out reaction's parameters, Christensen and Yuen (1985) parameterized the boundary between layered convection and a transitional regime in the form

$$\mathbb{P}_{l-t} = aRa^b \tag{1.30}$$

where $\mathbb{P}_{l-t}$ is the phase parameter, a nondimensional number describing the 'strength' of the impact of the phase transformation on the convection, defined as

$$\mathbb{P} = \frac{\gamma \Delta \rho}{\alpha \rho^2 g D} \tag{1.31}$$

and the vigour of the convection is described by Ra. In (1.30), Christensen and Yuen (1985) found $a = -4.4$ and $b = -0.2$. Although the form of downwellings in 3D spherical shell simulations are fundamentally different to those in the 2D box models used by Christensen and Yuen (e.g. Tackley *et al.*, 1993), more recent work exploring the parameter space in a 3D spherical shell morphology (Yanagisawa *et al.*, 2010; Wolstencroft and Davies, 2011) have found a similar boundary in $\mathbb{P} - Ra$ space for the layered-transitional regime change, with Yanagisawa *et al.* (2010) reporting $a = -4.7$, $b = -0.2$, although Wolstencroft and Davies (2011) reported $a = -1.05$, $b = -0.1$, these studies having different input parameters. As well as constraining the potential convective regimes for different mantles and phase transformation parameters, the more explicitly parameterized phase transformations have been used to explore the impact of various phase transformation effects, including temperature-restricted reactions

(Bina and Liu, 1995), the kinetics of phase transformations (Agrusta *et al.*, 2014; King *et al.*, 2015), different phase transformations in different compositional end-members (e.g. Davies, 2008*a*; Yan *et al.*, 2020) and the impact of additional phase transformations in the deep mantle (e.g. Sidorin *et al.*, 1998, 1999; Nakagawa and Tackley, 2004; Bower *et al.*, 2013). In all these cases, explicit parametrisations have allowed geodynamicists to assess the importance of phase transformation effects on the geodynamics in the absence of certainty in the mineral physical data, or even in anticipation of it (e.g. Sidorin *et al.*, 1998, 1999; Murakami *et al.*, 2004; Oganov and Ono, 2004).

1.6.2 Assessing Geodynamic models with seismology

As geodynamic models produce a laterally and radially varying temperature field throughout the mantle volume, dependent on the implemented rheology and physics, there has always been a natural desire to compare the outputs of geodynamic models to the observations of the Earth's mantle (e.g. Glatzmaier, 1988). Prior to the introduction of Mantle Circulation Modelling (Bunge *et al.*, 1998), comparison was chiefly with respect to the spherical harmonic spectra of the velocity heterogeneity maps (more commonly referred to as seismic tomography today, e.g. Glatzmaier, 1988; Davies *et al.*, 1992) or the radial correlation functions of the seismic tomography models (e.g. Jordan *et al.*, 1993). Initially comparisons were made without reference to the finite resolution of the tomographic models (e.g. Glatzmaier, 1988), although with increasing computational resolution it became clear that the geodynamic models were of far higher resolution than the seismic tomography models (e.g. Davies *et al.*, 1992; Tackley *et al.*, 1994), and the spectra of the thermal fields were truncated to the spherical harmonic degree that the tomographic model was quoted out to (e.g. Jordan *et al.*, 1993; Tackley *et al.*, 1994). However, this still neglected two important complications. Firstly, that the mapping of temperature anomalies to anomalies in V_S is nonlinear and varies in depth (e.g. Robl *et al.*, 2025) and secondly that the lateral distribution of resolved and unresolved regions is highly heterogenous on Earth due to the uneven distribution of seismic sources and stations (e.g. Davies *et al.*, 1992). For comparisons to seismic tomography, these have been addressed with increasingly complicated mappings from geodynamic thermal structure to seismic structure (e.g. Goes *et al.*, 2004; Schuberth *et al.*, 2009*b*), although some simplification to these may be acceptable (Robl *et al.*, 2025). Similarly, the handling of resolution, particularly that which is geographically variable has become much more sophisticated, with workers considering first the ray-paths (Bunge and Davies, 2001) and later the

'resolution operator' $\underline{\underline{\mathcal{R}}}$, directly related to the matrix coefficients $\underline{\underline{G}}$ and its inverse $\underline{\underline{G}}^{\dagger}$ (Schuberth *et al.*, 2009*a*; Ritsema *et al.*, 2007). The formation of the resolution operator is expensive, and since few are published this means that comparatively few tomographic models are directly comparable with geodynamic models at present.

As discussed above in relation to the seismic observations of the mantle (Section 1.4.3), the principle result from seismic tomography in the lower mantle are two large antipodal low velocity regions, interpreted either as thermal anomalies or as regions of distinct compositional material (e.g. Dziewonski *et al.*, 1977). Since the early 2000s then, many geodynamicists have modelled mantle convection with the intention of producing basal mantle structures comparable with the LLSVPs (e.g. Ni *et al.*, 2002; Tan and Gurnis, 2005; Davies *et al.*, 2012, 2015*b*; Jones *et al.*, 2021; Flament *et al.*, 2022; Huang *et al.*, 2022; Kreielkamp *et al.*, 2022; Yuan and Li, 2022; Shi *et al.*, 2024; Guerrero *et al.*, 2024; Desiderio and Ballmer, 2024; Hu and Gurnis, 2025; Krauss and McNamara, 2025, and many more). In addition to matching observations of the low V_S province's morphology and $V_S : V_P$ ratios, these geodynamicists are motivated by geochemical trends in Neodymium, Lead, Niobium, Helium, Strontium and Hafnium systematics that have previously been explained by mixing of enriched end-members with depleted bulk mantle (e.g. Hart *et al.*, 1992; Hofmann, 1997, 2014; Davies *et al.*, 2015*a*), although it is increasingly clear that it is not necessary to have LLSVP-scale chemically distinct domains to produce all these trends (e.g. Davies *et al.*, 2015*a*; Panton *et al.*, 2022, 2025) although a recent analysis of synthetic isotopic trends from thermo-chemical mantle circulation models did favour those with a primordial layer initial condition (e.g. Béguelin *et al.*, 2025*a*). The preservation of primordial provinces in the lower mantle is generally found to be favoured by this material being intrinsically dense (e.g. Huang *et al.*, 2022), more viscous (e.g. Desiderio and Ballmer, 2024) and by a depth-dependent thermal conductivity (e.g Guerrero *et al.*, 2023), and are destabilised by a concentration of heat-producing elements within piles and a temperature-dependent conductivity (e.g. Guerrero *et al.*, 2024). Many geodynamic models are now evaluated with reference to seismic tomography, including global mantle circulation models (e.g. Mao and Zhong, 2019), as well as regional models of specific scenarios, such as the interaction of a plume with the MTZ (e.g. Styles *et al.*, 2011*b*).

However, as discussed above (Section 1.4), seismic tomography is not the only constraint on the Earth's interior from seismology. Additionally, global constraints are provided by the 1D radial $V_S, V_P, \& \rho$ structure (e.g. Jeffreys and Bullen, 1940), observations on the topography of the discontinuities (e.g.

Shearer and Masters, 1992), and higher-order observations on Earth structure such as seismic anisotropy (e.g. Pisconti *et al.*, 2019). Comparisons between geodynamically-predicted 1D radial structure, although comparatively simple to calculate, are comparatively uncommon in the literature (e.g. Dannberg *et al.*, 2017), but global observations are potentially biased and therefore will also require filtering (e.g. Styles *et al.*, 2011*a*). Until recently, there were not examples of comparisons of geodynamic models to discontinuity-topography observations, but this is beginning to change (e.g. Papanagnou *et al.*, 2023). Similarly, workers are integrating predictions and observations of seismic anisotropy into assessments of geodynamic models (e.g. Ward *et al.*, 2024; Faccenda *et al.*, 2024).

1.6.3 Problems This Thesis Aims to Address

This thesis then addresses some of these outstanding questions in the modelling of the mantle's dynamics and comparison to observations, in particular by considering a more complex picture of MTZ phase relations and non-tomographic seismic observables. Chapter 2 addresses more complex phase boundary morphologies using explicit parametrisations of the phase boundaries' effect on the geodynamic flow. Chapter 3 demonstrates a method for calculating the MTZ discontinuities' topography, and provides an initial filter for the sensitivity of the *SS*-precursors used to observe the discontinuity. Chapter 4 applies this to a suite of MCMs to identify the impact of radial viscosity structure, primordial initial condition, and CMB temperature on predicted discontinuity topography. Experiments are undertaken to explore if the positive correlation of d410-d660 topography can be explained from this suite of MCMs and the applied phase relations.

Chapter 2

On the Global Geodynamic Consequences of Different Phase Boundary Morphologies

A version of this chapter has been published in EGU Solid Earth – *Morgan* et al. *(2025*a*). Whilst this paper was co-authored with members of my supervisory team, their contributions were not greater than the usual for a thesis chapter.*

Abstract

Phase transitions can influence mantle convection patterns, inhibiting or promoting vertical flow. One such transition is the ringwoodite-to-bridgmanite plus periclase transition around 670 km depth, which has a negative Clapeyron slope and therefore reduces mantle flow between the upper and lower mantle. Interactions between different transitions and significant Clapeyron slope curvature can potentially result in complexities in mid-mantle geodynamics – affecting the stagnation of slabs and free upward motion of plumes.

Here, I consider two examples where non-linear phase boundary morphologies have been invoked to explain mid-mantle dynamics: (1) the intersection of the ringwoodite-to-bridgmanite plus periclase transition with the bridgmanite-to-akimotoite and ringwoodite-to-akimotoite plus periclase transitions, forming a 'branching' morphology, and (2) the curvature of the garnet-to-bridgmanite transition. Using simple mantle convection or circulation simulations, I find that the dynamic impact of these example phase transitions are limited by either the uniqueness of thermodynamic state or the low magnitude of the phase buoyancy parameter respectively. Therefore it is unlikely that these phase boundary morphologies will, by themselves, prevent

material exchange across the mid-mantle.

2.1 Introduction

Jumps in mid-mantle material properties (including density) have been a feature of 1D seismological models since the 1940s (e.g., Jeffreys and Bullen, 1940; Dziewonski and Anderson, 1981; Kennett and Engdahl, 1991), and since the early 1950s have been associated with phase transitions (e.g., Birch, 1952). Since the equilibrium pressure of these transitions is dependent on temperature (via the Clapeyron slope $\gamma = \frac{dP}{dT}$), temperature anomalies in the mid-mantle can shift the depth of the transition, creating topography on the phase transformation surface, and the associated surface of the seismic discontinuity (e.g., Shearer and Masters, 1992). Where the Clapeyron slope is negative, this topography generates buoyancy forces that counteract thermal buoyancy (see Figure 14). Christensen and Yuen (1985) introduced a phase buoyancy parameter '$\mathbb{P}$' as a nondimensional number to describe the pro- or contra-convective strength of a phase change:

$$\mathbb{P} = \frac{\gamma \Delta \rho}{\alpha \rho^2 g D} \tag{2.1}$$

where α represents the thermal expansivity, ρ and $\Delta\rho$ represent the characteristic density and density change due to the phase transition respectively, g is the acceleration due to gravity, and D denotes the thickness of the convective layer.

The density jump associated with the *Rw* (Ringwoodite) $\rightarrow$ *Brm* (Bridgmanite) + *Pc* (Periclase) reaction can layer mantle convection in 2D (e.g., Christensen and Yuen, 1985) and 3D (e.g., Tackley *et al.*, 1994; Bunge *et al.*, 1997) numerical models if the phase buoyancy parameter is sufficiently negative. If the counter-convective effect of the phase transition is large, but not so large as to layer convection, global models enter a 'transitional regime' with impeded transfer across the phase boundary, and the deflection of downwellings and upwellings (e.g. Wolstencroft and Davies, 2011). In regional models moderately counter-convective phase transitions, combined with high mid-mantle viscosity contrasts can result in the deformation of slabs as they enter the deep mantle (e.g., Čížková and Bina, 2019). The phase buoyancy parameter necessary to induce a layered or transitional mode of global convection varies as a function of the vigour of convection described by the

Rayleigh Number given by

$$Ra = \frac{\alpha \rho g \Delta T D^3}{\kappa \eta} \tag{2.2}$$

where ΔT is the non-adiabatic temperature difference between the top and bottom of the convecting layer, D is the thickness of the convecting layer, η is the viscosity of the mantle, and κ is the thermal diffusivity. At Earth-like vigour ($Ra \sim 8 \times 10^6$) Wolstencroft and Davies (2011) found a value for $\mathbb{P} < -0.21$ and $\mathbb{P} < -0.085$ for layered and transitional modes respectively. For the Rw-out reaction this corresponds to critical Clapeyron slopes of -7.85 and $-3.18\,\mathrm{MPa\,K^{-1}}$ respectively.

The phase transitions Ol (Olivine) $\rightarrow Wd$ (Wadsleyite) (associated with the 410 km depth discontinuity) and $Rw \rightarrow Brm + Pc$ (associated with the 660 km depth discontinuity, hereafter '660') are likely the most important in mid-mantle dynamics (mineral physics suggests $\mathbb{P}_{\mathrm{Ol-out}} = 0.024$ and $\mathbb{P}_{\mathrm{Rw-out}} = -0.022$ – using parameters in Table 1). These, however, are not the only reactions in the mid-mantle; experimental and computational mineral physics has long shown that an extended series of phase transitions happen through the mid mantle, resulting in a complex patchwork of mineral stability fields (e.g., Stixrude and Lithgow-Bertelloni, 2011). Recently, seismologists have shown that the simple reactions do not fully explain the topography of the '410' and '660' seismic discontinuities (Cottaar and Deuss, 2016), and mineral physicists have proposed that phase diagram morphologies promote slab stagnation with additional counter convective forcings on cool regions in particular, leaving upwellings unaffected (e.g., Chanyshev *et al.*, 2022; Ishii *et al.*, 2023). It is, therefore, interesting to consider these morphologies and to consider in particular their impact on the Earth's mantle dynamics.

Recently, some numerical codes have implemented buoyancy forces using tables of computed thermodynamic properties either directly from differences in density (e.g. Ita and King, 1994; Nakagawa *et al.*, 2009) or by reformulating the governing equations in terms of entropy (e.g., Dannberg *et al.*, 2022; Li *et al.*, 2024), and these forces (assuming spatial gridding in the tables and geodynamic modelling doesn't 'miss' minor reactions) should all be 'complete' – capturing the effect in buoyancy forces of the density changes found in these thermodynamic tables, irrespective of how many or of what morphologies these phase transitions have in P-T space. The aim of this work is to consider from a simpler theoretical perspective how large a role these more complicated phase diagram morphologies could play and to inform intuitions about the extent that reactions described by a single Clapeyron slope approximate phase boundaries in Earth materials.

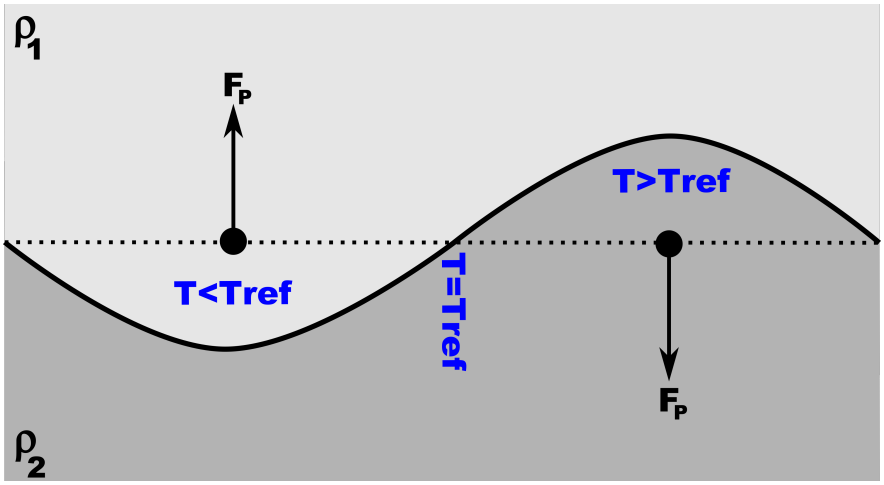

Figure 14: Generation of buoyancy forces (F_P) due to thermally driven topography on the equilibrium depth of a phase transition with a negative Clapeyron slope. Temperatures are given relative to a reference temperature T_{ref}, defined as the temperature where the phase boundary sits at some reference depth (dotted line). Where $\gamma = \frac{dP}{dT} < 0$ and $T < T_{\text{ref}}$, the equilibrium pressure is greater than that at T_{ref}, so the phase boundary deepens. Since the less dense upper material (ρ_1) is laterally adjacent to denser material ($\rho_2 > \rho_1$), this produces a positive buoyancy force, opposing the effect of the thermal buoyancy.

Here, I consider two examples – the post-spinel reactions *via* Akimotoite and the post-garnet reaction – which represent two basic morphologies beyond the well understood 'linear' phase boundary morphology: 'branching' and 'curving' morphologies respectively.

2.1.1 Branching Phase Boundaries: Post Spinel Reactions *via* Akimotoite

At cooler temperatures, bridgmanite in the post-spinel reaction ($Rw \rightarrow Brm + Pc$, hereafter reaction 'Z') is replaced by the ilmenite group mineral Akimotoite (e.g., Yu *et al.*, 2011) – $Rw \rightarrow Ak$ (Akimotoite) + Pc (hereafter reaction 'A') followed by transformation of $Ak \rightarrow Brm$ (hereafter reaction 'B') (See Figure 15 a). Recently, there has been interest in the potential geodynamic role of reaction 'B' whose Clapeyron slope is also negative but significantly larger in magnitude than that of the global reaction 'Z', and so mineral physicists and seismologists have suggested that reaction 'B' might potentially provide a mechanism to aid the stagnation of slabs (e.g., Cottaar and Deuss, 2016; Chanyshev *et al.*, 2022).

This is not the first contribution to the geodynamic literature that considers the effect of a 'branching' phase boundary morphology on mid-mantle dynamics. Using a phase function (after Christensen and Yuen, 1985), Liu *et al.*

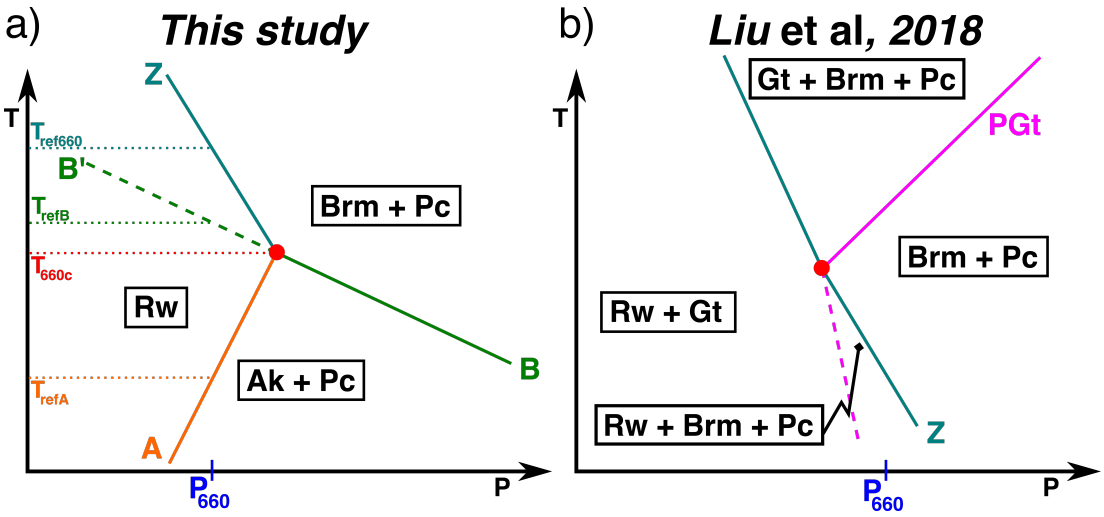

Figure 15: Sketch diagrams of branching phase diagram morphologies as implemented in geodynamic simulations. Temperature and pressure ranges are different between panes – the pressure at 660km depth (P_{660}) is included in for reference. *a)*: Sketch phase diagram of olivine system in the 660 phase boundary region. The reference temperature for reactions 'A' (orange line) and 'B' (green line) is calculated by projecting out from the triple point, described by temperature T_{660c} – for reaction B this is done along the pseudo-boundary beyond the triple point (dashed line labelled 'B′'). *b)*: Sketch pyrolite (60% olivine, 40% garnet) phase diagram implemented by Liu *et al.* (2018) at the intersection of the post spinel reaction (blue line labelled according to my convention as 'Z') and the post garnet reaction (magenta line labelled as 'PGt'). Note that the PGt implemented by Liu *et al.* in their geodynamic simulations is much shallower than the post garnet reaction I consider below since they are motivated by a different set of data (Hirose, 2002). Liu *et al.* (2018) do not consider the role of the post-garnet reaction at temperatures beneath the intersection – the dashed magenta line here represents this neglected necessary phase boundary.

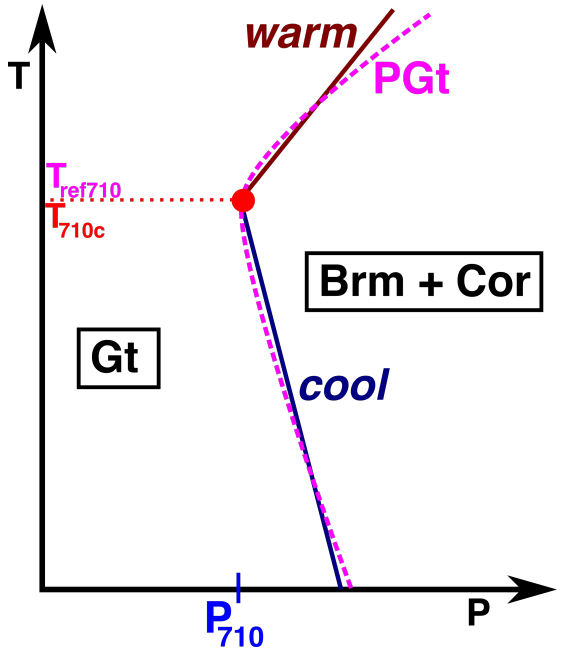

Figure 16: Sketch phase diagram of post-garnet reaction with temperature-dependent phase boundary. Smooth magenta dashed curve shows the phase boundary fitted by Ishii *et al.* (2023), straight navy and maroon lines sketch the implementation strategy here of treating the curved phase boundary as two straight boundaries meeting at a critical temperature. Pressure at 710 km depth (P_{710}) where the sheet mass anomaly is implemented is indicated. Phases Ishii *et al.* (2023) found to be stable indicated – *Cor* = corundum.

(2018) considered the effect of a sharp post-spinel reaction and broad linear post-garnet reaction interacting on a plume, forming a similar branched morphology except flipped in temperature (i.e. the 'trunk' is on the cooler side, and the 'branches' are on the warmer side of the critical temperature – see Figure 15 b). The phase diagram used by Liu *et al.* (2018) does not conserve entropy and volume changes around the phase boundary intersection since beneath the intersection temperature they should still have a garnet-out reaction, which they neglect to include. However, taking their implemented phase boundary buoyancy forces as-is, they show that the post-garnet reaction with a positive Clapeyron slope has a strong impact on the local phase boundary topography and significantly reduces the counter-convective effect of the post-spinel reaction on the long length-scale velocity field (Liu *et al.*, 2018).

2.1.2 Curving Phase Boundaries: Post Garnet Reaction with Variable Clapeyron Slopes

Recently, Ishii *et al.* (2023) suggested that due to the temperature-dependent heat capacity of garnet at lower mantle pressures, the post-garnet reaction

would have a negative Clapeyron slope at cooler temperatures, and a positive Clapeyron slope at warmer temperatures (see Figure 16). Additionally, Ishii *et al.* (2023) suggest that due to the presence of a small amount of stishovite, the post-garnet reaction is narrow instead of a broad, divariant[1] reaction, as has generally been assumed. Ishii *et al.* (2023) suggest that their temperature-dependent Clapeyron slope is responsible for slab stagnation whilst permitting plumes to pass unimpeded through the lowermost mantle transition zone. I describe this phase boundary morphology as a 'curving' morphology. A strongly curved post-spinel transition has also recently been suggested (Dong *et al.*, 2025). Here I consider the effects of a curved post-garnet transition on dynamics, but the intuitions gained with post-garnet can also be transferred to the effects of post-spinel.

2.1.3 This Contribution

In this contribution I illustrate the potential effects of these phase boundary morphologies. In Section 2.2 I describe the implementation of phase boundary topography buoyancy forces in TERRA, and how I modify the current implementation for a curving and branching morphology, and show the impact of these forces in simple thermal convection models to build intuitions about the controls and limitations of their impacts on flow. In Section 2.3 I illustrate the (non)-impact of the curving morphology on a mantle with a more Earth-like model setup. As I am considering the role of these diverse phase transitions on convection, I do not consider the role of some other factors such as radial viscosity structure (e.g. Garel *et al.*, 2014; Cerpa *et al.*, 2022), the temperature dependence of rheology (King and Ita, 1995), or the kinetics of phase transformations (King *et al.*, 2015) which have been suggested and shown in numerical simulations to have an effect on the behaviour of downwellings in the mid-mantle.

2.2 Simple Thermal Convection Models

To illustrate the potential dynamics that these diverse phase boundary morphologies can produce, I run 20 simulations using the mantle convection code TERRA (e.g., Baumgardner, 1983; Panton *et al.*, 2022) with parameters detailed in Table 2. I consider in turn the implementation of phase boundaries in TERRA, the implementation of branching phase boundaries and their possible effects, and finally the implementation and effects of curving phase

[1] i.e. occurs over a finite pressure interval, where two assemblages co-exist at equilibrium

Symbol	Parameter	Value	
t	Simulation Duration	4.5 Gyr	
ρ_0	Reference Density	$4500\ \mathrm{kg\,m^{-3}}$	[a]
α	Thermal Expansivity	$2.5 \times 10^{-5}\ \mathrm{K^{-1}}$	[b]
k	Thermal Conductivity	$4\ \mathrm{Wm^{-1}\,K^{-1}}$	[c]
C_P	Specific Heat Capacity	$1100\ \mathrm{J\,kg^{-1}\,K^{-1}}$	[d]
T_{surf}	Surface Temperature	300 K	
T_{CMB}	Core Mantle Boundary (CMB) Temperature	3000 K	
H	Internal Heating	$0\ \mathrm{W\,kg^{-1}}$	
γ_{410}	$\frac{dP}{dT}$ of the $Ol \rightarrow Wd$	$+1.5\ \mathrm{MPa\,K^{-1}}$	
γ_{660}	$\frac{dP}{dT}$ of the $Rw \rightarrow Brm + Pc$	$-1\ \mathrm{MPa\,K^{-1}}$	
η_0	Reference Viscosity	$10^{23}\ \mathrm{Pa\,s}$	[e]
$\Delta\rho_{410}/\overline{\rho_{410}}$	Density change for $Ol \rightarrow Wd$	6.37 %	
$\Delta\rho_{660Z}/\overline{\rho_{660Z}}$	Density change for $Rw \rightarrow Brm + Pc$	8.7 %	
$\Delta\rho_{660A}/\overline{\rho_{660A}}$	Density change for $Rw \rightarrow Ak + Pc$	4.5 %	* [f]
$\Delta\rho_{660B}/\overline{\rho_{660B}}$	Density change for $Ak + Pc \rightarrow Brm + Pc$	4.2 %	* [f]
$\Delta\rho_{\mathrm{PGt}}/\overline{\rho_{710}}$	Density change for $Gt \rightarrow Brm + Cor$	3.13 %	† [g]
γ_{warm}	$\frac{dP}{dT}$ of the $Gt \rightarrow Brm + Cor$ on the warm arm	$2.5\ \mathrm{MPa\,K^{-1}}$	† [e]
Initial Condition: All models initialized from a temperature field (identical across simulations) with small random anomalies away from the average temperature structure.			

[a] – Reasonable typical mantle density, e.g. Dziewonski and Anderson (1981)
[b] – Typical values for mantle materials (p. 61, Poirier, 2000)
[c] (p. 122, Clauser and Huenges, 1995)
[d] (Panton, 2020)
[e] (Deschamps and Cobden, 2022)
[f] (Kojitani *et al.*, 2022)
[g] (Ishii *et al.*, 2023)
* – for Ak simulation, not included in PGt or reference simulations
† – for PGt simulations, not included in Ak or reference simulations

Table 1: Values taken as constant across all convection simulations.

Simulation Number	γ_{cool} [MPa.K^{-1}]	γ_{hot} [MPa.K^{-1}]	$T_{710\text{c}}$ [K]	γ_{660B} [MPa.K^{-1}]	$T_{660\text{c}}$ [K]	Regime
100	·	·	·	·	·	W
101	·	·	·	-4.4	1400	W
102	0	2.5	1200	·	·	W
103	-1.5	2.5	1200	·	·	W
104	-3	2.5	1200	·	·	W
105	-9	2.5	1200	·	·	W
106	-12	2.5	1200	·	·	W
107	-18	2.5	1200	·	·	S
108	0	2.5	1850	·	·	W
109	-1.5	2.5	1850	·	·	W
110	-3	2.5	1850	·	·	W
111	-9	2.5	1850	·	·	W
112	-12	2.5	1850	·	·	W
113	-18	2.5	1850	·	·	S
114	0	2.5	2500	·	·	W
115	-1.5	2.5	2500	·	·	W
116	-3	2.5	2500	·	·	W
117	-9	2.5	2500	·	·	W
118	-12	2.5	2500	·	·	W
119	-18	2.5	2500	·	·	S

Table 2: Simple thermal convection simulations, varied parameters and dynamic regimes classified as – whole mantle convection ('W') or whole mantle convection with downwelling stagnation ('S').

boundaries. My simulations are not particularly Earth-like. Instead, the models in this section are 'toy' models designed to illustrate the dynamic effects of buoyancy forces due to the topography of the phase transition surface. Therefore, key physics that may, for instance, change the dynamics of slabs in the MTZ, such as temperature dependent viscosity, a radial viscosity jump, or Earth-like surface kinetics are omitted. I will consider a more sophisticated (but still comparatively simple) pair of simulations in Section 2.3.

2.2.1 Implementation of Phase Transitions

I implement all the reactions (post-olivine, post-spinel and the more complex examples considered below) using the sheet-mass anomaly method (e.g., Tackley *et al.*, 1993; Bunge *et al.*, 1997). This more simple method allows a direct consideration of phase boundary transition parameters. In a Boussinesq approximation, the method adds a buoyancy stress ($\Delta\sigma$) due to the topography of the phase transition as

$$\Delta\sigma = \gamma \frac{\Delta\rho}{\rho}(T - T_{\text{ref}}) \tag{2.3}$$

on the nodes at the reference depth of the phase transition. In this expression, T is the temperature at the node and T_{ref} is the reference temperature (see Figure 15, a) of the phase boundary (temperature where the phase boundary sits at the reference depth (i.e. 410km or 660 km in depth)), $\Delta\rho$ is the density difference associated with the phase change and γ is the Clapeyron slope of the phase transition.

2.2.2 Reference Model

To compare the effect of including branching and curving morphologies, I first consider a reference model with a linear post-spinel reaction (Simulation Number 100). All the other simple convection models are based on this model setup. The simulations are run in TERRA which solves the equations of the conservation of mass, momentum, and energy in a spherical shell (the geometry of a planetary mantle) using the parameters listed in Table 1. The models are run for 4.5 Gyr (to quasi thermal steady state, see Figure 17), and the reference model is visualized in Figure 18a. In all simulations, as well as the deeper mantle transition zone reactions considered in this chapter, I include the olivine-out reaction at 410 km depth. For these simple simulations I use an isoviscous rheology and take the Boussinesq approximation; these are both significant simplifications away from the real Earth but allow us to assess the

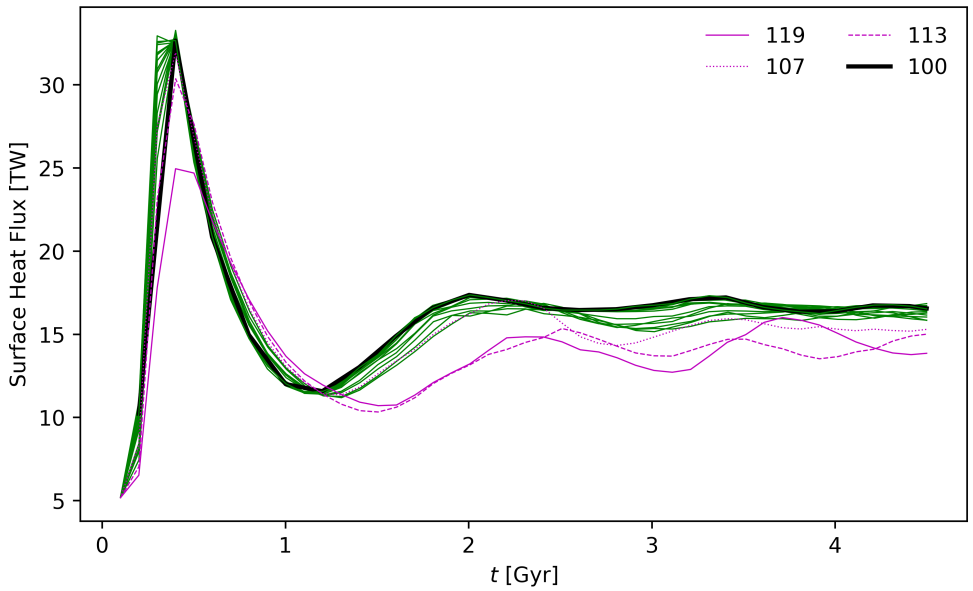

Figure 17: Evolution of surface heat flux of simple convection simulations in Table 2, illustrating that the simulations reach quasi-steady state by the end of the simulation. Simulations are coloured according to their regime of convection in Figure 23, with select simulations highlighted in legend – Simulation 100 (the reference case) is in a heavy black line, Simulation Numbers 107, 113 and 119 are in magenta with dotted, dashed, and solid lines respectively are all in regime 'S', featuring downwelling stagnation in the thermal structure. Other simulations (in regime 'W', whole mantle convection) are in green line – see discussion of dynamic regimes in Section 2.2.6.

impact of the phase boundary topography buoyancy forces. In taking the Boussinesq approximation, I do not include the direct effect of the enthalpy of reaction on the temperature field. This latent heat effect is generally smaller than the effect of the phase boundary topography and has the opposite effect on the convection (e.g., Ita and King, 1994; Steinberger, 2007; Dannberg *et al.*, 2022), hence the work here represents an upper bound on the potential effect of the phase transition on the dynamics. Similarly, since a temperature dependent rheology would tend to stiffen cold downwellings (that are subject to the additional counter convective forces discussed in this paper), and stiff downwellings in free convection models have been shown to be less sensitive to stagnation than downwellings in an isoviscous mantle (e.g. Zhong and Gurnis, 1994; King and Ita, 1995), this simplification again leads to an overestimation of the potential effect of these phase boundaries. In a mantle with a jump in viscosity in the mid-mantle, as is anticipated in the Earth, thermally stiffened downwellings may instead promote slab-roll back and therefore the formation of horizontal stagnant slabs (e.g. Chen *et al.*, 2022).

I do not include the effect of laterally varying composition on the relative

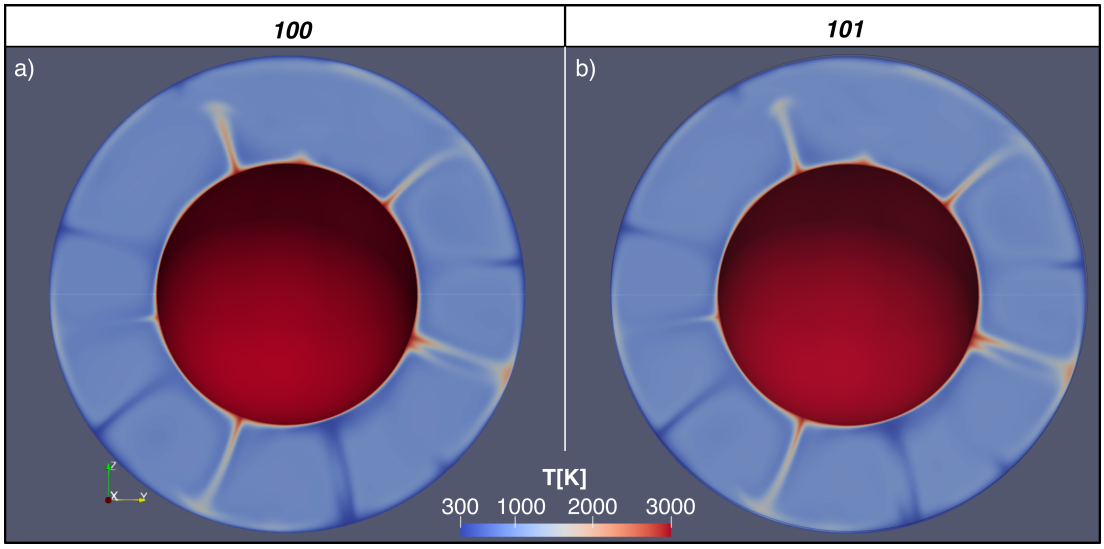

Figure 18: Visualisation of convection simulations after 4.5Gyr of evolution *a)* Reference case (Simulation Number 100) – post-olivine and post-spinel reactions included, but no other reactions included. *b)* branching case (Simulation Number 101) – Akimotoite reactions implemented using values suggested by Kojitani *et al.* (2016, 2022). Note that there is no significant difference between the thermal structure of the simulations, as expected.

strength of the reactions. Whilst the mantle as a whole has a pyrolytic composition (~ 60 % olivine and ~ 40 % garnet in the upper mantle e.g. Bina and Helffrich 2013), compositional heterogeneities generated by melting at the surface result in regions enriched and depleted in garnet and pyroxene in the upper mantle – in entirely enriched regions (high in basalt) of the mantle, no post-spinel reaction is expected (and the post-garnet reaction – see below – would be at its maximum strength), and in entirely depleted regions of the mantle the post-spinel reaction should be at its maximum strength. I assume that each reaction affects all of the material around it, and thus provide an overstated upper bound on the influence of reactions on mantle flow.

2.2.3 Implementing Branching Phase Transitions (Post-Spinel *via* Akimotoite)

The sheet-mass anomaly approximation (Tackley *et al.*, 1993) assumes that the length scale of the topography on the phase boundary is less than or similar to the length scale of the thermal structure that drives the flow. For a downwelling body whose temperature is 500 K below the critical temperature of the reactions 'A', 'B', and 'Z', and with Clapeyron slopes of $\gamma_A = +1.5$ and $\gamma_B = -6$ MPa/K and a mid-mantle radial pressure gradient of 40 MPa/km, I estimate a maximum separation between the phase transition surfaces inside the

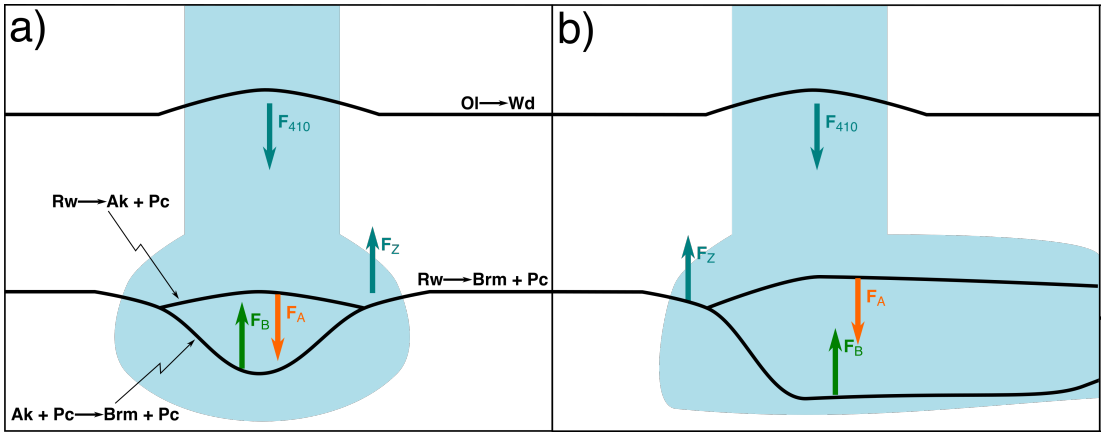

Figure 19: Sketches illustrating the forces due to phase boundary topography of reactions A & B (F_A and F_B respectively) in cool downwellings, which are sketched in pale blue fill. *a)*: In a vertical slab, where the split phase transition region is comparatively small, and the opposing phase transition topography buoyancy forces act on near-identical regions; *b)*: And in a stagnating slab, where the phase transitions spread further apart the forces act on distinct regions. F_{410} denotes the force due to the $Ol \rightarrow Wd$ reaction, at 410 km depth, F_Z the force due to the $Rw \rightarrow Brm + Pc$ reaction (reaction 'Z' in Figure 15a).

downwelling body as on the order of 100 km
($(1.5 + 6\ [\mathrm{MPa.K^{-1}]}) \cdot (500\ [\mathrm{K}])/(40\ [\mathrm{MPa.km^{-1}}])$). In my global convection models (with a comparatively high mantle viscosity of 10^{23}Pa s), my slabs end up much wider than this separation between the equilibrium phase transformation depths, allowing us to consider the phase transition boundary topography force from both the reactions 'A' and 'B' as acting at similar depths (see Figure 19). We are probably at the edge of where this approximation is valid; moving toward weaker and temperature dependent geological mantle rheologies (and therefore narrower downwellings) would break this simplification for these reactions. However, the theoretical understanding developed below suggests significant effects on global dynamics are unlikely. Given that this approximation overstates the dynamic effect branching reactions can have on mantle flows, I expect my conclusions to be robust. Therefore, Equation 2.3 becomes

$$\Delta\sigma_{660} = \begin{cases} \gamma_Z \cdot \frac{\Delta\rho_Z}{\rho}(T_{660} - T_{\mathrm{ref660}}) & T_{660} \geq T_{660\mathrm{c}} \\ \\ \gamma_A \cdot \frac{\Delta\rho_A}{\rho} \cdot (T_{660} - T_{\mathrm{ref}A}) + \gamma_B \cdot \frac{\Delta\rho_B}{\rho} \cdot (T_{660} - T_{\mathrm{ref}B}) & T_{660} < T_{660\mathrm{c}} \end{cases} \tag{2.4}$$

where $T_{660\mathrm{c}}$ is the temperature of the triple point, where reactions A, B, and Z meet (see Figure 15 a).

I do not have free choice over the values of the Clapeyron slopes and density

	γ_Z [MPa K^{-1}]	γ_A [MPa K^{-1}]	γ_B [MPa K^{-1}]	T_{660c} [K]
Yu *et al.* 2011	-2.9	1.2	-6	1400
Ye *et al.* 2014	-2.5	·	·	·
Hernández *et al.* 2015	·	1.65	-3.5	1565
Kojitani *et al.* 2016	-1	·	·	·
Kojitani *et al.* 2022	·	1.8	-4.4	1440
Chanyshev *et al.* 2022	-0.1	·	-8.1	·

Table 3: Values for parameters recently calculated by mineral physicists. '·' indicates that this value is not evaluated in the publication.

changes at branching intersections, since entropy and volume changes are properties of state alone. The changes in entropy and volume from one state to another must be equal regardless of the path taken. With reference to Figure 15a, the entropy and volume changes must be the same whether the assemblage changes from Rw to $Brm + Pc$ via reaction 'Z' or via reactions 'A' and 'B'. Assuming $\Delta V \ll V$ and re-writing Equation 2.4 in terms of volume and entropy change we get

$$\Delta\sigma_{660} = \begin{cases} \frac{-\Delta S_Z}{V} \cdot (T_{660} - T_{\text{ref}}) & T_{660} \geq T_{660c} \\ \\ \frac{(-\Delta S_A - \Delta S_B)}{V} \cdot (T_{660} - T_{\text{ref}}) & T_{660} < T_{660c} \end{cases} \tag{2.5}$$

As $\Delta S_A + \Delta S_B = \Delta S_Z$, the temperature-dependence of the phase boundary topography buoyancy force has to be the same either side of the triple point if I apply these forces using a sheet-mass anomaly approximation.

2.2.4 Results for Thermodynamically Consistent Branching Phase Transitions

In order to demonstrate the (non-)effect of implementing a thermodynamically consistent branched morphology using the implementation described above, a simulation based on the reference case was run, but with $\gamma_A = 1.8$ MPa K^{-1} and $\gamma_B = -4.4$ MPa K^{-1} (i.e. the values of Kojitani *et al.* (2016, 2022), but these are similar to other published values for the Clapeyron slopes – see Table 3). This is visualized after 4.5 Gyr in Figure 18b, where it is obvious that the simulations are very nearly identical, highlighting that the combined phase boundary buoyancy forces of reactions 'A' and 'B' result in an extremely similar resultant force to what reaction 'Z' would have produced. I further verify this in Figure 20, where I compare the radial temperature histograms for the two simulations – demonstrating again that they are nearly identical. It is worth

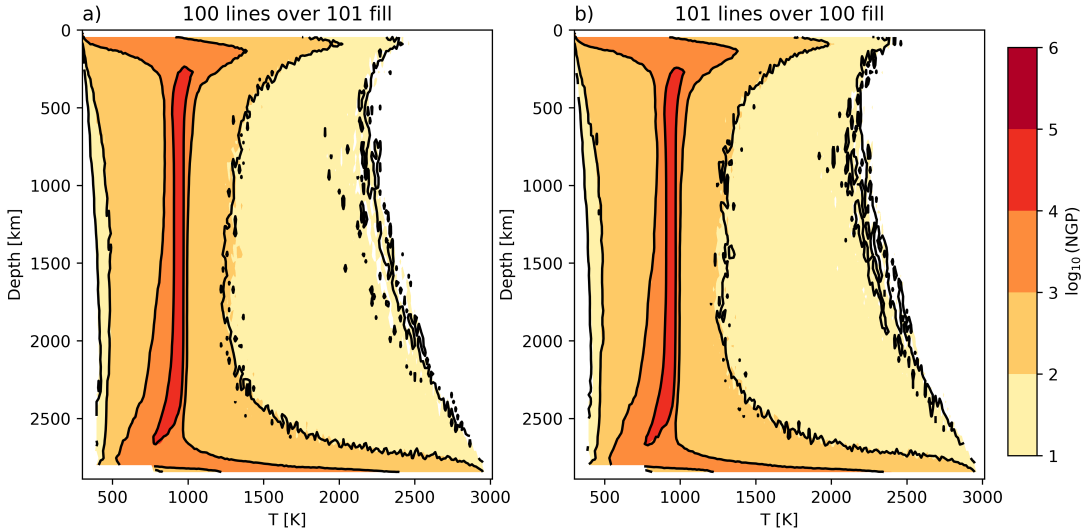

Figure 20: Radial temperature histograms coloured by number of grid points ('NGP') for Reference Simulation 100 and Akimotoite Simulation 101 with contours of the reference (100) and Ak (101) simulations' radial temperature histograms overlaid respectively *a)* and *b)*.

assessing if the residual between the temperature fields presented in Figure 18 is useful in verifying if they are identical. This is presented in Figure 21. Inside the convective cells, including around 660 km depth, where the branching phase transformation is implemented, the residual is extremely low (< 100 K). However, near the upwellings and downwellings, large residual temperature anomalies are present in excess of 500 K in radial structures. This indicates a lateral motion of the upwelling and downwelling limbs between the simulation 100 and 101. This is not indicative of different dynamics between the two simulations, but rather that the final dump of simulation 100 happens a little later than that of simulation 101 (inspecting the detailed simulation logs, the final convection iteration (no. 7101) starts at 4.44 Gyr in simulation 101, and 4.45 Gyr in simulation 100, and simulation 100 has a slightly larger time-step). Clearly, Figures 18 and 20 gave a clearer assessment of the similarity of the two geodynamic models. To use the residual on the temperature field to verify the identical nature of the geodynamic models would require some modification to the time-stepping so that it strictly re-calculates the final convection iteration to the input duration of the simulation, or abandoning the adaptive time-stepping, which is computationally extremely advantageous.

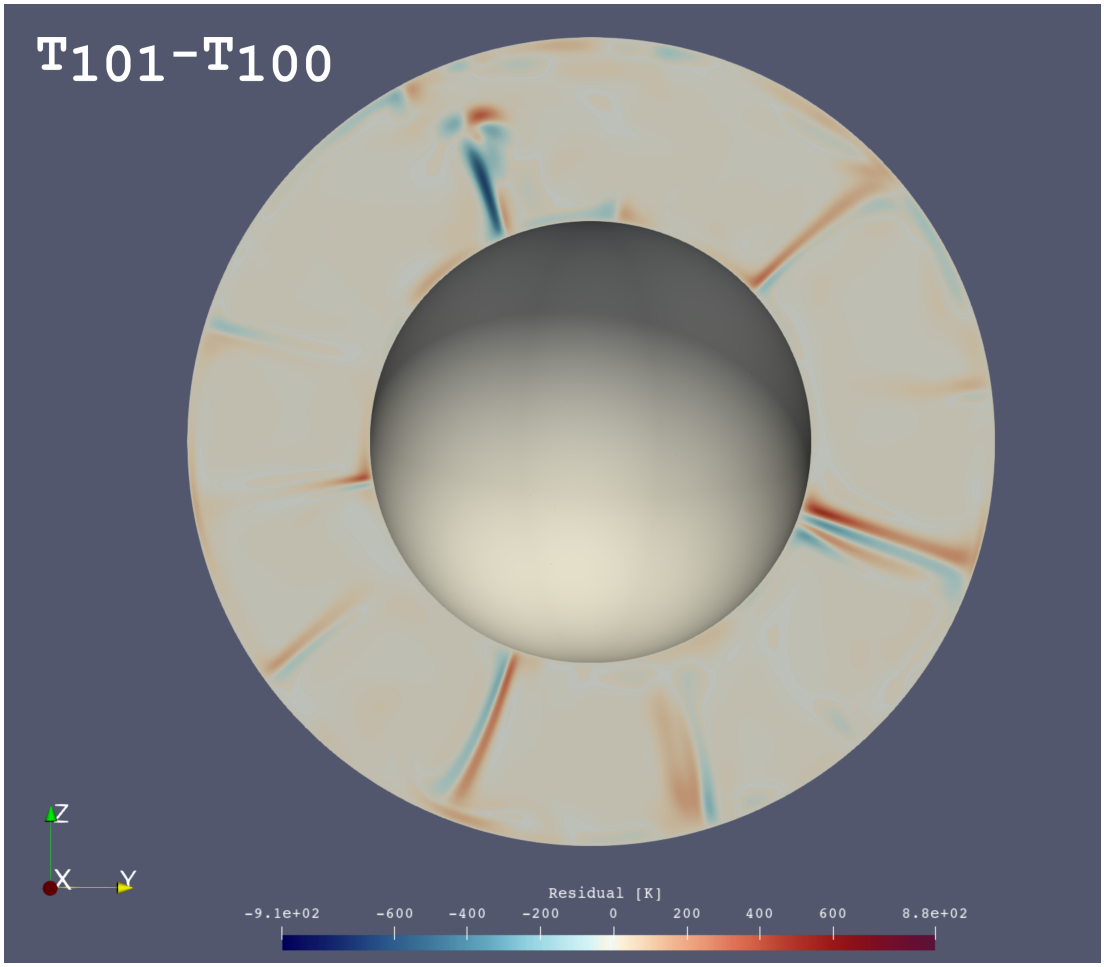

Figure 21: Temperature residual between simulation 100 (reference) and 101 (thermodynamically consistent akimotoite implementation) after 4.5 Gyr of evolution, whose temperature fields are separately presented in Figure 18.

2.2.5 Implementing Curving Phase Transitions (Post-Garnet)

As illustrated in Figure 16, the curving post-garnet reaction is here implemented using two straight lines to approximate the parabolic form suggested by Ishii *et al.* (2023). Since the phase boundary topography implied by Ishii *et al.* (2023) is relatively modest, the sheet-mass anomaly approximation in TERRA is suitable for application to this reaction. I calculate the buoyancy stresses at 710 km depth due to this topography as

$$\Delta\sigma_{710} = \begin{cases} \gamma_{\text{warm}} \cdot \frac{\Delta\rho_{\text{PGt}}}{\rho}(T_{710} - T_{\text{ref710}}) & T \geq T_{710\text{c}} \\ \\ \gamma_{\text{cool}} \cdot \frac{\Delta\rho_{\text{PGt}}}{\rho} \cdot (T_{710} - T_{\text{ref710}}) & T < T_{710\text{c}} \end{cases} \tag{2.6}$$

where γ_{warm} and γ_{cool} are the Clapeyron slopes above and below the critical temperature. By choosing the depth at which the post garnet phase boundary force is implemented at as 710 km (the minimum depth of the phase boundary found by Ishii *et al.* (2023)), this means that a single reference temperature T_{ref710} describes both the warm and cool legs of the 'curved' reaction, and is also the temperature at which the Clapeyron slope of the reaction changes $T_{710\text{c}}$. To explore the role that this curving reaction can apply I vary two parameters explicitly – $T_{710\text{c}}$ and γ_{cool} in the ranges of 1200 to 2500 K and 0 to -18 MPa K^{-1} respectively over 18 simulations (see Table 2).

2.2.6 Results for Curving (Post-Garnet) Phase Transition

Select simulations with a post-garnet inspired curving phase change are visualized in Figure 22. At the highest magnitude of γ_{cool} considered here (-18MPa K^{-1}) (Figure 22a) many downwellings fail to enter the lower mantle. Decreasing the value of γ_{cool} (compare results in Figure 22c) results in a mode of convection similar to that seen for the reference case (see Figure 18a), with a similar resulting thermal evolution (casenumber 106 plots close to the reference case in the surface heat flux and radial mass flux plots in Figure 17 and Figure 24).

Effect of $T_{710\text{c}}$

As well as the magnitude and sign of the Clapeyron slope, another important parameter in determining the vigour of convection is $T_{710\text{c}}$ – which controls the portions of the mantle affected by pro- and contra-convective forcings from the

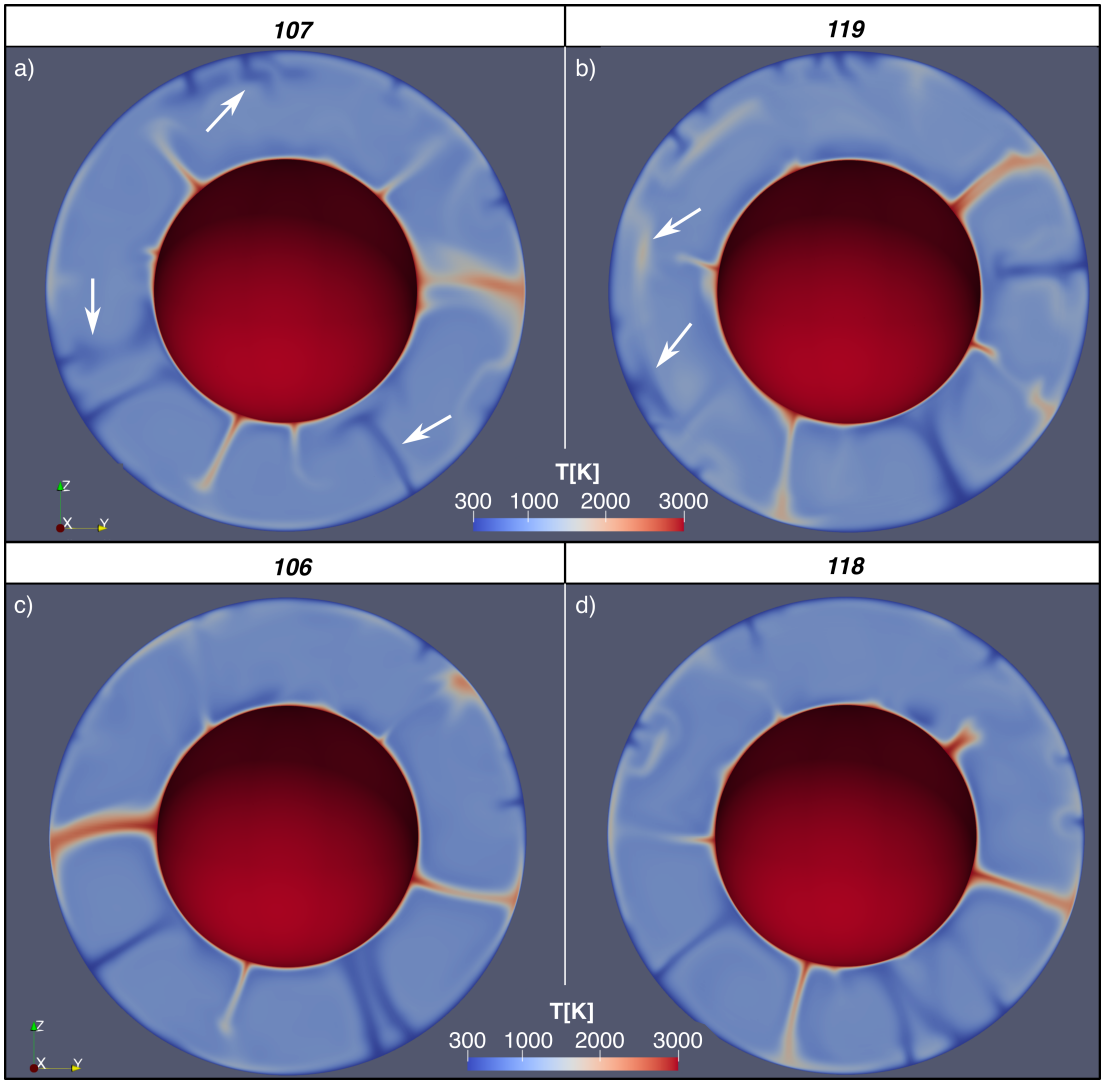

Figure 22: A great circle slice through the temperature field of 3D convection simulations with PGt reaction present after 4.5 Gyr. *a) & b)* where $\gamma_{\text{cool}} = -18$ MPa K^{-1} after 4.5Gyr of evolution *a)* Simulation Number 107, $T_{710\text{c}} = 1200$K *b)* Simulation Number 119, $T_{710\text{c}} = 2500$K and *c) & d)* where $\gamma_{\text{cool}} = -12$ MPa K^{-1} after 4.5Gyr of evolution *c)* Simulation Number 106, $T_{710\text{c}} = 1200$K *d)* Simulation Number 118, $T_{710\text{c}} = 2500$K. Arrows indicate convective flows discussed in the text.

phase boundary topography, with higher values of T_{710c} meaning that more of the downwellings are effected by the cool-arm of the PGt reaction. With an increasing proportion of the Earth's mantle subject to a counter-convective forcing in cold downwellings in Figure 22b, stagnation becomes more likely. Considering Figure 22 a and b, where the simulations have a higher magnitude of γ_{cool} (-18 vs -12 MPa K^{-1}) than in Figure 22 c and d – we again see more downwellings stagnating in the right hand panel and large volumes of cold material building up in the mid mantle (e.g., stagnation at $\sim$ '8 O'Clock' Figure 22b). In Figure 22a, by comparison, cold material is able to start entering the lower mantle with less negative thermal buoyancy (e.g., the downwelling at '9 O'Clock' descending with a bulge of stagnated material in the mid mantle, or at '11 O'Clock a pile of cold material in the Mantle Transition Zone (MTZ) starting to descend into the lower mantle). This illustrates that increasing the value of T_{710c}, whilst not exerting a large enough influence to change the mode of convection here, is changing the magnitude of the local-counter convective effect on the downwellings. Considering the relative mass-flux at 720km depth (see Figure 24), we see that Simulation 107 has a much higher mass flux than the other 'S' cases, suggesting that at even lower T_{710c}, we might expect whole mantle convection even at extremely negative values of γ_{cool}.

Dynamic Regimes

I categorize the 18 simulations with the curved post-garnet reaction into two groups based on the presence or absence of stagnant cold material in the mid-mantle; 'whole mantle convection' ('W') and 'whole mantle convection with downwelling stagnation' ('S'), see Table 2 and Figure 23. Simulations that I categorized as 'S' have lower surface heat fluxes when they reach quasi-steady state that those in regime 'W' (compare magenta and green lines in Figure 17). The simulations with stagnating slabs and higher values of T_{710c} (Simulation Numbers 113 and 119) have lower heat fluxes at 4.5 Gyr than the simulation with a lower value of T_{710c} (Simulation Number 107 although this varies over the simulation duration). A regime diagram of these models plotted with their values of T_{710c} and γ_{cool} is shown in Figure 23. Note that there is no change of regime until much higher magnitude values of γ_{cool} than those suggested by Ishii *et al.* (2023) to apply for the actual Earth. As illustrated in Figure 22, there is some variation in downwelling behaviour within these regimes, but T_{710c} plays a secondary role to γ_{cool}. In Figure 23 I include a sketched boundary between the two regimes; the slope of this line is inferred to be positive since there is more stagnation in Simulation 119 than Simulation 107 – but with this suite of simulations the exact position of the regime boundary is difficult to constrain. I

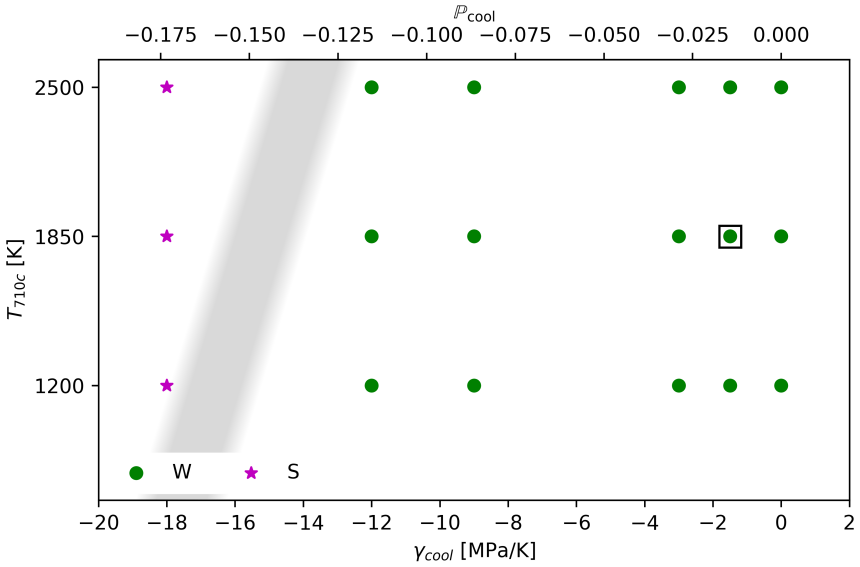

Figure 23: Regime diagram of model runs plotted on their values of T_{710c} and γ_{cool}. Simulations in the mode of whole mantle convection and in a mode with slab stagnation are marked 'W' and 'S' respectively. The approximate region and inferred slope polarity of the boundary between these regimes is indicated by the grey shading. Simulation 109, which takes the values proposed by Ishii *et al.* (2023) for γ_{cool} and T_{710c}, is highlighted by a black square.

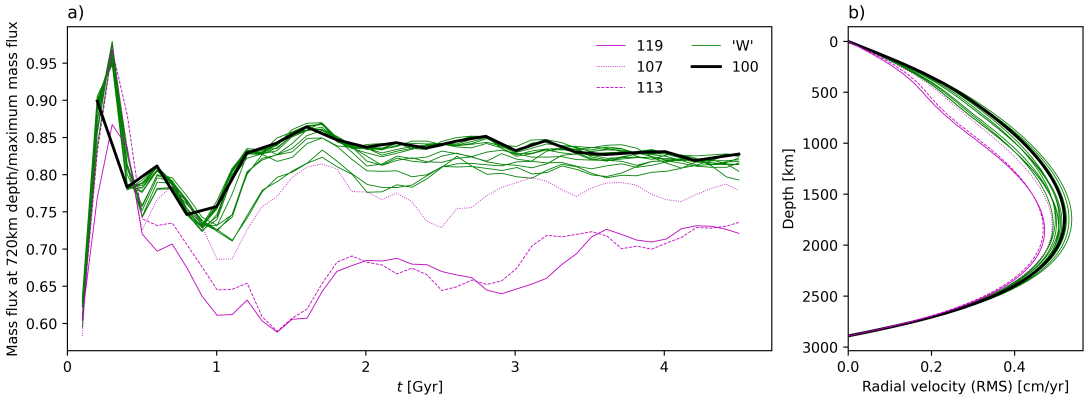

Figure 24: *a)* Evolution of mass flux at 720 km depth of simple convection simulations in Table 2 and *b)* End-of simulation RMS of radial velocity of simulations in Table 2. Simulations are coloured according to their regime of convection in Figure 23, with select simulations highlighted in legend – Simulation 100 (the reference case) is in a heavy black line, Simulation Numbers 107, 113 and 119 are in magenta with dotted, dashed, and solid lines respectively are all in regime 'S'. Other simulations (in regime 'W') are in green line – see discussion of dynamic regimes in Section 2.2.6.

emphasise that this change in dynamic regime does not occur until a much more negative phase parameter than suggested by current data for the garnet-out reaction (Ishii *et al.*, 2023).

As well as considering the morphology of the downwellings (as in Figure 22), I also consider the effect of the phase transition on the flow of material through the mid-mantles of my simulations. In Figure 24b I plot the root-mean-square of the radial component of velocity as a function of depth for each of the simulated mantles. Simulations 119 and 113 have lower radial velocities in a broad region of their mid-mantles compared to the simulations undergoing whole-mantle convection (e.g. Simulation 100). Simulation 107, which I classified as being in regime 'S' by inspection of its thermal structure has slightly lower radial velocities than the 'W' cases. I also present (Figure 24a) the ratio of mass flux at 720km depth and the maximum mass flux during the evolution of the simulated mantles. Again, after the first mantle overturn, Simulations 119 and 113 have a much weaker mass flux than the simulations in the whole-mantle convection regime. The relative mass flux in these simulations increases during the model evolution, with major upswings in mass flux, with percent-of-maximum mass flux variations on 100Myr timescales. Simulation 107 has a higher mass flux than the other 'S' cases, but its flux is still a step lower than the mass flux of the 'W' regime simulations, and evolves in a fashion distinct from those simulations. This likely represents that in simulation 107 there is regional ponding on some downwellings (around 12 O'Clock, Figure 22 a), whereas others descend directly (4 O'Clock) strongly enough that there is sufficient downwelling to permit upwellings to rise unimpeded, unlike in 119 (Figure 22 b) where there is some ponding of material in the mid-mantle (9 O'Clock).

2.2.7 Discussion on Simple Thermal Convection Models

Using these simple mantle convection models, I have been able to demonstrate the non-effect of a branching reaction (Figure 18) morphology of ringwoodite out via akimotoite and to demonstrate some of the behaviours possible for a curving phase boundary (Figure 22). By varying T_{710c} and γ_{cool} I have illustrated that the cold-arm of the post garnet reaction does not change the mode of global convection significantly until γ_{cool} is an order of magnitude greater than that suggested from the experiments of Ishii *et al.* (2023). Similar to Bina and Liu (1995), I also found a dependence in convective style on the temperature where the Clapeyron slope changes, but found that γ_{cool} had a much larger impact in my simulations than T_{710c}. Given that multiple factors about the set up of these

simulations favour these phase boundaries being able to have a large effect on the mode of convection, this suggests that in the real Earth, this phase boundary morphology is unlikely to be responsible for the stagnation of slabs.

2.3 Thermochemical Mantle Circulation Models at Earth-like Vigour

The simple mantle convection models of the previous section are non-Earth-like in several respects. Firstly, I have assumed that there is no radiogenic or shear heating and that the models are incompressible – meaning that the mid-mantles in my simulations end up being much cooler on average ($\sim$ 950 K) than the real Earth's mantle (e.g. $\sim$ 1650 K (Waszek *et al.*, 2021)). Further, the convection simulations were isoviscous with a high reference viscosity, so did not represent the temperature and depth dependence of viscosity, which can influence downwellings at the base of the MTZ (e.g., Garel *et al.*, 2014). Together, these result in a Rayleigh number of $\sim 10^5$ compared to the Earth's value of $\sim 10^7$ – which may understate the contra-convective effect since global phase transitions have a greater effect at higher Rayleigh number (e.g., Tackley *et al.*, 1993; Wolstencroft and Davies, 2011). In the following sections I describe two significantly more sophisticated Mantle Circulation Models (MCMs) incorporating ('TC1') and excluding ('TC0') the effect of the post-garnet reaction. *Simulation TC0 was run by Dr James Panton for the MC2 project.*

2.3.1 Method

My more Earth-like simulations are also run in TERRA, but instead of a free-slip surface, the surface motion is imposed using the plate motion history of Müller *et al.* (2022). These plate motions are scaled by a factor of 0.5 (that is, the plate motions are slowed down to mantle velocities) so that the RMS surface motions match those produced by the simulated mantle in convection (found during model initialisation, see below).

The model rheology is also more Earth-like than the previous simulations, with a reference viscosity closer to the Upper Mantle viscosity (see Table 4). Viscosity varies according to[2]

$$\eta = \eta_0 \cdot f_r \cdot e^{V_a \cdot Z' - E_a \cdot T'} \tag{2.7}$$

[2]In the published paper, this viscosity law was misstated (Morgan *et al.*, 2025*a*). A correction to the published paper is now in preparation.

where η is the local bulk viscosity, η_0 is the reference viscosity, f_r is the radial viscosity factor (see Figure 25), E_a is the non-dimensionalized activation energy, T' is the non-dimensionalized temperature given by $T' = 0.5 - \frac{T - T_{\mathrm{CMB}}}{T_{\mathrm{surf}} - T_{\mathrm{CMB}}}$, V_a is the non-dimensionalized activation energy, and Z' is the non-dimensionalized depth. Whilst this rheology law introduces a depth- and temperature-dependence that I did not have in my simpler convection simulations above, the temperature dependence is less pronounced than that used in other studies (e.g. King, 2009; Javaheri *et al.*, 2024). As discussed in relation to the simple convection simulations above, underestimating the stiffening of cold slabs likely leads to us overestimating the effect the curved phase transition has on the dynamics. The addition of radial viscosity layering and a kinematic surface boundary condition introduces additional physics that may favour the formation of stagnant slabs. Although the plate motion reconstruction used is sophisticated, and therefore includes some trench motion, it is unlikely to be perfect. Müller *et al.* (2022) report trench retreat rates principally in the range -2.5 (i.e. advance) to 5 cm/yr, which they consider acceptable compared to the current global reported range of trench retreat reported by Schellart *et al.* (2008) in the range of 0 to 2 cm/yr. However, whilst the long term trench retreat rates may match present observations, the plate motion history stages used in the MCMs are 1 Myr periods with constant plate motions within them, meaning that the surface motions jump at the end of each stage, only approximating continuous trench retreat. However, the constrained downwelling history does force the downwellings to enter the Earth's mantle in a Earth-like geometry and planform, constraining and guiding the convection and producing more Earth-like dynamics than for free-convection simulations without a strain localising rheology.

Composition is tracked on particles created and advected using the method of Stegman (2003). I model melting in the upper parts of the mantle, generating enriched (basaltic) material at the surface, and depleted (harzburgitic) material in the source regions (Van Heck *et al.*, 2016). Variations in enrichment affect the intrinsic density – through most of the mantle this means that basalt is ~ 2 % denser than lherzolite ('ambient mantle'), but between 660 km and 740 km depth, basalt is 5 % less dense than lherzolite as the post-garnet reaction is deeper than the post-spinel, and basalt is enriched in garnet compared to lherzolite and harzburgite (e.g., Yan *et al.*, 2020). Aside from this 'basalt density filter' effect (which does not result in a strong concentration of basalt in the deeper parts of the mantle transition zone in these simulations) I do not implement a compositional effect on the phase boundary buoyancy forces. The limited segregation of basalt in the mid-mantle may be due to the

Symbol	Parameter	Value	
ρ_0	Reference Density	$4500\ \mathrm{kg\,m^{-3}}$	**a**
α	Thermal Expansivity	$2.5 \times 10^{-5}\ \mathrm{K^{-1}}$	**b**
k	Thermal Conductivity	$4\ \mathrm{Wm^{-1}\,K^{-1}}$	**c**
C_P	Specific Heat Capacity	$1100\ \mathrm{J\,kg^{-1}\,K^{-1}}$	**d**
T_{surf}	Surface Temperature	300 K	
T_{CMB}	Core Mantle Boundary (CMB) Temperature	4000 K	
H	Internal Heating	$0\ \mathrm{W\,kg^{-1}}$	
γ_{410}	$\frac{dP}{dT}$ of the $Ol \rightarrow Wd$	$+1.5\ \mathrm{MPa\,K^{-1}}$	
γ_{660}	$\frac{dP}{dT}$ of the $Rw \rightarrow Brm + Pc$	$-1\ \mathrm{MPa\,K^{-1}}$	
η_0	Reference Viscosity	$4 \times 10^{21}\ \mathrm{Pa\,s}$	
E_a	Non-Dimensionalized Activation Energy	1.75	**f**
V_a	Non-Dimensionalized Activation Volume	1	
$\Delta\rho_{410}/\overline{\rho_{410}}$	Density change for $Ol \rightarrow Wd$	6.37 %	
$\Delta\rho_{660Z}/\overline{\rho_{660Z}}$	Density change for $Rw \rightarrow Brm + Pc$	8.7 %	
$\Delta\rho_{\mathrm{PGt}}/\overline{\rho_{710}}$	Density change for $Gt \rightarrow Brm + Cor$	3.13 %	† **e**
γ_{cool}	$\frac{dP}{dT}$ of the $Gt \rightarrow Brm + Cor$ on the cool arm	$-1.5\ \mathrm{MPa\,K^{-1}}$	† **e**
γ_{warm}	$\frac{dP}{dT}$ of the $Gt \rightarrow Brm + Cor$ on the warm arm	$2.5\ \mathrm{MPa\,K^{-1}}$	† **e**
B_{Bas}	Basalt Buoyancy Number	0.44	
Initial Condition: All models initialized from a temperature field (identical across simulations) with small random anomalies away from the average temperature structure.			

a – Reasonable typical mantle density, e.g. Dziewonski and Anderson (1981)
b – Typical values for mantle materials (p. 61, Poirier, 2000)
c (p. 122, Clauser and Huenges, 1995)
d (Panton, 2020)
e (Ishii *et al.*, 2023)
f Dimensionalized meaning discussed in Section 1.3.5
† – for TC1, not included in TC0

Table 4: Values taken as constant across the mantle circulation simulations.

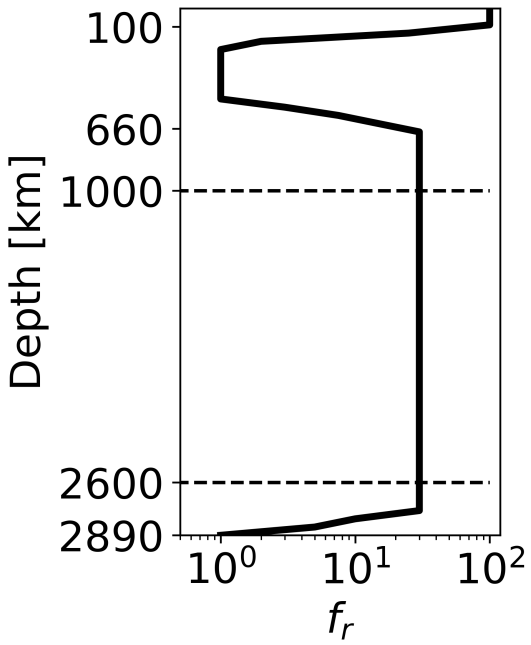

Figure 25: Radial viscosity factor (f_r) variation with depth. Note sharp steps in viscosity at the base of the lithosphere and upper mantle, as well as at the CMB. This radial viscosity structure is chosen to capture key features of the Earth's radial viscosity structure, including a viscosity jump in the mid-mantle.

mantle rheology chosen here. Whilst less viscous than the convection simulations above, the simulated upper mantle is a factor of four more viscous than the Earth's is expected to be (e.g. Haskell, 1935; Mitrovica, 1996). In less viscous flows compositionally dense or buoyant material is more easily able to segregate, so in a less viscous mantle, or mantle region, additional accumulation of gravitationally stabilised enriched material is easier.

Model Initialisation

Both these simulations under go a two-stage initialization process. First, a convection simulation (with free-slip on both boundaries) is run for 2 Gyr with no active chemistry, and without the post-garnet phase boundary forces implemented. The purpose of this stage is to generate a quasi-steady state thermal structure. In the second stage of initialization for both the models, initial velocities of the Müller *et al.* (2022) plate motion history are used for 400 Myr, particles are initiated, melting is turned on, and the post-garnet phase boundary buoyancy forces are implemented into the simulation but only for TC1. This stage allows mantle structures to develop in response to the imposed surface motions and also allows the effect of the additional phase boundary buoyancy force to come into effect in TC1. Unrealistic flows and related effects arising from the onset of tectonic and igneous processes are allowed to dissipate

by the time the main simulation starts. The main simulation is then started with evolving scaled surface velocities imposed as described above.

Choice of Parameters for this Comparison

I have chosen model parameters (see Table 4) to demonstrate the maximum plausible geodynamic effect of a sharp, curved post-garnet reaction with the parameters suggested by Ishii *et al.* (2023). To do this I continue to assume that the phase transitions affect all the mantle material at a node and use a comparatively high T_{CMB} of 4000 K to promote vigorous convection, a state in which counter-convective phase boundary topography forces are more impactful (e.g., Wolstencroft and Davies, 2011).

2.3.2 Results

The thermal and composition fields for the reference simulation ('TC0') and the MCM with the curved post-garnet phase boundary morphology ('TC1') are visualized in Figure 26 and Figure 27. In both simulations, cold slabs descend into the lower mantle, carrying enriched and depleted material to the CMB. Some slabs descend directly, while others stagnate in the mid mantle (e.g. the slabs beneath the North-West Pacific Figure 26 A & B about one or two O'Clock).

2.3.3 Discussion of Thermochemical Simulations

Simulations TC0 and TC1 appear to operate in a similar convectional regime and with comparable kinematics (Figure 26). There are differences between the two simulations – for example, the coldest regions associated with the Nazca slab (Figure 26 C & D, 7-10 O'Clock) appear more continuous in the simulation with PGt – however, the introduction of the novel phase boundary topography forces does not cause global slab stagnation, or create significant changes in regional slab stagnation. Considering the upwellings, again it is difficult to argue that they are effected by the curved post-garnet phase boundary so much that it creates a distinct mode of convection. In Figure 26, some of the upwellings in TC1 appear stronger than upwellings in similar places in TC0 (e.g. panels a & b, 7 O'Clock, panels c & d, 9 O'clock), but elsewhere the upwellings in TC0 seem stronger than in TC1 (e.g. in panels c & d around 8 O'Clock). Considering Figure 28, the high temperature 10^2 Number of Grid Points (NGP) contour is tighter towards the radial mean temperature profile around 720 km depth, which might suggest a slightly promoted upwelling flux through the mid

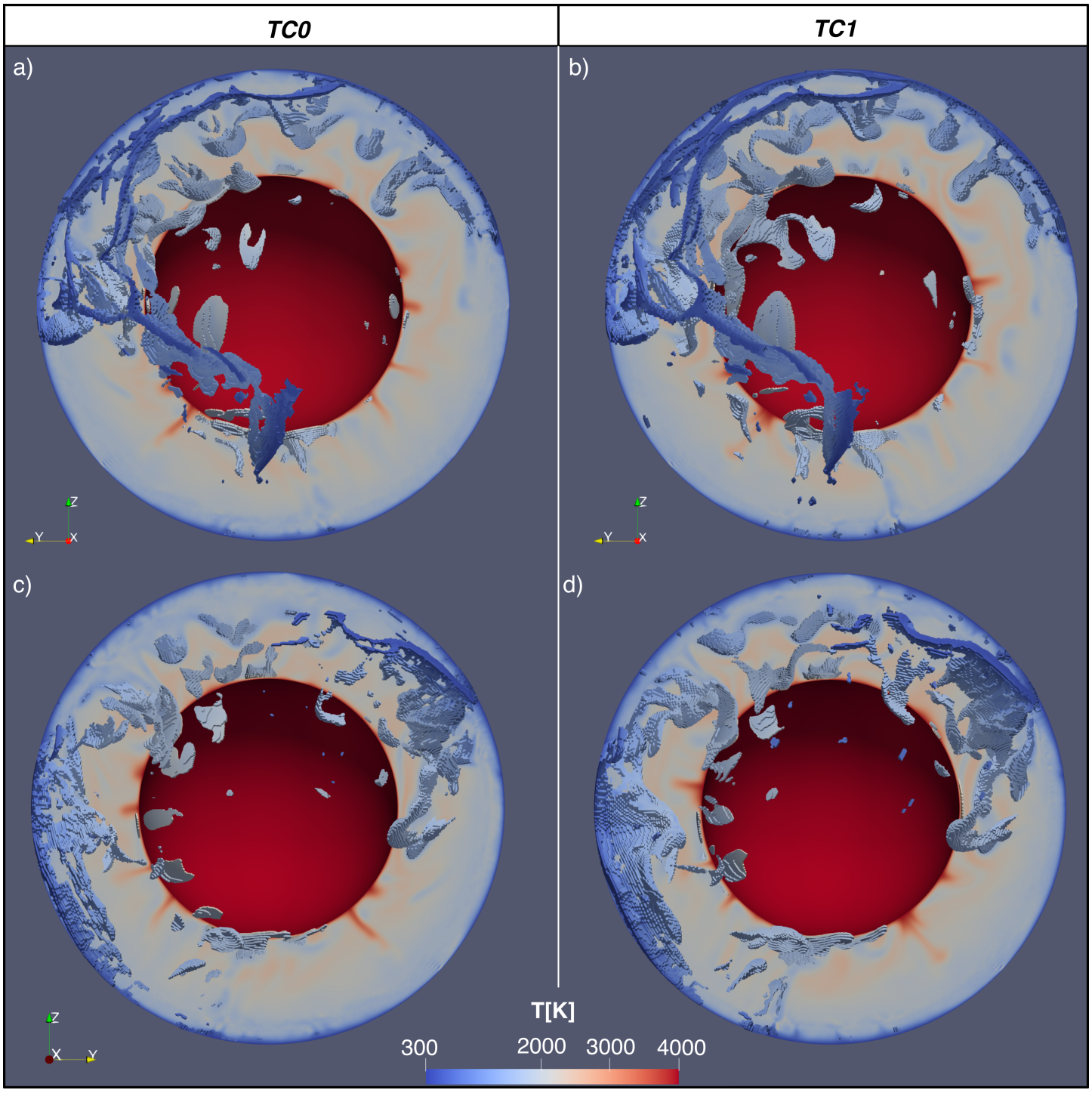

Figure 26: Comparison between reference MCM (TC0, *Left*) and MCM with curved PGt phase transition morphology (TC1, *Right*). Temperature visualized on latitudinal slice through 90°, as well as on 'voxels' beneath 500K below the radial average temperature. *a)* and *b)* show the Western Hemisphere; *c)* and *d)* show the Eastern Hemisphere. Composition visualized in Figure 27.

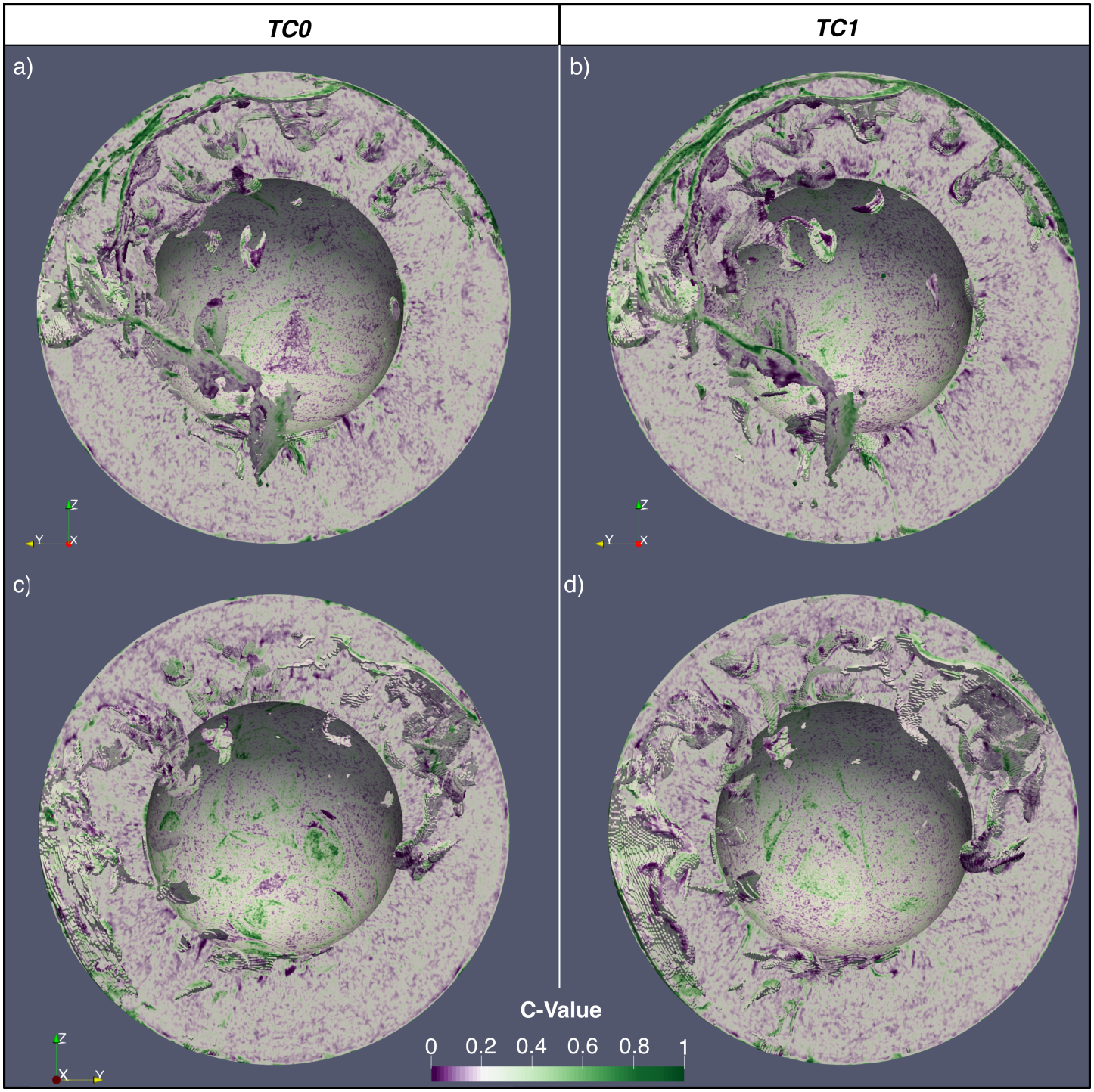

Figure 27: Comparison between reference MCM (TC0, *Left*) and MCM with curved PGt phase transition morphology (TC1, *Right*). C-Value, describing composition between depleted (0, Harzburgitic), ambient (0.2, Lherzolitic), and enriched (1, Basaltic) visualized on latitudinal slice through 90°, as well as on 'voxels' beneath 500K below the radial average temperature.*A* and *B* show the Western Hemisphere; *C* and *D* show the Eastern Hemisphere.

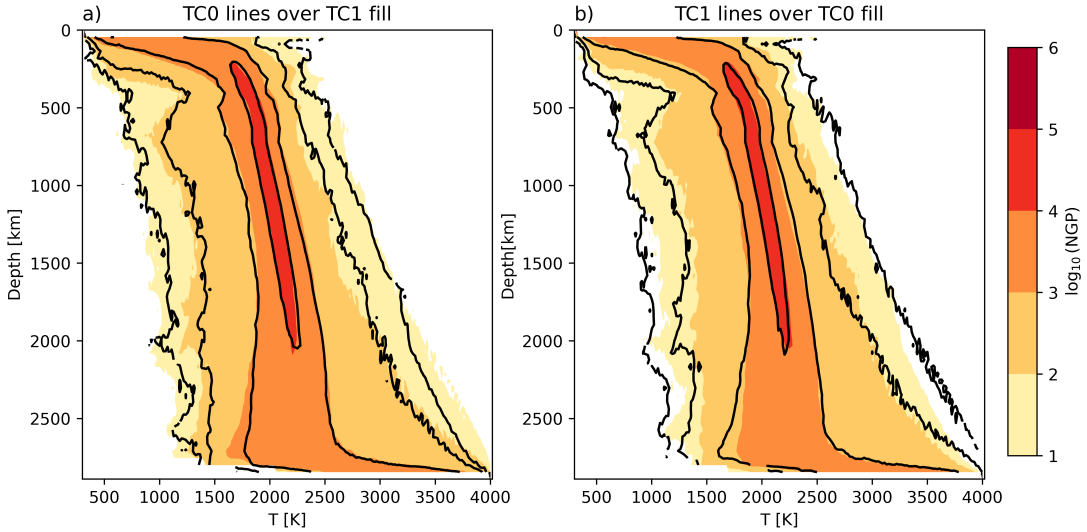

Figure 28: Radial temperature histograms coloured by number of grid points ('NGP') for PGt simulation TC1 and reference simulation TC0 with contours of the reference (TC0) and PGt (TC1) simulations' radial temperature histograms overlaid respectively *a)* and *b)*.

mantle, but only very slightly. This suggests that while the new forces from the endothermic (affecting downwellings) and exothermic (affecting plumes) branches of the post-garnet reaction do have an effect on mantle processes, the effect is small and does not change the mode of mantle circulation.

The radial temperature histograms of the reference case, TC0, and simulation with the curved post-garnet transition, TC1, are extremely similar (Figure 28), suggestive of a near identical thermal evolution. In my previous convection simulations, models with large-scale slab stagnation had a distinct thermal evolution (Figure 17). When we look at the extreme nodes (the 10^2 and 10^1 Number of Grid Points (NGP) contours), I do see minor differences – for example, the coldest temperatures in Model TC1 are colder at most depths than for the reference model. These minor differences highlight that while there are buoyancy forces associated with a curved post-garnet reaction, they do not significantly change the kinematics or thermal structure of the model.

Whilst the viscosity law of these circulation models is not as strongly temperature dependent as is likely the case in the Earth, this means that my downwellings are not as viscous as they might otherwise be – rendering them more vulnerable to stagnation than downwellings in the actual Earth (King and Ita, 1995). This supports my extension of this conclusion about the non-impact of the phase boundary morphology from these simplified geodynamic simulations to the Earth's mantle dynamics.

2.4 Discussion

2.4.1 Branching Phase Boundaries: Thermodynamically Possible Phase Diagrams Prohibit Additional Effect of Post-Spinel *via* Akimotoite *versus* Direct Post-Spinel

I have demonstrated above (Equation 2.5) that under the sheet-mass anomaly approximation, the phase boundary buoyancy forces for two branches must sum to the force of the 'trunk' reaction, and have shown that under this condition, no effect on mantle dynamics are observed (see Figure 18). This is potentially contrary to some of the suggestions in the mineral physics and seismology literature (e.g., Cottaar and Deuss, 2016; Chanyshev *et al.*, 2022). Of course this prohibition only applies strictly where reactions 'A' and 'B' are close enough spatially that the forces can be treated as acting on the same region. As 'A' and 'B' (the akimotoite-in and -out reactions respectively) move further apart a distinct counter-convective effect of reaction 'B' could emerge in extremely localised regions of slabs – these regions would be largest in slabs that are horizontal in the lowermost MTZ. Since these regions of slabs would sit within a downwelling exerting a viscous downwards drag and still relatively close beneath reaction 'A' encouraging the descent of material on to them, for reported values of $T_{660\mathrm{c}}$, γ_A and γ_B it is difficult to envisage there being much of a dynamic effect in the Earth's mantle.

2.4.2 Curving Phase Boundaries: Phase Buoyancy Parameter ($\mathbb{P}$) Implied by Mineral Physics too Small to Effect Global Dynamics

In my simple convection simulations, I was able to produce downwellings that stalled in the mid-mantle whilst upwellings rose unimpeded through the post-garnet transition at values of $\gamma_{710\mathrm{cool}}$ much greater than those suggested for PGt. Furthermore, in a simulation with realistic surface motions and a curved phase boundary with parameters similar to those suggested for the post-garnet reaction by Ishii *et al.* (2023) I observed no additional slab stagnation compared to a simulation without the curved phase boundary. This result is expected, as the phase buoyancy parameter (using the parameters in Table 4) for the cool post garnet is -0.014 – much less than that which would be expected to induce a layered or transitional dynamic regime. This is a much smaller magnitude than the value of -0.10 found by Ishii *et al.* possibly due to them assuming the

thickness of the convecting layer is the above the phase boundary, whereas I assume it is the full depth of the mantle. This is the choice used elsewhere in the geodynamic literature (e.g. Tackley *et al.*, 1994; Bunge *et al.*, 1997; Wolstencroft and Davies, 2011), since this is the thickness of the layer that would convect without the presence of an extremely counter-convective phase transition.

It is worth considering how well current theoretical models of a global linear reactions align with the temperature-restricted reactions considered in my simulations.

For example, at a Rayleigh number of 1.4×10^5 (the same as in my simulations from Section 2), Wolstencroft and Davies (2011) predicted regime changes from whole-mantle convection to 'transitional' convection at $\mathbb{P} < -0.25$ and to layered convection at $\mathbb{P} < -0.32$. These thresholds are considerably more negative than the value of $\mathbb{P} \sim -0.175$ at which I see a regime change (see Figure 23). This discrepancy may be explained by the temperature-restriction, which could truncate cold thermal structures, making them more vulnerable to downwelling stagnation (Tackley *et al.*, 1993). Wolstencroft and Davies (2011) assume their regime boundaries follow the form $\mathbb{P} = \alpha Ra^{-\beta}$, where α and β are constants. As the Rayleigh number increases, the slopes of these curves tend to flatten. This suggests that the disparity in the value of $\mathbb{P}$ at which regime changes occur for global and regional reactions may be less pronounced at high Rayleigh numbers than in the simpler convection simulations presented here.

I have shown that for the parameters suggested by Ishii *et al.* (2023), the post-garnet reaction is unlikely to significantly affect convection in the Earth's mantle. To have a significant effect on convection, the reaction would need a larger Clapeyron slope or density change to increase the magnitude of $\mathbb{P}$ by a factor of four or more. Alternatively, the mantle would need to have a much higher Rayleigh Number, possibly even higher than that considered reasonable for the Hadean (e.g. Li *et al.*, 2024).

Dong *et al.* (2025) suggest a post-spinel boundary that curves steeply, with a near-zero slope at 1500 K decreasing to a Clapeyron slope of $\sim -4\text{MPa.K}^{-1}$ near the Wad-Rw-Brm triple point ($\sim$ 2200K). The Clapeyron slope near the triple point implies a phase buoyancy number of -0.11, which is much larger than for the value of $\mathbb{P} = -0.014$ implied for the cool-arm of the post-garnet reaction based on the numbers of Ishii *et al.* (2023). In a mantle with Earth-like vigour, this value of $\mathbb{P}$ is likely within the range that could have a dynamic impact if it were relevant to all upwellings and downwellings (e.g. Christensen and Yuen, 1985; Wolstencroft and Davies, 2011). However, very little of the mantle is in the temperature range just beneath the triple point where this strong counter-convective forcing would apply. By analogy with the results

presented above in Figure 23, this would be similar to having a very low T_{710C}, which Simulation 107 demonstrated can result in a pattern of convection closer to whole mantle convection than that seen at higher T_{710C} with the same Clapeyron slope (Figure 24). It is likely therefore that for the purposes of geodynamic simulation a linear post-spinel reaction with a lower magnitude Clapeyron slope is a satisfactory approximation. This approximation does not apply to seismic observations, for which curvature may still need to be considered.

2.5 Conclusions

Using a combination of simple mantle convection models and selectively considering more complex mantle circulation models I have illustrated some of the dynamic effects that non-linear phase boundary morphologies can produce when applied to geodynamic simulations. Where entropy and volume changes for a single reaction are dependent on temperature, as Ishii *et al.* (2023) have proposed for the post-garnet reaction, then distinct counter-convective and pro-convective forcings are possible on upwellings and downwellings – but for the density changes and Clapeyron slopes suggested for the post-garnet reactions, this does not significantly affect global dynamics.

I have also highlighted that changes in entropy and volume must be conserved where reactions branch – and this is a critical constraint on the phase boundary buoyancy forces; the post spinel reaction remains a good approximation for total geodynamic effect of the olivine system reactions at the base of the mantle transition zone.

Chapter 3

Thermochemical Prediction of Seismic Discontinuity Topography from Mantle Circulation Models

A version of this chapter has been published in Geophysical Journal International – *Morgan* et al. *(2025*b*). Whilst this paper was co-authored with members of my supervisory team, their contributions were not greater than the usual for a thesis chapter.*

Abstract

Mantle Circulation Models (MCMs) are routinely assessed against seismic tomographic models, but many other seismic observations exist that may be able to discriminate between different mantle models. One such observation is the topography of d410 and d660, discontinuities in the MTZ. I demonstrate a method for the prediction of seismic discontinuity topography from thermochemical MCMs. I find the discontinuity depth by using the peak reflectivity at each location in this modelled mantle transition zone, taking account of compositional as well as thermal variations. I make some comparisons of these predicted topographies with those observed using SS-precursors, developing a simple smoothing filter to capture the distribution of sensitivity of a published topography model – finding that such filtering has a significant impact on the predicted discontinuity topographies. I also consider the significance of lateral variations in reflectivity or reflection amplitude in my predicted datasets and the real Earth. Finally, I consider what aspects of mantle transition zone discontinuity structure would be matched by the predicted discontinuity structure from an Earth-like MCM – particularly the

mean depths of the discontinuities, the amplitude of the topography and the shape of its spherical harmonic spectra. The MCM used in this chapter was not found to have a favourable predicted d410 or d660 structure when compared to a published SS-precursor model, which is interpreted as the model being over-viscous. Additionally, the predicted unfiltered topographies are much rougher than those recovered by SS-precursors, suggesting that wavefront effects may be important in properly understanding the observation of the discontinuities.

3.1 Introduction

Discontinuities in the material properties of the Earth's mantle are a long-standing feature of 1D seismological models (e.g. Jeffreys and Bullen, 1940) and for over 75 years have been associated with phase transitions (e.g. Birch, 1952), where the stable material phase changes due to increasing pressure. In the mantle transition zone the principal discontinuities around 410 and 660 km depth (hereafter referred to as 'd410' and 'd660') are usually associated with the reactions Ol (Olivine) $\rightarrow Wd$ (Wadsleyite) (e.g. Ringwood and Major, 1970) and Rw (Ringwoodite) $\rightarrow Brm$ (Bridgmanite) + Pc (Periclase) (e.g. Ito *et al.*, 1984). As these are chemical reactions, variations in the depth of the phase transition due to temperature variations in a convecting mantle (potentially impacting the regime of the convection, e.g. Christensen and Yuen 1985) have been expected for a long time, as was the possibility of their seismic observation by Verhoogen (1965).

Topography on d410 and d660 was first recognised in the early 1990s (e.g. Revenaugh and Jordan, 1991*a*; Shearer and Masters, 1992), using ScS reverberations and SdS underside reflections (SS precursors). Since then, many global studies have been published, principally using SS precursors (e.g. Flanagan and Shearer, 1998; Gu *et al.*, 1998, 2003; Lawrence and Shearer, 2008; Houser *et al.*, 2008; Houser and Williams, 2010; Houser, 2016; Yu *et al.*, 2017; Huang *et al.*, 2019; Guo and Zhou, 2020; Waszek *et al.*, 2021) as well as a larger number of contributions using Receiver Function methods in regions with a high density of seismic stations (e.g., Chevrot *et al.*, 1999; Collier and Helffrich, 2001; Thompson *et al.*, 2011; Lee *et al.*, 2014; Cottaar and Deuss, 2016; Maguire *et al.*, 2018; Keifer and Dueker, 2019; Rao *et al.*, 2020; Yu *et al.*, 2020; Agius *et al.*, 2021; Liu *et al.*, 2023; Burky *et al.*, 2023; Bonatto *et al.*, 2024; Glasgow *et al.*, 2024).

Global studies largely find peak-to-peak topography amplitude on the order of $\sim$ 40km on both discontinuities, and a strong positive correlation between the

observed depths of d410 and d660 (e.g., Gu *et al.*, 1998; Houser and Williams, 2010; Guo and Zhou, 2020; Waszek *et al.*, 2021). This last observation runs counter to the expected anticorrelation from the opposing Clapeyron slopes of the olivine-out and ringwoodite-out reactions. It is important to recognize that a correlation in mapped topography does not necessarily imply a true correlation in the physical topography of the 410 km and 660 km deep discontinuities. A discrepancy may arise for several reasons: (a) SS-precursor resolution is limited and differs between d410 and d660, (b) global coverage of the SS-precursors is incomplete, and (c) the conversion from differential arrival times to discontinuity depths relies on simplifying assumptions, such as mantle homogeneity and locally flat, sharp discontinuities.

Even if the correlation in mapped topography does reflect a genuine correlation, the underlying cause remains uncertain. There is currently no consensus among the seismology, mineral physics, or geodynamics communities regarding the dominant mechanism driving such a correlation. Explanations have included (i) The 3D nature of mantle thermal structure (e.g. Shearer and Masters, 1992; Goes *et al.*, 2022), (ii) compositional variations (e.g. Houser *et al.*, 2008), and (iii) a positive Clapeyron slope at high temperatures controlling d600 (e.g. Houser and Williams, 2010; Waszek *et al.*, 2021) have all been suggested. Whilst the mantle transition zone is likely to be a region with strong variations in water content, and regions with high water content are expected to favour the stability of wadsleyite and ringwoodite as these phases hold more water than those shallower or deeper in the mantle (e.g. Ohtani, 2021), it is considered unlikely that this will result in a positive correlation of d410 and d660 (Houser, 2016; Muir *et al.*, 2021).

SdS topographies are typically corrected for mantle structure (using 3D seismic velocity tomography models) and crustal structure (which might advance or delay the SS phase compared to a global average, meaning that a discontinuity is interpreted as shallower or deeper than it is actually) using the model CRUST 1.0 or its predecessors (Laske *et al.*, 2012); however the lithosphere also has an extremely heterogeneous structure (e.g., Pasyanos *et al.*, 2014) which is not usually corrected for – this could also explain the positive d410-d660 correlation (e.g. Tauzin *et al.*, 2022). In light of this it is often suggested that variations in Mantle Transition Zone (MTZ, the region lying between d410 and d660) thickness – assessed by the difference in S410S and S660S travel times – is a better constrained observation on MTZ structure than observations of the discontinuities (e.g. Waszek *et al.*, 2021). Further, MTZ thickness variations correlate better with anomalies in V_S structure, which are more uncontroversially understood in terms of thermal anomalies (e.g. Lebedev

et al., 2003).

As the topographies of d410 and d660 are recognised as being dominantly controlled by temperature, there is a long-standing understanding that it should be possible to invert the depths of the discontinuities and their topography for the average and range of temperatures in the mantle transition zone. Shearer and Masters (1992) estimated a temperature range at 660 km depth of between $300 - 600$K based on a simple calculation from their observed topography and contemporary estimates of the Clapeyron slope of the post-spinel reaction. However, subsequent workers (e.g. Deuss *et al.*, 2006) showed that the d660 could not be understood simply using the post-spinel reaction - and that other reactions and potentially compositional variations were important in controlling the depth of the seismic discontinuity. Ritsema *et al.* (2009) used the differential travel-times of S410S and S660S phases (i.e. a proxy for MTZ thickness) to constrain the mantle potential temperature in the North Pacific (1650 ± 100 K). Waszek *et al.* (2021) inverted SdS data separately for 410 and 660 topographies and then used the calculated MTZ thicknesses to invert for an average potential temperature of 1630 K with 'peak-to-peak variations' of ~ 350K. All of these inversions assume a single global mineral physics model - usually a mechanically mixed (MM) pyrolite model with f_{Bas}, basalt fraction, ~ 0.2. The effect of lateral composition variations has only recently been considered. Tauzin *et al.* (2022) inverted reflection amplitude and transition zone thickness for composition as well as potential temperature, finding that f_{Bas} varied from 0.0 to 0.8 in the mid mantle and a similar mantle potential temperature to Waszek *et al.* (2021) but a slightly higher temperature range of ~ 450 K. However, because seismic waves have limited resolution, the range of discontinuity depths recovered from seismic observations will be an underestimate. Therefore, the range of temperatures recovered will also be underestimated. Yu *et al.* (2023) principally used a global stack of S410S and S660S arrivals and the amplitude-offset relationship in that stack to illustrate an elevated basalt content around d660 compared to d410.

The MTZ is dynamically complex - and discontinuity topographies could represent a useful constraint on geodynamic models in the mantle transition zone. Papanagnou *et al.* (2023) outlined a method for predicting seismic discontinuity topography using the thermal structure of a geodynamic model, and examined the effect of using diverse mineral physics tables on the predicted topographies - which had a large effect when applied globally. Many geodynamic codes are now able to produce thermo-chemical outputs (e.g. TERRA (Baumgardner, 1983; Bunge and Baumgardner, 1995; Stegman, 2003), ASPECT (Kronbichler *et al.*, 2012; Heister *et al.*, 2017), stag3D (Tackley and

Symbol	Parameter	Value	
k	Thermal Conductivity	$4\ \mathrm{W m^{-1} K^{-1}}$	**a**
C_P	Specific Heat Capacity	$1100\ \mathrm{J kg^{-1} K^{-1}}$	**b**
T_{Surf}	Surface Temperature	300 K	
T_{CMB}	CMB Temperature (average over run)	4007 K	**c**
γ_{410}	$\frac{dP}{dT}$ of $Ol \rightarrow Wd$	$+1.5\ \mathrm{MPa K^{-1}}$	
γ_{660}	$\frac{dP}{dT}$ of $Rw \rightarrow Brm + Pc$	$-1\ \mathrm{MPa K^{-1}}$	
η_0	Reference Viscosity	$4 \times 10^{21}\ \mathrm{Pa s}$	
E_A	Non-dimensionalized Activation Energy	1.75	**d**
V_a	Non-Dimensionalized Activation Volume	1	
B	Basalt buoyancy number	0.66	
$\frac{\Delta\rho_{410}}{\rho_{410}}$	$Ol \rightarrow Wd$ density change	6.37 %	
$\frac{\Delta\rho_{660}}{\rho_{660}}$	$Rw \rightarrow Brm + Pc$ density change	9.08 %	
Initial Condition: The mantle circulation model is initialised from a mantle convection model run for 2 Gyr. The mantle is preconditioned for 200 Myr using the first stage of the plate model.			

a (p. 122, Clauser and Huenges, 1995)
b (Panton, 2020)
c cooling CMB condition, see main text.
d Dimensionalized meaning discussed in Section 1.3.5

Table 5: Parameters used in mantle circulation model 'm_cc_066_u'

Xie, 2002)) - including those generated by geological processes (such as melting (e.g. Van Heck *et al.*, 2016)) and then dispersed through the silicate Earth over Earth history. Recent work (e.g. Yan *et al.*, 2020) suggests that the mantle transition zone could host significant compositional heterogeneity.

Here I present a new method for predicting discontinuity topography in thermochemical mantle circulation models. Further, a comparison to global observations with a seismologically-motivated filter for the sensitivity of the SS-precursors is illustrated. The MCM used here was previously introduced to the literature by Davies *et al.* (2025), and I use it to illustrate the minor effect of different mixing models and the more significant effect of the filtering applied, and demonstrate how a single MCM is evaluated against a published topography model. This model also appeared as 'TC0' in Chapter 2 of this thesis.

3.2 Methods

3.2.1 Geodynamic Model

I demonstrate my method using a single mantle circulation model 'm_cc_066_u'[1] - detailed at length in Davies *et al.* (2025) *and run by Dr.*

[1] 'm_cc_066_u' was referred to as 'TC0' in chapter 2

James Panton for the MC2 project. This model was run using the mantle circulation code TERRA (Baumgardner, 1983), which solves the equations for the conservation of mass, momentum and energy (1.3-1.5) on an icosahedral grid refined to give a grid spacing of $\sim$ 45km in the mid-mantle. Model parameters are summarised in Table 5. At this resolution we are not able to resolve upper mantle viscosities strictly compatible with the Haskell constraint of 1×10^{21} Pa.s, but instead use a slightly higher reference viscosity of 4×10^{21}Pa.s, which will result in slightly stronger thermal anomalies that are broader thin in the real Earth. The upper boundary is driven using the plate motion model of Müller *et al.* (2022). Viscosity varies according to

$$\eta = \eta_0 \cdot f_r \cdot e^{V_a \cdot Z' - E_a \cdot T'} \tag{3.1}$$

where η_0 is the reference viscosity, f_r is a prefactor that creates a radial variation in viscosity (Figure 29), V_a is a non-dimensionalized activation energy, Z' is a non-dimensionalized depth, E_a is the non-dimensionalized activation energy and T' is the non-dimensionalized temperature. 'm_cc_066_u' was run using a cooling core mantle boundary (CMB) thermal boundary condition (Davies, 2015), and is internally heated according to concentration of heat producing elements distributed on particles (see below) in the simulated mantle (Panton *et al.*, 2022), and is compressible with a Murnaghan equation of state (Bunge *et al.*, 1997). The radial viscosity structure features a $\sim$ 100 km thick lithosphere that is 100$\times$ more viscous than the upper mantle, allowing thermal conduction to dominate there, and features a more viscous lower mantle, as favoured by geodetic constraints (e.g. Hager *et al.*, 1985). The simulation undergoes a two-stage initialisation process. Firstly, a convection simulation is run for 2 Gyr as a solely thermal model in order to produce a mantle in quasi-steady state. The convecting mantle is then primed for the circulation simulation by the initial velocities of the (Müller *et al.*, 2022) being applied for 200 Myr as well as the initiation of particles, compositional variation and the parameterized melting scheme (Van Heck *et al.*, 2016). Then, this thermochemical structure is used as the initial condition to the circulation model, where the surface evolves using 1 Gyr of plate motion history from the Müller *et al.* (2022) model. The thermochemical structure at 410 and 660km depth in simulation m_cc_066_u is illustrated in Figure 30. Additionally, the lack of basalt segregation is highlighted in Figure 31, which shows that overall the simulated mid-mantle has a low abundance of basalt, except for where it is delivered through it in downwellings' and upwellings' cores (Figure 32). The high remaining fraction of Lherzolite in Figures 31 and 32 highlights an

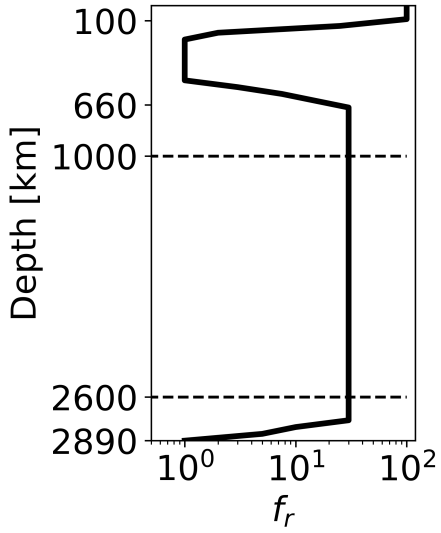

Figure 29: Variation of viscosity pre-factor with depth. 1000 and 2600 km depth are marked with dashed lines.

unrealistically low processing rate in this simulation. A comparison to seismic observables sensitive to the detail of the thermochemical structure in the MTZ is then motivated to demonstrate this method, see what we can gleam about the discontinuities by considering a synthetic MTZ structure, and to evaluate a MCM with reasonable parameters. However, like any geodynamic model, this MCM's ability to reproduce Earth structure is limited, and I do not expect a perfect agreement between the model and the Earth, particularly noting the underprediction of downwelling stagnation around d660 (see Figure 30), and the comparatively underprocessed chemistry in the mid-mantle (Figure 31).

Composition in TERRA

For full details of the implementation of particles and melting in TERRA, the reader is referred to Stegman (2003), Van Heck *et al.* (2016), and Panton *et al.* (2022), and the description in Section 1.5.3 of this thesis. TERRA advects particles through its simulations by interpolating the flow calculated on the regular icosahedral grid nodes onto the particles, and advecting them forwards accordingly. These particles can be used as passive tracers, but here have an active effect on the flow due to density anomalies dependent on their bulk composition. In m_cc_066_u, basalt is 5% less dense than lherzolite between 660 and 740km depth. This results in a slight 'basalt density filter' effect where basaltic material is more buoyant than pyrolitic material in the lower mantle transition zone, but the resulting radial basalt segregation is not as extreme as that advocated for by Yan *et al.* (2020) or that Tauzin *et al.* (2022) suggest by inversion of global SS precursor structure. Elsewhere, basalt is denser than

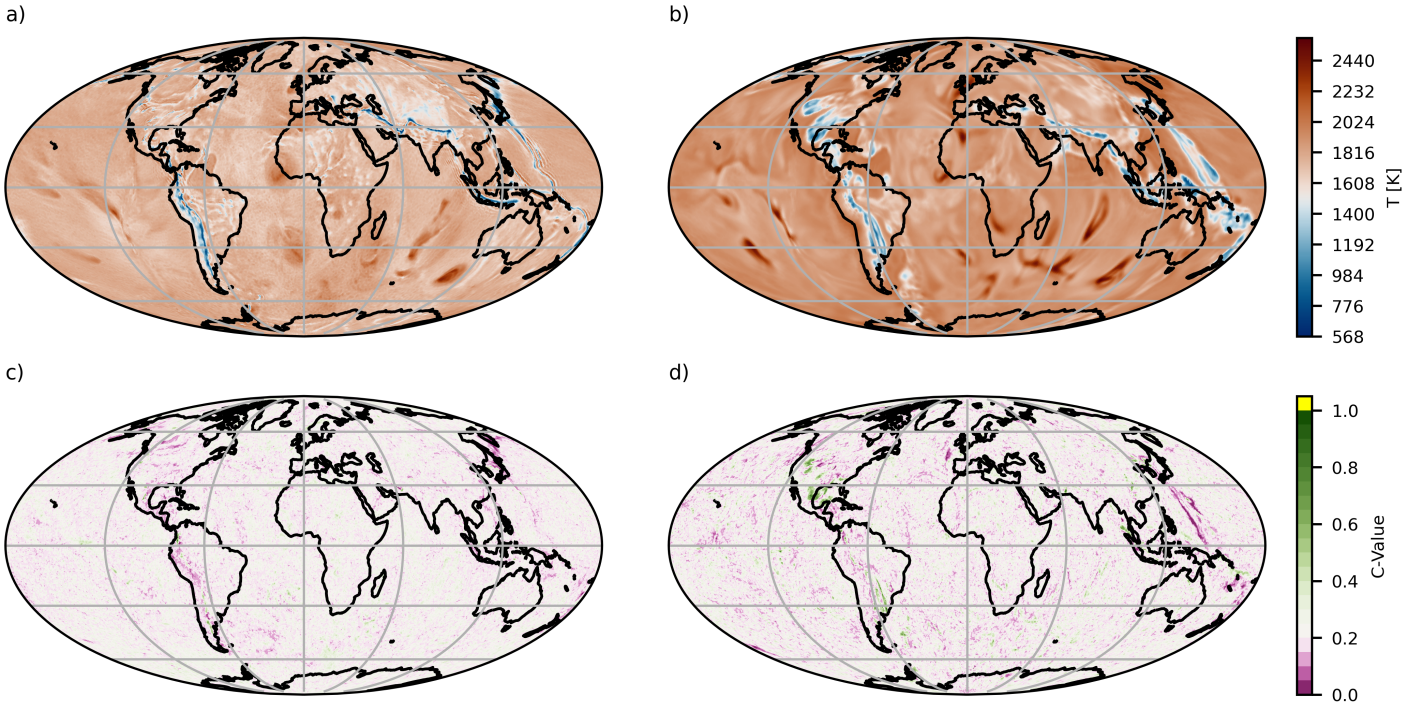

Figure 30: Thermochemical structure of simulation 'm_cc_066_u'. *a)* Thermal structure at 410 km depth b) Thermal structure at 660 km depth c) C-Value structure at 410 km depth *d)* C-Value structure at 660 km depth

pyrolite or harzburgite.

Bulk composition is described using a parameter (C) that varies between 0 and 1 in this simulation[2] describing the relative depletion or enrichment of the particle - a C-value of 0 represents entirely depleted material (i.e. Harzburgite (Hzb)), of 0.2 represents bulk mantle material (i.e. Lherzolite (Lhz)), and of 1 represents entirely enriched material (i.e. Basalt (Bas)/Pyroxenite). Particles are initialised with an even distribution throughout the whole mantle with half of all particles being lherzolitic, 40% harzburgitic and 10% basaltic - resulting in an initial average C-Value of 0.2. The particles are then advected through the simulation, following the whole-mantle circulation. If the pressure-temperature conditions of the particle put it over the solidus in the shallow mantle, it undergoes partial melting - melt is extracted towards the surface resulting in particles near the surface becoming enriched (basaltic) while the melt source particle become depleted (harzburgitic). As well as bulk composition, various geochemical parameters (e.g. Panton *et al.*, 2022) including abundances of heat producing elements evolving with melt and radioactive decay are recorded on the particles but are not of interest here.

[2]Although in simulations with a primordial layer initial condition, this introduces material of $C = 2$ to the lowermost mantle.

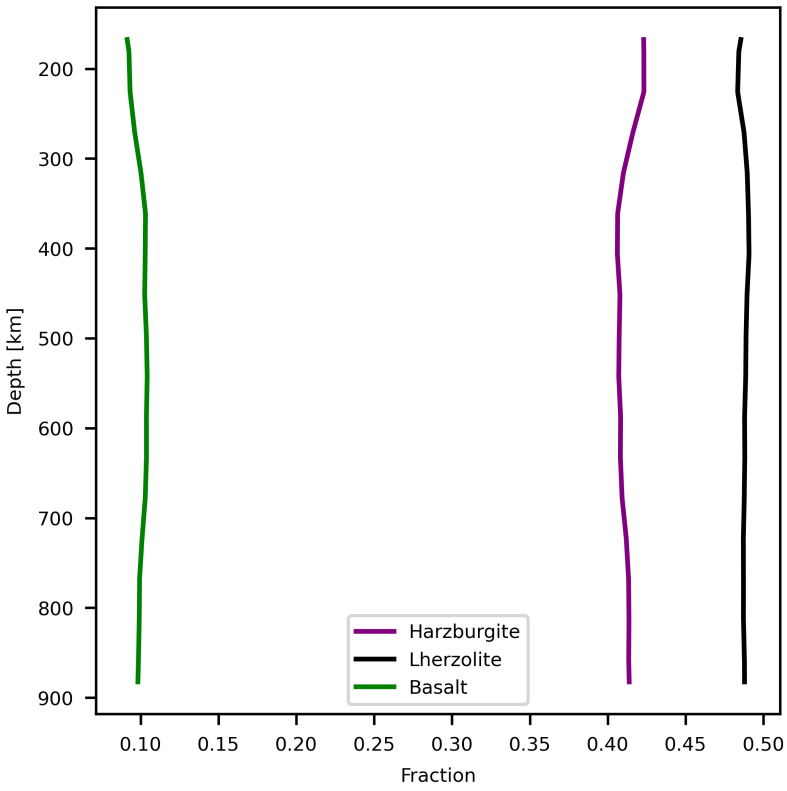

Figure 31: Radial distribution of compositional end-members in the simulated mid-mantle of 'm_cc_066_u'. End-members coloured analogous to their position on C-Value colour-bar in Figure 30, i.e. harzburgite is purple, lherzolite is black and basalt is green.

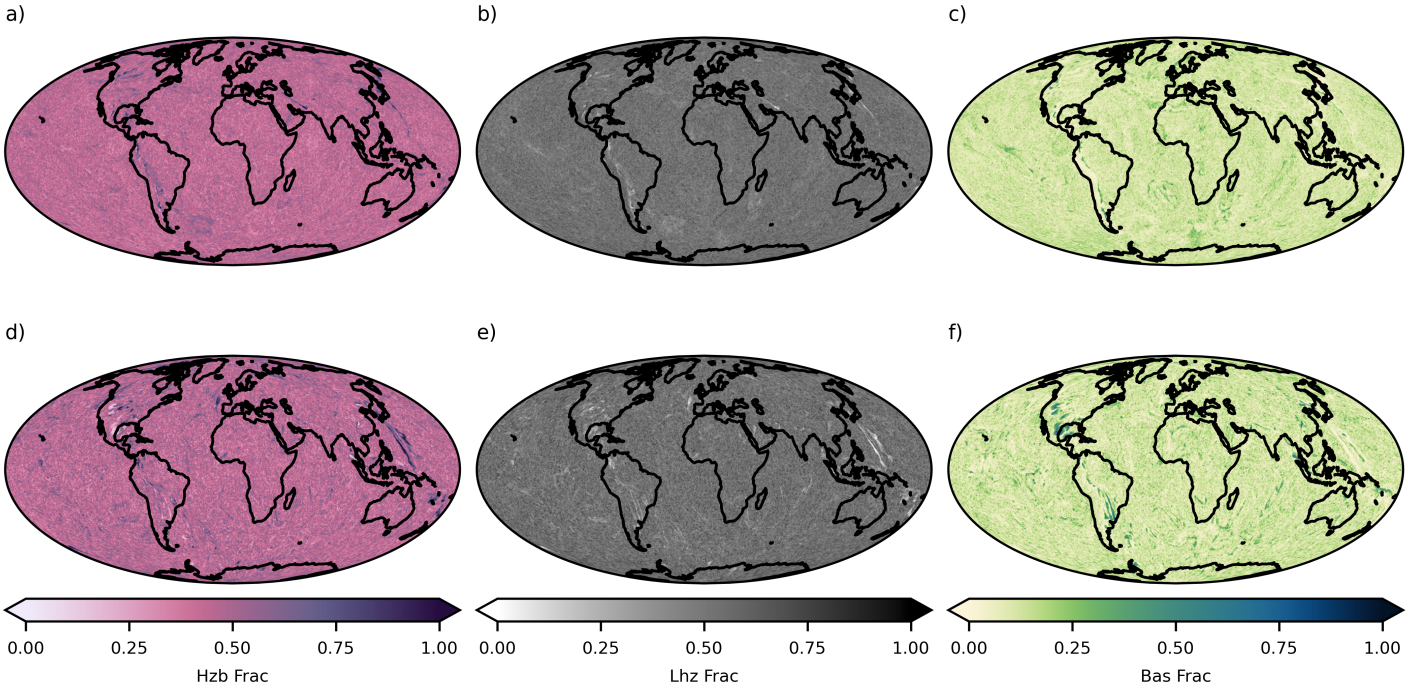

Figure 32: Lateral distribution of the abundance of compositional endmembers in the MTZ of 'm_cc_066_u'. *a-c)* near d410, *d-f)* near d660. *a & d)* abundance of harzburgite at d410 & d660 respectively, *b & e)* abundance of lherzolite at d410 & d660 respectively *c & f)* abundance of basalt at d410 & d660 respectively

3.2.2 Mineral Physics Models

In order to predict the discontinuity topography, I require look-up tables of density (ρ), P-wave velocity (V_P) and S-wave velocity (V_S) in pressure-temperature space for each of my assumed end-member compositions. The tables used by Davies *et al.* (2025) are used here as well. The end member lithologies are described using six oxide components (see Table 6) - chosen to fit published datasets for Harzburgite, Lherzolite and Basalt (Baker and Beckett, 1999; Walter, 2003; White and Klein, 2014, respectively).

Table 6: Assumed molar composition for the three characteristic lithologies; harzburgite, lherzolite and basalt.

	Harzburgite (Hzb) (Baker and Beckett, 1999)	**Lherzolite** (Lhz) (Walter, 2003)	**Basalt** (Bas) (White and Klein, 2014)
SiO_2	36.184	38.819	52.298
MgO	56.559	49.894	15.812
FeO	5.954	6.145	7.121
CaO	0.889	2.874	13.027
Al_2O_3	0.492	1.963	9.489
Na_2O	0.001	0.367	2.244

Equilibrium mineral assemblages (with resultant elastic and thermodynamic properties) are calculated by Gibbs free energy minimisation using Perple_X (Connolly, 2009), with thermodynamic data from Stixrude and Lithgow-Bertelloni (2005, 2011, 2022) The isotropic elastic seismic velocities are corrected for anelasticity using the model 'Q7g' (Goes *et al.*, 2004; Maguire *et al.*, 2016). The V_S structure of the lherzolite, harzburgite basalt and pyrolitic assemblage (MM18) are shown in Figure 33. *These tables were supplied to me by Dr Robert Myhill.* The phase-transformation parameters in the MCM are not set so as to be consistent with those in the mineral-physics tables, leading to an inherent self-inconsistency in this workflow. In particular, the Clapeyron slope on the ringwoodite-out phase transformation in the geodynamic model is -1 MPa.K^{-1}, whereas in the mineral physics table it is closer to -2 MPa.K^{-1}. At the convective vigour of this MCM, this difference does not change the dynamic regime (e.g. Wolstencroft and Davies, 2011), but in principle this could change the thermal structure and our assessment of the MCM. This unphysical inconsistency is balanced against the additional complexity using the tables allows us to incorporate in our synthetic discontinuities, that previous work has shown cannot be considered simply as the olivine- and ringwoodite-out reactions (e.g. Cottaar and Deuss, 2016).

3.2.3 Prediction of Seismic Velocity Discontinuity ('Local Mechanical Mixing & Reflectivity')

Whilst composition is tracked on the fine scale-length of the particles, the total proportion of harzburgite, lherzolite and basalt in the region surrounding each node is also recorded. This then allows us to predict the thermochemical discontinuity topography on the regular TERRA grid at a spacing of $\sim$ 45km laterally in the mid-mantle, far finer than the the thermochemical structure that SS precursors are sensitive to given that the lateral extent of the first Fresnel zone of S660S and S410S are both $\sim$ 1000 km (Guo and Zhou, 2020), and the full Fresnel zones have sensitivity that extend for several times as far dependent on the azimuth to the source-receiver pair and bands of positive- and negative-sensitivity extending away from the ray-theoretical bouncepoint (e.g. Dahlen, 2005).

Vertically, however, a 45km vertical resolution is far too coarse to resolve the phase transition, so I first interpolate the data from the coarse TERRA grid onto a finer vertical grid centred on a target depth (for this work 410km and 660km) for each horizontal position (see Figure 34 a). This then requires some assumption about how thermal and compositional structure is distributed

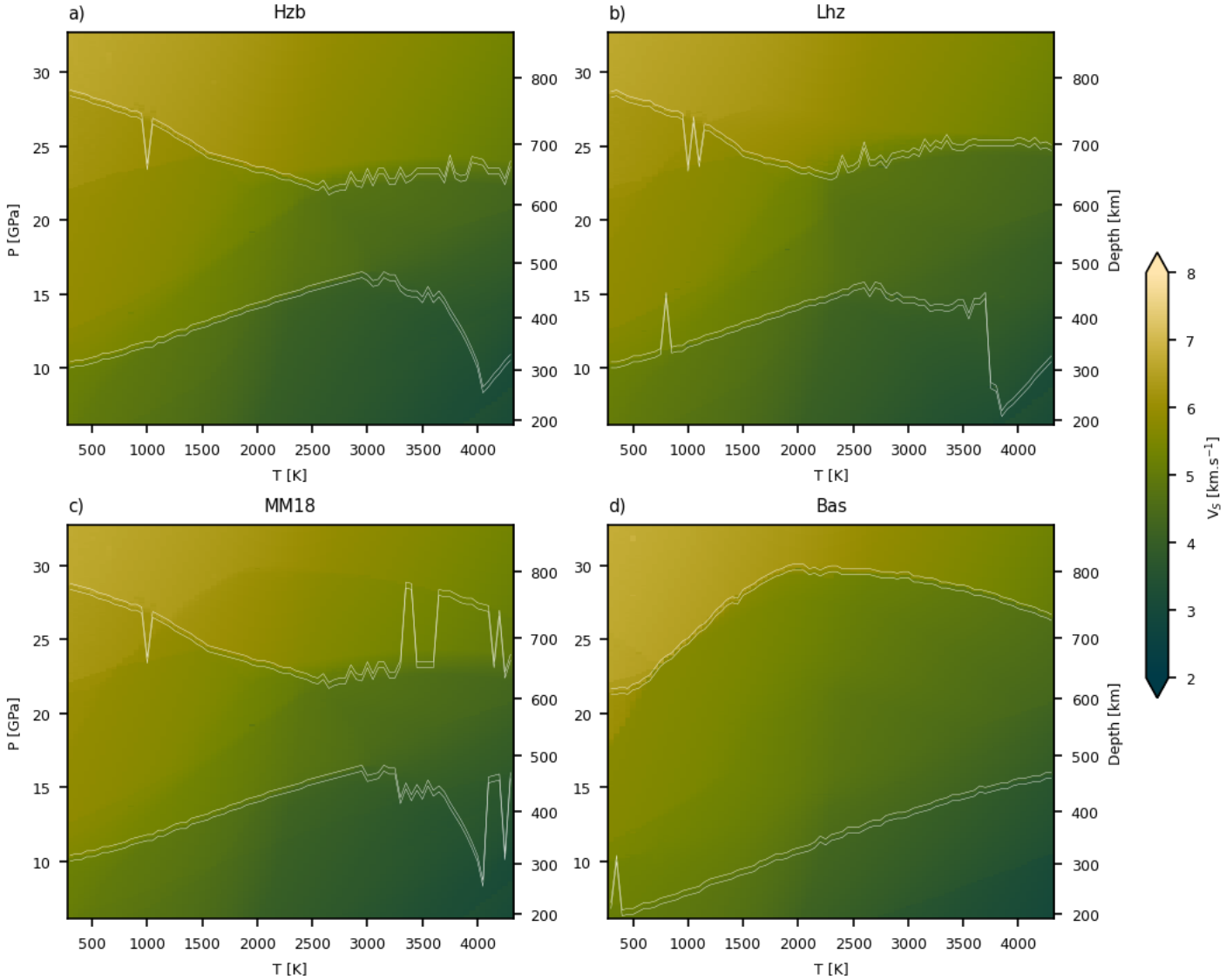

Figure 33: V_S structure of mineral physics tables for end-member compositions used in this study. *a)* Harzburgite, *b)* Lherzolite, *c)* MM18 a 'pyrolite' composition mechanical mixture of 18% Basalt and 82% Harzburgite, *d)* Basalt. V_s structure shown by color fill and the peak reflectivity pressures in the '660' and '410' regions are outlined by fine white lines 0.2 GPa above and below the picked pressure. Where the lines appear to "jump" around, this is due to two reactions within the depth window for d410 and d660 having similar reflectivities, and some numerical issue produces 'dark' spots on the reaction that is picked at other temperatures. At higher temperatures, the breadth of the garnet-out reaction creates a broad region of elevated reflectivity (see Figure 35), so the depth of peak reflectivity is less distinct here.

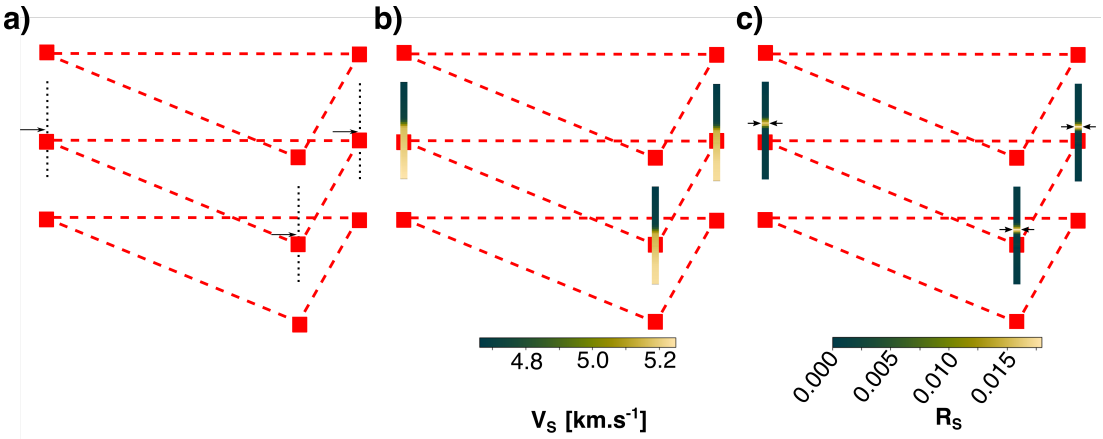

Figure 34: Sketch of method introduced here. *a)* The gridding used for the geodynamic modelling is too coarse for the purposes of finding the discontinuity structure, so the thermal and chemical structures are interpolated onto a finer grid centred on a reference depth (i.e. 410 or 660 km). *b)* temperature, pressure and composition at each interpolated location is used to compute V_S, V_P and ρ. *c)* These are then used to compute S-wave reflectivity R_S at each interpolated location, and the highest reflectivity is used as the discontinuity depth at that location.

between the grid-points the geodynamic model is solved on. In models of the mid-mantle, thermal structure is usually assumed to be much smoother than chemical structure as thermal diffusivity ($\sim 7.5 \times 10^{-7}$ m^2.s^{-1}, Ricard 2007, p. 41) is much higher than chemical diffusivity ($\sim 10^{-17}$ m^2.s^{-1}, Hoffman and Hart 1978) in mantle materials. Temperature then is usually (e.g. Papanagnou *et al.*, 2023; Van Heck *et al.*, 2016) interpolated linearly (as thermal diffusion governed by Fourier's law is linear). Given, then, that the the chemical diffusivity is ten orders of magnitude smaller than the thermal diffusivity, I use a nearest neighbour scheme[3]

This allows the integration of the chemical heterogeneity from the MCM into my discontinuity prediction. Given recent geodynamic and seismological work (e.g. Yan *et al.*, 2020; Goes *et al.*, 2022; Tauzin *et al.*, 2022; Yu *et al.*, 2023) chemical heterogeneity is expected to be quite high in the Earth's mantle and particularly its mantle transition zone, which motivates the inclusion of chemical heterogeneity in the prediction of the discontinuity topographies.

A mechanical mixing calculation is performed between the tracked

[3]In theory I could, in the same way composition is brought from the particles to the geodynamic grid, bring composition onto the refined radial grid used for interrogating the mineral physics tables. The current scheme is employed rather than this one since the computational (particularly in RAM and storage space) cost of accessing the particle-data is very high, and since the splitting and merging algorithms used to maintain a uniform density of particles do this on the length scale of the geodynamic grid, there would likely be areas without sufficient particles to take a meaningful average on.

compositions at each point to evaluate ρ, V_S and V_P on this refined grid; (Figure 34 b). To gain a representative estimate of the bulk properties, a harmonic average is used for densities and velocities

$$\frac{1}{\Psi^{P,T}_{\text{Bulk}}} = \frac{f_{\text{Lhz}}}{\Psi^{P,T}_{\text{Lhz}}} + \frac{f_{\text{Hzb}}}{\Psi^{P,T}_{\text{Hzb}}} + \frac{f_{\text{Bas}}}{\Psi^{P,T}_{\text{Bas}}} \tag{3.2}$$

Where $\Psi^{P,T}_{m}$ represents either one of the seismic velocities (V_S, V_P) of the material (m) at the relevant pressure (P) and temperature (T). I refer to this calculation, where the fraction of each end-member in the averaging scheme varies according to the local abundance of each end-member, as 'local mechanical mixing' to differentiate it from the assumption of a uniform mechanical mixture globally. The choice of averaging scheme of velocity is non-trivial, the harmonic scheme is justified for the seismic velocities by the observable (travel time) being on the numerator. For densities, an arithmetic average is used so that the observable (mass) is on the numerator as well.[4]

Having produced the high-resolution density and velocity profiles at each lateral grid node, I predict the topography as observed by SS precursors, assuming vertical incidence. First, the vertical reflectivity is calculated for each depth i as the impedance contrast across that depth, (e.g. Stein and Wysession, 2003, p. 33)

$$R^i_S = \frac{(\rho^{i+1} + \rho^i)(V^{i+1}_S + V^i_S) - (\rho^{i-1} + \rho^i)(V^{i-1}_S + V^i_S)}{(\rho^{i+1} + \rho^i)(V^{i+1}_S + V^i_S) + (\rho^{i-1} + \rho^i)(V^{i-1}_S + V^i_S)} \tag{3.3}$$

To then find the discontinuity depth, the peak vertical reflectivity is found at each lateral node, and the corresponding depth used (Figure 34 c) since I assume the peak vertical reflectivity is associated with the depth of the discontinuity. The peak vertical reflectivity represents an upper bound for the actual reflectivity for the offsets used in SS precursor studies since the SS-precursor phase is not strictly vertically incident on the discontinuity. Whilst for 410, this is usually unambiguous as across compositions it is generally controlled by the Ol-out reaction (until the coesite-stishovite (e.g. Liu *et al.*, 1996) reaction dominates at high basalt fraction), the region around 660 is much more complex. At cool temperatures the spinel-out reaction is accomplished via akimotoite (e.g. Yu *et al.*, 2011) and at high basalt fraction the spinel-out reaction is replaced by the deeper garnet-out reaction (e.g. Hirose, 2002) - together these can result in multiple peaks and broad regions of

[4]In the published version of this chapter, Morgan *et al.* (2025*b*), I used a geometric average for density as well as the seismic velocities. Comparison between the figures here and in Morgan *et al.* (2025*b*) reveal no perceptible difference, highlighting the minimal role of the exact averaging scheme used.

elevated reflectivity (see Figure 35). For simplicity I pick the depth of maximum reflectivity.

3.2.4 The 'Bouncepoint-Spherical Cap Filter' – a Simple Filter for SS Precursors

Later, I will compare these predicted topographies to those observed using SS-precursors, and here describe a simple filter to permit a meaningful comparison.

As the distribution of sources, receivers, and therefore bounce-points, are highly non-uniform and SS-precursor sensitivity extends away from the ray-theoretical bounce-point (e.g. Neele *et al.*, 1997; Dahlen, 2005; Guo and Zhou, 2020) I implement here a first-order approximation of the sensitivity of the precursors to mantle transition zone seismic structure distributed with the ray-theoretical bounce-points. I approximate the sensitivity of the precursor (typically of period ~ 20 s), which is actually a complex region of positive and negative traveltime sensitivity, as a spherical cap of radius 500 km (a visual comparison is presented in Figure 37). This spherical cap represents a multi-azimuthal average of *SS-SdS* traveltime sensitivity and is similar in size to the first Fresnel zone of the SS precursor (e.g. Dahlen, 2005). Similar caps are typically used in stacking these SS precursor data (e.g. Houser *et al.*, 2008; Guo and Zhou, 2020). As well as this finite-far-field sensitivity seismic waves cannot resolve infinitely thin radial seismic impedance structures. Usually it is assumed that impedance contrasts less than a quarter wavelength thick cannot be resolved (e.g. Chambers *et al.*, 2005*a*). Using array processing does allow a smaller effective Fresnel zone to be formed (e.g. Rost and Thomas, 2009) between a seismic source and an array of receivers, but due to the additional labour required for the array processing, coverage is at present much more limited than for more conventional SS-precursor studies (e.g. Saki *et al.*, 2024), although it allows the consideration of important effects, such as out-of-plane energy, yielding a more accurate assessment of reflector depths (e.g. Rochira and Thomas, 2023).

This 'filter' is very simple and does not capture all of the complexities of the physics of seismic ray reflection. In regions with many bounce-points and a reasonable spread of azimuths (e.g. the North Pacific) use of the true sensitivity kernels is unlikely to have a significant impact on the expected topography. However, in poorly constrained regions I likely under-predict the high spherical harmonic degree structure compared to that retrieved by a realistic kernel. I also do not consider the effect of earthquake focal mechanisms (which would create a

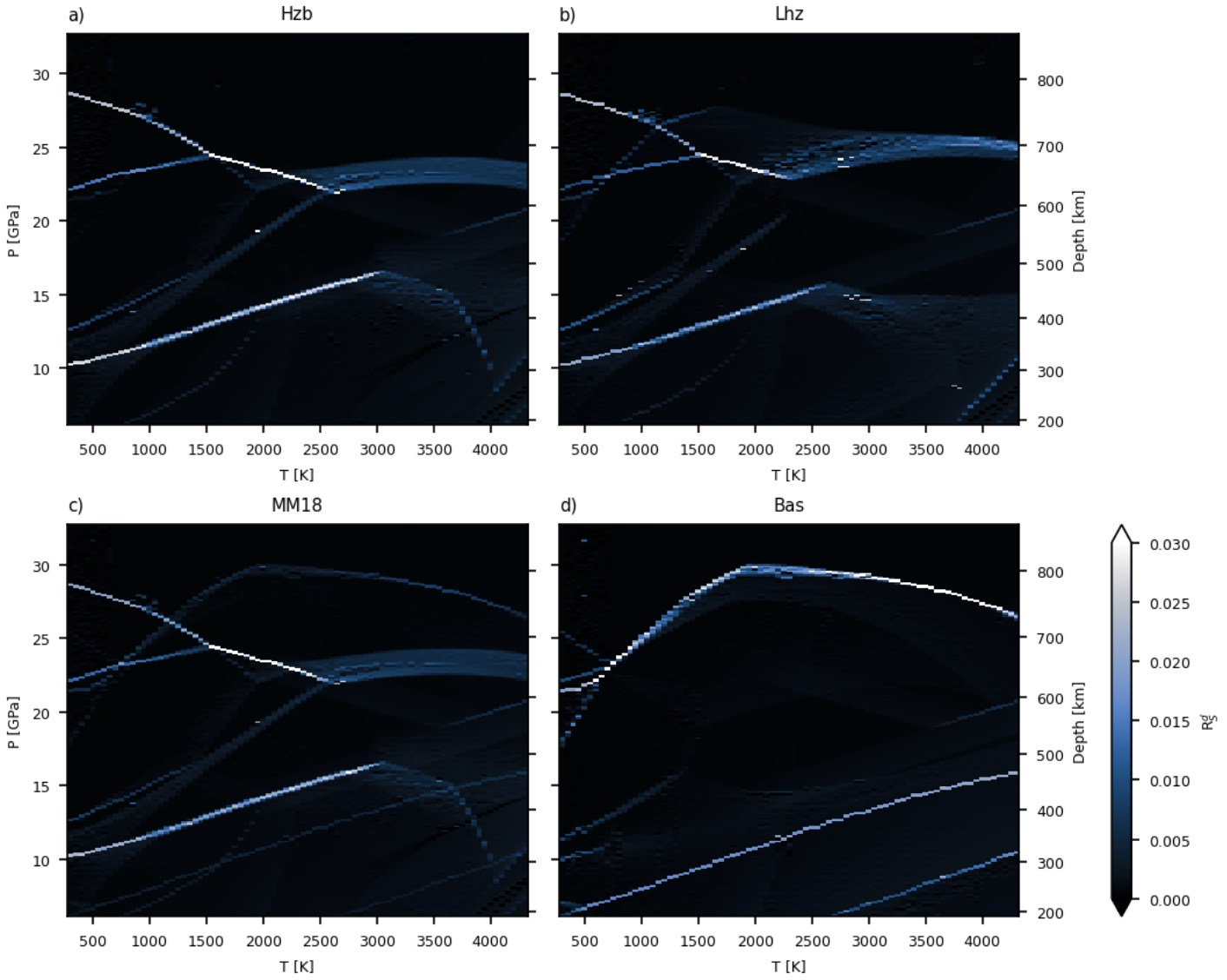

Figure 35: SS reflectivity, R_S, structure of mineral physics tables for end-member compositions used in this study. *a)* Harzburgite, *b)* Lherzolite, *c)* MM18 a 'pyrolite' composition mechanical mixture of 18% Basalt and 82% Harzburgite, *d)* Basalt. Where R_S is high, and appears bright on the figure, the discontinuity is more easily identified. Broad transformations with gradual changes in density and seismic velocity produce dull regions, where the discontinuity is harder to identify.

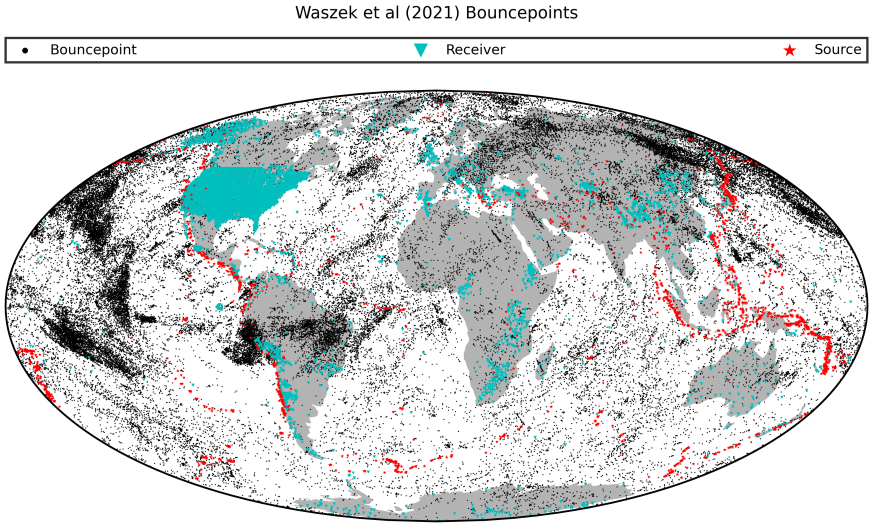

Figure 36: Distribution of seismic sources (red stars) and receivers (cyan triangles) used in Waszek *et al.* (2021). Bounce-points (Black dots) are then calculated as the mid-point along great circles between source-receiver pairs. Bounce-points are distributed unevenly, with clusters in the North Pacific, beneath NE Asia, Central & Eastern Europe, and Central South America.

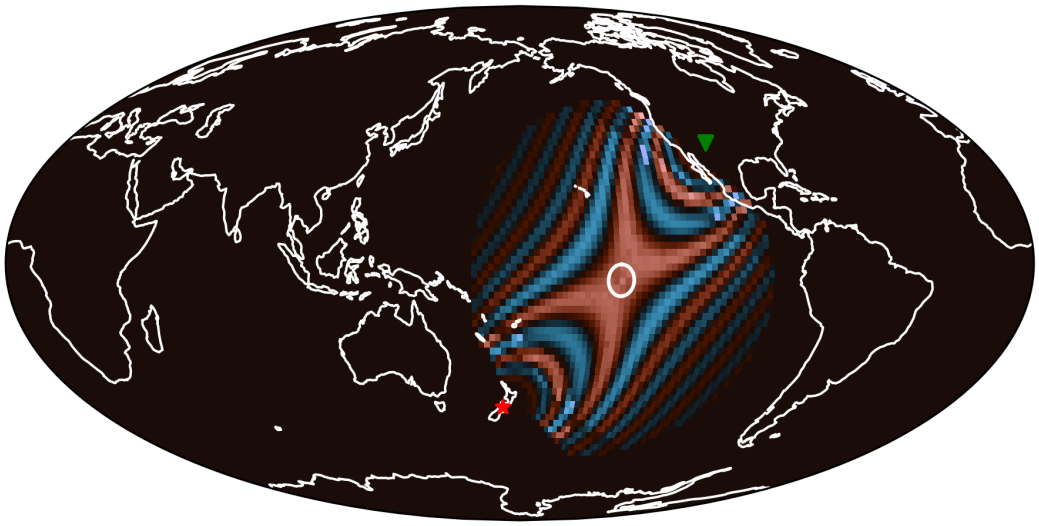

Figure 37: Finite sensitivity kernel of *SS-S400S* of traveltime (see Section 4.4.5), compared to the 500 km radius spherical cap employed here as a multi-azimuthal average of the sensitivity of the pre-cursor.

null-sensitivity along the nodal planes (Zhao and Chevrot, 2003)) or anisotropic velocities in the mid-upper mantle (Huang *et al.*, 2019) since I judge these to have a secondary impact on recovered topographies compared to the above.

To produce the filtered predicted discontinuity topographies, I do the same upscaling and local mechanical mixing procedure described above, but instead of focusing on the region around the discontinuities, I predict the fine-scale material property structure on the length scale of the thermodynamic tables (2.5km) radially throughout the MTZ. For a 20s period SS precursor just beneath d660, a quarter wavelength is 30km, so I use a rolling window 30km thick to find the radial reflectivity structure through the whole MTZ at each lateral point. I then pick the depths with the brightest reflection around 410km ($200 - 480$ km) and 660km ($600 - 850$ km depth) depth as the depths of the discontinuities. To filter the predicted topographies for the lateral sensitivity of the SS precursor, I take a simple average of the discontinuity depth within a radius of 500 km of the bounce-points for the source-receiver pairs used by Waszek *et al.* (2021).

These are then compared directly to the Waszek *et al.* (2021) topography model. In this study I approximate the spatial averaging of the SS-precursor performed by Waszek *et al.* as exact reproduction of the processing in that study would require original data from the study. I expect that the exact choice of spatial averaging would have a negligible impact on the results.

Figure 38: Topography on 410 (*a, d, g*) and 660 (*b, e, h*) discontinuities and MTZ thickness variations (*c, f, i*) calculated by method described here for model 'm_cc_066_u' compared to the topography found for the Earth by Waszek *et al.* (2021) in the bottom row (*j, k, l*). The other rows denote different methods of mechanical mixture. *'TC3MM'*: topography predicted by three end-member local mechanical mixing calculation using a equilibrium assemblage table for Lhz. *'TC2MM'*: topography predicted by two end-member local mechanical mixing calculation using a Mechanical Mixture table of 80% Hzb, 20% Bas for Lhz. *'MM18'*: topography predicted by a global mechanical mixing calculation of 18% Bas and 82% Hzb.

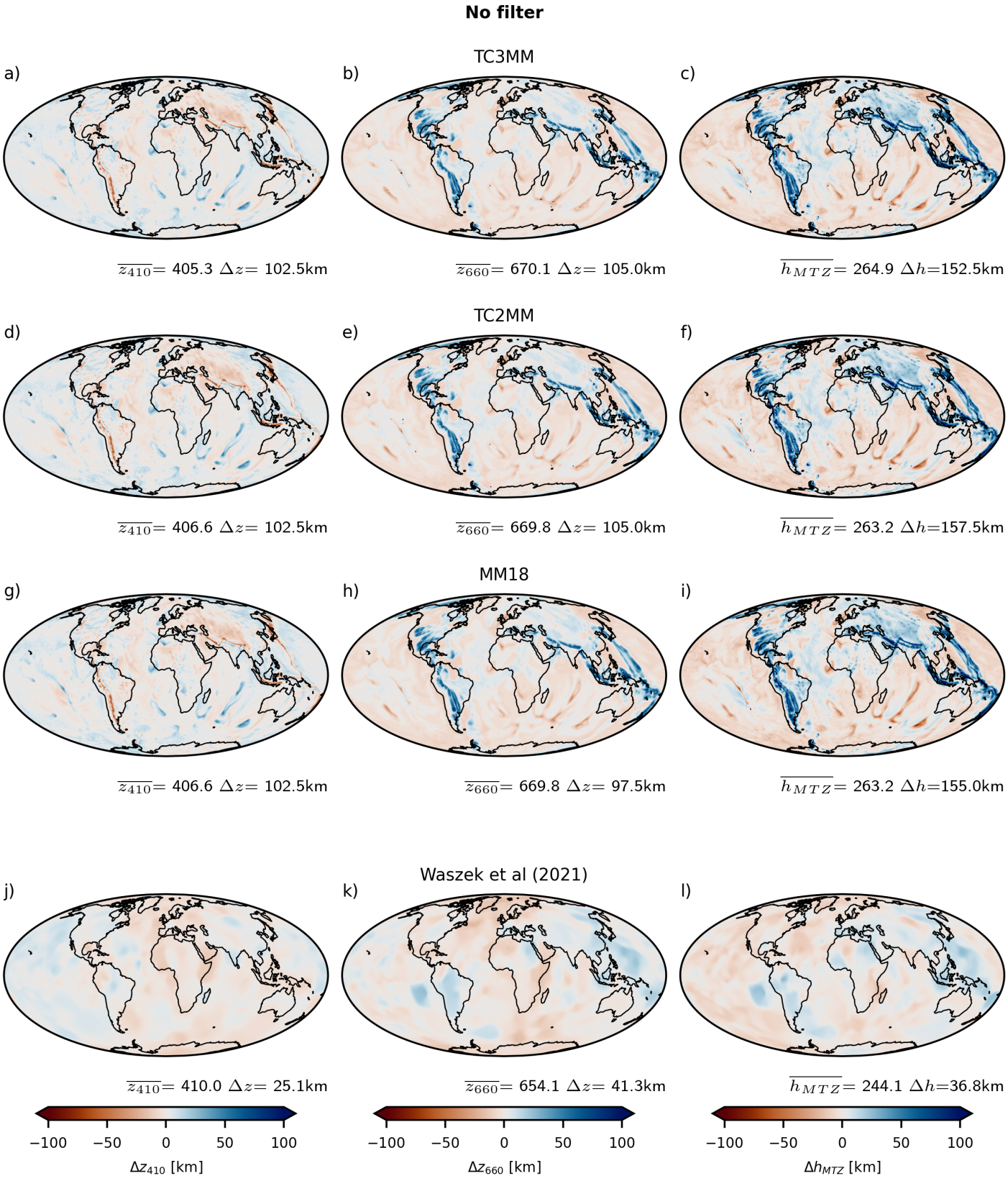
No filter
TC3MM
a)
b)
c)
$\overline{z_{410}}$= 405.3 Δz= 102.5km
$\overline{z_{660}}$= 670.1 Δz= 105.0km
$\overline{h_{MTZ}}$= 264.9 Δh=152.5km
TC2MM
d)
e)
f)
$\overline{z_{410}}$= 406.6 Δz= 102.5km
$\overline{z_{660}}$= 669.8 Δz= 105.0km
$\overline{h_{MTZ}}$= 263.2 Δh=157.5km
MM18
g)
h)
i)
$\overline{z_{410}}$= 406.6 Δz= 102.5km
$\overline{z_{660}}$= 669.8 Δz= 97.5km
$\overline{h_{MTZ}}$= 263.2 Δh=155.0km
Waszek et al (2021)
j)
k)
l)
$\overline{z_{410}}$= 410.0 Δz= 25.1km
$\overline{z_{660}}$= 654.1 Δz= 41.3km
$\overline{h_{MTZ}}$= 244.1 Δh=36.8km
−100 −50 0 50 100
Δz_{410} [km]
−100 −50 0 50 100
Δz_{660} [km]
−100 −50 0 50 100
Δh_{MTZ} [km]

3.3 Results

3.3.1 Local Mechanical Mixing with Three Endmembers: TC3MM

First I consider the topographies calculated with three end members, referring to this local mechanical mixing model as 'TC3MM' (since this takes account of the full thermochemical structure with three-endmembers). The global discontinuity topography predicted by this method is illustrated in Figure 38 a, b & c. The topography on these reactions is dominated by the focused upwellings (approximating plumes) and downwellings (approximating slabs) that pass through the MTZ of the model - but there are other regions of complex topography particularly on d410 above flat-lying slabs such as beneath Eastern North America and NE Brazil (this detail can also be seen on Figure 43a). On d410, as suggested by the classic understanding that the discontinuity is controlled by the olivine-out reaction with a positive Clapeyron slope, hot upwellings are associated with a deepening of the discontinuity and cool downwellings are associated with an elevation.

On d660, the broad-scale structure follows the trends expected if I assume the topography is dominantly controlled by the ringwoodite-out reaction, which has a negative Clapeyron slope (i.e. that the downwellings have a deeper associated discontinuity and the upwellings have a shallower discontinuity). The much wider spatial extent of the topography associated with downwellings on d660 compared to d410 (e.g. Western Pacific) is noticeable. This is explained by the greater viscosity around d660 than d410 in the geodynamic model (the viscosity in the geodynamic model starts to increase in the lower part of the mantle transition zone, so is already elevated compared to around d410 see Figure 29).

3.3.2 Effect of Different End-Member Assumptions in the Local Mechanical Mixing Calculation

One of the distinctive aspects of the method presented here compared to previous work (Papanagnou *et al.*, 2023) is that I consider the effect of lateral variations of composition on discontinuity topography. I can also predict the topography by the same peak R_S method, but by assuming a fixed (mechanically mixed) composition or by assuming instead that lherzolite represents a mechanical mixture of harzburgite and basalt get a sense of the effect the local mechanical mixing and the number of endmembers has on the topography. The effects are small, but the discontinuities predicted using these

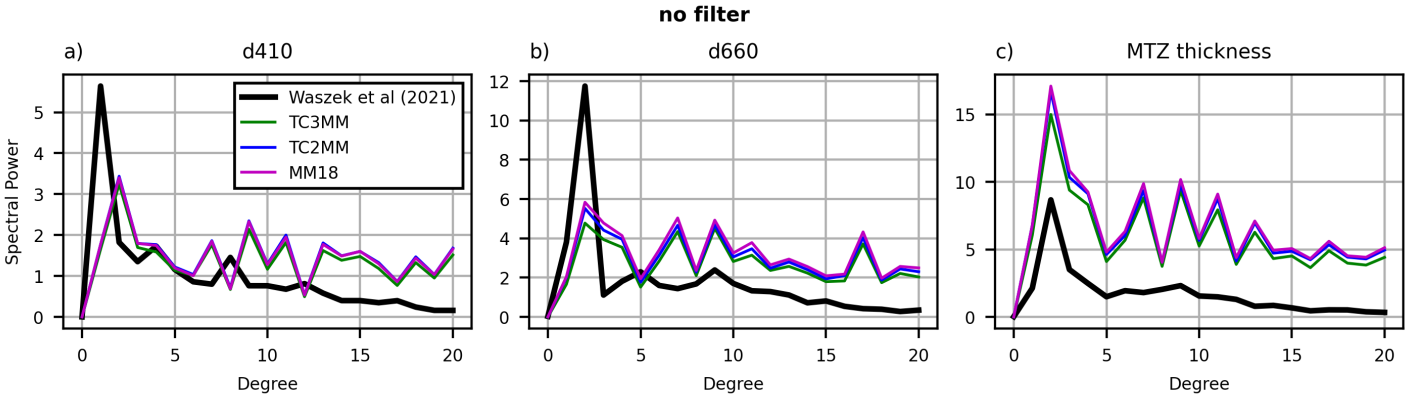

Figure 39: Power spectra of *a)* 410 discontinuity topography, *b)* 660 discontinuity topography, *c)* MTZ thickness variations for predicted seismic structures with different mechanical mixing methods, as discussed in text, TC3MM – local mechanical mixing with three endmembers, TC2MM – local mechanical mixing with two endmembers, MM18 – global mechanical mixture. Power spectra of topography calculated by Waszek *et al.* (2021) are included for reference.

simpler chemical assumptions have more power in the spherical harmonic spectra than TC3MM at most spherical harmonic degrees (Figure 39). This represents a slightly rougher discontinuity surface without the smoothing of V_S, V_P and ρ that comes from the mechanical mixture.

Reducing the Number of Endmembers to Two: TC2MM

I track composition in TERRA on three end members (see above). This implicitly assumes that the entire mantle has not been completely processed (i.e. undergone melting at the surface and then re-introduced to the mantle interior as fertile and depleted material Béguelin *et al.* e.g. 2025*b*) since Earth's solidification, and that at the start of the model evolution (1.2 Gyr before present), a large part of it was un-processed (i.e. Lherzolitic). I can change this assumption by replacing the Lherzolite tables (representing a pyrolitic equilibrium assemblage) of seismic properties with a mechanical mixture of basalt and harzburgite, corresponding to $f_{Bas} = 0.2$ – representing the same bulk composition but as a mixture of the two end members. I refer to this local mechanical mixing model as 'TC2MM' (since I have reduced my consideration of the thermochemical structure to two endmembers). The resulting discontinuity topographies are shown in Figure 38 d, e, & f – with no significant differences in the distribution of topographic anomalies compared to a, b, c. On d410, the topographic anomalies in Figure 38 d are generally shifted to deeper values, with a deepening of the average discontinuity depth globally. On d660 (Figure 38 e), the average discontinuity depth becomes shallower (but only by 300m).

Uniform Global Mechanical Mixture: MM18

Similarly to the section above, I can form a table representing a global mechanical mixture by mixing my end-member tables of Lhz, Hzb and Bas. A commonly assumed global mantle composition is a pyrolite model - a mechanical mixture of $\sim 20\%$ basalt and $\sim 80\%$ harzburgite - following previous work (Papanagnou *et al.*, 2023; Ritsema *et al.*, 2009), I use a value of $f_{Bas} = 0.18$ (the 'MM18' pyrolite model with no lateral variations) for this comparison. The resulting calculated topography is shown in Figure 38 g, h, & i. As this global mechanical mixture has only two end-members a comparison is best made with the local mechanical mixture TC2MM. The average discontinuity depths are similar between the two models, and very few differences can be seen on d410 or d660.

3.3.3 Effect of Bouncepoint-Spherical Cap Filter on Recovered Discontinuity Topographies

So far, I have only calculated the geographic distribution of peak reflectivity depth and have not considered how this is observed seismically. Above (section 3.2.4), I described a simple filter that captures some of the key physics of the global *SS*-precursor observation of the discontinuities, i.e. that each reflection samples a region around the ray-theoretical bounce-point and that these bouncepoints are distributed extremely unevenly across the Earth. I consider the effect of that filtering on recovered topographies here.

The topographies of d410 and d660 calculated from the MCM shown in Figure 38 are filtered by this method and shown in Figure 40. Note the significant reduction in the peak-to-peak amplitude of topography, and how the focused elevation of topography on the d410 beneath subduction zones in the unfiltered predicted topography is broadened to a similar width as that seen in the observed topography of d660. Fine-scale features such as the lateral offset of d410 and d660 due to steps in the surface motion patterns (e.g. beneath the Hindu-Kush) are lost. Power spectra for the filtered predicted topographies are plotted in Figure 41. For d660 and MTZ thickness variations, filtering reduces the difference between the topographies predicted with different mixing methods (compare Figures 39 and 41), although on d410 there appears to be increased sensitivity to the filtering method. Irrespective of the mixing method, at high spherical harmonic degree the power on d410, d660 and MTZ thickness variation is significantly reduced when the 'filtering' is applied. Whilst the bouncepoint-spherical-cap filtering improves the match between the predicted topographies and the topography reported by Waszek *et al.* (2021) (compare

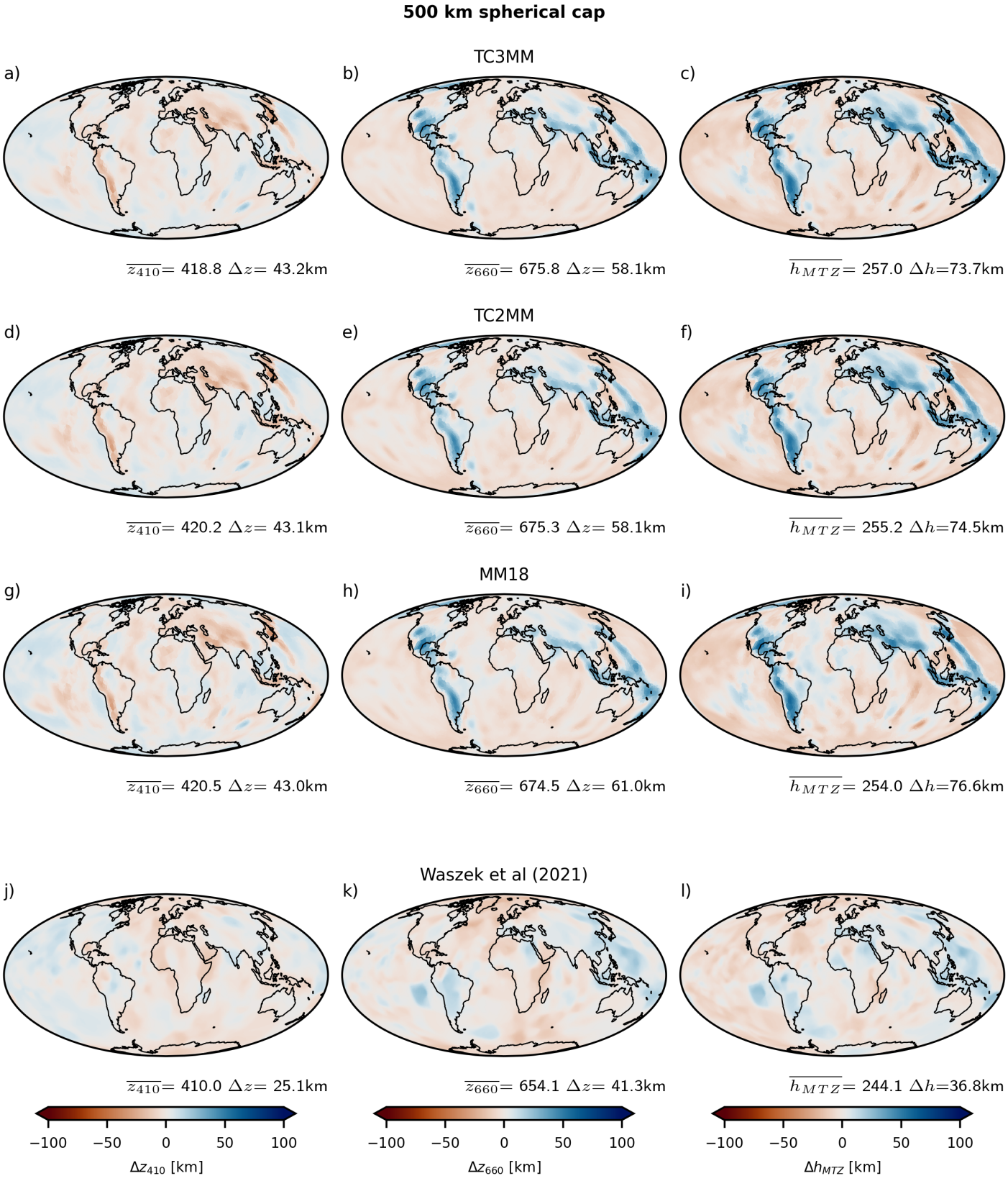

Figure 40: Topography on 410 (*a, d, g*) and 660 (*b, e, h*) discontinuities and MTZ thickness variations (*c, f, i*) calculated by the method described here, then filtered using a 500 km spherical-cap-bouncepoint method, compared to the topography on 410 and 660 and MTZ thickness variations described by Waszek *et al.* (2021) in *j, k* and *l* respectively.

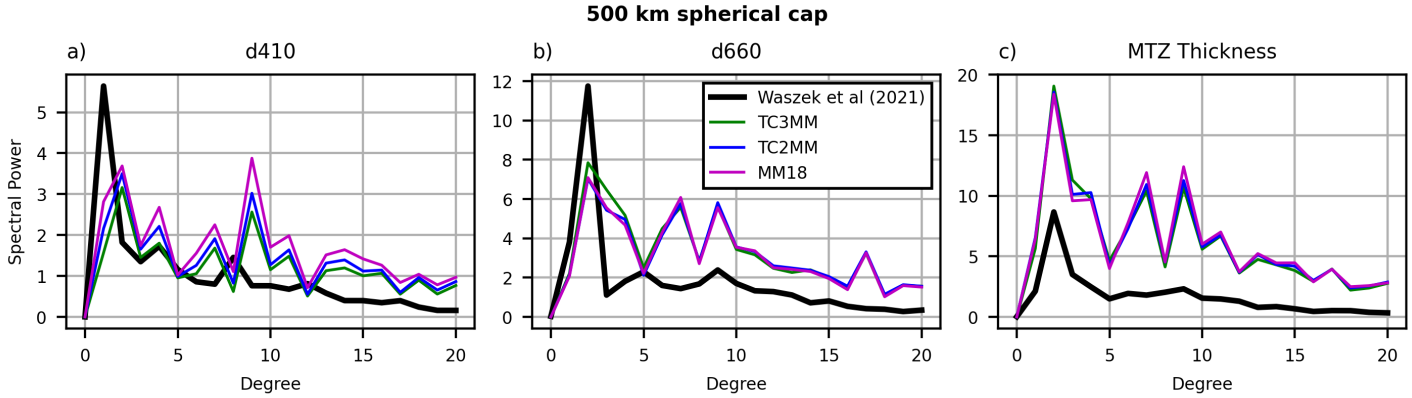

Figure 41: Power spectra of *a)* 410 discontinuity topography, *b)* 660 discontinuity topography, *c)* MTZ thickness variations for filtered predicted seismic structures with different mechanical mixing methods, as discussed in text, TC3MM – local mechanical mixing with three endmembers, TC2MM – local mechanical mixing with two endmembers, MM18 – global mechanical mixture. Power spectra of topography calculated by Waszek *et al.* (2021) are included for reference.

the coloured lines to the black line in Figures 39 and 41) at high spherical harmonic degrees ($l > 7$), it does not significantly reduce the spectral power at medium spherical harmonic degree ($3 < l < 7$) or increase it at low spherical harmonic degree ($l < 3$), where there is a particularly strong mis-match between the predicted unfiltered power spectra and the seismologically observed topography structure. I might interpret this mis-match as a degree 2 structure present in the Earth but not in this MCM. For instance, I could invoke thermochemical piles swept by a history of downwellings guiding the position of upwellings, or the impact of continents insulating domains of the upper mantle beneath them, but without a broader suite of MCMs it is not possible to conclude at this point. I also note that other published d410-d660 structures (e.g. Houser, 2016; Guo and Zhou, 2020) do not have the same dominant degree 2 structure recovered by Waszek *et al.* (2021), so this may instead be a quirk of the averaging scheme they employ.

I illustrate the effect of varying the spherical cap radius in Figure 42. Even with a comparatively small cap radius (250 km), the predicted topography is

Figure 42: Variation in post-filtered topography with radius of cap used in bounce-point-spherical-cap filter. *a), c), e)* topography on 410 discontinuity with spherical cap radius 250, 500, and 1000; *km* respectively; *b), d), f)* topography on 660 discontinuity with spherical cap radius 250, 500, and 1000; *km* respectively; *g)* power spectra of 410 discontinuity with varying spherical cap radius; *h)* same as for *g*, but for 660 discontinuity. *i)* same as for g and h but for MTZ thickness

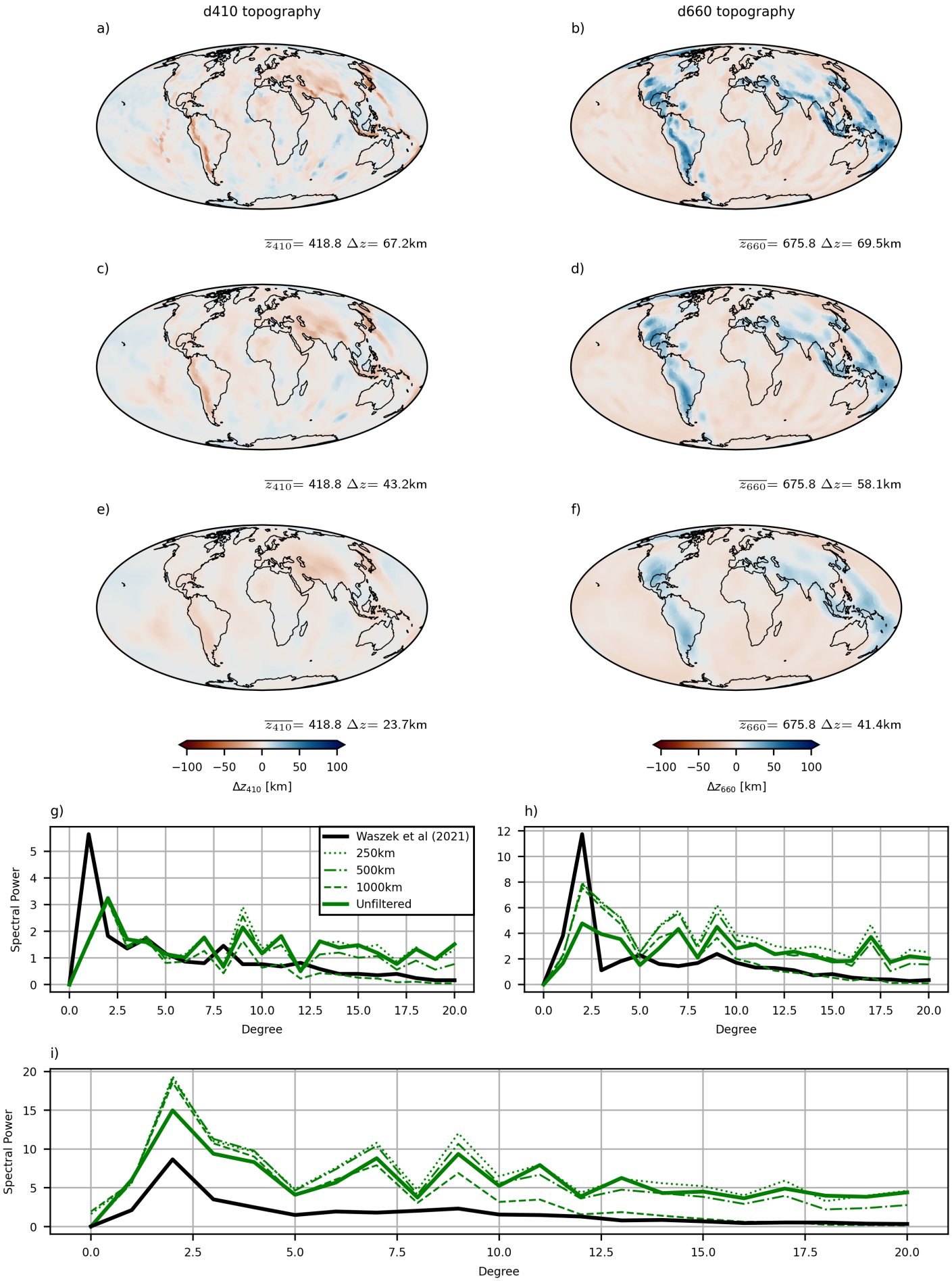
d410 topography
d660 topography
a)
b)
$\overline{z_{410}}$= 418.8 Δz= 67.2km
$\overline{z_{660}}$= 675.8 Δz= 69.5km
c)
d)
$\overline{z_{410}}$= 418.8 Δz= 43.2km
$\overline{z_{660}}$= 675.8 Δz= 58.1km
e)
f)
$\overline{z_{410}}$= 418.8 Δz= 23.7km
$\overline{z_{660}}$= 675.8 Δz= 41.4km
−100 −50 0 50 100
Δz_{410} [km]
−100 −50 0 50 100
Δz_{660} [km]
g)
h)
Waszek et al (2021)
250km
500km
1000km
Unfiltered
Spectral Power
Degree
i)
Spectral Power
Degree

considerably smoothed (Figure 42 a & b). With a larger cap than that which I use here in the main text (1000 km radius), topography structure is further smoothed and the peak-to-peak amplitude is slightly underpredicted, and the power on high spherical harmonic degrees ($l > 7$) topography amplitude is under-predicted (Figure 42 g & h).

Considering the variations in MTZ thickness (Figure 42i), there is an overprediction of power at all spherical harmonic degrees for spherical caps smaller than 1000 km, and for a cap of radius 1000 km a good fit is only observed at high spherical harmonic degree ($l > 12$), where structure on d410 and d660 is completely smoothed by the cap. On d410 and d660 this largest cap predicts a spectra that matches the Waszek *et al.* (2021) spectra from $l \sim 3$ out to $l = 20$. This suggests that the length scales of the topographies on d410 and d660 are individually reasonably correct for this large cap, but that they result in an excessively rough transition zone thickness structure – i.e. that they are excessively anti-correlated for this combination of MCM and mineral physics tables.

I additionally illustrate the effect of filtering regionally in Figure 43. Small-scale downwellings around 410 km depth, which produced narrow ridges on d410 are washed out in the filtered topography. Complex topography within the downwellings on d660 is lost, as well as the slight shallowing of the discontinuity beneath Florida and the Eastern Gulf of Mexico.

Predicted Dip of Discontinuity Surfaces

As the unfiltered topography is characterised by variations over short length scales it has some slope everywhere but apart from in downwellings and immediately around upwellings is reasonably smooth (with slopes of less than 45°). However, the discontinuity surface is predicted to be significantly steeper (around 70° slope) around downwellings (See Figure 44). On filtering, whilst the recovered topography is smoother, sub-vertical regions around upwellings and downwellings remain. The seismological significance of this will be discussed in section 3.4.2.

Lateral Variations in Reflectivity of Predicted Discontinuity Structures

The relative amplitude of SS precursors to the main SS arrival is also of interest since it has been used to invert for the basalt fraction in the mantle transition zone (Tauzin *et al.*, 2022), and I have taken the discontinuity reflectivity as a proxy for this amplitude ratio – see discussion in section 3.4.2. I plot the lateral

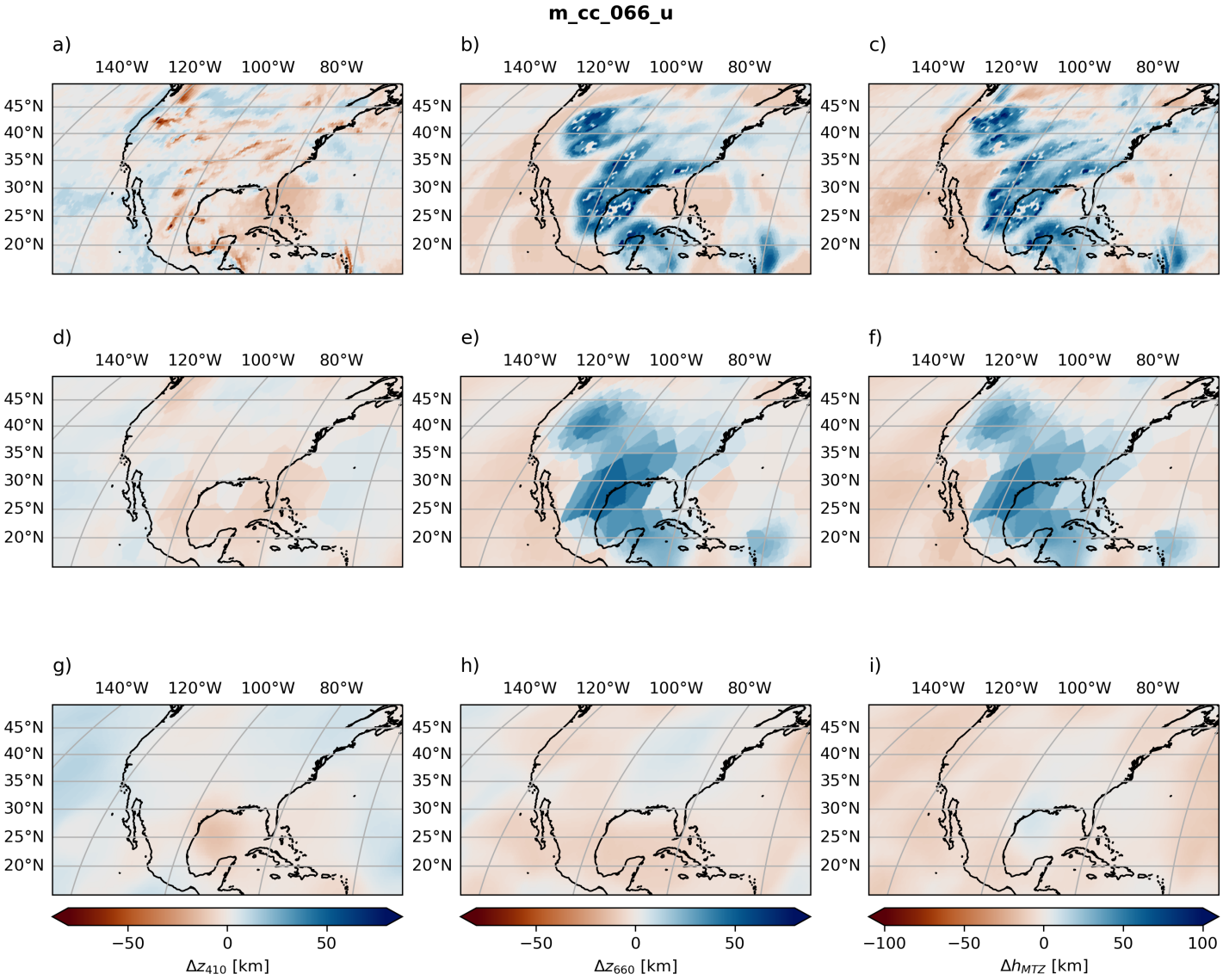

Figure 43: d410 (*a, d, g*), d660 (*b, e, h*) and MTZ thickness (*c, f, i*) topographies predicted beneath the USA and neighbouring regions from m_cc_066_u (*a–c*), predicted and filtered with a 500 km radius spherical cap (*d–f*) and the Waszek *et al.* (2021) model in the region (*g–i*).

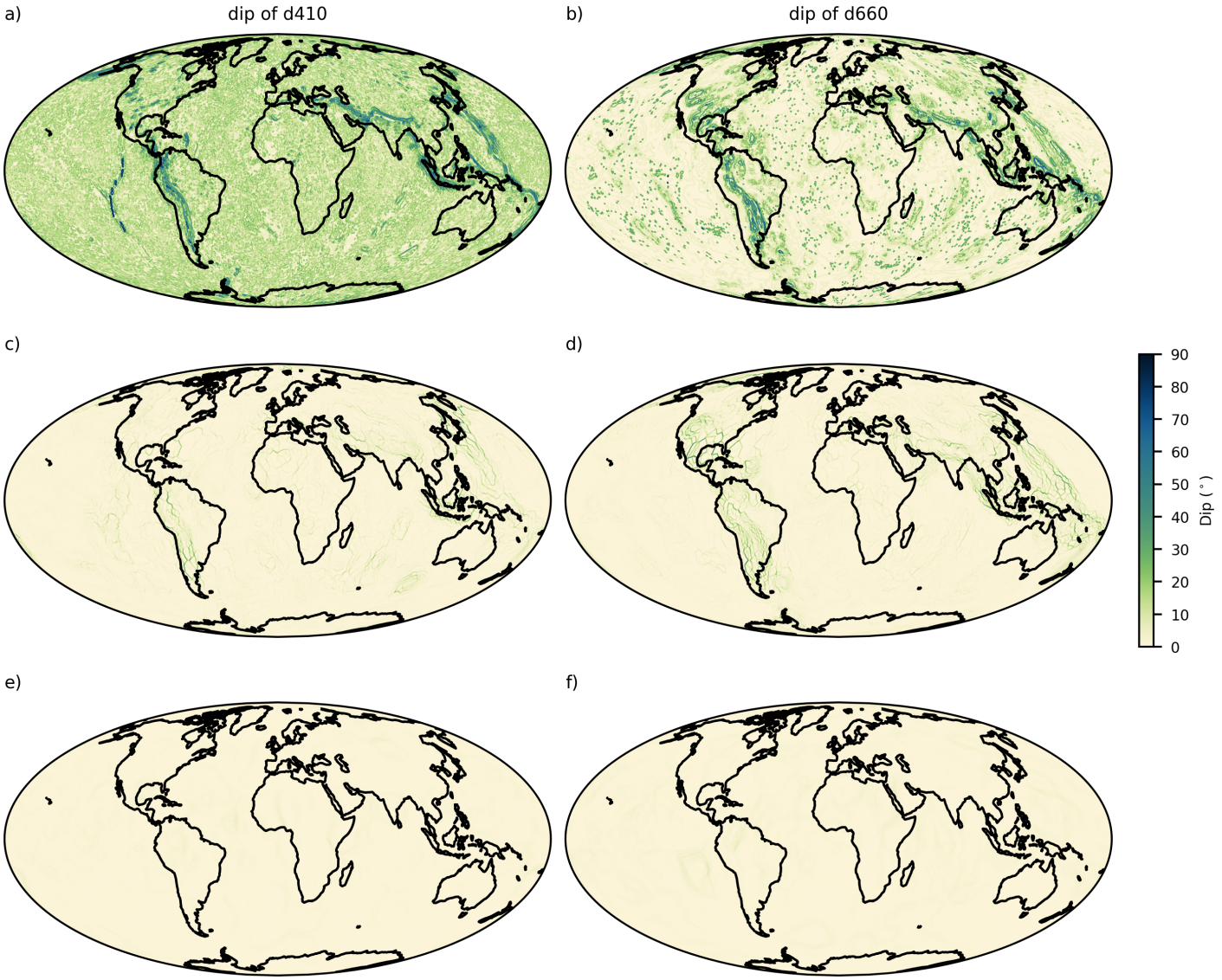

Figure 44: Dip of surface of (*a*, *c*, & *e*) d410 and (*b*, *d*, & *f*) d660 for unfiltered predicted topography (TC3MM) (*a* & *b*), filtered (500 km radius bouncepoint spherical cap) predicted topography (*c* & *d*), Waszek *et al.* (2021) topography model (*e* & *f*)

distribution of peak R_S^{410} and R_S^{660} in Figure 45. The mismatch between the geographic distribution of high R_S^d regions predicted by this simulation and areas with high SS precursor amplitudes in published data (Waszek *et al.*, 2021; Tauzin *et al.*, 2022) is strong. Local mechanical mixing is more important in local variations in R_S^d structure than for the discontinuity topography, with the 'bright' spots around upwellings less intense, and more short-wavelength structure noticeable (Figure 46) than in the reflectivity structure predicted from a global mechanical mixture. The variations I find here in d660 reflectivity due to variations in the thermal structure of the MCM are of a similar magnitude to those interpreted to be due to chemical variations within the mantle, but have a different geometry – being aligned along downwelling and upwelling centres, unlike in the Waszek *et al.* (2021) dataset where high amplitude regions are not obviously associated with the location of slabs or large plumes in the Earth. The variations in the reflectivity of d410 are smaller than on d660, but again are closely associated with the distribution of downwellings and upwellings in the MCM. I expand on the significance of the reflectivity variations in section 3.4.2

3.4 Discussion

3.4.1 Comparison to Previous Work Predicting d410 and d660 from MCMs

Papanagnou *et al.* (2023) also predicted d410 and d660 topography from a MCM, in their case a model published by Nerlich *et al.* (2016), which has a higher resolution than the MCM used here, allowing Nerlich *et al.* to use an upper viscosity of 1×10^{21} Pa.s, a quarter of that in the MCM used here, in line with the Haskell constraint and likely resulting in thermal anomalies that are narrower and smaller in amplitude than in the simulation I have used from

Figure 45: R_S (Shear wave reflectivity) on d410 (*a, c, e, g*) and d660 (*b, d, f, h*) for each of the mechanical mixing methods considered in this chapter TC3MM (*a* & *b*), TC2MM (*c* & *d*), and MM18 (*e* & *f*) are compared qualitatively to the amplitude of the SS precursor (*g* and *h*), filtered using the bouncepoint spherical cap of radius 500 km (and 'thickness' of 30km. Note the poor fit in geographic distribution of reflectivity between that predicted based on the geodynamic thermochemical structure and that from Waszek *et al.* (2021). The average reflectivities of d410 and d660 are more different (e.g. for TC3MM 0.066 and 0.073 respectively) than the average normalised amplitude of the precursors in the Waszek *et al.* dataset (0.038 and 0.037 respectively).

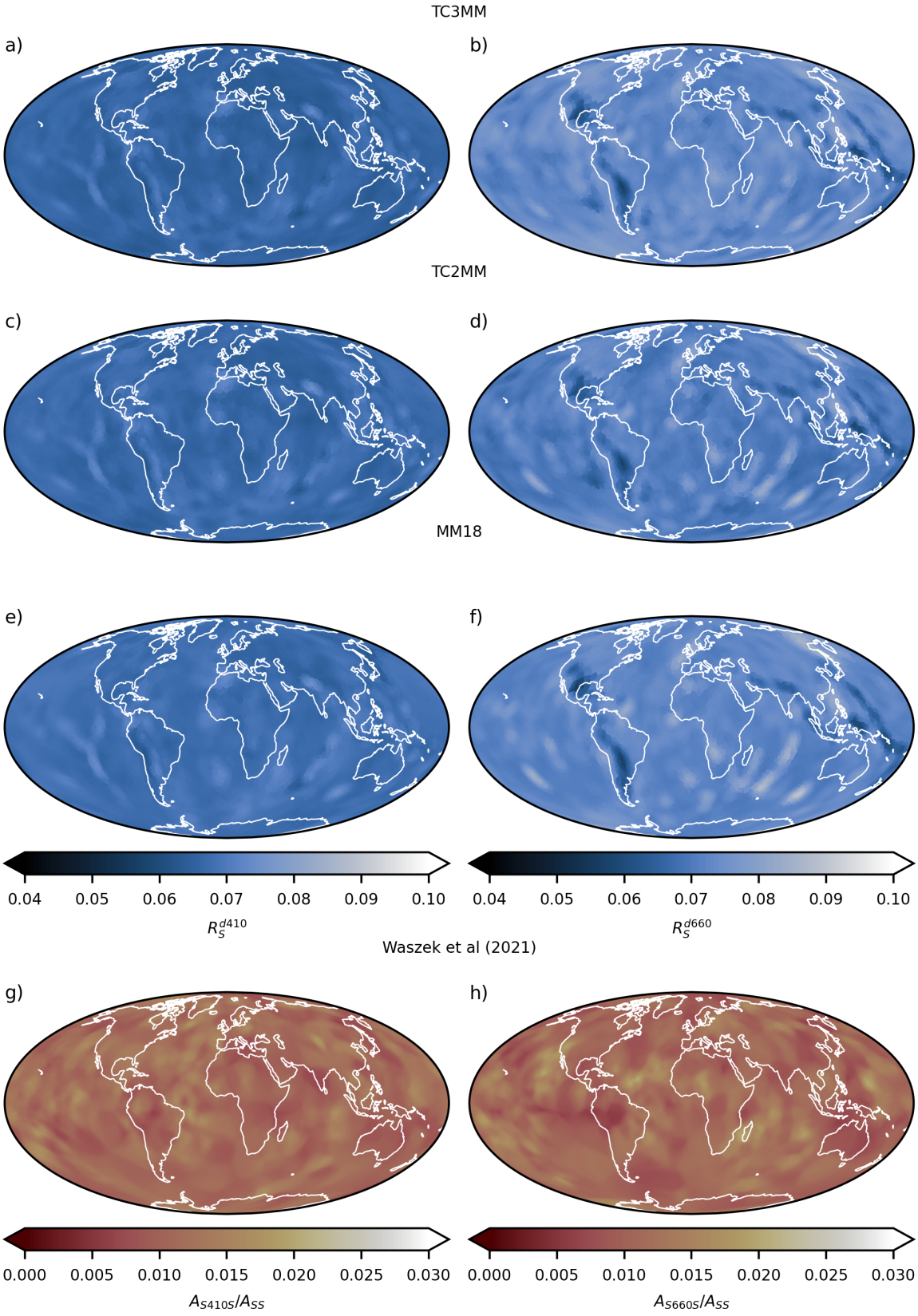
TC3MM
a)
b)
TC2MM
c)
d)
MM18
e)
f)
0.04 0.05 0.06 0.07 0.08 0.09 0.10
R_S^{d410}
0.04 0.05 0.06 0.07 0.08 0.09 0.10
R_S^{d660}
Waszek et al (2021)
g)
h)
0.000 0.005 0.010 0.015 0.020 0.025 0.030
A_{S410S}/A_{SS}
0.000 0.005 0.010 0.015 0.020 0.025 0.030
A_{S660S}/A_{SS}

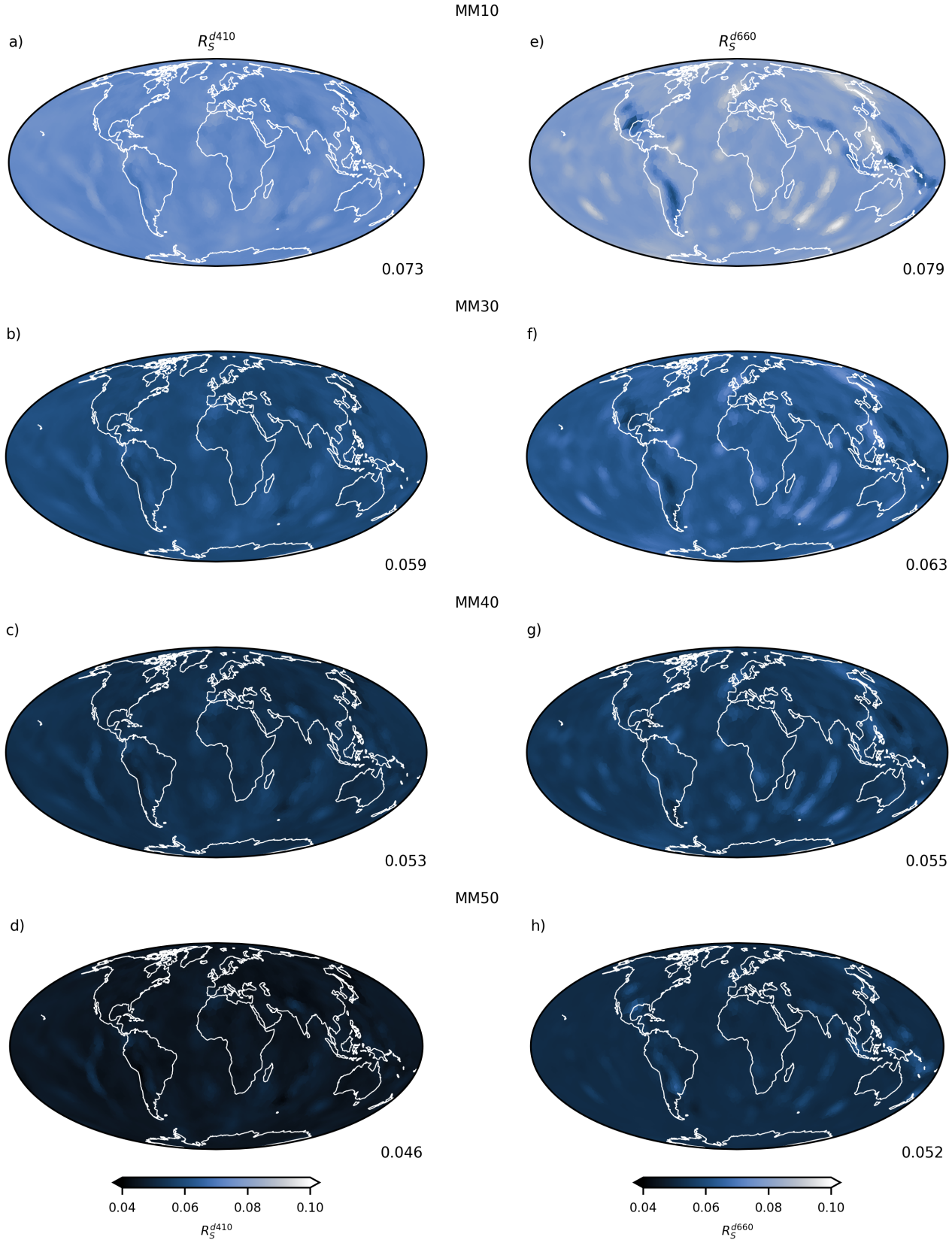

Figure 46: R_S on d410 (a–d) and d660 (e–h) for varying global mechanical mixtures MM10 (a & e), MM30 (b & f), and MM40 ((c & g) and MM50 (d and h).

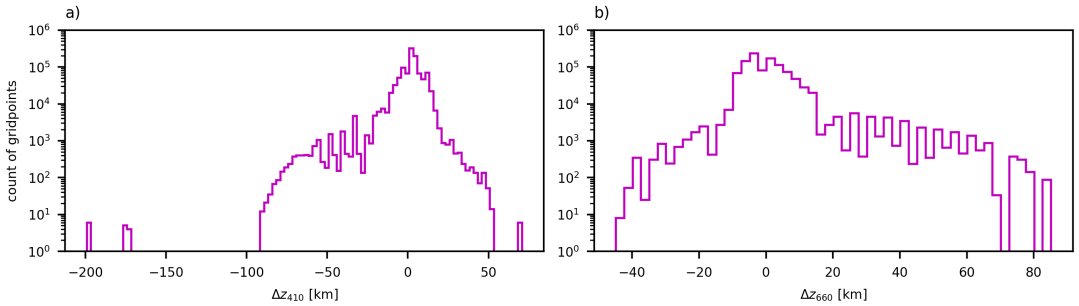

Figure 47: Histograms of *a)* d410 and *b)* d660 topography predicted from the geodynamic model 'm_cc_066_u', unfiltered using the MM18 compositional assumptions.

Davies *et al.* (2025). Their CMB temperature is also significantly higher (4200 vs 4007 K here), which may explain why the depression of d660 they predict in upwelling centres due to the garnet-out control of the d660 is not present in our predicted topographies. Since Papanagnou *et al.* (2023) did not consider the resolution of the SS-precursor or lateral chemical heterogeneity, a comparison is made with the unfiltered topographies with the global mechanical mixture 'MM18' in Figure 38 (g, h, & i). If the filtering scheme used here were to be applied to the topographies predicted by Papanagnou *et al.* (2023), I would expect the extremely localised deflections of the discontinuities to be spread out and in particular the shallowing of the d660 in the upwelling cores are unlikely to be recovered by this filter. Spectrally, I would not expect the topographies predicted by Papanagnou *et al.* (2023) to provide a markedly improved fit to the Waszek *et al.* dataset due to the comparatively low power at degree two on both discontinuities for the comparable mantle composition of MM18 (their Figure S11).

The depth anomaly ranges quoted in the figures in this chapter are from the 0.1^{st} to 99.9^{th} percentile, and with reference to Figure S19 of Papanagnou *et al.* (2023), I predict slightly broader ranges of discontinuity depths than they do, which is not surprising considering the higher viscosity used in the MCM of this study. Plotting a histogram of the topography on d410 and d660 for the unfiltered MM18 model in Figure 47 I can make a more detailed comparison to the topographies predicted by Papanagnou *et al.* (2023). The range and distribution of predicted depths of d410 predicted by me from the geodynamic model 'm_cc_066_u' (Davies *et al.*, 2025) (Figure 47) is very similar to that predicted by Papanagnou *et al.* (2023) (their Figure S19) for a less viscous mantle for a similar mantle composition. Histograms of d660 depths are more different than for d410 with out topography distribution extending to greater depths than that which Papanagnou *et al.* (2023) predict for the same

composition and their mantle circulation model. This is likely due to the detail of the viscosity structure used in the geodynamic simulations; whilst usually described as a 'jump at 660 km' depth, due to the finite resolution in mantle convection or circulation models it is always necessary for this jump to be spread over several radial grid nodes. Davies *et al.* (2025) chose to implement this so that the jump to the lower mantle viscosity is completed at 660 km depth (i.e. the viscosity at d660 is $\sim 1.2 \times 10^{23}$ Pa.s), whereas Nerlich *et al.* (2016) chose to implement the jump so that it is centred on 660 km depth (i.e. the viscosity at d660 is only $\sim 6 \times 10^{21}$Pa.s, and so the convective temperature anomalies will be smaller and more localised than around d660 in m_cc_066_u, which is reflected in the tighter range of depths predicted by Papanagnou *et al.* (2023) for d660). This choice in radial viscosity structure, rather than the factor of four difference in reference viscosity, has a larger effect on the predicted discontinuity topographies and in particular in explaining the difference in predicted d660 depth-frequency distribution and range between this work and that of Papanagnou *et al.* (2023).

3.4.2 Comparison to SdS-derived Topography

For global geodynamic simulations, the natural point of comparison are global SS-precursor topographies (e.g. Waszek *et al.*, 2021; Guo and Zhou, 2020; Houser, 2016). As an example I here make a comparison to the topography model of Waszek *et al.* (2021), derived from SS precursors in seismograms filtered for a period of $15 - 50$ s. A naive comparison between my calculated topographies in the geographic (Figure 38) and spectral domains (Figure 39) is not encouraging – my peak-to-peak topography is much larger ($\sim$ 100 km on d410 and d660) than that found by Waszek *et al.* (2021) ($\sim$ 28 km and $\sim$ 45 km respectively), and my structure is focused on short-wavelengths (high spherical harmonic degree) particularly around downwellings.

Influence of Bouncepoint Spherical Cap Filter on d410 and d660 Structure.

The topography that I naively predicted from a mantle circulation model with a lateral temperature range of $\sim$ 2000 K in the MTZ that drives vigorous convection compared poorly to the topography recovered from SS-precursors ($\sim$ 100 km on each of d410 and d660, 150 km on the transition zone thickness variations compared to $\sim$ 40 km observed on all three in recent studies (e.g. Houser, 2016; Guo and Zhou, 2020; Waszek *et al.*, 2021)). However, when a seismologically-motivated cap of radius 500 km is applied, the topographies

become of similar amplitude to those inverted by Waszek *et al.* (2021) and Tauzin *et al.* (2022) to a much smaller temperature range of 400 K. Of course, this is dependent on the cap size, and many models in principle could be over-smoothed until they are compatible with observations, but given the contribution to total sensitivity away from the first Fresnel zone is small with increasing radius (e.g., Guo and Zhou, 2020, their Figure 4) doing this would not be seismologically motivated. I note that the range of depths for d410 and d660 when filtered with the largest cap (radius 1000 km) in Figure 42 are within a couple of kilometres of the ranges for d410 and d660 reported by Waszek *et al.* (2021), but that this is likely an unphysical over-smoothing, and that whilst the appropriate cap (500 km radius) is within the correct order of magnitude, it is still overpredicting the topography significantly.

Predicted Discontinuity Topography Extremely Steep around Downwellings

I highlighted the steep dips on the d410 and d660 predicted topography surfaces (see section 3.3.3). Here I sketch some seismological implications. Such a steep discontinuity topography structure could significantly complicate the physics of reflection, potentially changing the location of bounce-points away from the mid-point of the source-receiver great circle (e.g. Rochira and Thomas, 2023) and significantly changing the reflectivity-offset curve. Whilst the global topographies inverted in SS-precursor studies, such as the Waszek *et al.* (2021) model I compare to here, are smooth and rolling (dips not exceeding 15°) there is some evidence that the discontinuity surface in the Earth could be considerably rougher, at least in places. Rochira and Thomas (2023) showed that some SS- and PP-precursors that could be interpreted as reflectors in the deeper mid-mantle (e.g. Waszek *et al.*, 2018) were, when the back-azimuth was taken into account in the bounce-point location, more accurately located around d410 and d660. Whilst these out-of-plane reflections could be due to compositional or thermal structure associated with the downwelling in the study region, SdS reflected out of the great-circle plane is also a possibility (Rochira and Thomas, 2023). Neele *et al.* (1997); Neele and Regt (1999) considered the topography of a discontinuity around slabs with a similar magnitude to that presented here, showing the smearing of the intense deflection away from the slab regions they were imposed within, also creating effects far from the downwelling slab. However, the discontinuity deflections I predict are much steeper than the sinusoidal topographies used by Neele *et al.*, and I expect significant deflections both due to slabs and upwellings. To properly assess the validity of the simple spherical cap filter, I would need to propagate seismic

waves through regions of my predicted mantle transition zone reflectivity structures to see what structures are recovered, compared to the 'filtered' topographies presented here.

Significance of Lateral Reflectivity Variations in the Earth and Predicted Discontinuity Structures

Tauzin *et al.* (2022) use the observed variations of MTZ thickness and the amplitude of SS precursors to invert for the thermochemical structure – principally using MTZ thickness variations to recover temperature and the amplitude of the SS-precursor for basalt fraction. However, I find significant variations in discontinuity reflectivity due to thermal variations (see Figure 45 and Figure 46).

The relative amplitude of the SS precursor phase should be mainly controlled by the reflectivity of the discontinuity, that I used for the prediction of the depth of the discontinuities, but is also controlled by any attenuation along the ray-path, which is not trivial to assess. For now, I accept R_s^d as a proxy for A_{SdS}/A_{SS}, but note these potential sources of error. Another major component is the variation in angle of incidence of the SS-precursor with the discontinuity surface, either due to variation in the source-receiver separation (which Waszek *et al.* correct for in their reported SS-precursor amplitude model), or the variation in the dip of the discontinuity (which I do not consider in this analysis, since where this is important more complex wave-front healing physics may also be in play). Interrogating my tables I produce a similar relationship between MTZ thickness and R_S for varying f_{Bas} and T (i.e. that R_S^d varies principally as a function of f_{Bas} and MTZ thickness as a function of T) as found by Tauzin *et al.* (2022) (Figure 48) – which suggests that using R_S^{410} or R_S^{660} as an initial proxy for SS precursor amplitudes is not unreasonable.

The average reflection amplitude of S410S and S660S is similar in the Waszek *et al.* (2021) dataset (d410 is 2.5% brighter than d660), but in the discontinuity structure predicted from this simulation, d660 is significantly (10%) brighter than d410, using the three-end-member mechanical mixing (TC3MM, Figure 45). Varying the fraction of basalt in a global mechanical mixture (Figure 46) allows $R_S^{660} \sim R_S^{410}$ where $f_{\text{Bas}}^{660} > f_{\text{Bas}}^{410}$. This geodynamic model doesn't have an accumulation of enriched material in the MTZ around d660, but this suggests that a better fit to the Earth may be observed for a geodynamic simulation with basalt enrichment in the basalt density filter (e.g. Davies, 2008*a*; Yan *et al.*, 2020).

Plotting histograms of SdS amplitude from the Waszek *et al.* (2021) model and values of R_S^d predicted for this geodynamic model (Figure 49), I highlight

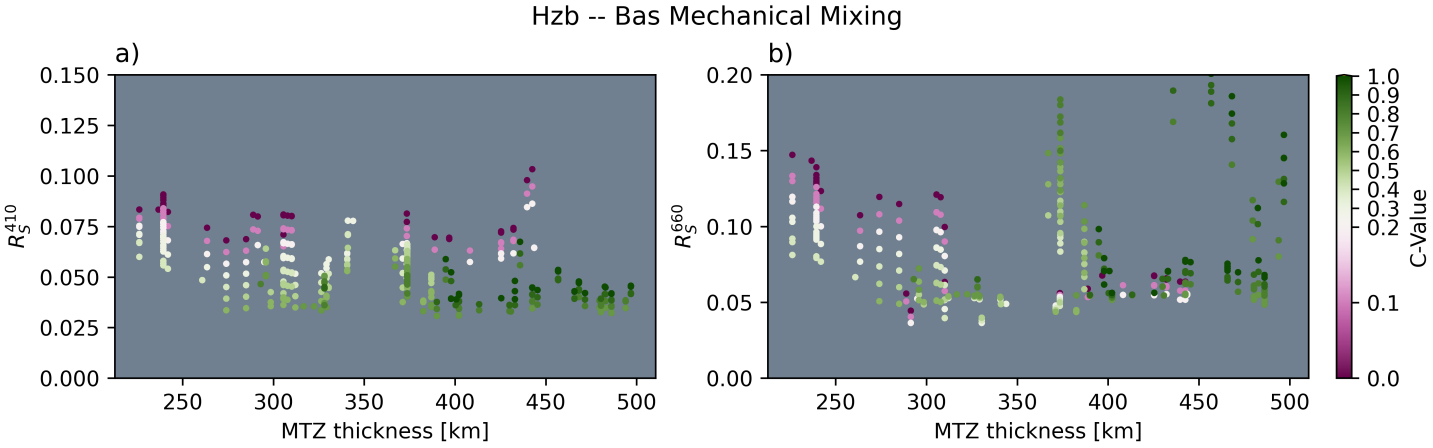

Figure 48: Interrogation of the tables used here, picking a discontinuity showing distribution of R_S^d and MTZ thickness on *a)* d410 and *b)* d660.

how the reflectivity is much less variable for the predicted discontinuities than the observed precursor amplitudes. This could suggest that this geodynamic simulation underestimates the compositional variability in the mantle transition zone, particularly given the range of reflectivity predicted for the various global mechanical mixtures (see Figure 50). Further, given our overprediction of the relative reflectivity of d660, it appears very likely that there are regions with additional basaltic material in the Earth's mantle transition zone, as has been found from previous seismological work (Khan *et al.*, 2009; Cammarano *et al.*, 2009; Munch *et al.*, 2020; Bissig *et al.*, 2022; Tauzin *et al.*, 2022; Yu *et al.*, 2023) Other factors, such as the roughness of the discontinuity surface may also play an important role (see above).

3.4.3 Relative Importance of Thermal and Compositional Heterogeneity for Discontinuity Topography

When considering the predicted topographies by this method (Figure 38) for a MCM with moderate compositional variations I find that the local mechanical mixing has essentially no effect, particularly once filtered for what is seismically visible (Figure 40). I do show some subtle differences in the reflectivity structure for discontinuities picked from different mixing assumptions (Figure 45), but in the model I have shown here there is not a drastic difference for the different assumptions about composition mixing.

If I vary the composition of the whole mantle according to different proportions of basalt and 'pyrolite' in a global mechanical mixture in the range of $0.1 < f_{bas} < 0.5$ I see no significant change in predicted filtered topographies (see Figure 51), highlighting that for moderate changes in mantle composition,

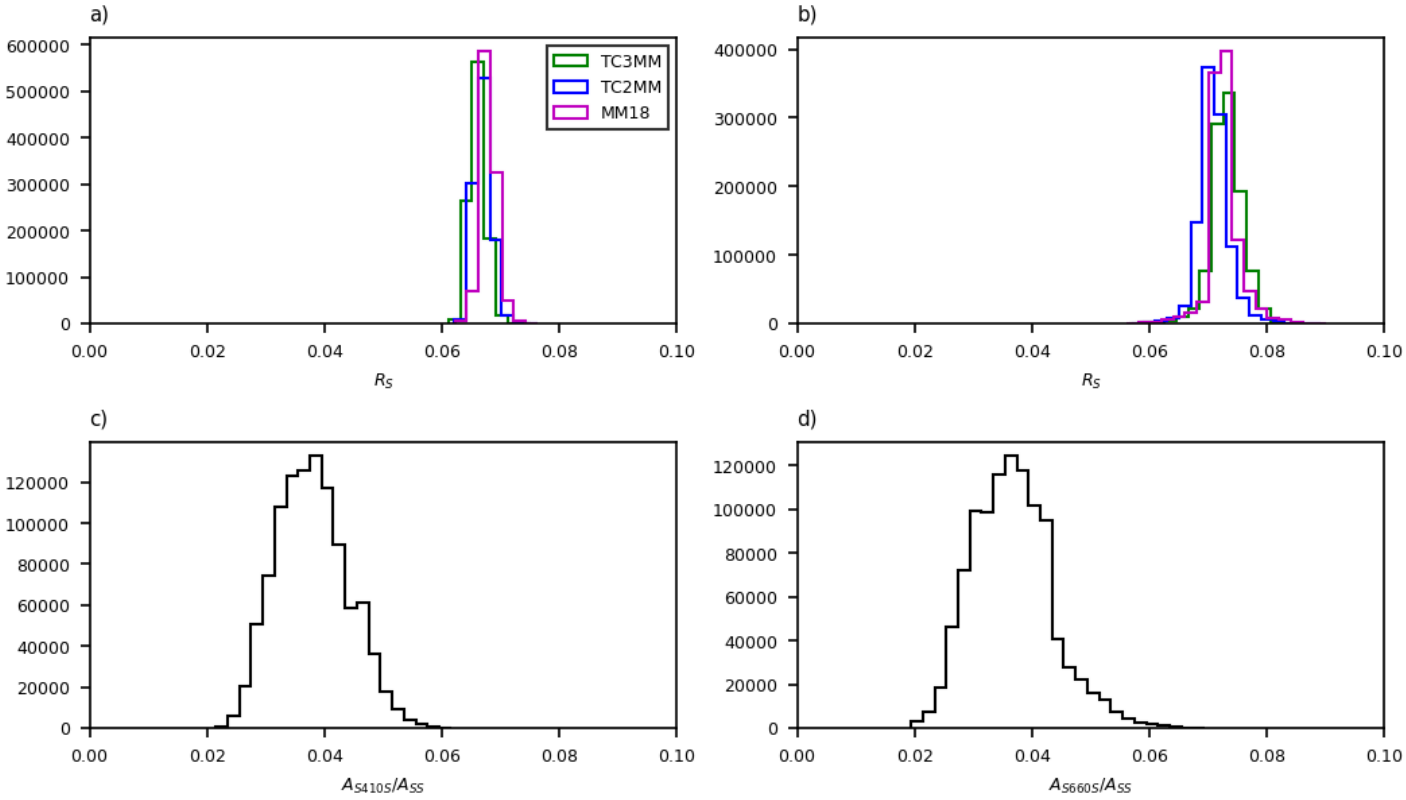

Figure 49: Histograms of *a)* R_S^{410} and *b)* R_S^{660} for the topographies predicted from the geodynamic model considered here using the local mechanical mixing assumptions and normalised SS-precursor amplitude histograms on *c)* d410 and *d)* d660 from (Waszek *et al.*, 2021).

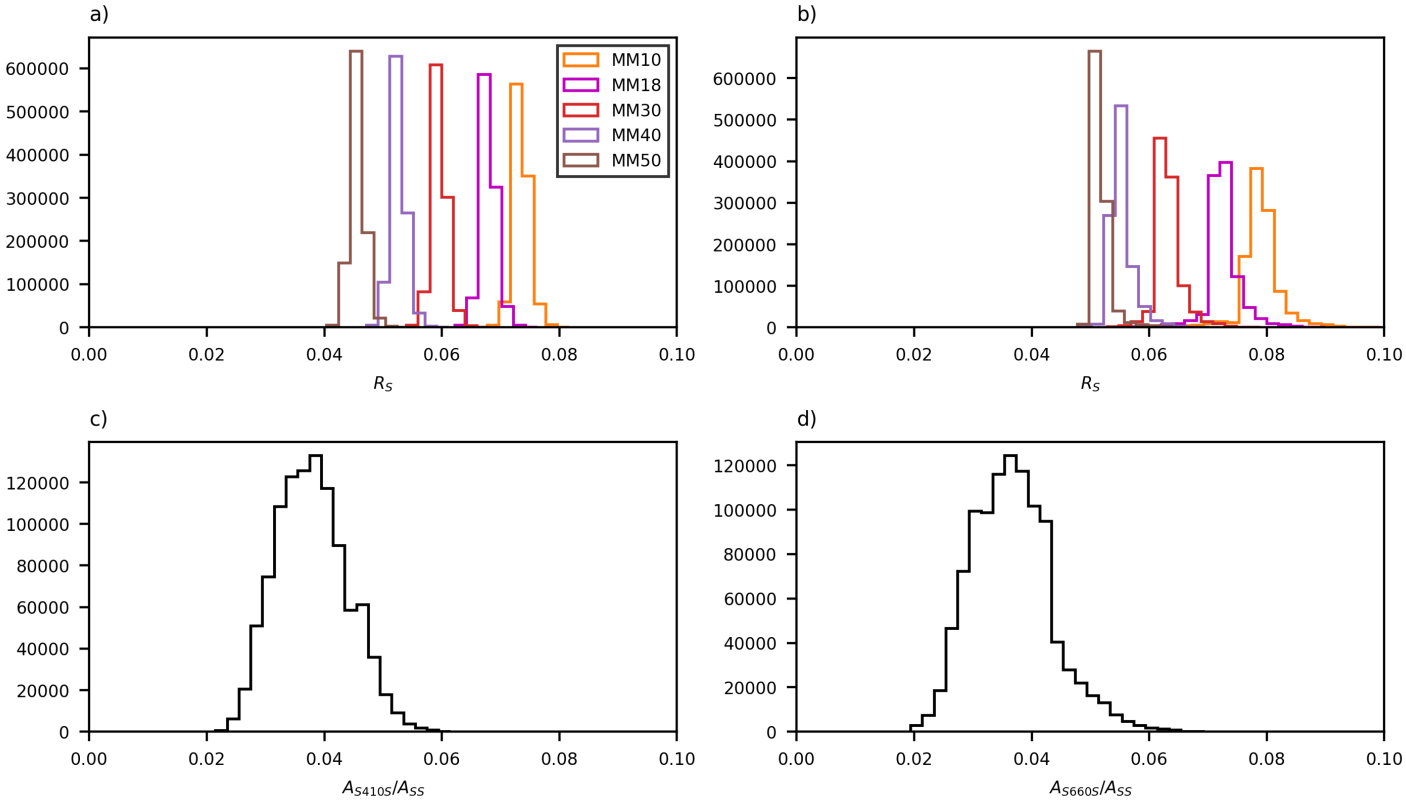

Figure 50: Histograms of *a)* R_S^{410} and *b)* R_S^{660} for the topographies predicted from the geodynamic model considered here using the different global assumed mechanical mixture compositions and normalised SS-precursor amplitude histograms on *c)* d410 and *d)* d660 from Waszek *et al.* (2021).

any changes are limited to changes in lateral reflectivity structure.

This highlights that for reasonable mantle transition zone compositions, d410 and d660 topographies predicted from a MCM are explained principally by the decomposition of olivine and ringwoodite (not precluding a role for other reactions at extremes of temperature), and that the reflectivity is affected by the relative abundance of enriched basaltic material which controls the relative importance of the garnet-out reaction compared to the ringwoodite-out reaction.

3.4.4 Is MTZ Discontinuity Structure a Useful Constraint on MCMs?

Topography of d410 and d660

Fitting the *SS*-precursor observed topographies of d410 and d660 in the Earth from a MCM is a complex combination of thermochemical structure, the correct application of mineral physics tables, and any seismological filtering. I have shown that a very simple seismology-motivated smoothing filter obscures much of the fine detail of topography structure expected from a geodynamical simulation, and have discussed the dominance of thermal structure as a control on d410 and d660 structure rater than composition for moderate variations in basalt content.

The thermal structure of the mid-mantle is dominated by downgoing slabs and upwelling plumes, and is also expected to control the transition zone discontinuity structure. The location and morphology of the downgoing slabs are largely a function of the surface motion history, which in MCMs is imposed at the surface. However, the remainder of the thermal structure is a function of the reaction of the convecting mantle to the imposed downwellings and does vary between geodynamic models with different dynamic structures, particularly variations in rheology and mineral physics. The geodynamic significance of interpretations of the topographies of individual discontinuities is disputed, due to the potential dominance of uncorrected upper mantle velocity structure in the differential travel-times of the SS and SdS phases (e.g., Tauzin *et al.*, 2022). This makes it challenging to interpret poorly fitting (geographically or spectrally) predicted individual topographies in terms of geodynamics.

Variations in MTZ Thickness

As the transition zone thickness is determined by the differential travel times of S660S and S410S, without reference to the SS phase, it should not be sensitive to upper mantle velocity structure variations (e.g. Tauzin *et al.*, 2022). Sadly

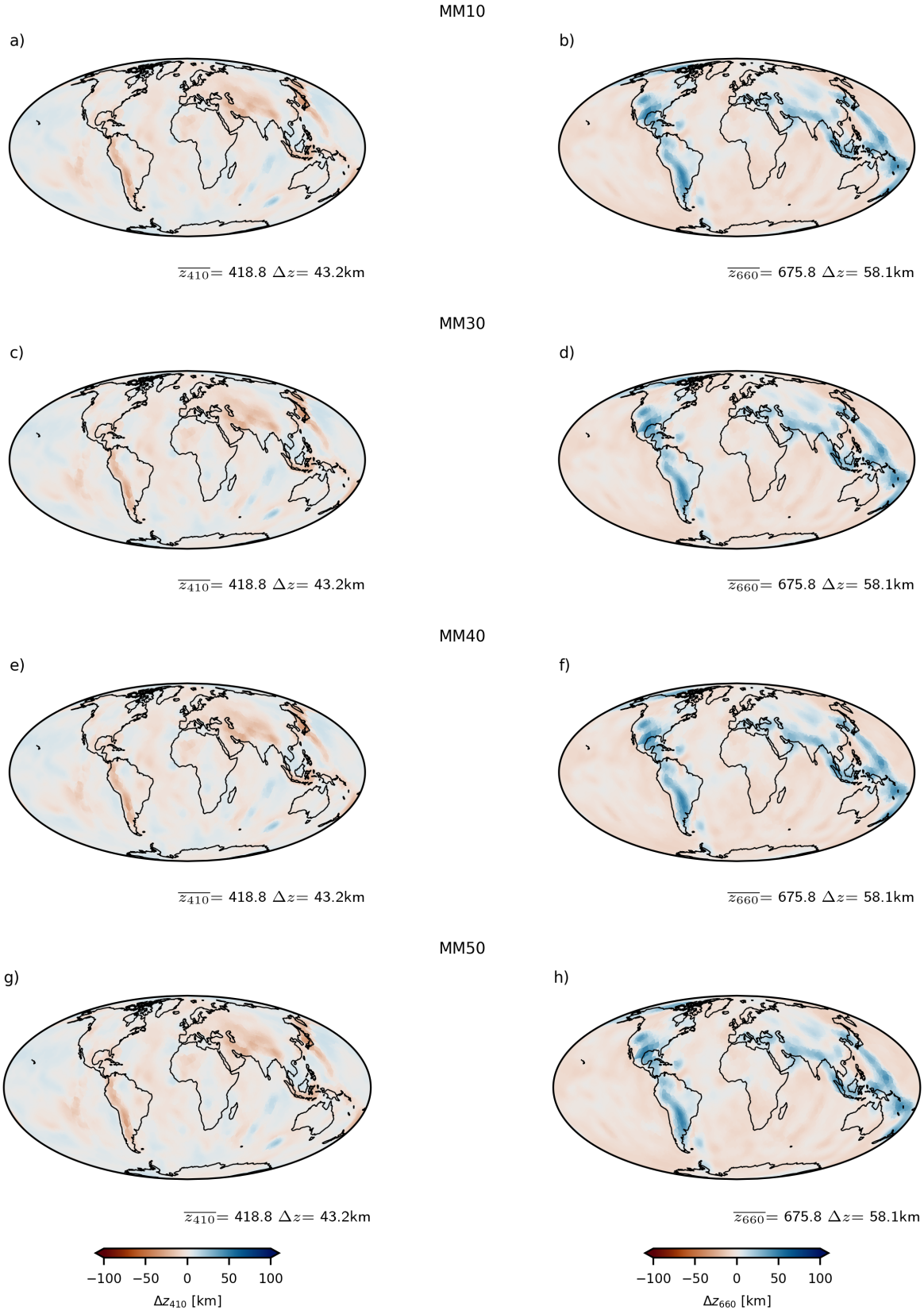

Figure 51: Filtered topography on d410 (*a*–*c*) and d660 (*e*–*g*) for varying global mechanical mixtures MM10 (*a* & *e*), MM30 (*b* & *f*), and MM40 (*c* & *g*) and MM50 (*d* and *h*)

this approach limits the ability to consider separately the thermal structure at 410 and 660km depth, although generally the offset in convective thermal structures between 410 and 660 km depth is generally expected to be small compared to the 1000 km width of the SS precursors' first Fresnel zone. This potentially suggests that variations of transition zone thickness can give a sense of the fit between the simulated and true Earth's lateral thermal structure at the scale lengths SS precursors are sensitive to. However S410S-S660S differential traveltime may not be a simple proxy for MTZ thickness as Koroni *et al.* (2017) showed S410S has significant sensitivity to discontinuity structure at 670 km depth, although this was at longer periods than those used by SS-precursor studies. I do not consider this further here, but note that it is still worth considering d410 and particularly d660 individually in addition to the transition zone thickness.

Reflection Amplitude Structure

Fit to reflection amplitude structure is more complex – as reflection amplitude structure has a strong compositional component, it is sensitive to the longterm evolution and residence of melt-derived heterogeneity in the lower mantle transition zone (Tauzin *et al.*, 2022). The amount and distribution of basaltic material at the base of the MTZ should be a function of the history of melt-production, history of convection, the relative behaviours of enriched and depleted material in the MTZ, other heterogeneities in the mantle, as well as the uncertainties in mineral physics and seismological filtering of the mantle transition zone. However, even in a well mixed mantle such as that produced by this MCM, lateral variations in R_S^d exist, largely driven by thermal structure instead of compositional variations. Therefore, lateral variations in reflectivity may be a more discriminating metric than the discontinuity depth variations, and so a well fitting MCM may not emerge until our knowledge of mid-mantle dynamics, mineral physics and seismology is much improved.

Characteristics of an Earth-like MCM

If an Earth-like MCM were found, the resulting discontinuity structure when filtered for the sensitivity of SS precursors should match the predicted depths of d410 and d660, as well as the amplitude of the discontinuity topographies and transition zone thickness. The spherical harmonic spectra of the predicted discontinuities should peak on degree 1 or 2 and then decay approximately monotonically with increasing spherical harmonic degree. These reflect the correct thermal structure globally (average discontinuity depths) and the

correct lateral variations of temperature (discontinuity topographies). From the predicted reflectivity structure the global distribution of 'bright' and 'dark' spots should match the reported amplitude structure, indicating a reasonable thermochemical structure. However, I anticipate this as a challenging metric to match since the amplitude of reflected waves is a function of the thermal and chemical structures (the latter of which is sensitive to the history of the delivery of compositional heterogeneity to the mantle transition zone), and is possibly more sensitive to the correct 'seismological treatment' than the discontinuity topographies.

Limitations of the Candidate Model

Whilst I do predict the mean depths of d410 and d660 well, I over predict the topography on both discontinuities (by a factor of about 1.7 for d410 and 1.5 for d660). The thickness of the MTZ is slightly over-predicted, as are the range of MTZ thickness variations. Spherical harmonic power is over-predicted at high degree for d410 and d660, and underpredicted at low degree, but the the power of the MTZ thickness variation spectra is overpredicted at all degrees. I suggest this reflects an excessive anti-correlation of d410 and d660 predicted by this method from this MCM compared to those recovered from the Earth using SS-precursors. This suggests a poor match between the thermal structures of this MCM and Earth's. However, there are many regions where the distribution of thick and thin regions of the MTZ is encouraging (see Figure 40).

The comparison between the predicted reflectivity structure and the amplitude structure is less straight-forward. I do not consider the reflectivity of the Earth's surface underside. Similar to the effect of shallow structure on travel times, the reflectivity of the Earth's surface could be highly dependent on regions of partial melt, the thickness of lithosphere or crust, the presence of oceans and icecaps and the roughness of surface topography. However, I do not correctly predict the relationship between the mean reflectivity values of d410 and d660, which the Waszek *et al.* data suggest are similar, but with d410 slightly brighter than d660. I predict d660 as slightly brighter than d410, which might reflect the under prediction of basalt fraction around 660km depth in this simulation.

Whilst this assessment has shown that m_cc_066_u is not an ideal geodynamic model, it highlights the utility of considering the discontinuity topography as I have here, as it has allowed us to take a mantle circulation model (Davies *et al.*, 2025) with reasonable inputted parameters and critically assess its mantle transition zone structure, and potentially informs the parameter space where I might seek a better-fitting model. The caveat of this,

of course, is that I have predicted the seismic discontinuities for a single set of Clapeyron slopes for each reaction at each end-member. Particularly on the ringwoodite-out reaction there is strong disagreement between various studies (computational and experimental) on the expected Clapeyron slope. In the tables, the ringwoodite-out slope is similar to that reported by Ye *et al.* (2014) of -2.5 MPa.K^{-1}, but recent estimates range down to -0.1 MPa.K^{-1} (e.g. Chanyshev *et al.*, 2022). Clearly if the true Clapeyron slope varies significantly from the values in the mineral physics tables used here, the assessments of geodynamic models may vary substantially. Without explicit uncertainties on the mineral physics tables (which may well be extremely high around the phase transformations), it is easy to take the highly uncertain mineral physics tables used here as a point of confidence around which everything else must revolve.

3.5 Conclusion

I predict the topography of d410 and d660 for a thermochemical MCM. The Fresnel Zone of SS precursors has a significant impact on the recovered topography, and when I apply a simple filter to my predicted topographies I can compare the predicted topographies of d410 and d660 to those inverted from SS precursors meaningfully. Lateral chemical variations seem to have a limited role in controlling the topography predicted from a well-mixed thermochemical MCM, although appear important in explaining the discontinuity reflectivity structure.

I assessed a candidate mantle circulation model using its discontinuity topography and reflectivity structure, finding the range of discontinuity depths were too large on both d410 and d660 and that reflectivity structure predicted from this model does not match global observations well. This is interpreted as suggesting a smaller range of temperatures and more recycled heterogeneity in the MTZ than in the geodynamic model considered here. This allowed us to critically assess the discontinuity structure predicted from a MCM, suggesting that either the thermochemical structure is not Earth-like or that the simple treatment of the SS-precursor interaction with the discontinuities we used here is not sufficient. Alternatively, the phase relations assumed in the tables of seismic parameters used to calculate the discontinuities may be wrong, invalidating the assessment of the geodynamic model. I also note that the discontinuities predicted from this geodynamic simulation are much rougher than the sub-horizontal discontinuities recovered by SS-precursor studies from the Earth and expect this could have some impact on the observation of the discontinuities.

Data Availability

The thermochemical field of the mantle circulation model m_cc_066_u is available for download via Zenodo (Davies *et al.*, 2024, available at https://doi.org/10.5281/zenodo.13960492), and similar mineral-physics tables are released there. The topographies were calculated using Python3 codes 'TERRA-tumulus' released publicly here: `https://doi.org/10.5281/zenodo.15630096`. I compared my topographies to the model released by Waszek *et al.* (2021) available via the ISC's Seismological Dataset Repository (available at `https://doi.org/10.31905/7M3LMG8X`). All maps have been produced using Cartopy (Met Office, 2010). All colourmaps are taken or adapted from (Crameri *et al.*, 2020). All spherical harmonic routines accomplished using pyshtools Wieczorek and Meschede (2018).

Chapter 4

Constraining Mantle Circulation Models in the Mid-Mantle Using Predicted Seismic Discontinuity Topographies

Abstract

As discussed in chapter 3, the topography on d410 and d660 is potentially a useful constraint on geodynamic models, sensitive to both the dynamics in the mid-mantle and the dynamics of the upper and lower thermal boundary layers that control the positions and geometries of upwellings (warm anomalies) and downwellings (cool anomalies) in the mid-mantle.

In order to evaluate the discriminating power of the predicted topographies on mantle dynamics, a suite of mantle circulation models are presented where CMB temperature, initial compositional condition and radial viscosity structure are varied. The MCMs are then evaluated with reference to the d410 and d660 structure of the Waszek *et al.* (2021) model. None of the MCM-predicted topographies provide a good match with all aspects of observed seismic discontinuity structure, but an improved match is observed on d660 with models where the viscosity is reduced near 670 km depth. Various putative explanations (including the overall vigour of convection, enrichment of the lower MTZ in basalt affecting d660, metastable olivine affecting d410, and some complications arising from the sensitivity of the SS-precursor) for the correlation of d410 and d660 are evaluated, although none of the simple implementations reproduce the positive correlation recovered by modern seismology.

4.1 Introduction

In chapter 3 I illustrated how d410 and d660 topography were controlled by the thermochemical structure of the mid-mantle. It is worth briefly considering what parameters of a geodynamic model we could choose to change to affect the thermochemical structure of the mid-mantle.

First, let us consider the upwellings and downwellings that traverse the mantle from the lower and upper thermal boundary layers respectively. The temperature of the Earth's surface is well known, and within 50 K or so, has remained constant over recent geological history (Judd *et al.*, 2024). The position of downwellings in the mantle today is controlled by the location of subduction zones at the Earth's surface (e.g. Bunge *et al.*, 2002; Goes *et al.*, 2008). Modern plate reconstructions are reasonably consistent over the last few hundred million years (e.g. Müller *et al.*, 2022), suggesting that our knowledge of the past locations of subduction is well constrained. However, there are regions where there are significant uncertainties on plate and trench motions, particularly in the Pacific domain (e.g. Chen *et al.*, 2025), which given the control of plate and trench motions on downwelling stagnation (e.g. Tsuchida and Kameyama, 2020) may prove problematic. Therefore, I do not vary the surface temperature or velocity boundary conditions in this suite of simulations. The lower boundary layer is much less well constrained. Firstly, the thermal boundary condition is not well known (e.g. Deschamps and Cobden, 2022). This is important since this would control the maximum temperature in the mid-mantle in the strong upwellings and, since the minimum is largely set by the fixed surface temperature, the range of temperatures in the mid-mantle. This could also affect the compositional structure since the excess temperature of a plume controls its buoyancy, and therefore its ability to bring compositionally distinct, intrinsically dense material out of the deep mantle and into the upper mantle and basalt density filter. The CMB temperature therefore will be varied in the simulations shown in this chapter. There is no knowledge of the velocity history along the lower boundary layer, but piles of compositionally distinct material can act to guide where upwelling plumes initiate (e.g. Steinberger and Torsvik, 2012) and influence their excess temperature (e.g. Steinberger *et al.*, 2025). The presence or lack of piles (aka BMSs [basal mantle structures]) and particularly their stability over geological time is a contentious subject in geodynamic community, but their presence is considered a variable of interest here.

Within the convecting mantle, the form of the upwellings and downwellings is a function of the rheology and of the strength of any counter-convective

forcings from mid-mantle phase transitions. Due to the nature of the method used to generate the tables of seismic properties used in this work, we cannot vary explicitly (say) the Clapeyron slope of the post-spinel reaction for the seismological calculations, although this would be trivial to vary for the geodynamic calculations. Therefore this current experimental set-up is not intrinsically self-consistent. However, the values of the density change and Clapeyron slopes of the Ol-out and Rw-out reactions are set in the TERRA simulations so that they are similar to those in the mineral-physics tables.

Variations to rheology are also of interest. As discussed in Chapter 1, beyond the upper mantle, the radial viscosity structure is poorly constrained (Mitrovica and Forte, 2004; Steinberger and Calderwood, 2006), so we consider MCMs with various plausible mid- and lower-mantle viscosity profiles. As a reference viscosity structure, we will consider a "classic" structure that has a factor of 30 jump at 660 km depth (e.g. Hager *et al.*, 1985), and no further jumps in viscosity until a weakening directly above the CMB. Another popular viscosity structure (Steinberger and Calderwood, 2006) involves a smooth rise (or "hill") in viscosity radially through the mid mantle, and other authors instead favour a jump, but deeper at 1000 km depth (e.g. Fei *et al.*, 2023). Rudolph *et al.* (2015) suggest that a low viscosity channel could exist beneath the d660, which they report affects the radial correlation spectra of V_S anomalies predicted from geodynamic models between 1000 and 400 km depth. Mao and Zhong (2018) As well as these variations from the reference model in the mid-mantle, speculatively the reference model is varied by weakening the lowermost few hundred kilometres of the mantle, to encourage the initiation sites of upwellings to be less determined by the position of imposed downwellings. This is motivated by reference to suggestions that post-perovskite (which occupies much of the lowermost mantle) may be weaker than Bridgmanite (e.g. Li *et al.*, 2014). It would also be interesting to vary the temperature- and strain-dependence of the rheology, but given the limited ability of TERRA to resolve such lateral viscosity variations, that is not done here.

The low resolution of the mantle circulation models used here means that the simulations are not run at Earth-like vigour or realistic reference viscosities. This low resolution was chosen to generate a larger suite of simulations with different parameters to illustrate the impact of changing them on d410 and d660, but this is traded off against a higher reference viscosity and less vigorous convection than on Earth. This reduced resolution also means that I am unable to consider here the impact of a thin, weak aesthenosphere that Cerpa *et al.* (2022) have shown to be important in controlling slab morphologies. However, the present study does allow us to consider some potential controls on

d410-d660 topographies, including most of the common geodynamic explanations of the d410-d660 positive correlation in this discussion, potentially allowing us to shed some light on that conundrum.

4.2 Methods

4.2.1 Geodynamic Models

I ran 25 simulations using the mantle circulation code TERRA, which solves the stokes equations (1.3-1.5) in a spherical shell. The simulations presented here were ran at "mt= 128" resolution – i.e. a ~ 45 km grid spacing in the mid-mantle. These are comparatively simple models, with a relatively high reference viscosity, which may make the structure excessively radial. This increased viscosity means that convective flows are broader and have a higher temperature anomaly to overcome the viscous resistance, which will effect the lengthscale and amplitude of the predicted topography. The rheology law employed here is extremely simple, being newtonian with only radial and thermal variation. These models do not allow for strain localisation in the crust and lithosphere, instead relying on the imposed surface velocity boundary condition to force localised downwellings, as characterise the Earth's surface. Together, these model conditions mean that I do not expect a good fit from any individual MCM presented here, but rather hope to illustrate the variety of different topography structures that might be generated with different input geodynamic parameters. The constant parameters in this suite of simulations are summarised in Table 7.

Rheology

As the d410-d660 structure is sensitive to the morphology of thermochemical structure, the rheology is of particular interest. Additionally, we require the thermal structure of our simulations to be well resolved in the upper mantle, so for this resolution are forced to take a comparatively high reference viscosity of $\eta_0 = 1 \times 10^{22}$ Pa.s. Temperature- and depth- dependent rheology in TERRA is implemented such that it varies

$$\eta(z, T) = \eta_0 f_r(z) e^{V_A Z' - E_A T'} \tag{4.1}$$

with η_0 being the reference viscosity, $f_r(z)$ is a depth-dependent prefactor, varied here, V_A is a non-dimensionalized activation volume, Z' is the non-dimensionalized depth, E_A is the non-dimensionalized activation energy,

Symbol	Parameter	Value	
ρ_0	Reference Density	$4500\ \mathrm{kg\,m^{-3}}$	
α	Thermal Expansivity	$2.5 \times 10^{-5}\ \mathrm{K^{-1}}$	
k	Thermal Conductivity	$4\ \mathrm{Wm^{-1}\,K^{-1}}$	a
C_P	Specific Heat Capacity	$1100\ \mathrm{J\,kg^{-1}\,K^{-1}}$	b
T_{Surf}	Surface Temperature	300 K	
γ_{410}	$\frac{dP}{dT}$ of $Ol \rightarrow Wd$	$+1.5\ \mathrm{MPa\,K^{-1}}$	
γ_{660}	$\frac{dP}{dT}$ of $Rw \rightarrow Brm + Pc$	$-1\ \mathrm{MPa\,K^{-1}}$	
η_0	Reference Viscosity	$4 \times 10^{22}\ \mathrm{Pa\,s}$	
E_A	Non-dimensionalized Activation Energy	1.75	c
V_A	Non-Dimensionalized Activation Volume	1	
$\frac{\Delta\rho_{410}}{\rho_{410}}$	$Ol \rightarrow Wd$ density change	6.37 %	
$\frac{\Delta\rho_{660}}{\rho_{660}}$	$Rw \rightarrow Brm + Pc$ density change	9.08 %	

[a] (p. 122, Clauser and Huenges, 1995)
[b] (Panton, 2020)
[c] Dimensionalized meaning discussed in Section 1.3.5

Table 7: Parameters held constant in mantle circulation models

and T' is the non-dimensionalized temperature. As noted the radial viscosity variation ($f_r(z)$) is of interest here, and the applied radial viscosity structures are shown in Figure 53a. Viscosity structure 19 is our reference with a "canonical" 30× jump at 660 km depth. Viscosity structure 9 has a 'hill' in viscosity in the lower mantle, inspired by Steinberger and Calderwood (2006). Viscosity structure 18 is a modification of viscosity structure 19 by the reduction of viscosity in the lowermost mantle. Viscosity structures 12 and 15 have a 30× jump in viscosity around 1000 km depth, but have different plate scaling factors – see Table 8. Viscosity structure 16 denotes the simulation with a low viscosity channel at 660 km depth. Whilst TERRA is a very capable code, its ability to handle lateral variations in viscosity structure is limited. Although adaptations have recently been implemented (e.g. Plimmer *et al.*, 2024) due to the possibility of developing fine, under-resolved, thermal structure, the temperature dependence is maintained at a moderate value of non-dimensionalized activation energy of $E_A = 1.75$, and a non-dimensionalized activation volume of $V_A = 1$. This rheology law underestimates the lateral variation in viscosity, as it understates the temperature dependence of viscosity, does not include weakening effects due to strain-rate (e.g. Gülcher *et al.*, 2022) or phase transformation (e.g. Agrusta *et al.*, 2014) and therefore is a crude approximation to the more complex rheology of the Earth's mantle.

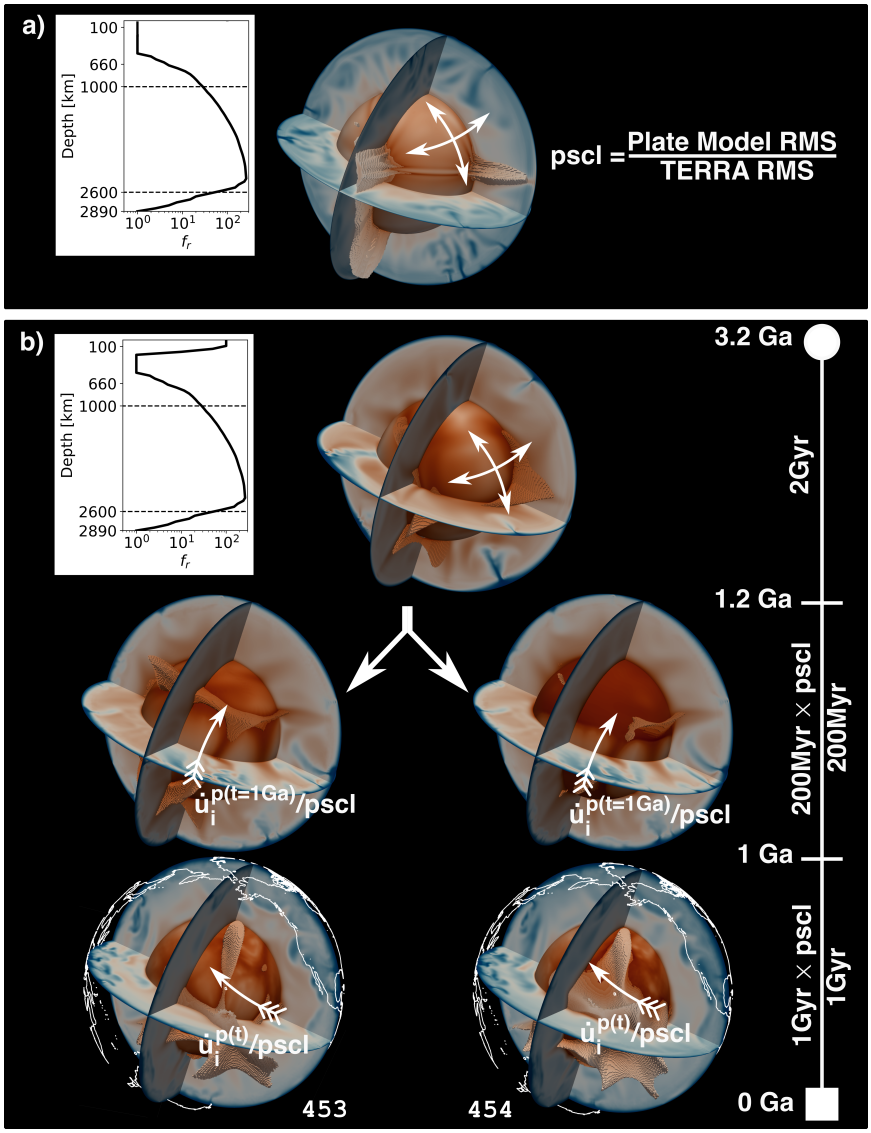

Figure 52: Summary diagram of spin-up processes for mantle circulation modelling. *a)* Procedure for the calculation of the plate scaling factor (pscl). A TERRA convection simulation (free-slip boundary condition indicated by perpendicular double-headed arrows), with the same reference and radial viscosity structure (but with viscous lithosphere removed, compare f_r in b) is ran to find an average RMS surface velocity, to find the plate scaling factor against an RMS velocity for Earth. *b)* Procedure for Mantle Circulation Modelling (Bunge *et al.*, 1998). *Top panel*; an initial thermal structure is generated (see text) in a 2 Gyr long thermal mantle convection model. This is used to initiate MCMs with two different compositional initial conditions, *middle panel*; one with a primordial layer initial condition (454, right, observe region on CMB with high temperature within pile), and one uniform (453, left). These are run for 200 Myr of scaled time with the first plate stage of the Müller *et al.* (2022) plate motion model, indicated with the single indicative fletched arrow on the surface. *Bottom row*, the modern-day thermochemical structure is produced by allowing the surface boundary condition to evolve through the different plate motion stages ($\dot{u}_i^{p(t)}$), scaled by the plate scaling factor. *Right* Timeline showing the different periods of Earth evolution the different stages of mantle circulation model simulate, left model time, right scaled time. Scaled ages where the models are visualised here and restarted shown in Ga

Model Initiation and Set-up

The TERRA mantle circulation models were run with a 3-step process, as is common for this class of model (e.g. Panton *et al.*, 2025), see Figure 52. First an initial temperature field was generated using a convection simulation without any compositionally distinct material. For all the simulations presented here, thermal fields were generated using viscosity structure 9, inspired by the structure inverted by Steinberger and Calderwood (2006). Care was taken to ensure a consistent internal heating rate[1] and CMB temperature between this 'spin-up' stage and the next step (Figure 52b, top row). This first stage was run for 2Gyr when the modelled mantle has reached thermal quasi-steady state. The simulated mantles are then primed for the time-varying surface condition by the equivalent of 200Myr of the first stage (that represents the tectonic system 1 Gyr ago) of the Müller *et al.* (2022) plate motion history (Figure 52b, middle row). This plate motion history is scaled by a plate scaling factor (see Table 8) that slows the boundary condition motions down to the surface velocities of a convecting mantle with the same rheological structure, but without a lithosphere (Figure 52a). This has proved necessary for all MCMs following Bunge *et al.* (1998) in order to prevent downwellings being forced into the mantle interior faster than it can flow. This produces unphysical temperature anomalies around downwellings, leading them to be un-resolved. The plate scaling factors used here are comparatively large compared to other simulations at similar vigour in order to suppress these instabilities in the model mantle under fast-spreading ridges in particular in the present day Earth. I use a reference surface RMS velocity of 8 $\mathrm{cm.yr^{-1}}$, motivated by the faster periods in the Müller *et al.* (2022) plate motion model (their Figure 7b). This plate scaling means the total runtime of the simulation is extended by a factor of the plate scaling factor, and the timescale of radiogenic decay is adjusted also. It is during this priming stage that the particles are initiated according to the compositional initial condition. Finally the model is restarted, and the surface boundary condition is allowed to evolve according to the Müller *et al.* (2022) plate motion history from 1 Gyr ago to the present day (Figure 52b, bottom row).

The Suite of Simulations

Three key variables have been discussed above; CMB temperature, the presence of a BMS and the radial viscosity structure. These are varied together. The

[1]In the spin-up convection simulations a time-dependent heating rate was used, initiated from $3.2Ga$ ($1Gyr$ circulation + $0.2Gyr$ preconditioning + $2Gyr$ convection). In some development models, this care wasn't taken and primordial layers with extremely high buoyancy numbers were destroyed during the convection simulations.

simulations are listed in Table 8, and the parameter space is sketched in Figure 53. The average CMB temperature at the end of the simulation $T_{MTZ^+}^{t=0\text{Ma}}$, defined just above the CMB at 406 km depth is listed, since it is worth considering if these simulated mantles have a comparable adiabat to the Earth's. Previous workers (e.g. Ritsema *et al.*, 2009; Waszek *et al.*, 2021) have used the topography of SS-precursors mantle potential temperature around 1630 K. Assuming an adiabatic gradient of $\sim 0.4K.km^{-1}$ (e.g. Poirier, 2000, p. 204), this is about 1790 K at the top of the MTZ. This is warmer than all but the hottest models presented here, with simulations 453, 455, 456, 457, 461, 463, 483, 484, 485, 486 within 100 K. Petrological estimates on the mean potential temperature are substantially lower, with estimates from mid-ocean ridges (e.g. Li *et al.*, 2025) producing an estimate of 1350 ± 12 °C $\equiv 1623$ K of potential temperature (1785 K at the top of the MTZ), in loose agreement with estimates from MTZ thickness. Recent work using a global stack of SS- and PP-precursors favoured the petrological estimate of mantle potential temperature (Yu *et al.*, 2023), as did seismological work using V_S anomalies in the upper mantle beneath mid ocean ridges (Bao *et al.*, 2022).

4.2.2 MTZ Topography Calculation and Comparison

Discontinuity topography is calculated using the regional mechanical mixing procedure described in Chapter 3, and then filtered using the bounce-point spherical cap filter (see section 3.2.4) to allow a fair comparison with the Waszek *et al.* (2021) discontinuity topography model. In the models which are initialised with a primordial layer, this material (which has a C-value of 2) is treated as having a basaltic composition for the purposes of calculating the seismic structure, and this motivates $B_{\text{Pri}} = B_{\text{Bas}} = 0.5$ in most of the simulations with a primordial layer (Table 8). Here I use tables calculated from the Stixrude and Lithgow-Bertelloni (2005, 2011, 2022) datasets, and the compositions listed in Table 6, corrected for anelasticity using the model 'Q7g' (Goes *et al.*, 2004; Maguire *et al.*, 2016). In accepting a single set of mineral physics, however, I neglect to include the significant uncertainties that may completely invalidate any assessment of how Earth-like any individual model is. However, the lateral distribution of uplifted and depressed regions of the mantle is unlikely to be severely affected, and the principal effects may then be in scaling the amplitude of the predicted topography and of the spherical harmonic spectrum. In principle, changes in the Clapeyron slope will have an effect on the morphology of downwellings and upwellings, but all recent estimates are lower than the ~ -3 MPa.K^{-1} suggested by e.g. Wolstencroft and Davies (2011) for a

Case number	Viscosity Profile	T_{CMB} [K]	$T_{MTZ^+}^{t=0\text{Ma}}$ [K]	Plate Scaling Factor	B_{Bas}	B_{Pri}	Primordial Layer Thickness [km]
453	9	3800	1765	5.6	0.5	·	·
454	9	3800	1608	5.6	0.5	1.04	150
455	9	3600	1698	5.6	0.5	·	·
456	9	4000	1796	5.6	0.5	·	·
457	9	3600	1575	5.6	0.5	1.04	150
458	9	4000	1642	5.6	0.5	1.04	150
459	12	3600	1659	5.9	0.5	·	·
461	12	3800	1718	5.9	0.5	·	·
462	12	3800	1585	5.9	0.5	0.5	150
463	12	4000	1780	5.9	0.5	·	·
477	15	3800	1472	4.7	0.5	·	·
479	16	3800	1459	5.3	0.5	·	·
480	16	3800	1611	5.3	0.5	0.5	150
482	18	3800	1523	4.6	0.5	·	·
483	18	3800	1693	4.6	0.5	0.5	150
484	18	4000	1888	4.6	0.5	·	·
485	18	4000	1742	4.6	0.5	0.5	150
486	18	3600	1782	4.6	0.5	·	·
487	18	3600	1656	4.6	0.5	0.5	150
488	19	3600	1677	5.9	0.5	·	·
489	19	3600	1545	5.9	0.5	0.5	150
490	19	3800	1734	5.9	0.5	·	·
491	19	3800	1591	5.9	0.5	0.5	150
492	19	4000	1789	5.9	0.5	·	·
493	19	4000	1643	5.9	0.5	0.5	150

Table 8: Simulations ran to compare to d410-d660 discontinuity structure.

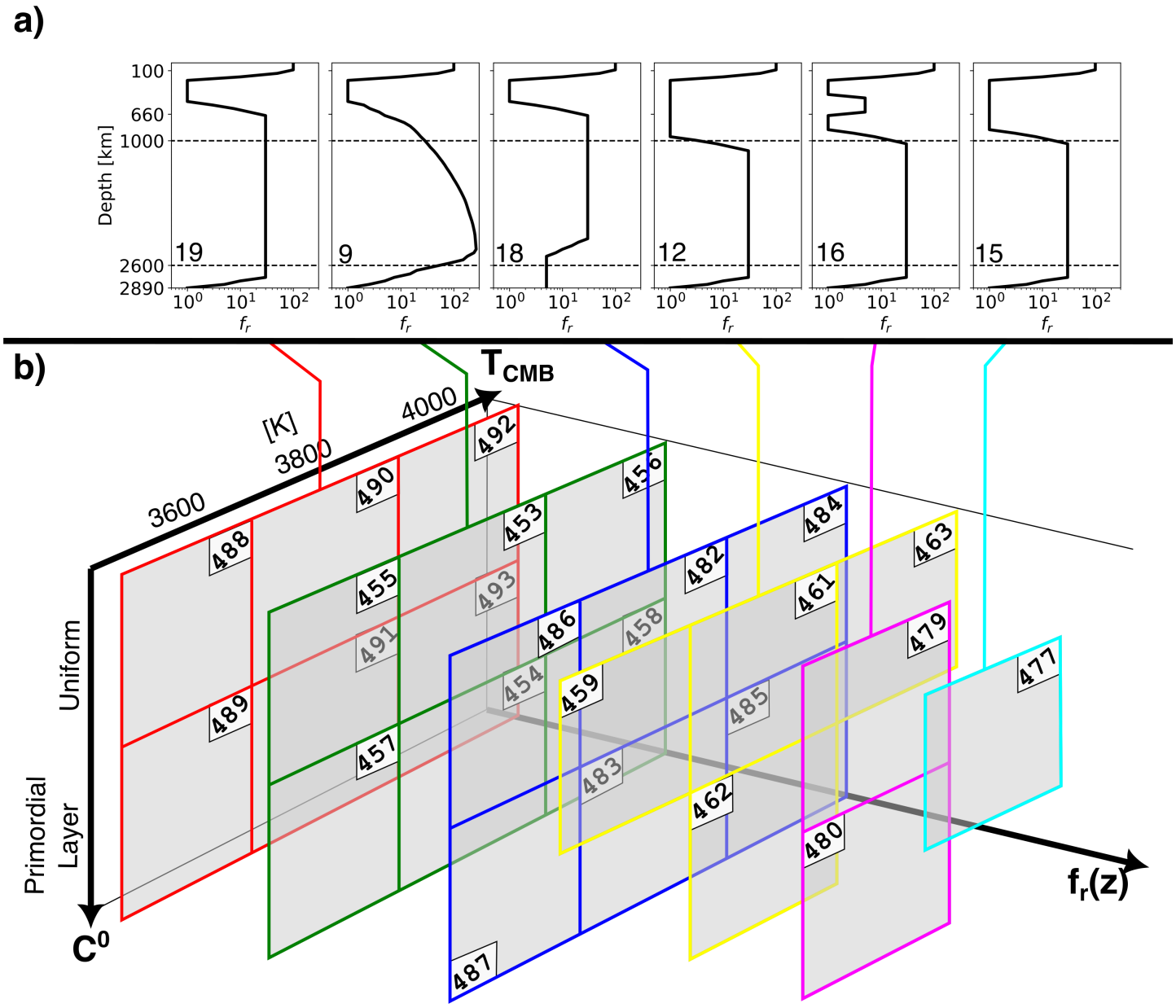

Figure 53: Summary of parameter space varied in the suite of simulations presented here. *a)* f_r (radial viscosity prefactor, see Eq. 4.1) of the viscosity structures used in this simulation suite. *b)* Sketch of the distribution of simulation runs in T_{CMB}, viscosity structure, C_0 (initial composition structure).

change of dynamic regime so such changes are not likely to be so very dramatic.

4.3 Results

4.3.1 Geodynamic Models: Thermochemical Structures

Before discussing the seismic discontinuity structures that the suite of models listed in Table 8 produce, I first describe the thermochemical structures produced by the geodynamics models. Illustrating each model completely is not possible here, but as the kinds of dynamics do not vary so much between the simulations with different T_{CMB} but the same viscosity structure and chemical initial condition, I illustrate in Figures 54, 55 and 56 the thermochemical structure for the simulations with $T_{CMB} = 3800$ K.

Simulation 490 and 491 (visualised in panels e and f, and g and h respectively of Figures 54 and 55) had the 'reference' viscosity structure (no. 19). Cold downwellings descend through the mantle sub-vertically from their trenches, but with the different histories of surface motion, a variety of slab morphologies are formed (compare the downwellings beneath South America on the equatorial slice and beneath the Himalaya on the 90$^{\text{th}}$ meridian in Figure 54e). In 490, large plumes rise from hot linear upwellings from the CMB, whereas in 491 they rise from hot domains centred beneath Pacific and Africa. These hot domains in simulation 491 are focused on large structures of enriched primordial material. In the African domain a 'superplume' reaches across the mantle of simulation 491, delivering enriched material to the basalt density filter, and in the Pacific large plumes are cored by primordial material delivered from the pile on the CMB.

Simulation 453 and 454 (visualised in panels m and n, and o and p respectively of Figures 54 and 55) had viscosity structure no. 9, which has a viscosity 'hill' in the mid-mantle (Figure 53a). Due to the increased mid-mantle

Figure 54: Thermal structure of indicative simulations visualised on three planes (along the equator, prime/180$^{\text{th}}$ meridians and the 90$^{\text{th}}$/270$^{\text{th}}$ meridians), a sphere 40 km above the CMB and on 'voxels' 500 K above the average temperature at that depth, with (*third and fourth columns*) and without (*first and second columns*) primordial layer in initial condition, visualised towards the Atlantic-Africa (*first and third columns*) and Pacific (*second and fourth columns*). *a, b)* Simulation 482, *c,d)* Simulation 483, *e, f)* Simulation 490, *g,h)* Simulation 491, *i, j)* Simulation 479, *k,l)* Simulation 480, *m, n)* Simulation 453, *o,p)* Simulation 454

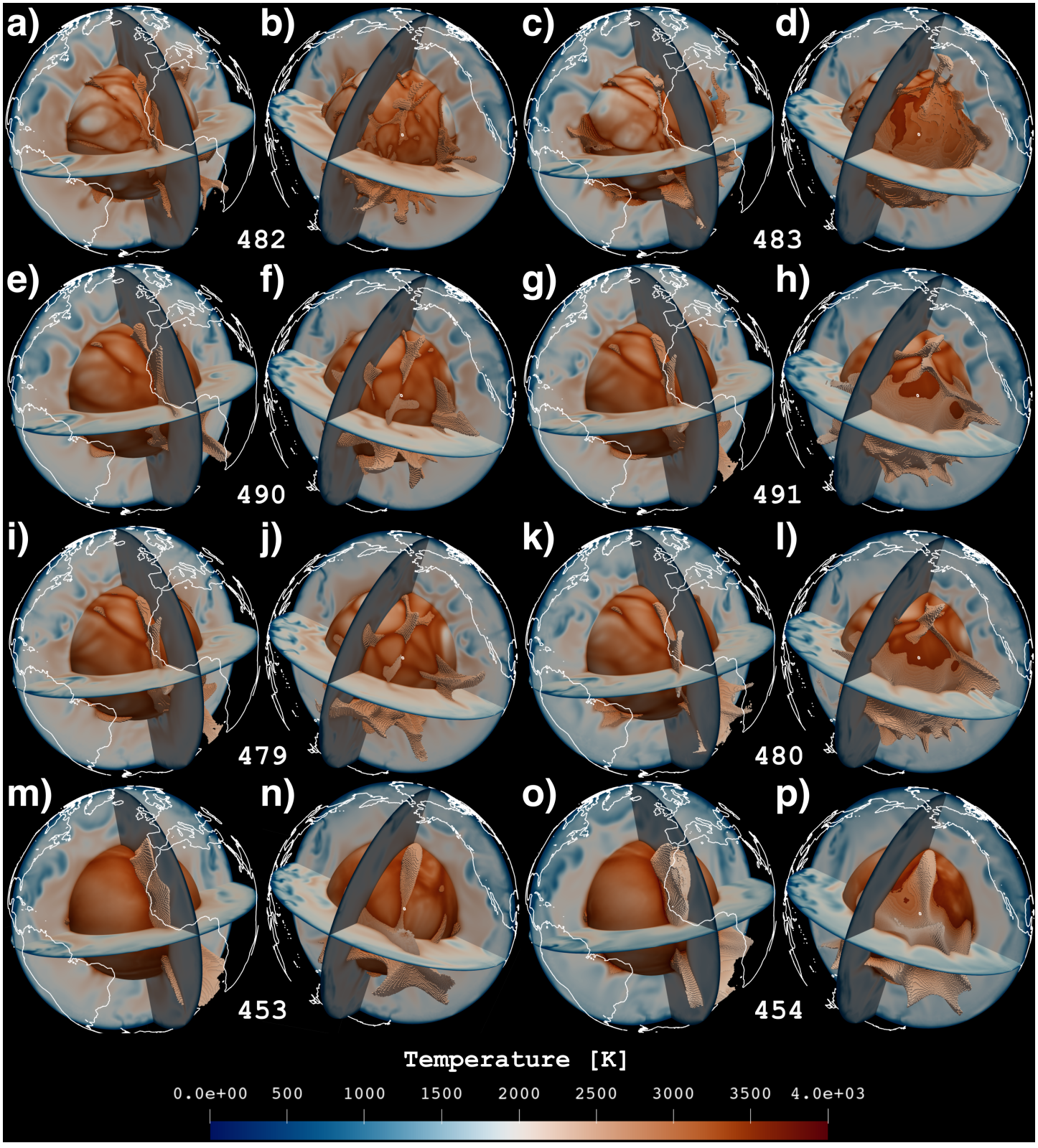
a)
b)
c)
d)
482
483
e)
f)
g)
h)
490
491
i)
j)
k)
l)
479
480
m)
n)
o)
p)
453
454
Temperature [K]
0.0e+00
500
1000
1500
2000
2500
3000
3500
4.0e+03

viscosity, downwellings from the upper mantle are more likely to stagnate, and the upwelling convection pattern is dominated by a couple of hot sheets that rise from the CMB to the upper mantle, before focussing into columns in the lower viscosity environment there. As this viscosity structure weakens in the lowermost mantle, basaltic heterogeneity is segregated in the lowermost mantle of simulation 453, particularly in the Pacific domain, forming 'clots' that sit above the CMB instead of piles on it. In places, this enrichment is then carried up into the mid-mantle by the upwellings. The form of downwellings is nearly identical between 453 and 454, and in the African domain the upwellings also form sheets with a similar morphology. In the Pacific domain, however, the primordial material forms a pile that guides upwellings around its edge, forming a crown-like region of warm material in the lower mantle.

Simulation 479 and 480 (visualised in panels i and j, and k and l respectively of Figures 54 and 55) had viscosity structure no. 16, which has a low viscosity channel (LVC) between 660 and 1000 km depth (see Figure 53a). This does seem to change the morphology of downwellings, for instance the flat-subduction beneath South America is reproduced here (e.g. Pons *et al.*, 2022), which is not the case for the other viscosity structures illustrated in Figure 54. Generally slabs seem to deflect away from their trenches more often than without the weak layers in the rheology and do not thicken so much (compare the subduction beneath the Himalaya in Figure 54f and j). Upwellings seem to have a similar morphology in the lower mantle as those in the simulations with the reference viscosity structure. Again, comparing with simulations 490 and 491, the chemical structures are reasonably similar, however in simulation 480 (Figure 55 k and l), the low viscosity at the base of the MTZ allows compositionally enriched material to more efficiently accumulate in the basalt density filter.

The final viscosity structure illustrated in Figures 54 and 55 is viscosity structure 18 which has a weakened lowermost mantle (see Figure 53), which is represented by simulations 482 and 483 (visualised in panels a & b and c & d respectively). The thermal structure of these simulations is comparatively distinct to those observed in the other simulations in Figure 54. The upwellings are more different than the downwellings are though; for this viscosity structure they resemble more the textbook 'mushroom head' plumes than the hot upwelling sheets found in the other simulations. The downwellings are a bit more deflected in the upper mantle than in the reference case, although they seem to fall much more convincingly vertically into the lower mantle, where they flow out along the CMB, clearly sweeping structures in the lowermost mantle. In the compositional structure, the low viscosity in the lowermost mantle allows the formation of piles of enriched basaltic material in the Pacific and African

domains of simulation 479, as well as allowing some accumulation in the basalt density filter in the Pacific of simulation 479 (see Figure 55b). The low viscosity of the lowermost mantle in simulation 480 promote a distinct degree 1 compositional structure, with a large pile extending over the Pacific and Indian Ocean domains of the CMB, delivering enriched material to the mid-mantle.

The thermochemical structure of simulations with an increase in viscosity around 1000 km depth are illustrated in Figure 56. Simulations 477 (Figure 56 a-d) and 461 (e-h) are very similar in their set-up – the viscosity jump in 462 is slightly deeper by $\sim$ 100 km, but the key difference is in the scaling factor applied to the plate motion history, which is such that plate motions in 462 are slowed down by a factor of 5.9 (the same as the reference simulation), whereas the motions in 477 are slowed by a factor of 4.7. Generally the thermal structures between these two simulations are extremely similar, although the downwellings are a little more continuous in simulation 477 than 461. Whilst the exact position and geometry of plumes is different between the two simulations, they are very similar. There are more significant differences when we compare the compositional fields – simulation 477 appears to be more extensively differentiated than 461, with more extensive regions of deep green and purple enriched and depleted regions than in the less-scaled case. Perhaps this is due to more decompression melting in simulation 477 than 462, meaning more mantle is processed but not as far as in 462, meaning that the depleted regions are less depleted so can melt again.

Simulation 462 (Figure 56 i-l) has the same set-up as 461, but with the imposed enriched layer initial condition. Similar to the other cases with this initial condition, this guides the position of upwellings beneath the Pacific. The high viscosity lower mantle combined with the reduction of viscosity around the basalt density filter promotes the delivery of material from the lower mantle to the basalt density filter, which in this model results in large sheets of enriched material sitting around 1000 km depth, particularly over the pile centred on the Southern Pacific.

Figure 55: Chemical structure of indicative simulations visualised on three planes (along the equator, prime/180$^{\text{th}}$ meridians and the 90$^{\text{th}}$/270$^{\text{th}}$ meridians), a sphere 40 km above the CMB and on 'voxel' with a C-Value above 0.4, with (*third and fourth columns*) and without *first and second columns* primordial layer in initial condition, visualised towards the Atlantic-Africa (*first and third columns*) and Pacific (*second and fourth columns*). *a, b)* Simulation 482, *c,d)* Simulation 483, *e, f)* Simulation 490, *g,h)* Simulation 491, *i, j)* Simulation 479, *k,l)* Simulation 480, *m, n)* Simulation 453, *o,p)* Simulation 454

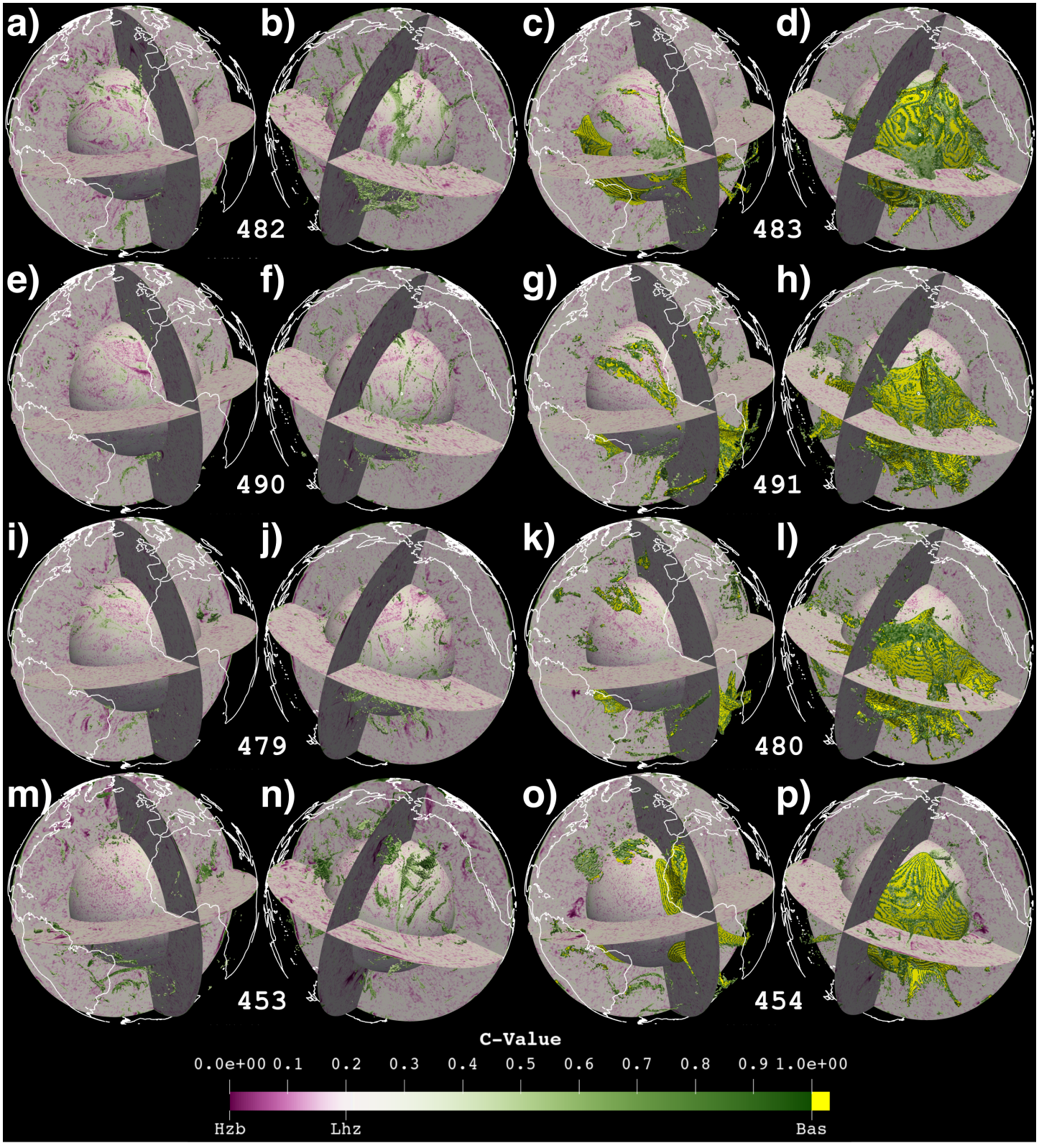
a)
b)
c)
d)
482
483
e)
f)
g)
h)
490
491
i)
j)
k)
l)
479
480
m)
n)
o)
p)
453
454
C-Value
0.0e+00 0.1 0.2 0.3 0.4 0.5 0.6 0.7 0.8 0.9 1.0e+00
Hzb
Lhz
Bas

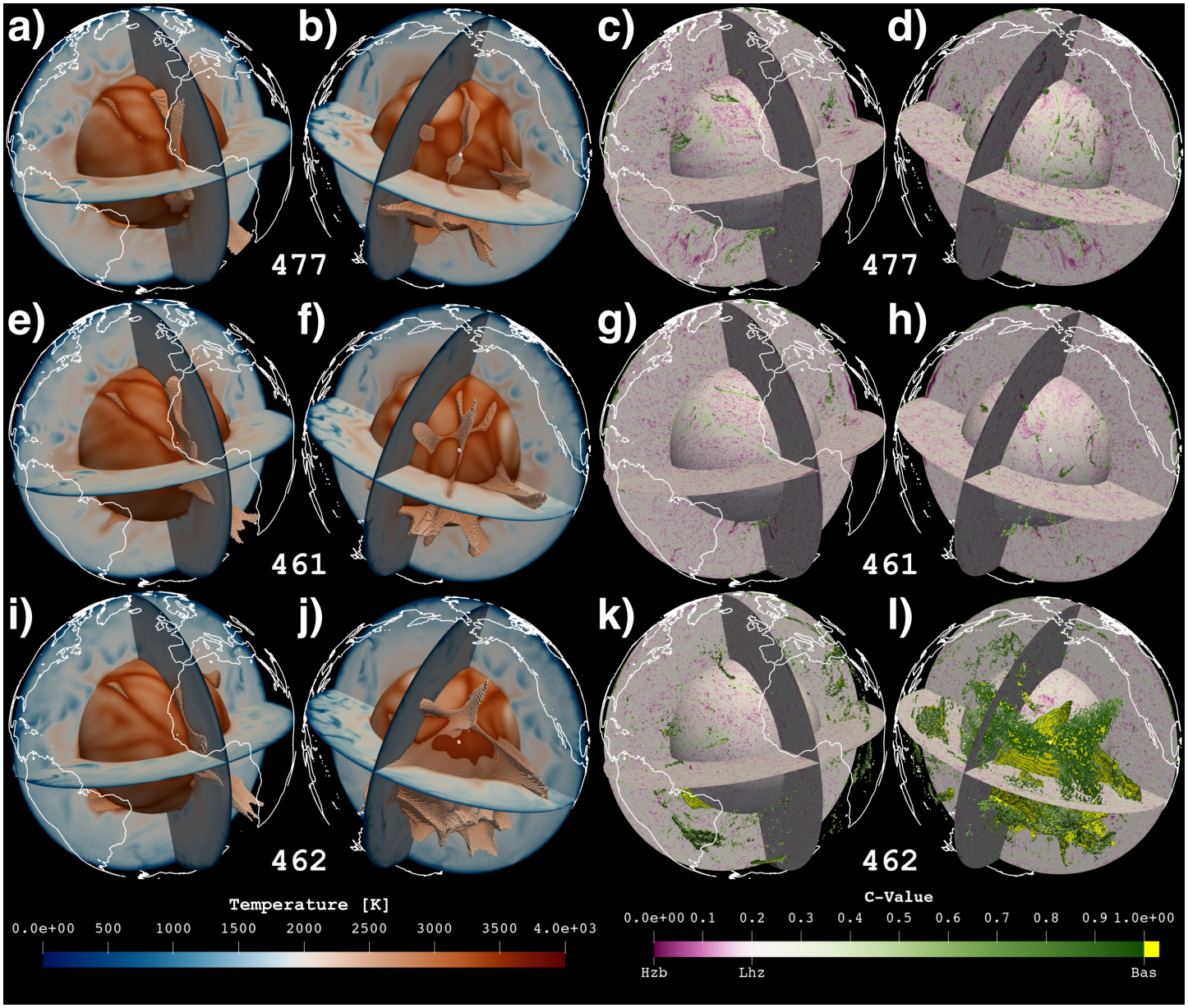

Figure 56: Thermal (*first and second columns*) and Chemical (*third and fourth columns*) structure of simulations where there is a viscosity jump around 1000 km depth, visualised as in Figures 54 and 55. Simulation *a-d)* 477, *e-h)* 461, *i-l)* 463.

4.3.2 Discontinuity Topographies

Prior to presenting the d410-d660 structure predicted for the mantle circulation models above, for reference, I plot the discontinuity structure reported by three recent studies (Houser, 2016; Guo and Zhou, 2020; Waszek *et al.*, 2021) in Figure 57. These seismically recovered structures are plotted on the same colour-bar used to plot the predicted topographies in the rest of the chapter, which will highlight the excess topography predicted from the MCMs. The Waszek *et al.* (2021) model on d410 is characterised by a depressed discontinuity across the Pacific domain, and an uplifted discontinuity across the Atlantic-Africa-Indian Ocean region. This is reflected in the dominant °1 signal in the spherical harmonic spectra. Regionally there are a couple of depressions in the North and South Atlantic, as well as beneath India and central Siberia, which are expressed in the low power, high spherical harmonic degree structure out to $\sim^{\circ}$ 15. On d670 there are strongly elevated regions beneath the North Atlantic, East Africa and Antarctica. Regionally, very strong depressions exist in the model beneath the Western Pacific subduction zones, as well as beneath South America where the Nazca Plate is subducted. Additionally, there are several strong depressions on d670 that are not associated with recent subduction, for instance offshore of Western South America and around North-East Africa. When the spherical harmonic spectra of Waszek *et al.*'s d670 model is plotted, there is a strong peak at °2, with significant power persisting to $\sim^{\circ}$ 15. The spherical harmonic power spectrum of MTZ thickness variations mirrors the peak on °2 seen on d670 (d410's spectra peaks on °1), with more significant power on the intermediate spherical harmonic degrees $\sim^{\circ}$ 7. The correlation between d410 and d660 may also be of interest. The correlation between the discontinuity structures expanded out to each spherical harmonic degree is shown in Figure 57j, with the Waszek *et al.* (2021) model showing a strong positive correlation at every spherical harmonic degree, although for low spherical harmonic degrees ($l < 3$), this is not statistically significant.

A subset of models are also compared to the topographies reported by Houser (2016), which on both d410 and d660 is dominated by shorter wavelength structure than those of Waszek *et al.* (2021). The clear °1 structure on d410 reported by Waszek *et al.* (2021) is also recovered by Houser, both in the spectra and mapped depressed discontinuity beneath the Pacific, Central Atlantic and Central Asia. However, there is much more short wavelength structure in the Houser (2016) than in Waszek *et al.*'s model, visible in the mapped topography, and the much higher power in the higher degree structure (Figure 57g). This likely reflects the differing stacking methods employed by the

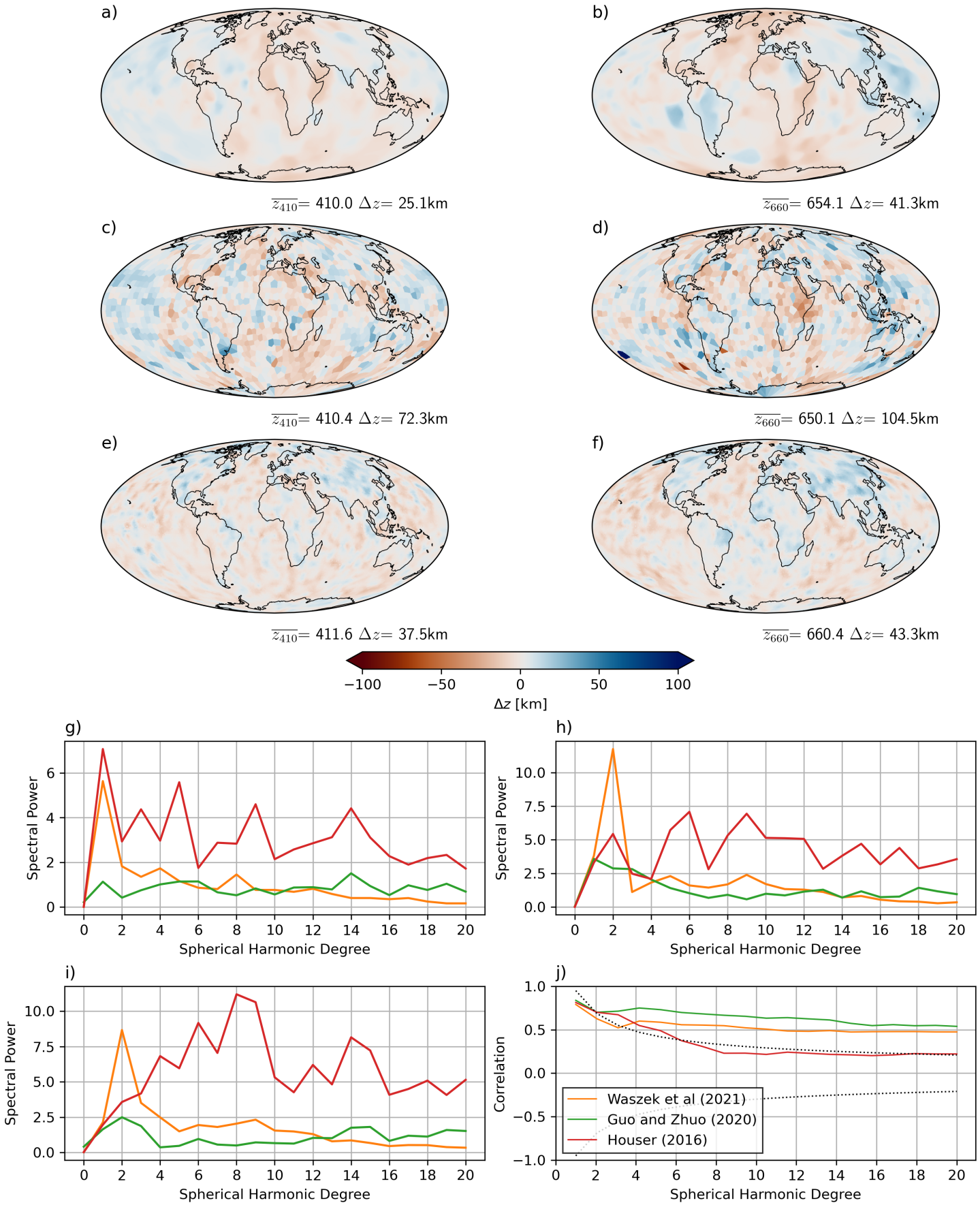

Figure 57: Published global d410 (*Left*) and d660 (*Right*) structure recovered using SS-precursors. *a, b)* Waszek *et al.* (2021), *c,d)* Houser (2016), *e,f)* Guo and Zhou (2020), *g)* Power spectra of d410; *h)* Power spectra of d660, *c)* Power spectra of MTZ thickness variations, *d)* d410-d660 correlation

two studies. The d660 structure recovered by Houser (2016), however, is less directly comparable to the Waszek *et al.* (2021) model. Houser (2016) reports depressions throughout most of the Pacific, and these depressions are, except for in the Western Pacific, unassociated with downwellings. Waszek *et al.* (2021) report much lower amplitude depressions with a similar morphology in the Pacific. As in Waszek *et al.* (2021), the strong degree one signal recovered on the d410 structure is not recovered in the MTZ thickness spectra, although the spectra at intermediate ($\sim^\circ$ 7) and higher spherical harmonic degrees than the other two models considered here. This is reflected in the weaker correlation between d410 and d660 than the other two models, and the correlation is only statistically significant between degrees one and six.

The final model I show in Figure 57 is that inverted by Guo and Zhou (2020) using finite-frequency sensitivity kernels. The recovered topography is much more gentle than in the Houser (2016) model, but is much rougher than that of Waszek *et al.* (2021). On d410, it is difficult to pick out a global pattern in the distribution of depressed and uplifted regions, with hills and valleys on the discontinuity distributed somewhat evenly across the Earth. However, there are regional depressions beneath central Asia through to North China as well as northern North America. This globally uniform, low amplitude, structure is reflected by the low and even power on nearly all spherical harmonic degrees. On d660, the distribution of depressions in the discontinuity are remarkably similar to those Guo and Zhou (2020) report on d410, although some linear features such as the arcing depression south of Hawaii on d410 are not reproduced on d660, where depressions are more strongly clustered beneath continents than on d410 producing a stronger $l < 3$ structure on the Guo and Zhou (2020) d660 structure than on d410. Power on the MTZ spectra is low at all degrees, although it increases with degree greater than 8 and there is a peak at $l = 2$. Looking at the correlation spectra of d410 and d660 for Guo and Zhou (2020) , there is a strongly positive correlation at all spherical harmonic degrees, reflecting the low power on the MTZ thickness spectrum.

Simulations here are only filtered with the sensitivity of the Waszek *et al.* (2021) model, although a filter for the sensitivity of the Houser (2016) is presented in section 4.4.2.

Viscosity Structure 19: Reference – 30× Jump at 660km Depth

The topographies predicted by the geodynamic simulations with the reference viscosity structure are shown in Figure 58, with the spherical harmonic spectra on d410, d660 and MTZ thickness variations in Figure 59 with d410-d660 correlation. For all of these simulations the amplitude of both d410 and d660 is

strongly overpredicted with the "best performing" of the simulations over-predicting the amplitude of topography variations by a factor of ~ 2 on both d410 and d660.

Spectrally, all models (apart from 493, which delivers a large amount of enriched material to the basalt density filter) with the "canonical" radial viscosity structure have a strong degree 2 structure on d410 and d660. On d410 this is a significant overprediction at small l, but on d660 the predicted power is similar to that recovered by Waszek *et al.* (2021) in this part of the spectrum. At higher spherical harmonic degrees, however, there is excess power leading to the overprediction of the total topography amplitude. The d660 spectra predicted from the thermochemical structure of simulation 493 is more distinct than those from the other simulations with this viscosity structure, with a fairly consistent power across all spherical harmonic degrees $l > 1$. This may reflect the more significant role played by the Gt-out reaction in controlling the depth of d660 in plume-centres that are enriched in Basalt, meaning that depressions on d660 are not just associated with downwellings but upwellings also, creating high l structure as well as a more moderate-length scale relative uplift in the discontinuity between the large scale circulation flows.

Geographically, the fit of the simulations with the Waszek *et al.* model is generally moderate. In the Pacific I reproduce the depression of d410 but not of d660, instead predicting an elevated discontinuity for all the geodynamic models. Whilst the enriched material delivered by the flow in 493 to the lower-mid-mantle does result in local control of d660 by Gt-out around plumes, the d660 is generally uplifted in the Pacific domain of these predicted topography structures. For all of these models, the uplift of d410 around downwellings is predicted as the dominant feature on d410, but does not dominate the topography models recovered from SS-precursor datasets (e.g. Waszek *et al.*, 2021; Houser, 2016; Guo and Zhou, 2020). The downwards deflection of d660 beneath central Asia is only reproduced in simulations with a primordial layer initial condition.

Figure 58: Filtered topography (variation from $\bar{z}_d$, the mean discontinuity depth) on d410 (*a, d, g, j, m, p*), d660 (*b, e, h, k, n, q*), and variation in MTZ thickness (*c, f, i, l, o, r*) for simulations with radial viscosity structure 19 (reference). Δz is shown for each model, corresponding to the range between the 0.1 and 99.9 percentiles.

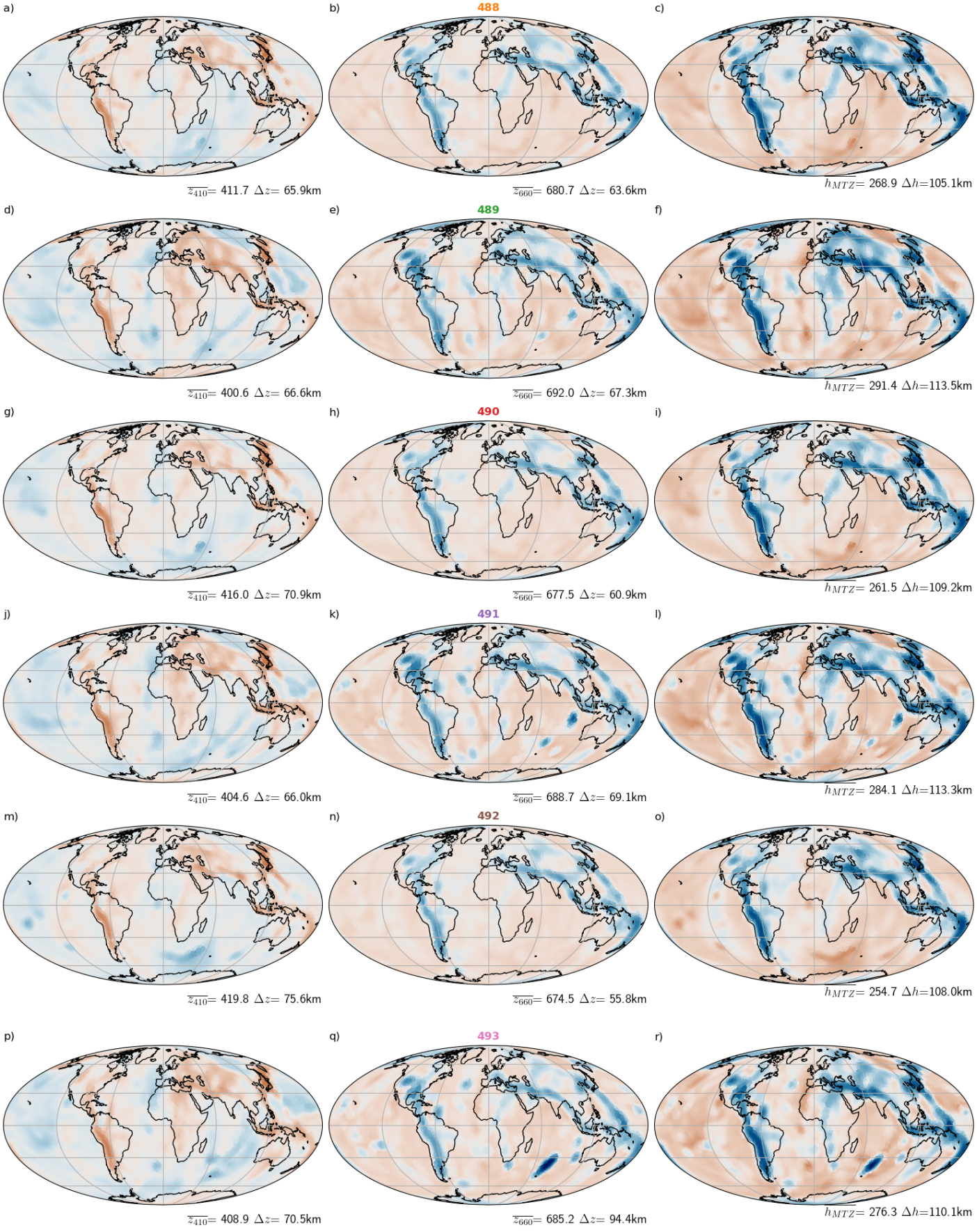
a)
$\overline{z_{410}}$= 411.7 Δz= 65.9km
b)
488
$\overline{z_{660}}$= 680.7 Δz= 63.6km
c)
$\overline{h_{MTZ}}$= 268.9 Δh=105.1km
d)
$\overline{z_{410}}$= 400.6 Δz= 66.6km
e)
489
$\overline{z_{660}}$= 692.0 Δz= 67.3km
f)
$\overline{h_{MTZ}}$= 291.4 Δh=113.5km
g)
$\overline{z_{410}}$= 416.0 Δz= 70.9km
h)
490
$\overline{z_{660}}$= 677.5 Δz= 60.9km
i)
$\overline{h_{MTZ}}$= 261.5 Δh=109.2km
j)
$\overline{z_{410}}$= 404.6 Δz= 66.0km
k)
491
$\overline{z_{660}}$= 688.7 Δz= 69.1km
l)
$\overline{h_{MTZ}}$= 284.1 Δh=113.3km
m)
$\overline{z_{410}}$= 419.8 Δz= 75.6km
n)
492
$\overline{z_{660}}$= 674.5 Δz= 55.8km
o)
$\overline{h_{MTZ}}$= 254.7 Δh=108.0km
p)
$\overline{z_{410}}$= 408.9 Δz= 70.5km
q)
493
$\overline{z_{660}}$= 685.2 Δz= 94.4km
r)
$\overline{h_{MTZ}}$= 276.3 Δh=110.1km
−100
−75
−50
−25
0
25
50
75
100
Depth [km]

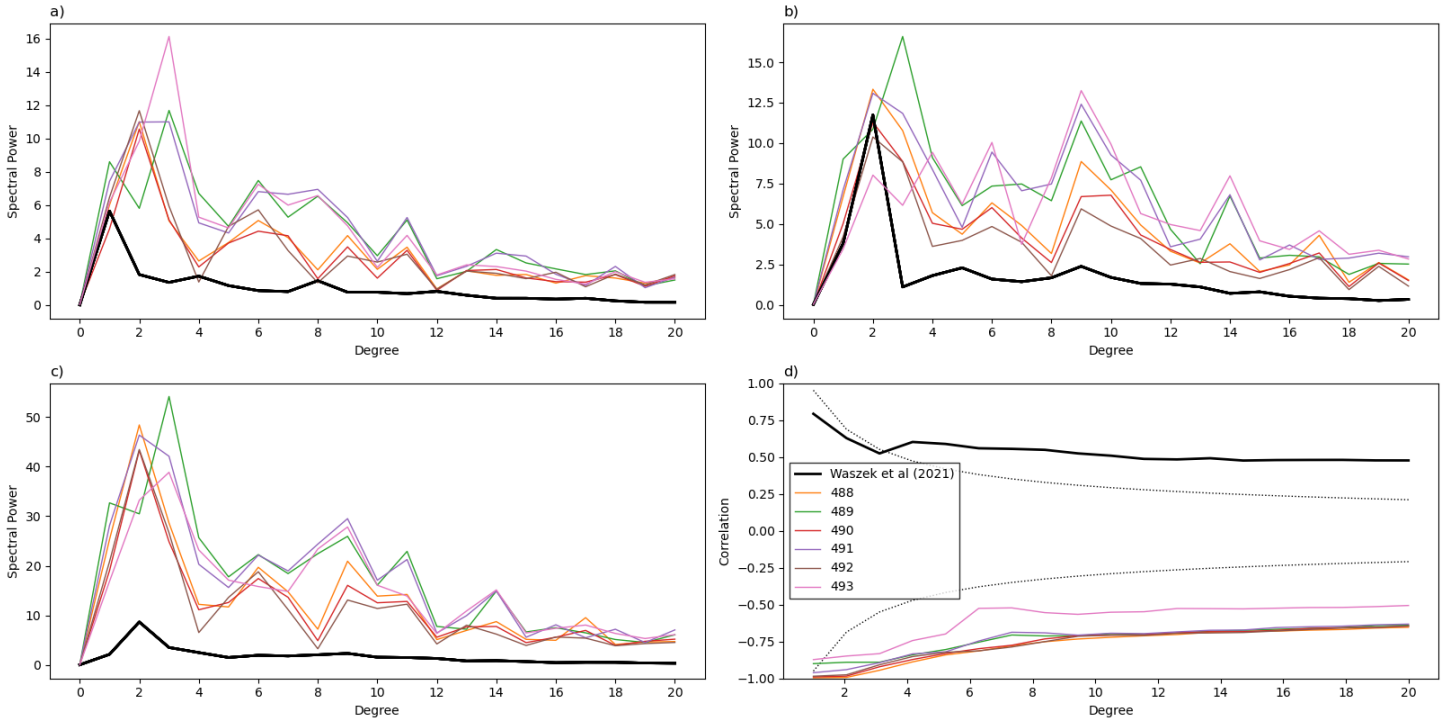

Figure 59: Spherical Harmonic data from the filtered topographies shown in Figure 58. *a)* Power spectra of d410; *b* Power spectra of d660, *c)* Power spectra of MTZ thickness variations, *d)* d410-d660 correlation

Viscosity Structure 9: 'Mid-Mantle Hill'

Like the reference simulations the simulations with a very strong viscosity hill in the lower mantle overpredict the amplitude of d410 and d660 topography for all CMB temperatures and compositional initial conditions (Figure 60). Absolute discontinuity depths are slightly closer to those observed in the Earth with increased CMB temperature.

Spectrally (see Figure 61), all of these simulations' predicted discontinuities all have a very strong $l = 2$ structure on d410, d660, and on the mantle transition zone thickness variations. On d660, the cases with a primordial layer initial condition have an increased power on $l = 6$, which for simulation 458 is similar in power to the power on $l = 2$. This is extremely dissimilar to global studies of d660 using SS-precursors that generally peak on low l (Guo and Zhou, 2020; Waszek *et al.*, 2021) before falling with increasing l without a large uptick in power at intermediate l or a have a relatively flat power spectra (Houser, 2016).

On d660 a geographical comparison with the Waszek *et al.* (2021) model is encouraging; similar depressions associated with downwellings are predicted from these geodynamic simulations as those retrieved from SS-precursor data (Figure 60). Further, the depression of d660 in Central Asia is correctly

predicted in these simulations, which was not the case for the MCMs with the reference viscosity structure above. In the Pacific there is more of a mixed picture. In the SE Pacific, the patterns of depressions and elevations of d660 is qualitatively similar to those reported by Waszek, although d410 does not match here. The picture is qualitatively reversed in the NW Pacific, where the depressed d410 predicted by these simulations is in agreement with the Waszek *et al.* topography model; which also predicts a depression on d660 which is not observed. Elsewhere, the deflections on d410 (which are generally very consistent between the simulations) do not make an especially convincing comparison to the structures imaged by Waszek *et al.* (2021), particularly in the Southern and Indian oceans where Waszek *et al.* (as well as other workers (Houser, 2016; Guo and Zhou, 2020)) image an elevated discontinuity and the dominant uplift of d410 around downwellings in the geodynamic simulations.

Viscosity Structure 16: Low Viscosity Channel Beneath 660km Depth

Simulations 479 (with no primordial enriched layer in its initial condition) and 480 (which does have a primordial layer imposed) have a low viscosity channel beneath 660km depth, and the jump in viscosity at 1000km depth. Predicted topographies and spherical harmonic data are shown in Figure 62. Average discontinuity depths predicted from these geodynamic models do not make a perfect comparison (479 over estimates the depth of d410 and d660 by a few km, and simulation 480 by a bit more on d660, but underpredicts the average depth of d410). On d660, both simulation 479 and 480 produce discontinuity topography ranges on the higher end of those recovered in global SS-precursor studies. On d410, the predicted topography amplitude is over a factor of 3 greater than that recovered by Waszek *et al.* (2021).

Spectrally, 479 does an extremely good job matching the spectra published by Waszek *et al.* apart from at $l = 2$ for d660. The addition of a primordial layer compositional initial condition has less of an impact on the d660 spectral misfit than for other radial viscosity structures. On d410 both simulation 479 and 480 perform poorly with large secondary peaks on $l = 7$.

Geographically, 479 performs well in the Pacific due to the low amplitude of

Figure 60: Filtered topography (variation from $\bar{z}_d$, the mean discontinuity depth) on d410 (*a, d, g, j, m, p*), d660 (*b, e, h, k, n, q*), and variation in MTZ thickness (*c, f, i, l, o, r*) for simulations with radial viscosity structure 9 (viscosity hill). Δz is shown for each model, corresponding to the range between the 0.1 and 99.9 percentiles.

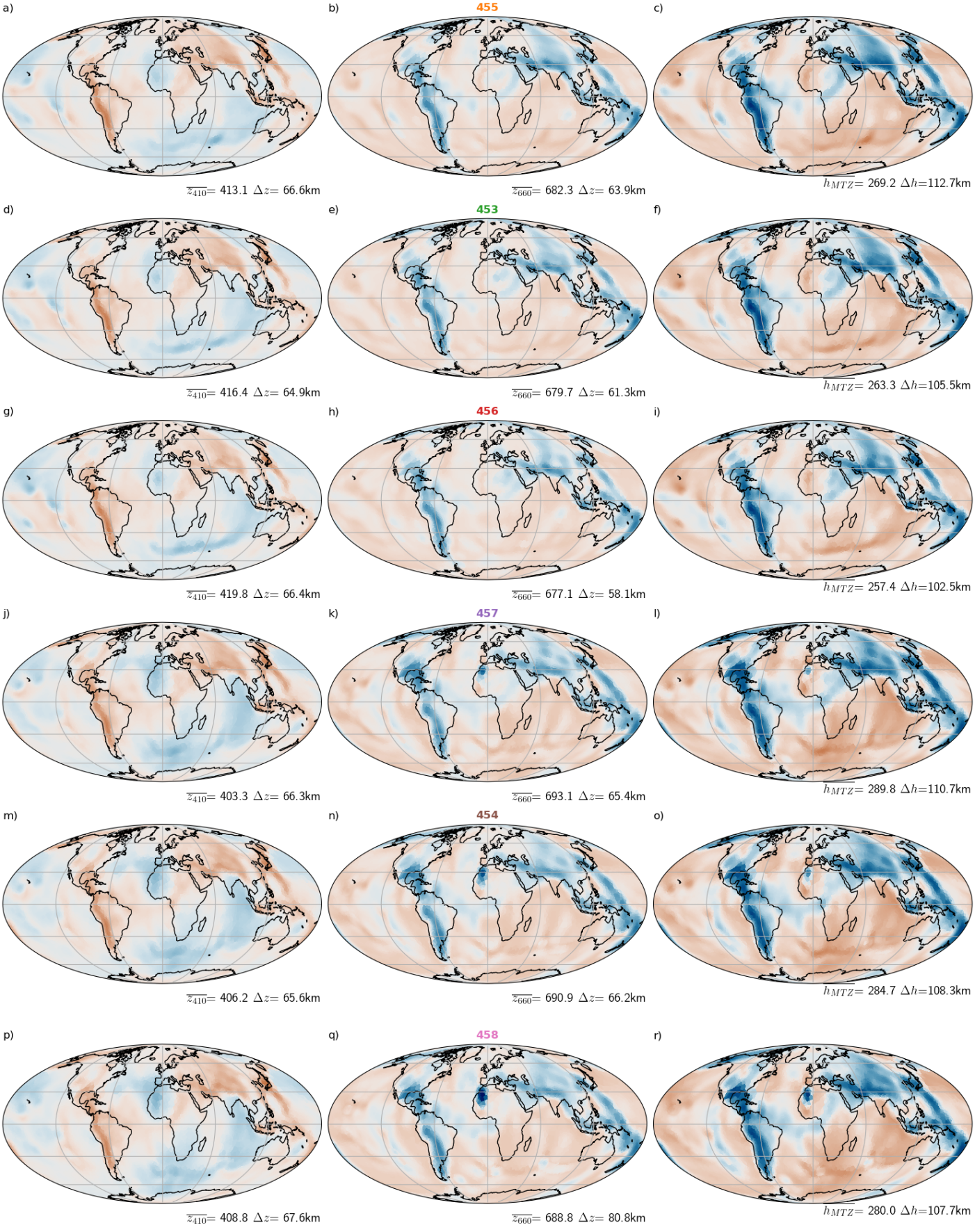
a)
b)
455
c)
$\overline{z_{410}}$= 413.1 Δz= 66.6km
$\overline{z_{660}}$= 682.3 Δz= 63.9km
$\overline{h_{MTZ}}$= 269.2 Δh=112.7km
d)
e)
453
f)
$\overline{z_{410}}$= 416.4 Δz= 64.9km
$\overline{z_{660}}$= 679.7 Δz= 61.3km
$\overline{h_{MTZ}}$= 263.3 Δh=105.5km
g)
h)
456
i)
$\overline{z_{410}}$= 419.8 Δz= 66.4km
$\overline{z_{660}}$= 677.1 Δz= 58.1km
$\overline{h_{MTZ}}$= 257.4 Δh=102.5km
j)
k)
457
l)
$\overline{z_{410}}$= 403.3 Δz= 66.3km
$\overline{z_{660}}$= 693.1 Δz= 65.4km
$\overline{h_{MTZ}}$= 289.8 Δh=110.7km
m)
n)
454
o)
$\overline{z_{410}}$= 406.2 Δz= 65.6km
$\overline{z_{660}}$= 690.9 Δz= 66.2km
$\overline{h_{MTZ}}$= 284.7 Δh=108.3km
p)
q)
458
r)
$\overline{z_{410}}$= 408.8 Δz= 67.6km
$\overline{z_{660}}$= 688.8 Δz= 80.8km
$\overline{h_{MTZ}}$= 280.0 Δh=107.7km
−100
−75
−50
−25
0
25
50
75
100
Depth [km]

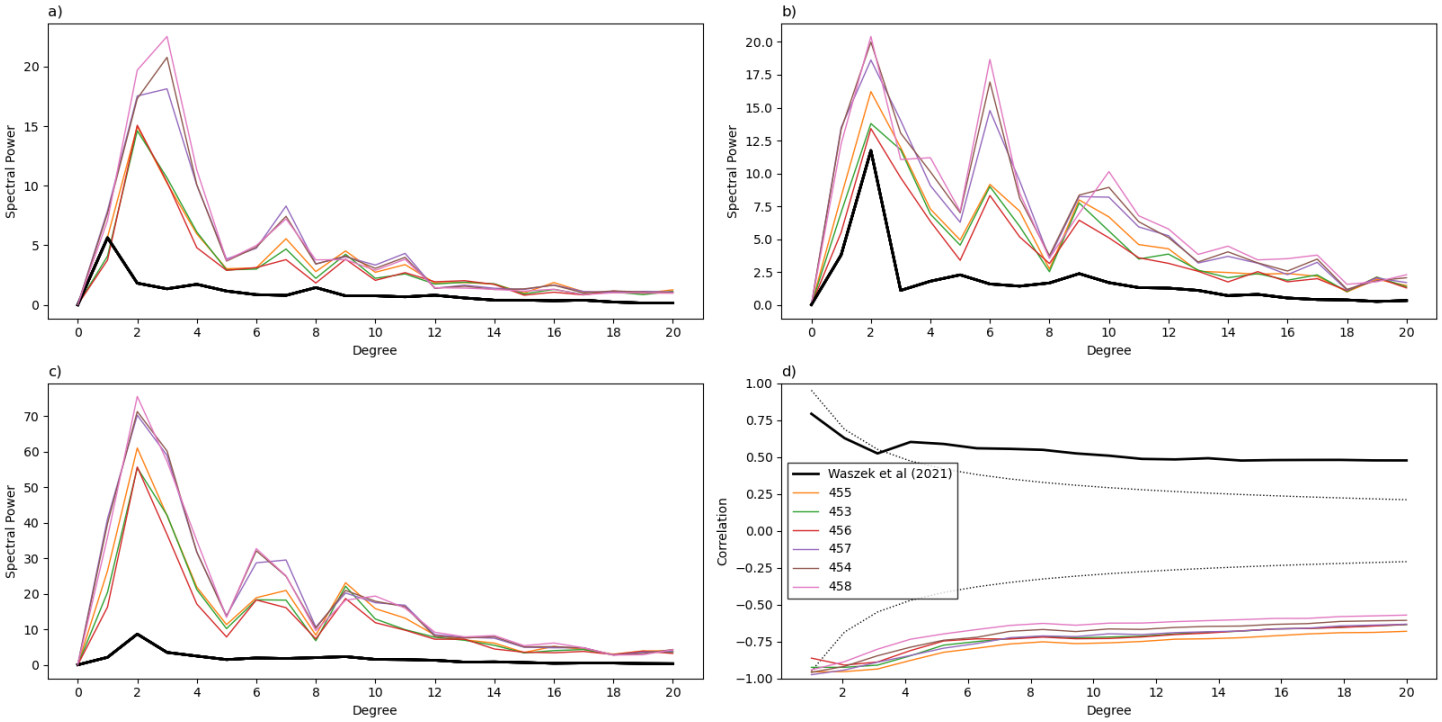

Figure 61: Spherical Harmonic data from the filtered topographies shown in Figure 60. *a)* Power spectra of d410; *b* Power spectra of d660, *c)* Power spectra of MTZ thickness variations, *d)* d410-d660 correlation

topography predicted on d660, but the localised depression on simulation 480's d660 can be favourably compared to similar features in the Pacific from global SS-precursor datasets. Depressions associated with downwellings are similarly recovered between 479 and 480 on d660, making comparisons here similarly favourable for both. Both 479 and 480 predict a trench from NE Africa towards the West African coasts, similar, but not identical to a feature recovered in the Waszek *et al.* (2021) model.

On d410, a geographical comparison is less favourable. Both 479 and 480 predict large depressed regions on d410 south of Southern Africa (which is generally observed to be uplifted in *SS*-precursor studies). Ridges on d410 around the downwellings are predicted but are not present in published data. Beneath the Pacific, d410 is predicted to be depressed for both 479 and 480 due to a warmer mantle under the Pacific, consistent with recovered datasets of d410, although the observed correlation of d660 to d410 in the Pacific (e.g. Houser and Williams, 2010) is not observed for these models as d660 is uplifted in these regions.

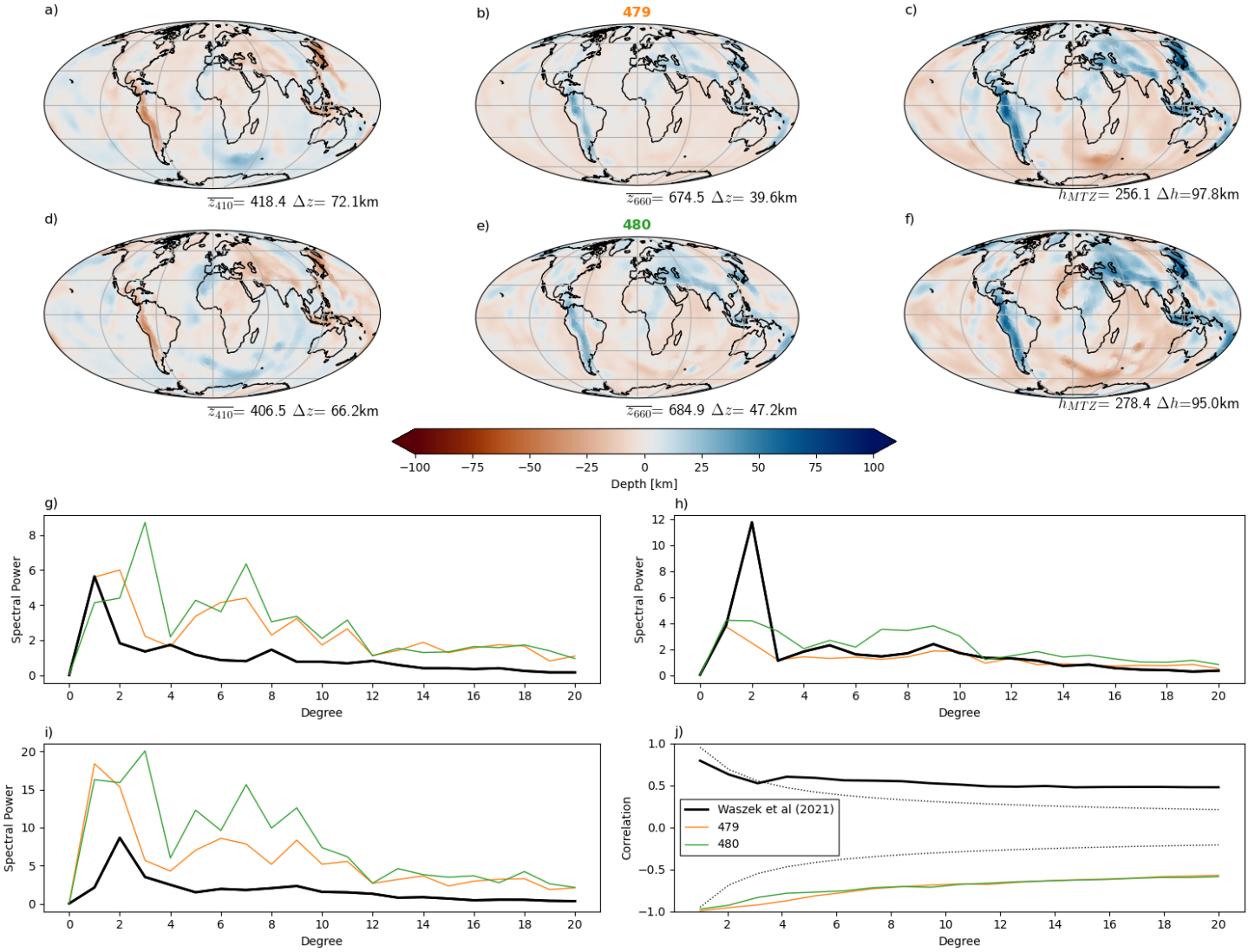

Figure 62: Filtered topography (variation from $\bar{z_d}$, the mean discontinuity depth) on d410 (*a, d*), d660 (*b,e*), and variation in MTZ thickness (*c,f*) for simulations with radial viscosity structure 16. Spherical Harmonic data from the filtered topographies; *g)* Power spectra of d410; *h* Power spectra of d660, *i)* Power spectra of MTZ thickness variations, *j)* d410-d660 correlation. Δz is shown for each model, corresponding to the range between the 0.1 and 99.9 percentiles.

Viscosity Structures 12 and 15: 30× Jump at 1000km Depth

I also consider a sub-suite of simulations where the jump in viscosity is deeper than the seismic discontinuity at 660km depth, and the predicted topographies are shown in Figure 63, with the spherical harmonic data for these simulated discontinuities in Figure 64. On d410, the average depth of the discontinuity is generally well predicted, but the amplitude of the topography is overpredicted quite significantly. On d660, the range of predicted discontinuity depths is consistent with those observed by Waszek *et al.* (2021) and other studies, although the average depth of the discontinuity is slightly overpredicted.

Again the d660 power spectra are very close to the Waszek *et al.* (2021) spectrum generally apart from at very low spherical harmonic degree (although power on 462's d660 spectra peaks on $l = 1$ and has significant power on $l = 2$ and $l = 3$ – possibly due to the effect of the primordial material guiding the relative position of upwellings and framing warm and cool sectors of the Earth when swept by imposed downwellings).

On d410, the power on low spherical harmonic degree is generally overpredicted for these models apart from 477, which has a lower plate scaling factor, instead of matching the plate scaling factor used in the reference cases. By having a different plate scaling factor, we allow less thermal diffusion to take place in the lithosphere in the "correctly" scaled model 477.

Geographically on d660, comparison to Waszek *et al.* (2021) dataset is generally reasonably favourable. Downwards deflections in the NE Pacific are comparable to published maps. Depressions are predicted beneath subduction zones globally, as well as in the back-arc beneath Central Asia. A downwards deflection of d660 is generally predicted beneath central Africa in these simulations, though in 463 and 461 this is very weak. On d410, as with our other geodynamic predictions of discontinuity structure, the global topography is dominated by the signal of the cold downwelling slabs, which create ridges of the discontinuity beneath trenches. Elsewhere, the models perform similarly on d410, for instance all predict a significant downwards deflection of d410 in the Southern Ocean South of South Africa - which is not repeated in any studies of d410 globally.

Figure 63: Filtered topography (variation from $\bar{z}_d$, the mean discontinuity depth) on d410 (*a, d, g, j, m, p*), d660 (*b, e, h, k, n, q*), and variation in MTZ thickness (*c, f, i, l, o, r*) for simulations with radial viscosity structure s 12 and 15. Δz is shown for each model, corresponding to the range between the 0.1 and 99.9 percentiles.

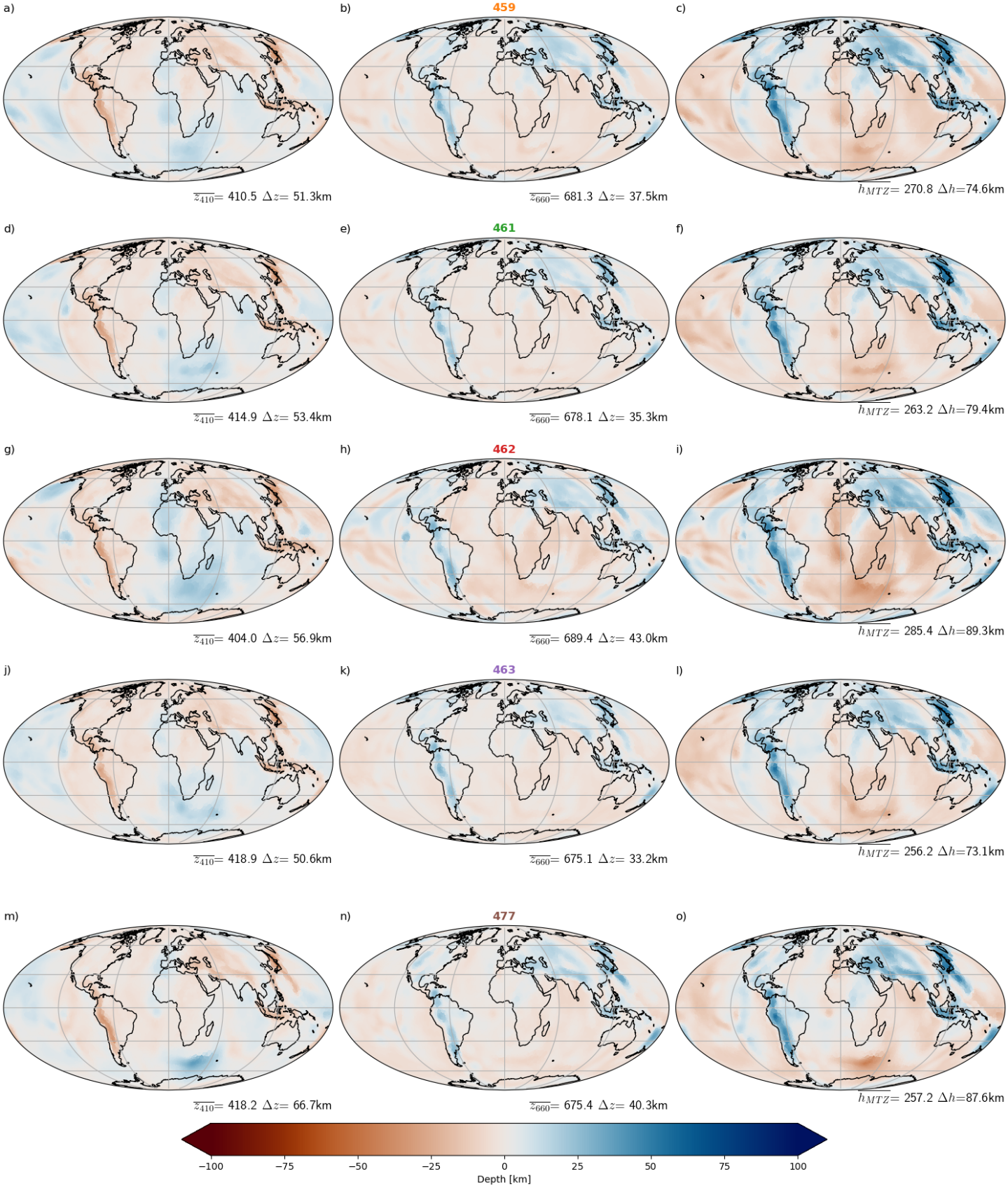
a)
b)
459
c)
$\overline{z_{410}}$= 410.5 Δz= 51.3km
$\overline{z_{660}}$= 681.3 Δz= 37.5km
$\overline{h_{MTZ}}$= 270.8 Δh=74.6km
d)
e)
461
f)
$\overline{z_{410}}$= 414.9 Δz= 53.4km
$\overline{z_{660}}$= 678.1 Δz= 35.3km
$\overline{h_{MTZ}}$= 263.2 Δh=79.4km
g)
h)
462
i)
$\overline{z_{410}}$= 404.0 Δz= 56.9km
$\overline{z_{660}}$= 689.4 Δz= 43.0km
$\overline{h_{MTZ}}$= 285.4 Δh=89.3km
j)
k)
463
l)
$\overline{z_{410}}$= 418.9 Δz= 50.6km
$\overline{z_{660}}$= 675.1 Δz= 33.2km
$\overline{h_{MTZ}}$= 256.2 Δh=73.1km
m)
n)
477
o)
$\overline{z_{410}}$= 418.2 Δz= 66.7km
$\overline{z_{660}}$= 675.4 Δz= 40.3km
$\overline{h_{MTZ}}$= 257.2 Δh=87.6km
−100
−75
−50
−25
0
25
50
75
100
Depth [km]

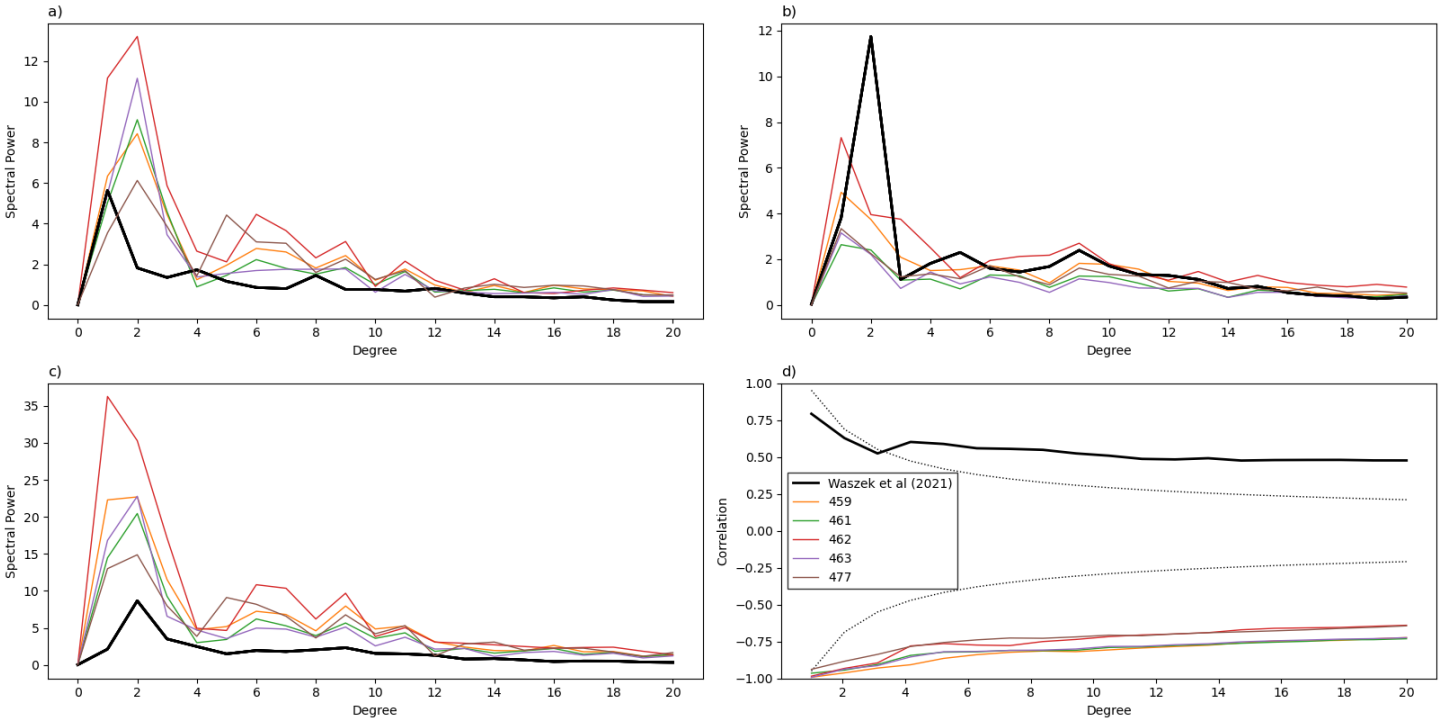

Figure 64: Spherical Harmonic data from the filtered topographies shown in Figure 63. *a)* Power spectra of d410; *b* Power spectra of d660, *c)* Power spectra of MTZ thickness variations, *d)* d410-d660 correlation

Viscosity Structure 18: Weak D″

Simulations 482-487 were ran with a radial viscosity structure modified from the reference structure to feature a 600km thick weak ($^1/_{10}^{\text{th}}$ of the mantle interior's viscosity) layer above the CMB (Figure 53a).

Fit to the average depth of d660 is generally very good across the simulations without a primordial layer, but the primordial cases have a slightly deeper d660 (Figure 65). The range of discontinuity depths was overestimated for all these simulations on d660, with the cases with a primordial layer having nearly double the observed topography, and the melting cases over-predicting the topography by a factor of 1.5. On d410, the average depth was well predicted by the primordial cases but slightly overpredicted by the simulations with only melting-derived chemical heterogeneity. For both compositional assumptions, the topography on d410 is overestimated by a factor of 2 (Figure 65).

Spectrally (Figure 66), fit on both d410 and d660 is unsatisfactory. For the primordial cases generally there is excess power on all spherical harmonic degrees, but misfit is particularly high on intermediate degrees on both d410 and d660 when compared to the Waszek *et al.* (2021) dataset. For the cases without the initially imposed primordial layer, fit is substantially better but is still not ideal. On d410 in particular, these cases have a lot of excess power on

$7 < l < 11$ compared to the spectra of published models. On d660, excess power is predicted on these spectra for $l > 3$, although their spectra does tend to peak on low spherical harmonic degrees, as seen in the published data.

Geographically, on d410, all the models correctly predict a depressed discontinuity surface beneath the Pacific, and generally agree with each other as a suite. Most of the simulations predict a depression of d410 south of Southern Africa, associated with a superplume, although this is less pronounced at low CMB temperatures and in simulations where a primordial layer is imposed. However, unlike in any published topography models the elevation of d410 around downwelling slabs is the dominant global feature. On d660, the signal is again dominated by the downwelling induced features, this time of depressions on the discontinuity surface. However, in these simulations, plumes dominantly cause a depression on the discontinuity surface since here the discontinuity is controlled by the garnet out-reaction due to the high fraction of basaltic material in the plumes. This is the case even for the simulations without an initially imposed primordial layer since the vigorous convection in D″ allows more basalt to accumulate in the domains where plumes form than in the simulations with a viscous lowermost mantle. As the position of upwellings is not prescribed in the same way as the downwellings, the positions of these depressions cannot be directly compared to global observations. However, the regions where these localised depressions occur are comparable to regions with non-subduction related depressions in d660 in the Earth (Pacific, Indian and South Atlantic Oceans). However, the depressions that are recovered in the filtered d660 structure are fewer and less uniform in distribution than in the SS-precursor datasets. This may be where the significantly higher viscosity of these simulations compared to the Earth's mantle results in fewer and stronger upwellings than are present in the true Earth.

Figure 65: Filtered topography (variation from $\bar{z_d}$, the mean discontinuity depth) on d410 (*a, d, g, j, m, p*), d660 (*b, e, h, k, n, q*), and variation in MTZ thickness (*c, f, i, l, o, r*) for simulations with radial viscosity structure 18. Δz is shown for each model, corresponding to the range between the 0.1 and 99.9 percentiles.

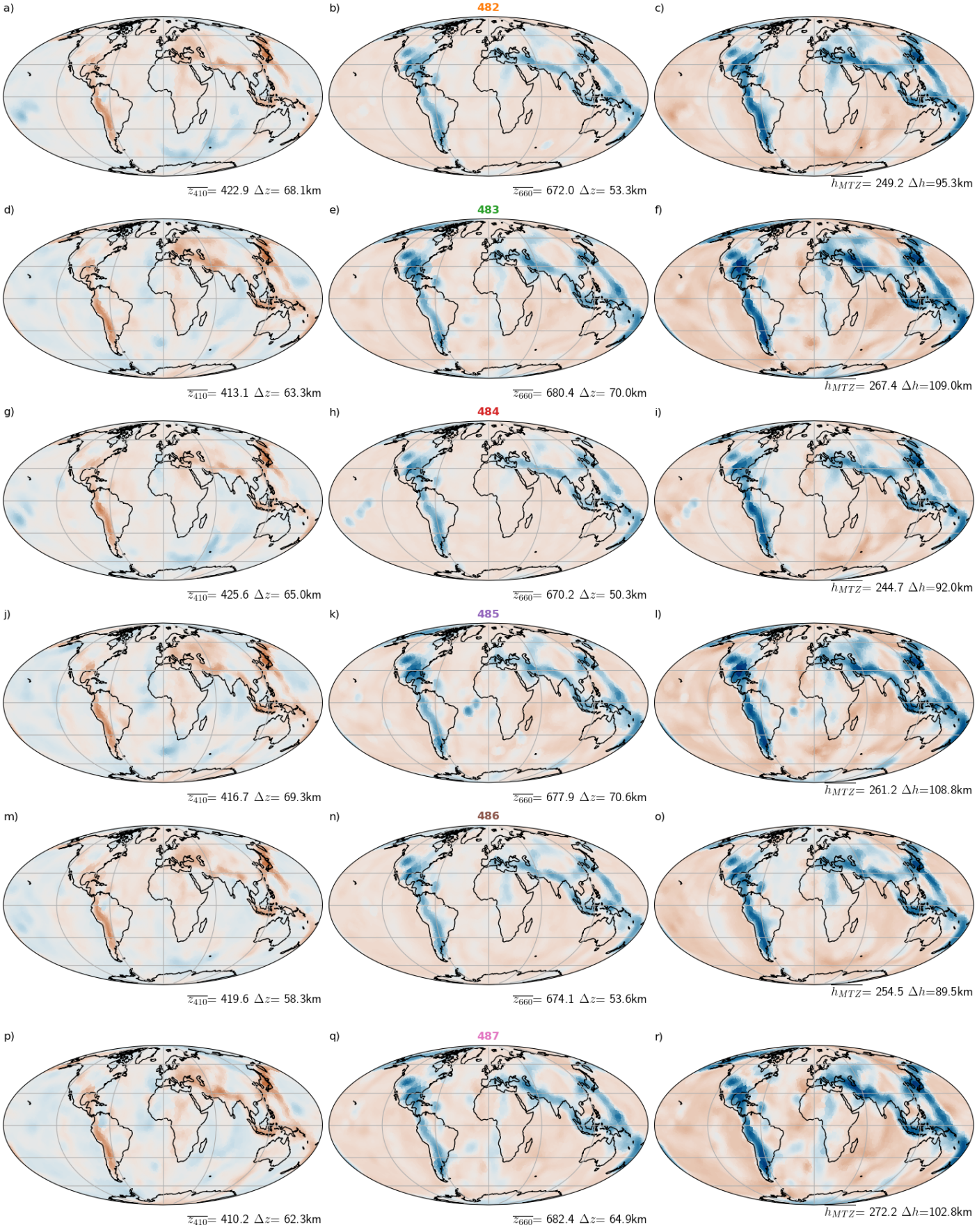
a)
b)
482
c)
$\overline{z_{410}}$= 422.9 Δz= 68.1km
$\overline{z_{660}}$= 672.0 Δz= 53.3km
$\overline{h_{MTZ}}$= 249.2 Δh=95.3km
d)
e)
483
f)
$\overline{z_{410}}$= 413.1 Δz= 63.3km
$\overline{z_{660}}$= 680.4 Δz= 70.0km
$\overline{h_{MTZ}}$= 267.4 Δh=109.0km
g)
h)
484
i)
$\overline{z_{410}}$= 425.6 Δz= 65.0km
$\overline{z_{660}}$= 670.2 Δz= 50.3km
$\overline{h_{MTZ}}$= 244.7 Δh=92.0km
j)
k)
485
l)
$\overline{z_{410}}$= 416.7 Δz= 69.3km
$\overline{z_{660}}$= 677.9 Δz= 70.6km
$\overline{h_{MTZ}}$= 261.2 Δh=108.8km
m)
n)
486
o)
$\overline{z_{410}}$= 419.6 Δz= 58.3km
$\overline{z_{660}}$= 674.1 Δz= 53.6km
$\overline{h_{MTZ}}$= 254.5 Δh=89.5km
p)
q)
487
r)
$\overline{z_{410}}$= 410.2 Δz= 62.3km
$\overline{z_{660}}$= 682.4 Δz= 64.9km
$\overline{h_{MTZ}}$= 272.2 Δh=102.8km
−100
−75
−50
−25
0
25
50
75
100
Depth [km]

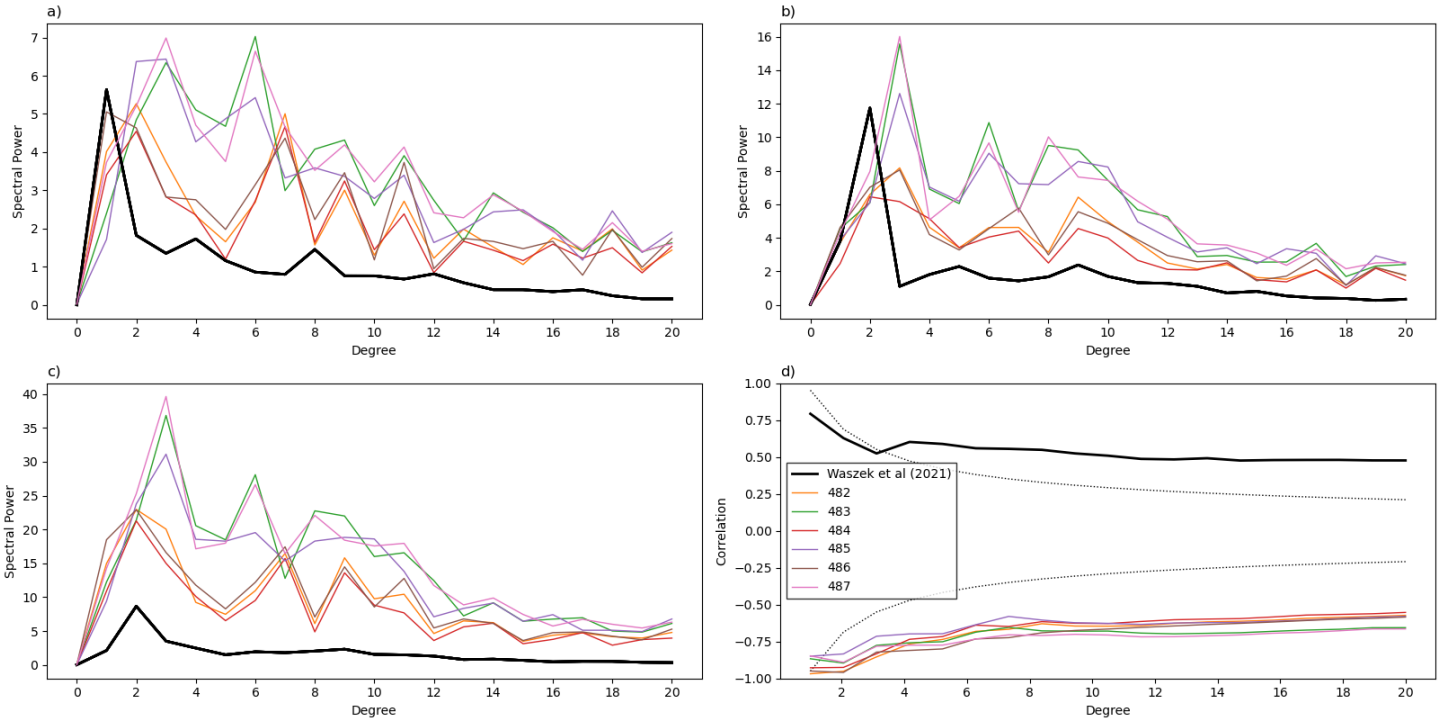

Figure 66: Spherical Harmonic data from the filtered topographies shown in Figure 65. *a)* Power spectra of d410; *b* Power spectra of d660, *c)* Power spectra of MTZ thickness variations, *d)* d410-d660 correlation

4.4 Discussion

4.4.1 Fit to Observed d410 and d660

In this suite of simulations none of the predicted d410 structures make a convincing comparison to the Waszek *et al.* (2021) dataset, geographically or spectrally.

The topography of d660, however was a substantially easier metric to approach a good fit to in this suite of simulations. For the set of mineral physics tables and seismological treatment used to predict the discontinuity topography for these geodynamic simulations, satisfactory fit to d660 is found on simulations 459, 461, 462, 463, 477, 479, and 480. These simulations all have viscosity structures where the jump to lower mantle viscosity is not imposed around 660, but at around 1000 km depth. This is suggestive either of a preference for a deeper jump in viscosity or, more likely, indicates the reference viscosity in these simulations is too high. Unlike the conclusions I drew in reference to the MCM 'm_cc_066_u' in Chapter 3, and other inferences I will attempt to gleam from this suite of simulations, this is probably not affected by the uncertainty on the phase transformation parameters, which for a fixed thermochemical structure may significantly change the amplitude of the predicted topography.

Mean Discontinuity Depths

As discussed in chapter 3, the average depth of d410 and d660, given the correct mineral physics should suggest the correct average thermal structure at the top and bottom of the mantle transition zone. Very few simulations produce average discontinuity depths within 10 km of the usual quoted depths for d410 (410 (e.g. Kennett and Engdahl, 1991) or 400 km depth (e.g. Dziewonski and Anderson, 1981)) and d660 (660 (e.g. Kennett and Engdahl, 1991) or 670 km depth (e.g. Dziewonski and Anderson, 1981)). Typically the average depths recovered by *SS* precursor studies are biased to be slightly shallower (650, Houser 2016; 660.4, Guo and Zhou 2020; 654.4 km depth Waszek *et al.* 2021), but across the suite of simulations we are biased to slightly deeper values on both discontinuities, indicating an overestimation in the radial thermal gradient in this suite of models as a whole. A few models (485, 486, 484, 483, 461, 463, 477, 479, 453, 456, 490) approach the nominal depths of both d410 and d660 – but generally the depths are overestimated. These had temperatures at the top of the MTZ that were within 100 K of the estimates for potential temperature from the thickness of the MTZ (Ritsema *et al.*, 2009; Waszek *et al.*, 2021), from the reflectivity-distance curve for *S660S* (Yu *et al.*, 2023), or petrological estimates for potential temperature (e.g. Li *et al.*, 2025), confirming that these simulations had a roughly Earth-like adiabat in their interior.

Range of Discontinuity Depths

Similarly, matching the range of discontinuity depths is some indication that the geodynamic model has an appropriate temperature range in the regions the phase transitions that control d410 and d660 and the *SS*-precursors are sensitive to. As a rule, the geodynamic models tend to result in overpredicted topography on both d410 and d660. This is due to the excessively high reference viscosity chosen and the consequent low Rayleigh number. Simulations with a lower viscosity around d660 (e.g. viscosity structures 12 and 15 (Figure 63) or viscosity structure 16 (Figure 62)) do successfully approach ranges recovered by *SS*-precursor studies. Viscosity structure appears to be the dominant control on this here when compared to the other varied parameters of this study (CMB temperature and a primordial layer in the compositional initial conditions), but the true impact may be simply a proxy for favouring increased convective vigour.

Geographical

Since these simulations are mantle circulation models, we impose downwellings according to our understanding of the history of Earth's surface tectonics, meaning that the thermal structure should be directly comparable to the Earth's, and so comparing their predicted and observed topographies in geographic space is also of interest. This is generally not a very favourable comparison on d410 for any of these simulations, although on d660, the correct pattern that is dominated by downwelling slabs is observed in many of the simulations here. Due to the strong anticorrelation of d410 to d660 (see below), patterns of MTZ thickness do not make a favourable comparison either.

Power Spectra

I have also illustrated the lateral variations in topography using the spherical harmonic power spectra. The story here is qualitatively similar to that we discussed for the geographic distribution of topography. There are several simulations[2] for whom fit to the spectra of the Waszek *et al.* (2021) model is acceptable but generally there is excess power at high spherical spherical harmonic degrees and too little power at $l \leq 2$.

4.4.2 Comparison to Other Datasets

So far we have compared our predicted topographies exclusively to the Waszek *et al.* (2021) model, however, several others exist, each selecting a different subset of data and handling it in a different way. Therefore it is worthwhile considering how a comparison to different datasets changes our assessments of the MCMs.

As I have done for the Waszek *et al.* (2021) model, I need to consider the sensitivity of any other model to the reflectivity structure of the mid-mantle. For the Waszek *et al.* (2021), due to their adaptive Voronoi cell caps,I was only able to produce a meaningful filter for the physical smoothing of the reflector, and was unable to account explicitly for any averaging in the stacking of traces. Whilst most authors discuss the origin and selection criteria for their source receiver pairs it is rare for the source-receiver pairs used to be explicitly listed (as Waszek *et al.* (2021) have done). If the model is released, more commonly the location of the spherical caps are released, as is the case for the Houser (2016) dataset that I now consider a comparison to. To allow me to consider the physical averaging as well as the processing averaging, I assume that the

[2]Such as 482, 486, 484, 480, and, compared to the suite of MCMs presented here, the MCM discussed at length in Chapter 3.

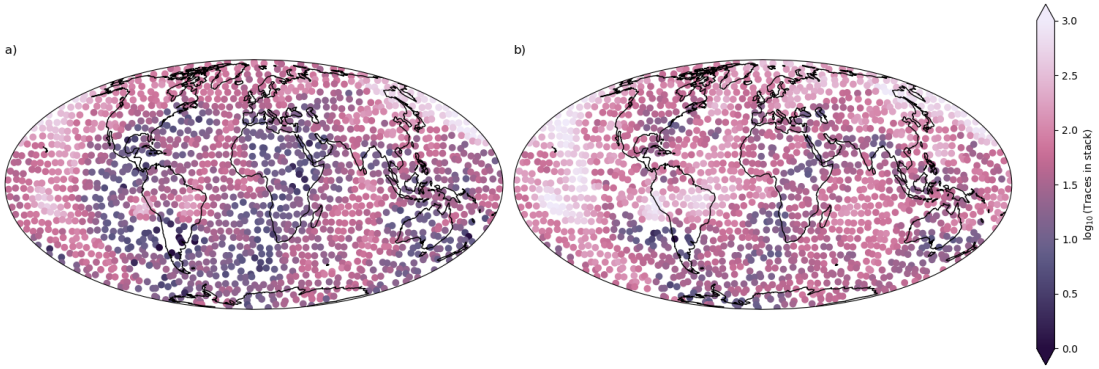

Figure 67: Distribution of bouncepoints *a)* reported by Houser (2016) and *b)* used by Waszek *et al.* (2021), reported in the same spherical caps as the Houser (2016) uses. Given *a)* and *b)* are similar, we take it that we can use the Waszek *et al.* (2021) bouncepoints to account for the physical averaging.

distribution of bouncepoints selected by Houser (2016) or by Waszek *et al.* (2021) are both large samples of a random (but not uniform) distribution, so they will be similarly distributed. We can verify this by comparing the number of stacks in each cap from of the Houser (2016) dataset and the Waszek *et al.* (2021) bouncepoints in Houser's spherical caps, see Figure 67. Using this, we take an average of the reflectivity structure around the Waszek *et al.* (2021) bouncepoints. These 'traces' are then 'stacked' in the 5° caps used by Houser (2016), where the peak reflectivity is used as the depth of the discontinuity in the cap.

Predicted discontinuity topographies, filtered in this way for the sensitivity of the Houser (2016) model are shown in Figure 68 for a subset of the MCMs ran. As might reasonably be anticipated the additional smoothing step results in a gentler topography on d410 and d660 for all the models shown. However, this is not to say that all detail on the discontinuities is washed out; as where there are regions of extreme topography, this can be recovered. For instance the depression due to a superplume delivering enriched material to the mid-mantle, leading to the Gt-out control of the discontinuity, in the Southern Ocean for simulation 493 is successfully recovered by the filtered topography as is the depression on the Gulf of Mexico's d660 in a large downwelling for simulation

Figure 68: Select topographies of the simulation suite filtered for the sensitivity of the Houser (2016) discontinuity model. *a -c)* respectively filtered d410, d660 topography, and MTZ thickness variations for simulation 479; *d-f)* ditto for simulation 489; *g-i)* ditto for simulation 493. *j)* Spherical harmonic spectra of d410 for the simulations above compared to the Houser (2016) model; *k)* ditto for d660; *l)* ditto for MTZ thickness variations. *m* d410-d660 correlation at successive l.

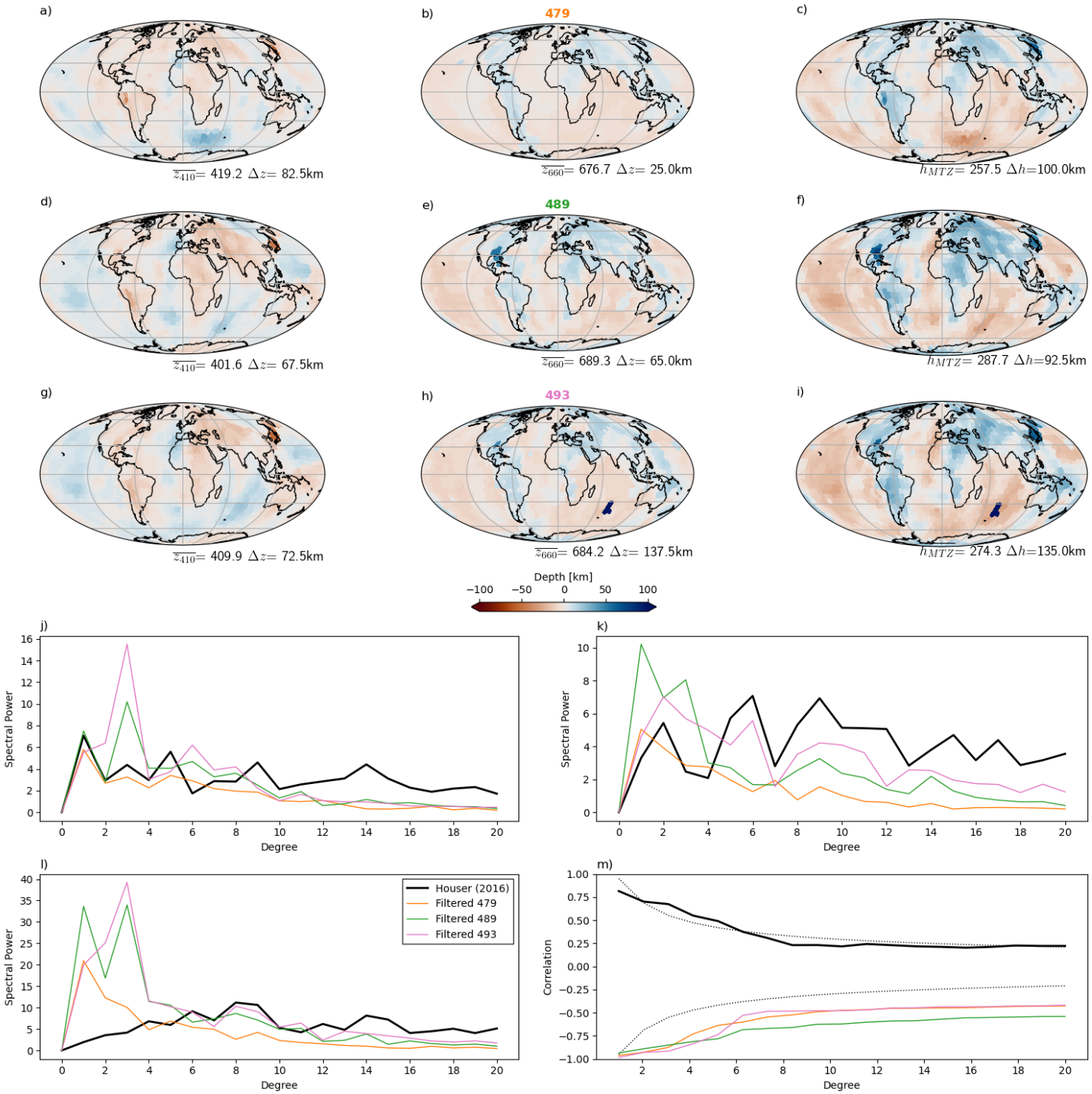
a)
$\overline{z_{410}}$= 419.2 Δz= 82.5km
b)
479
$\overline{z_{660}}$= 676.7 Δz= 25.0km
c)
h_{MTZ}= 257.5 Δh=100.0km
d)
$\overline{z_{410}}$= 401.6 Δz= 67.5km
e)
489
$\overline{z_{660}}$= 689.3 Δz= 65.0km
f)
h_{MTZ}= 287.7 Δh=92.5km
g)
$\overline{z_{410}}$= 409.9 Δz= 72.5km
h)
493
$\overline{z_{660}}$= 684.2 Δz= 137.5km
i)
h_{MTZ}= 274.3 Δh=135.0km
Depth [km]
−100 −50 0 50 100
j)
Spectral Power
Degree
k)
Spectral Power
Degree
l)
Spectral Power
Degree
Houser (2016)
Filtered 479
Filtered 489
Filtered 493
m)
Correlation
Degree

489. For all the simulations in Figure 68, the elevation of d410 above upwellings becomes much less continuous and more moderate, more like what is observed in global studies (e.g. Houser, 2016; Guo and Zhou, 2020; Waszek *et al.*, 2021), although an extreme deflection is recovered beneath Japan for these simulations.

4.4.3 d410-d660 Correlation

d410 in all of these predicted mid-mantles is dominated by the signature of downwelling slabs, which is not the case for the topography recovered by Waszek *et al.* (2021) (or Houser 2016; Guo and Zhou 2020). This slab controlled signal dominates globally, strongly anti-correlating with the similarly thermal signal on d660. This in turn leads to poor fit on MTZ thickness variations which is universally overestimated in these simulations. I consider here briefly possibilities to explain the positive correlation. I have repeatedly noted the poor geographical fit of d410 around downwellings, which might lead us to consider if the positive correlation of d410 and d660 is solely due to effects here.

The modern configuration of downwellings is illustrated in Figure 69, and I take points less than 500 km from a modern subduction zone to be 'close' to one. The topography on d410 and d660 in the Waszek *et al.* (2021) model is plotted as a 2D histogram in Figure 70a, showing the aforementioned positive correlation clearly. In Figure 70b, I show a similar plot, but for the points of the Waszek *et al.* (2021) model within the 500 km distance contour (white line in Figure 69). The positive correlation is still present, but much more slight than for the whole mantle and the data is skewed towards the quadrant where both d410 and d660 are depressed. Finally, I show the histogram for the mantle 'far' from a subduction zone in Figure 70c, where the positive correlation is still present. It is worth drawing two points from this; that firstly the region around downwellings are complex regions for d410-d660, and secondly that even if there is a positive correlation between d410 and d660 in the region of downwellings, an explanation is required for the positive correlation elsewhere in the mantle.

4.4.4 Geodynamic Explanations for d410-d660 Correlation

Overall Vigour of Convection

The reference viscosity of the simulations ran here is comparatively high and therefore the vigour of the simulations (characterised by the Rayleigh number) is quite low compared to the Earth. This may explain the overestimation of the amplitude of d410 topography in particular, as downwellings and upwellings must have a stronger temperature anomaly (and therefore deflect the phase

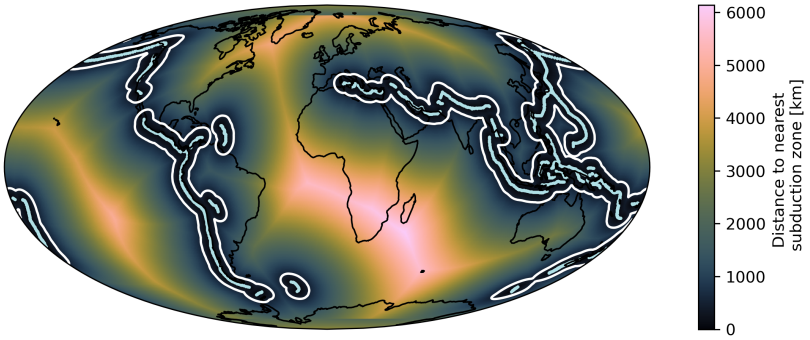

Figure 69: Distance from a subduction zone (pale blue lines) in the Bird (2003) modern plate boundary and motions model. The (500 km) contour is marked in white - this is the definition used here for 'near' a subduction zone.

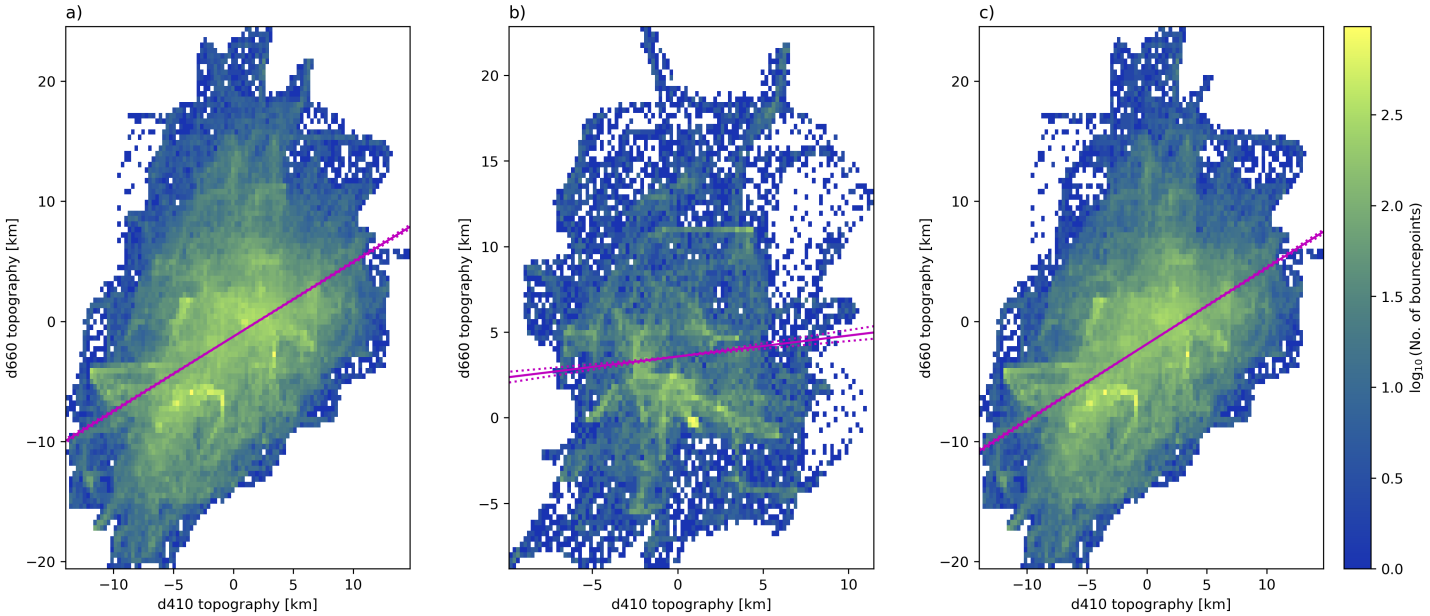

Figure 70: 2D histograms of topography on d410 and d660 in the Waszek *et al.* (2021) model. *a)* Global *b)* within 500 km of subduction zones and *c)* more than 500 km from a subduction zone. Magenta lines indicate lines of best fit calculated by a least-squares algorithm. Dotted magenta lines show a standard deviation in slope above and below the lines of best fit.

change depth more significantly) to convect against the viscous resistance. This may also reduce the deflection of upwellings and downwellings in the mid-mantle, both due to the dynamic impact of the phase transitions (e.g. Wolstencroft and Davies, 2011), and other structures in the mantle. These simulations of $\eta_0 = 1 \times 10^{22}$ Pa.s are at the lower limit of what thermal structures a TERRA simulation of this resolution can resolve. Increasing the resolution from $mt = 128$ to 256 corresponds to a 16× increase in computational cost. Whilst clearly this would benefit the assessment, I do not include it in the scope of this current work, but rather it highlights the importance of simulating the Earth's mantle at Earth-like vigour.

For an internally heated mantle, the vigour of convection is described using a modified version of the Rayleigh number;

$$Ra_H = \frac{\alpha \rho^2 g D^5 H}{\kappa k \eta} \tag{4.2}$$

where H is the total heat input into the mantle, from internal heating and the heat gradient across the CMB. For this class of simulations, $Ra_H \sim 1.6 \times 10^7$, whereas $Ra_H^E \sim 10^{10}$ (e.g. Ricard, 2007). Our poor recovery of d410-d660 correlation, whilst similar simulations perform acceptably on other metrics (e.g. Davies *et al.*, 2025) may reflect that the low-Ra MCM is able to predict the large global circulation of material through the mantle, but does not capture shorter-scale convection.

As I have indicated elsewhere in this thesis I have access to a suite of simulations *ran by Dr James Panton for the MC2 project*, and a few of these were ran at higher resolution and lower reference viscosity than the simulations that I considered above. I will now briefly consider the topography predicted from simulation '256_044_3800_lithscl', case number 262, which was ran at $mt = 256$ and $\eta_0 = 2 \times 10^{21}$ Pa.s. This results in an internally heated Rayleigh number of 4.6×10^7. This topography structure is illustrated in Figure 71. As expected, the amplitude of the recovered filtered topography is significantly lower than for a simulation with a similar set of input parameters, and the resulting flatter power spectra is not entirely unexpected either. However, the filtered topography shows a positively correlated d410-d660 structure, which we so far have not been able to generate from MCMs. Investigating further, and considering the unfiltered topographies, d410 is only uplifted in very small regions, and these ridges surrounded by a depressed discontinuity. In fact, the unfiltered topographies of d410 and d660 are anticorrelated (Figure 71j). If we then examine the thermal structure of simulations 262 and 490 at 400 km depth (Figure 72), we see the imposed downwellings surrounded by broad regions of

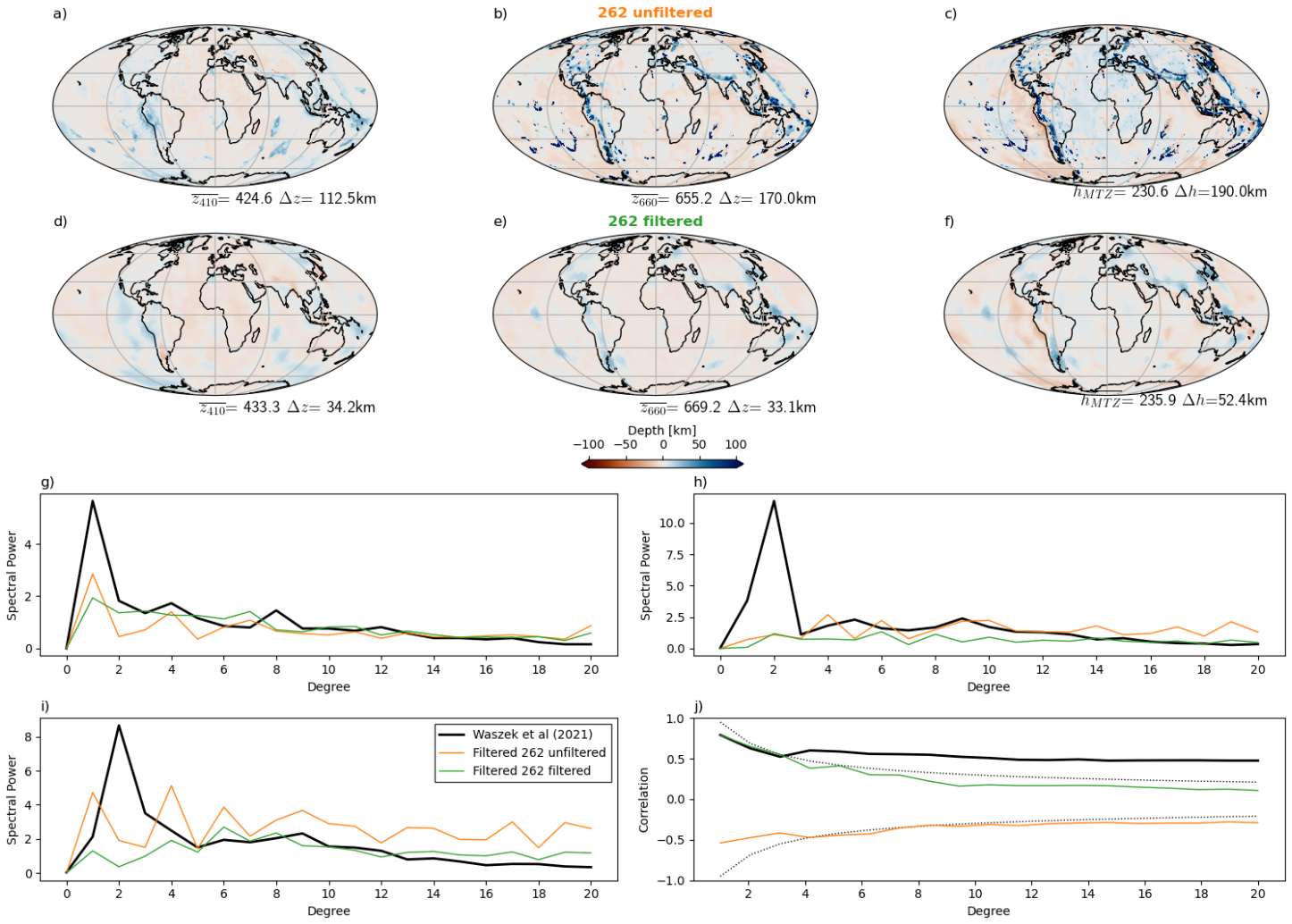

Figure 71: Predicted topographies for simulation 262, *a -c)* respectively unfiltered d410, d660 topography, and MTZ thickness variations for simulation 262; *d-f)* ditto for the filtered topographies; *g)* Spherical harmonic spectra of d410 for the filtered and unfiltered topography of simulation 262 compared to the Waszek *et al.* (2021) model; *h)* ditto for d660; *i)* ditto for MTZ thickness variations. *j)* d410-d660 correlation at successive l.

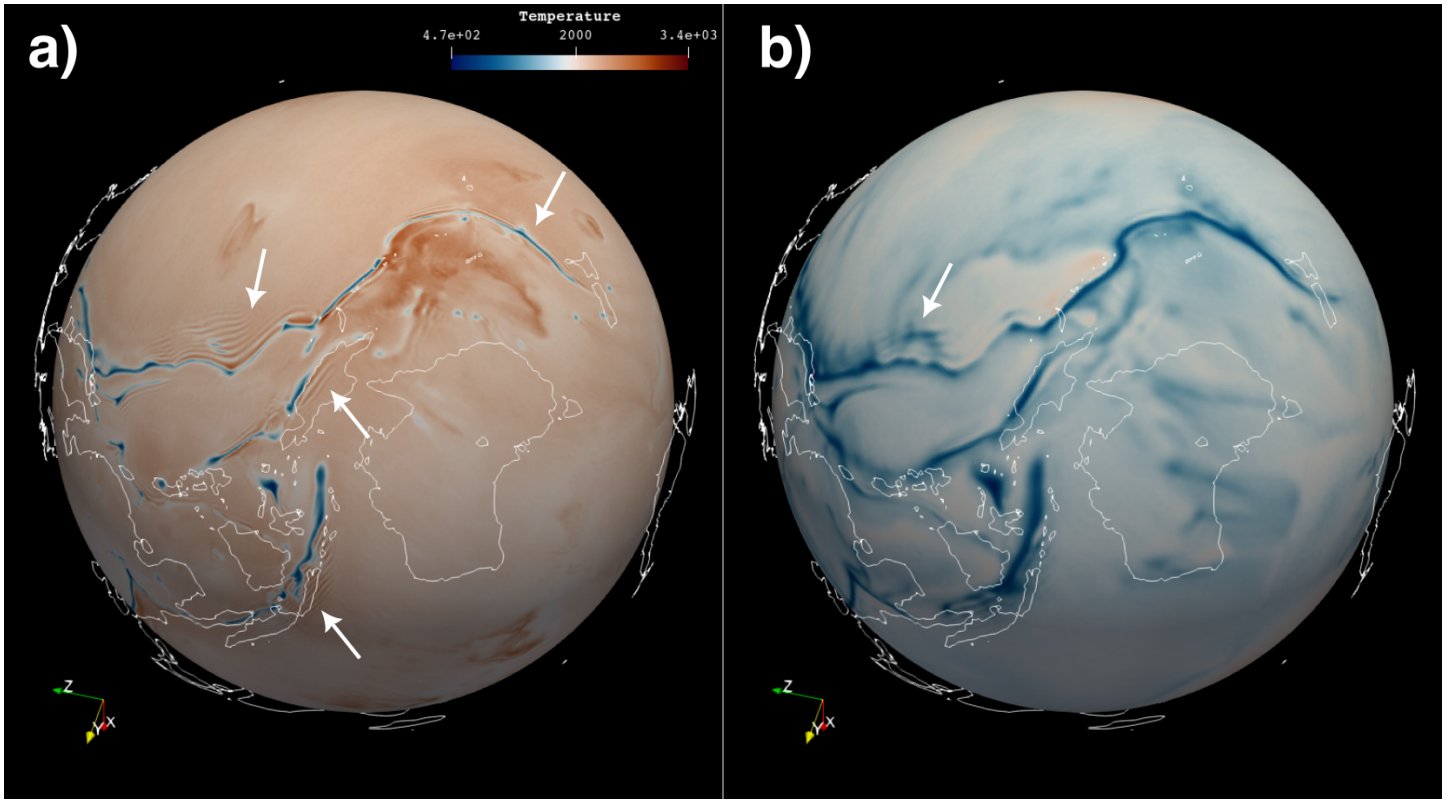

Figure 72: Thermal structure at 400 km depth *a)* Simulation 262, $\eta_{ref} = 2 \times 10^{21}$, see text for further description, *b)* Simulation 490, see notes in Table 8. Arrows indicate possible numerical instabilities.

numerical instability in the high vigour simulation. As the reference viscosity is lower, the geodynamic downwellings are smaller and therefore the discontinuity structure associated with the numerical instabilities in the thermal structure dominates the structure when averaged by the spherical cap. Whilst these numerical instabilities are not important in the global circulation and these models may still provide satisfactory fit to other metrics, they are not sufficiently resolved to consider d410-d660 topography correlation.

Testing if the d410-d660 correlation is the result of the changing morphology of convection with increasing vigour requires simulations appropriately resolved and with appropriate plate motion scaling for the mantle viscosity to ensure numerical instabilities do not dominate the seismological signal.

Additional Enrichment of the Deeper Part of MTZ in Basalt

An alternative suggestion that we could make, strictly for explaining d410-d660 correlation, is that the lower MTZ is further enriched in basaltic and primordial material than what has been produced by these simulations here. This would lead to a regional dominance of the $Gt \rightarrow Brm$ reaction, which for most temperatures of interest has a positive Clapeyron slope. However, as discussed

above, our fit to observed d660 structure is quite good for many of our simulations, but for d410 is quite poor. Global super-enrichment will not produce a satisfactory structure in the round.

4.4.5 Non-Geodynamic Explanations for d410-d660 Correlation

Meta-Stable Olivine

d410 is usually perceived as a comparatively simple discontinuity compared to d660, as it is controlled by a single phase transition ($Ol \rightarrow Wd$) and similar reactions happen in silica enriched assemblages ($Px \rightarrow Gt$). However, so far we have only considered *equilibrium* phase assemblages but have not considered the role of reaction kinetics in affecting different phase proportions and therefore discontinuity depths. It is widely thought that olivine can stay present, meta-stably in the cores of downwelling slabs for potentially hundreds of kilometres (e.g. Mosenfelder *et al.*, 2001), or even into the lower mantle (e.g. Kong *et al.*, 2022). The delayed reaction and associated resulting sudden volume reduction has been invoked to explain deep Earthquakes in Wadati-Benioff Zones (e.g. Lidaka and Suetsugu, 1992). Whilst these regions with a depressed d410 would be extremely localised, we have already seen how extremely narrow ridges and trenches on d410 and d660 get spread into broad deflections when observed using SS precursors (Chapter 3), so I consider here a simplified implementation to sketch the potential impact. In Figure 73 I show the filtered topography predicted for select simulations which I have modified so that if the temperature is less than 1000 K, the discontinuity is forced to sit at 490 km depth. Whilst this is an oversimplified implementation and we might expect a more complex structure with overlapping reflectors or regions of gradual impedance increase as the meta-stable olivine transforms to wadsleyite, it does allow us to get a sense of the order of magnitude of the impact of non-equilibrium effects on d410.

Figure 73: Select topographies of the simulation suite with the simplified implementation of meta-stable Olivine control on d410, filtered for the sensitivity of the Waszek *et al.* (2021) discontinuity model. *a -c)* respectively filtered d410, d660 topography, and MTZ thickness variations for simulation 479; *d-f)* ditto for simulation 463; *g-i)* ditto for simulation 489. *j-l)* ditto for simulation 493. *j)* Spherical harmonic spectra of d410 for the simulations above compared to the Waszek *et al.* (2021) model; *k)* ditto for d660; *l)* ditto for MTZ thickness variations. *m* d410-d660 correlation at successive l.

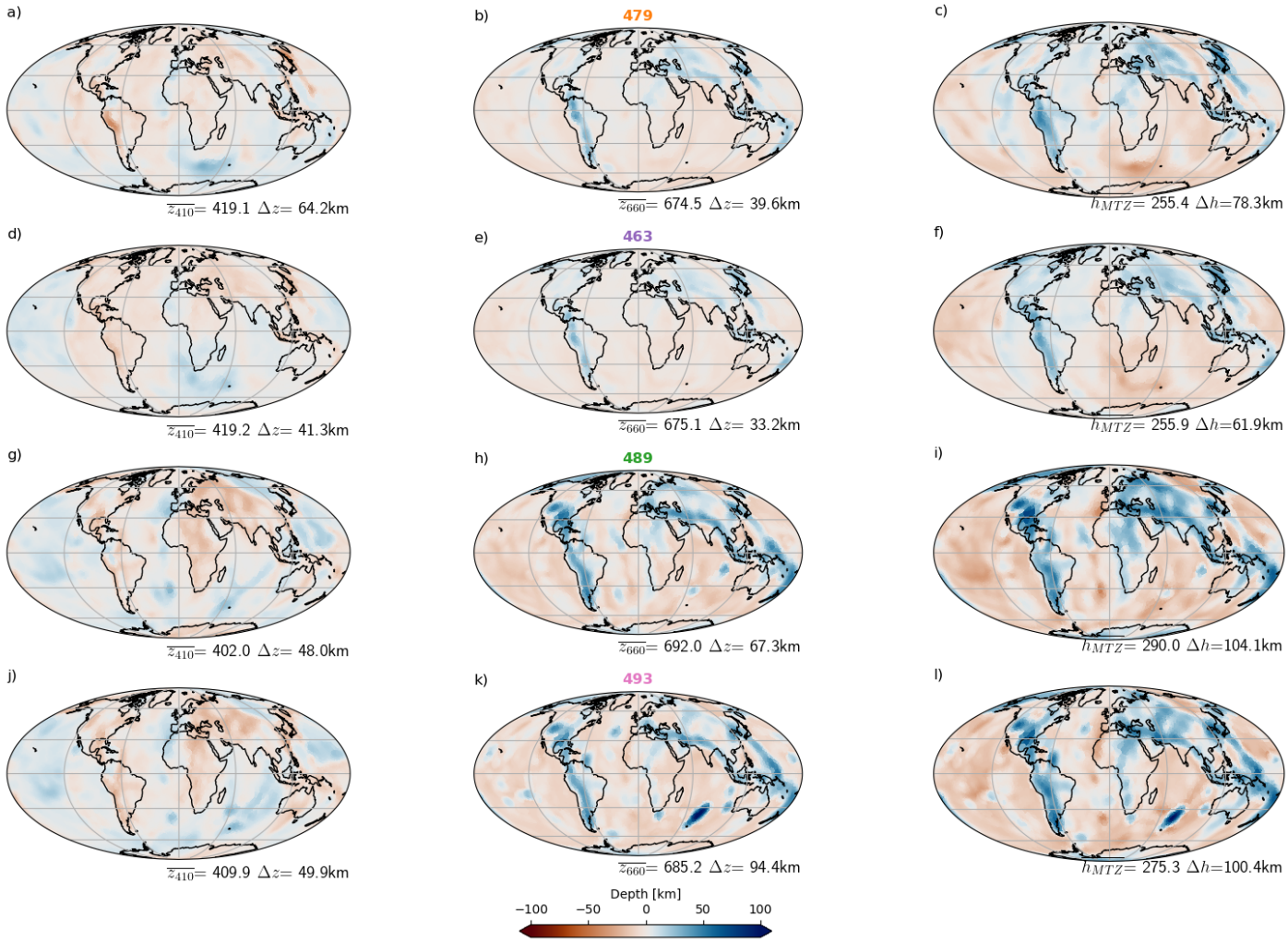
a)
$\overline{z_{410}}$= 419.1 Δz= 64.2km
b)
479
$\overline{z_{660}}$= 674.5 Δz= 39.6km
c)
h_{MTZ}= 255.4 Δh=78.3km
d)
$\overline{z_{410}}$= 419.2 Δz= 41.3km
e)
463
$\overline{z_{660}}$= 675.1 Δz= 33.2km
f)
h_{MTZ}= 255.9 Δh=61.9km
g)
$\overline{z_{410}}$= 402.0 Δz= 48.0km
h)
489
$\overline{z_{660}}$= 692.0 Δz= 67.3km
i)
h_{MTZ}= 290.0 Δh=104.1km
j)
$\overline{z_{410}}$= 409.9 Δz= 49.9km
k)
493
$\overline{z_{660}}$= 685.2 Δz= 94.4km
l)
h_{MTZ}= 275.3 Δh=100.4km
Depth [km]
−100 −50 0 50 100

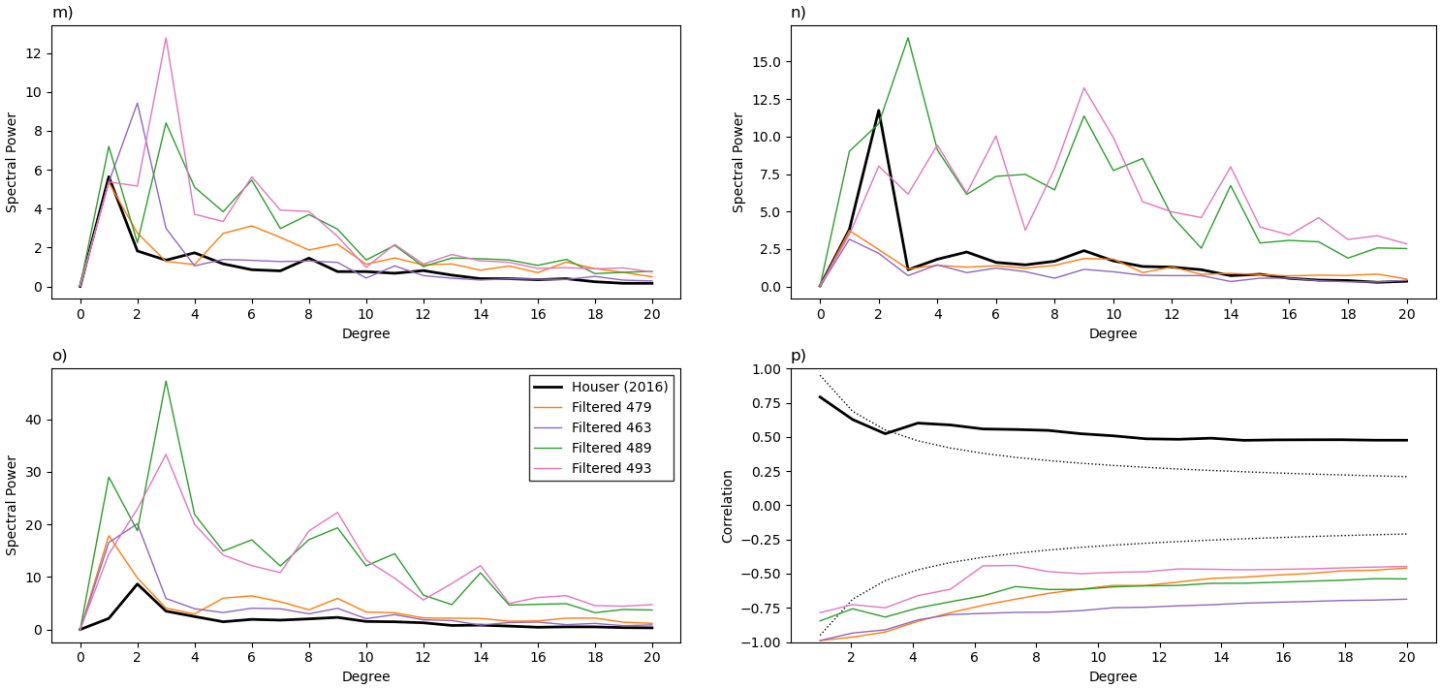
m)
Spectral Power
Degree
n)
Spectral Power
Degree
o)
Spectral Power
Degree
Houser (2016)
Filtered 479
Filtered 463
Filtered 489
Filtered 493
p)
Correlation
Degree

The effect on the average depth of the discontinuity is quite small (< 2 km), reflecting the extremely limited region of the mantle affected by the forced deflection of the discontinuity. The effect on the range depths d410 sits at is more significant, however, reducing the range by up to 20 km for the simulations illustrated in Figure 73, which highlights the the shallowest depths of d410 are associated with the centres of downgoing slabs, and have now been removed by this treatment.

Prior to the meta-stable Olivine treatment of d410, all of these simulations featured strong upwards deflections of the discontinuity at downwellings. These are either completely obscured (e.g. simulation 489 beneath Ecuador and Peru), markedly reduced in amplitude (e.g. all of the downwellings in simulation 463), or the strongest deflections are restricted in location (e.g. in simulation 479, strong upwards deflection of d410 is restricted to beneath Ecuador and Peru).

Spectrally, the effect of the inclusion of the metastability treatment is also evident. For simulation 479 power is reduced on $l > 1$, although most substantially at $l = 2$. Simulation 463 experienced a similar reduction in the power spectra of d410. These significant reductions in d410 power allows these simulations to approach more closely d410 spectra reported by Waszek *et al.* (2021). The power on d410 for simulations 489 and 493 are also decreased, particular at high spherical harmonic degrees ($l > 8$). However, due to the excess power on d660, these simulations still overpredict the power of the MTZ power structure at all l.

In terms of global d410-d660 correlation, the effects are generally quite minor. For all the MCMs here, at all spherical harmonic degrees, d410 and d660 are strongly anticorrelated, although the degree of anticorrelation is reduced slightly. However, the difference due to variations in dynamic structure between the simulations is much more significant.

All of the parameters used in this sketch implementation are rough order-of-magnitude approximations, but could be varied to have a more (or less) signifiant impact. For instance, increasing the temperature where the d410 is forced would increase the effect, particularly at lower l, but would not be particularly physically motivated.

Sensitivity of *S410S* Traveltime to d660 Structure

Koroni *et al.* (2017) used 3D wave propagation code SPECFEM3D_GLOBE (Tromp *et al.*, 2004) to examine the 3D sensitivity kernels of the SS-precursors, highlighting significant sensitivity of *S410S* to structure at 670 km depth. Briefly let's consider if this sensitivity could explain d410-d670 correlation.

Consider a seismologist interpreting a trace where the *SS* bouncepoint sits

above an uplifted d410 and depressed d660, as we predict around subduction zones. *S410S* travel time is increased (bringing it closer to the travel time of the *SS* phase) by the further distance to the d410 reflector in the uplifted region and this is interpreted by the seismologist to recover the upwards swinging topography. Additionally, the deflection of d660 also impacts the *S410S* phase's traveltime, as it must travel further through the ringwoodite stability field, which has a lower seismic velocity, further delaying its arrival. For the geodynamically anticipated relationship of d410 to d660 structure then this reinforces the anticipated anticorrelation rather than forcing a positive correlation as observed seismically. Further, since the topography is estimated by reference to the *SS* arrival, for ideal source-receiver separations, the sensitivity of the *SS* phase and the *S410S* phase should be nearly identical at d670. Therefore the effect should be small and reinforce the geodynamically anticipated anticorrelation of d410 and d660.

The Effect of Sensitivity Beyond the Spherical Cap

Thus far I have accepted the approximation in Chapter 3 of the sensitivity of the *S410S* and *S660S* to the discontinuity structure as spherical caps. Whilst this is the correct first-order approximation, it is known (e.g. Neele *et al.*, 1997; Dahlen, 2005) that the sensitivity kernels of *S410S* and *S660S* are more complex, extending thousands of kilometres away from the ray theoretical bouncepoint. It is possible to calculate the sensitivity kernels for *SS-S410S* and *SS-S660S* travel times and therefore of the precursors to discontinuity topography. Dahlen (2005) describes the sensitivity kernel (K) of *SdS* travel time to perturbations of the discontinuity d as (his equation 64)

$$K^{SdS} = \frac{1}{\pi}\frac{|\cos(f_-)|}{\beta_-}\sqrt{\frac{\cos^2(f)|J_{rs}|}{|J_{xs}||J_{xr}|}}\frac{\int_0^\infty \omega^3|\dot{m}(\omega)|^2\cos(\omega\cdot(T_{xs}+T_{xr}-T_{rs}))d\omega}{\int_0^\infty \omega^2|\dot{m}(\omega)|^2 d\omega} \tag{4.3}$$

where f is the angle of incidence of the ray on the discontinuity, β is shear wave velocity, $_-$ indicates the evaluation of a property on the underside of the discontinuity (and $_+$ would indicate the evaluation above the discontinuity), ω is the frequency of the seismic wave, $|J_{ab}|$ represents the magnitude of the Jacobian from a to b, and T_{ab} is similarly the traveltime between them, where a and b are positions along the ray path (Figure 74). To calculate the lateral variation in sensitivity for each pair of source (s) and receiver (r), the Jacobian and traveltime is calculated for every possible 'scattering point' x on the discontinuity d. Travel times were calculated using the *TauP* package (Crotwell

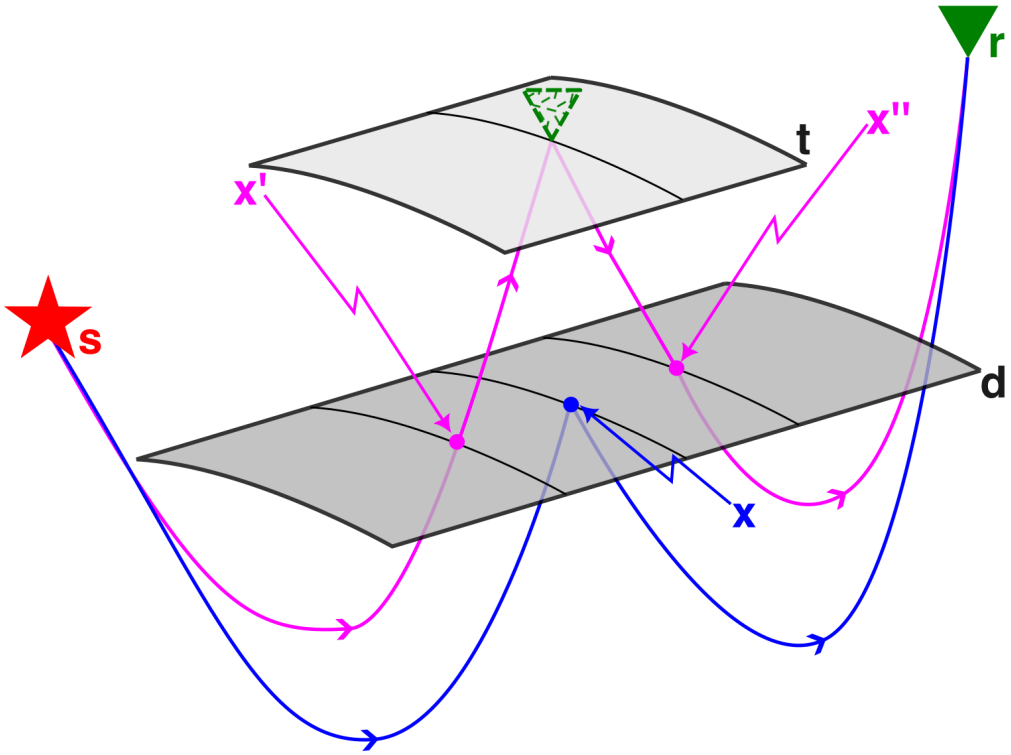

Figure 74: Sketch of the observation of discontinuity d using SdS (blue raypath) traveltime relative to SS travel time (magenta raypath). Both phases travel from the source s (red star) to the receiver r. The interaction of the phases is described in the text with reference to 'scattering points' x, x', and x'' representing the reflection point of SdS and the pierce points of SS.

et al., 1999) implemented in the python module *ObsPy* (Krischer *et al.*, 2015). Jacobians were calculated via the 'geometrical spreading factor' of Aki and Richards (1980, p99), related by Dahlen (2005) to the Jacobian by

$$|J_{rs}| = (\beta_t \mathcal{R}_{rs})^2 \tag{4.4}$$

where β_t is the shear wave velocity at the surface, and $\mathcal{R}_{rs}$ is the Aki and Richards geometrical spreading factor which describes the geometric focussing and defocussing of rays in different media. $|\dot{m}(\omega)|^2$ is the power spectrum of the pulse; I use that given by (Dahlen's 2005 equation no. 108)

$$|\dot{m}(\omega)|^2 = \frac{\omega^2\tau^2}{2\pi} \exp\left(\frac{-\omega^2\tau^2}{4\pi^2}\right) \tag{4.5}$$

where τ is the characteristic period of the phase, for *SS*-precursor studies this is 20 s. To calculate the finite-frequency kernel then, I use a similar range of frequencies as those allowed through bandpass filters used by *SS*-precursor studies, between periods of 15 and 50 s (the corresponding frequencies replace the upper and lower bounds respectively in 4.3) at a thousand linearly spaced intermediate frequencies.

However, the topography is determined by reference to the *SS* phase, which as it passes through the discontinuity, also has some sensitivity to the discontinuity of interest. Therefore, we desire K^{SS-SdS}, which is given by

$$K^{SS-SdS} = K^S_{x'} + K^S_{x''} - K^{SdS}_x \tag{4.6}$$

where x', x'', and x' refer to the points on d in Figure 74. The traveltime kernel of a transmitted S-wave is given by (Dahlen's 2005 equation no. 77)

$$K^S = \frac{-1}{2\pi}\left[\frac{|\cos(f)|}{\beta}\right]^+_- \sqrt{\frac{\cos^2(f)|J_{rs}|}{|J_{xs}||J_{xr}|}} \frac{\int_0^\infty \omega^3 |\dot{m}(\omega)|^2 \cos(\omega\cdot(T_{xs}+T_{xr}-T_{rs}))d\omega}{\int_0^\infty \omega^2|\dot{m}(\omega)|^2 d\omega} \tag{4.7}$$

and to evaluate them for each leg of the *SS* phase, I consider it as two S phases split at the surface bouncepoint (indicated by the dashed receiver symbol in Figure 74). I evaluate these kernels for the PREM (Dziewonski and Anderson, 1981) 1D seismic model at the depths they found their discontinuities (400 and 670 km depth) on a global 2° grid (although as phase geometries will prevent most points from receiving a direct S arrival from any given source, and similarly for the receiver, large areas have null-sensitivity). There is a linear trade-off between the number of points the kernel is evaluated at and the cost of the kernel calculation, so like Lawrence and Shearer (2008) I take this as a good

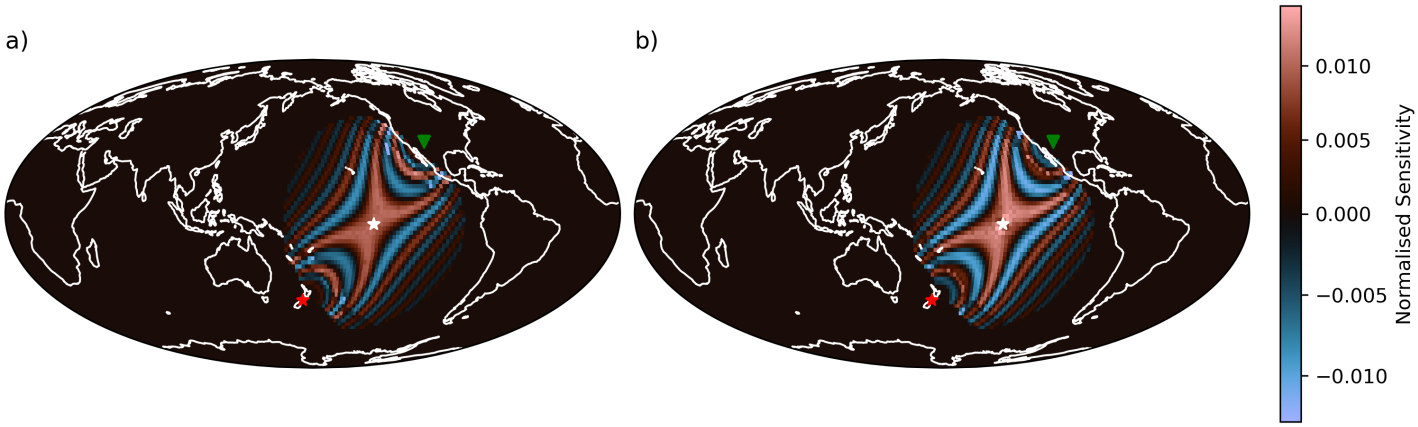

Figure 75: Sensitivity kernels to discontinuity topography evaluated on a 2° grid for PREM (Dziewonski and Anderson, 1981) seismic structure at *a)* d400 and *b)* d670. Illustrated for the 10/02/1998 Earthquake on the South Island of New Zealand to Albuquerque, New Mexico.

compromise resolution for this initial demonstration. To prepare the kernels to be used in the filtering here, they are normalised by the total global sensitivity on each kernel so that the kernel's value at each gridpoint corresponds to the proportion of the observed discontinuity depth for that bouncepoint is recovered from that location. Example sensitivity kernels are illustrated in Figure 75 for d400 and d670.

The unfiltered topography was gridded into the same 2° degree grid. Whilst this introduces an unphysical averaging stage in the reparametrisation (e.g. Schuberth *et al.*, 2009*a*; Robl *et al.*, 2025), for this simple demonstration problem this is an acceptable approximation.

However, the calculation of tens of thousands of these sensitivity kernels is computationally expensive, so as this is a demonstration problem I consider the impact of a more thorough consideration of sensitivity on 10% of bouncepoints that Waszek *et al.* (2021) report as using in the Pacific hemisphere. This is still a computationally intensive task, requiring a total of 24 hours on one ARCHER2 node of 128 CPUs for these 3788 bouncepoints to calculate both sensitivity kernels. Calculating the full set of kernels was impractical for the purposes of preparing this thesis, hence the use of the spherical cap here and in Chapter 3. The filtered topography of simulation 477 is shown in Figure 76 a-c. Qualitatively, the range of discontinuity depths away from upwellings and downwellings does not seem that different to the topography recovered using the bouncepoint spherical cap filter for simulation 477, although the quality of topography recovery is much poorer, with topography displaced thousands of kilometres away from the geodynamic source of the signal (e.g. uplifted d410 due to SE-Asia subduction zones underneath Australia). As this has only been

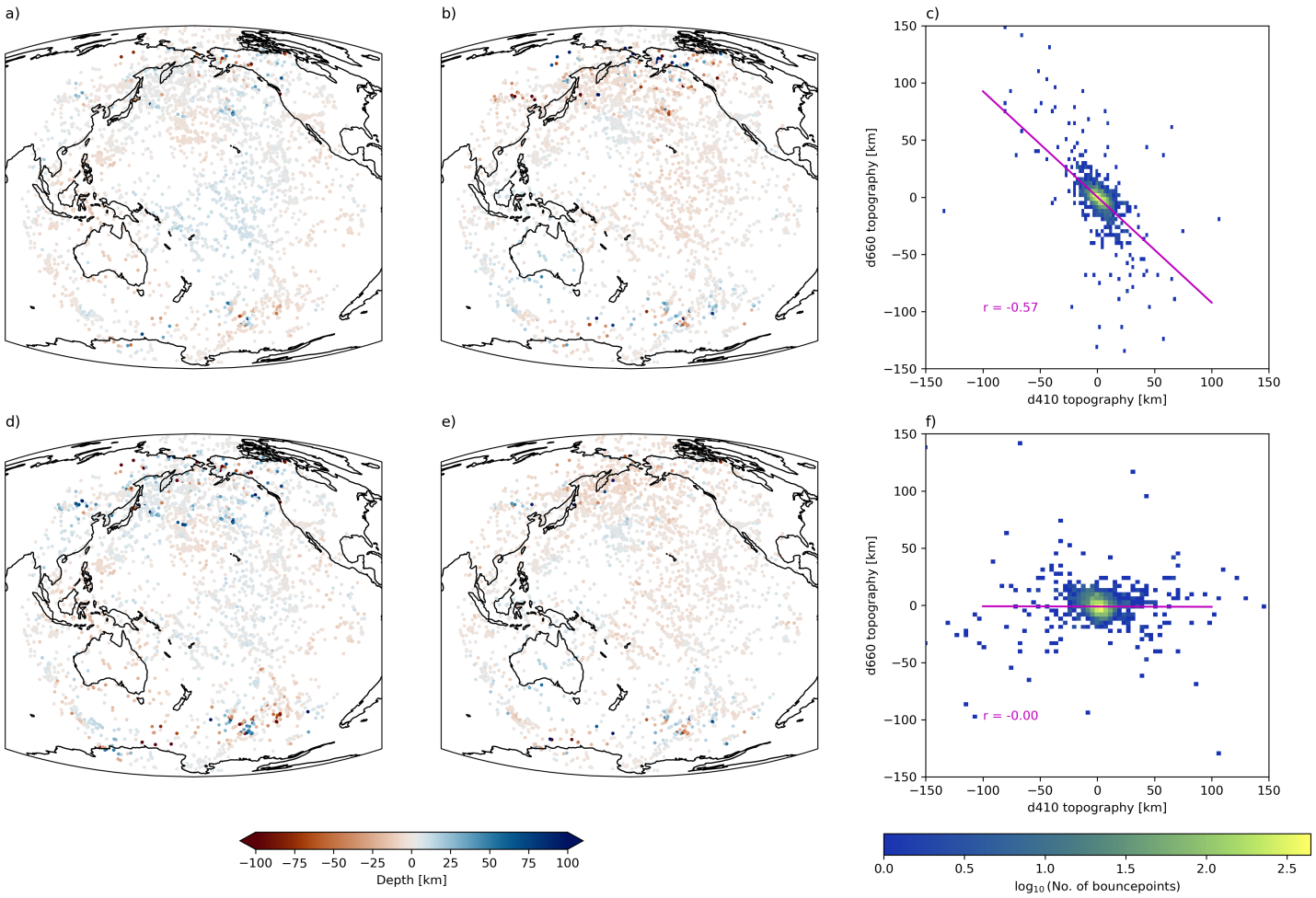

Figure 76: Mantle transition zone topography predicted from MCMs, filtered using finite frequency sensitivity kernels. *a)* d410 for simulation 477 *b)* d660 for simulation 477 *c)* d410-d660 correlation for simulation 477 *d-f)* ditto for simulation 479

evaluated on one hemisphere it is non-trivial to calculate the spherical harmonic spectra and correlation spectra as I have above. Instead I correlate the topography at each bouncepoint on d410 and d660. For simulation 477 this still results in a strong anticorrelation of d410 and d660 (Figure 76c).

Additionally in Figure 76d-f I filter the topographies from simulation 479 in the same way. Similarly this results in a reduced amplitude signal and topography with surprising sensitivity to topography thousands of kilometres away. Simulation 479 already had very muted d660 topography, but it is reduced so much here that d410 is independent of d660 (Figure 76f). This is still a fair ways away from producing a positive d410-d660 correlation but may be part of the solution in concert with some of the other suggestions above.

4.5 Conclusions

Having considered a suite of MCMs of varying radial viscosity structure, CMB temperature and compositional initial conditions, very few of these simulations made a favourable comparison to the Earth's mid-mantle discontinuity structure recovered using *SS*-precursors. Predicted d410, d660 and MTZ thickness structure appeared strongly sensitive to changes in mantle structure due to viscosity profile compared to the CMB temperature and BMS presence, although a secondary effect was often seen from piles. In particular, fit to d410 structure was not approached in any of the simulations in this suite, although some simulations approached d660 structure where the viscosity in the lower MTZ was relatively weak. No simulations approached the global positive correlation between d410 and d660 are strongly negatively correlated. I have considered various possibilities to explain the positive correlation, but none alone have proved to be sufficient.

Chapter 5

Discussion

Over the course of this thesis I have studied, from a geodynamicist's perspective, the impact of complex mineral phase stability fields on the flows of the mantle interior and our observations of the phase transitions in the mid-mantle.

5.1 Dynamic Impact of Phase Transitions

In chapter 2 I extended the sheet-mass approximation (Tackley *et al.*, 1993; Bunge *et al.*, 1997) used to implement phase boundary forces in TERRA for phase transitions in the lower mantle transition zone recently discussed in the literature, namely the ringwoodite decomposition *via* akimotoite (Chanyshev *et al.*, 2022) and the decomposition of garnet (Ishii *et al.*, 2023). Due to the limitations of thermodynamics and the suggested parameters respectively I did not consider either of these likely.

As I discussed in the chapter, this extension of the sheet-mass approximation was at the edge of its validity. Moving to lower, more Earth-like, viscosities increases the dynamic impact of phase transitions with the same parameters, so potentially could slightly increase the dynamic effect of the post-garnet reaction on the flow and maybe permit the akimotoite-out reaction to have a distinct impact, although my judgment is that this is somewhat unlikely. Conclusively addressing this would require high-resolution mantle circulation models at low viscosity and re-implementing the phase forces in a phase function scheme (Christensen and Yuen, 1985) so that the buoyancy forces moving between different radial grid layers is accurately handled. Given the expectation that this will produce a further null-result, I do not anticipate it being a future research priority. Although given the high Clapeyron slope of the bridgmanite to post-perovskite reaction (6.5 MPa.K^{-1}, Kuwayama *et al.* 2022) and the anticipated finite width of the bridgmanite-post-perovskite reaction, developing a implementation of the phase function method for TERRA may be

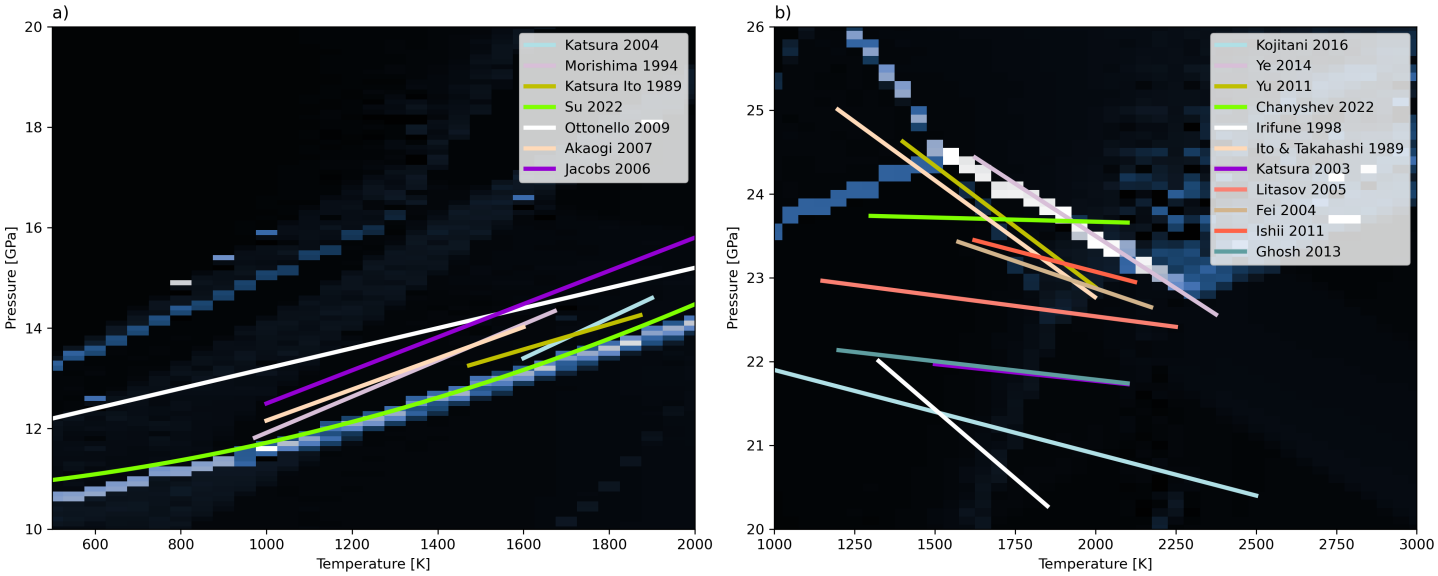

Figure 77: Reported phase boundaries in the region around *a)* d410 (Katsura *et al.*, 2004; Morishima *et al.*, 1994; Katsura and Ito, 1989; Su *et al.*, 2022; Ottonello *et al.*, 2009; Akaogi *et al.*, 2007; Jacobs *et al.*, 2006) and *b)* d660 (Kojitani *et al.*, 2016; Ye *et al.*, 2014; Yu *et al.*, 2011; Chanyshev *et al.*, 2022; Irifune *et al.*, 1998; Ito and Takahashi, 1989; Katsura *et al.*, 2003; Litasov *et al.*, 2005; Fei *et al.*, 2004; Ishii *et al.*, 2011; Ghosh *et al.*, 2013) plotted against the vertical reflectivity structure used in Chapters 3 and 4 for Lherzolite derived from the Stixrude and Lithgow-Bertelloni (2022) dataset.

necessary to allow lowermost mantle dynamics to be properly addressed.

5.2 Certainty in Mantle Transition Zone Equilibrium Phase Relations.

Much of the work and discussion in this thesis rests on results from mineral physics on the stability of mineral phases under mid-mantle conditions. These are either determined by use of laser heated diamond anvil cells (e.g. Morishima *et al.*, 1994) or other presses where samples are heated and compressed to mid-mantle conditions before the stable assemblage is analysed either by *in situ* X-ray diffraction (e.g. Morishima *et al.*, 1994), or by the sample first being quenched and then analysed (e.g. Katsura and Ito, 1989). Alternatively the stability fields are estimated computationally either *ab initio* with reference to the mineral structures (e.g. Yu *et al.*, 2011) or with reference to experimentally determined thermodynamic parameters at ambient pressure (e.g. Su *et al.*, 2022).

A variety of phase boundaries for the olivine to wadsleyite and ringwoodite to bridgmanite and periclase reactions are plotted in Figure 77 against the

reflectivity structure for Lherzolite seismic tables used in Chapters 3 and 4, which are determined by a Gibbs free energy minimisation from the Stixrude and Lithgow-Bertelloni (2024) dataset. On both d410 and d660 there is a significant spread in reported Clapeyron slopes of the key controlling reactions, as well as a broad spread in equilibrium pressures (largely due to different pressure gauges being used, e.g. Ye *et al.* 2014).

For the dynamics, the spread of Clapeyron slopes and reaction depths is unlikely to cause a significant issue – all of the slopes reported for olivine out are positive, as is commonly implemented in geodynamic simulations. The slopes reported for ringwoodite-out, especially recently (e.g. Chanyshev *et al.*, 2022), are quite low so that the resulting phase buoyancy parameter would not move an Earth-like convecting mantle into a layered convection regime (e.g. Wolstencroft and Davies, 2011).

For the prediction of seismically observed d410 and d660 topographies, this spread is likely much more important. Whilst the difference in a Clapeyron slope between -0.1 MPa.K^{-1} (Chanyshev *et al.*, 2022) and -2.5 MPa.K^{-1} (Ye *et al.*, 2014) on ringwoodite-out is not going to result in layered convection, for a 1000 K temperature range in the mid-mantle it is the difference in anticipating 2.5 km of topography and 62.5 km (assuming a mid-mantle pressure gradient of 40 MPa.km^{-1}), such a difference in ranges of topography would change our assessment of a geodynamic model quite significantly.

It is in the nature of the mineral physics datasets (e.g. Stixrude and Lithgow-Bertelloni, 2024) that are used to generate the look-up tables of seismic properties that particular parameters must be selected, informed by experimental studies. However, without explicit uncertainties in these tables, it is easy to mistakenly take the highly uncertain parameters of phase boundaries as confidently known (R. Myhill, *pers. comm.*). If, say, the Clapeyron slope in the Stixrude and Lithgow-Bertelloni (2024) dataset for ringwoodite to bridgmanite and periclase is higher than the actual value in nature, we would assess MCMs with lower temperature ranges in the mid-mantle more favourably when we considered the d660 structure. These would likely have a lower viscosity around the d660, and so we might underestimate the viscosity of the mid-mantle if the ringwoodite-out Clapeyron slope is overstated.

Further, recent work (Huang *et al.*, 2025) suggests d660, particularly the jump in V_P and V_S, may not be well explained by the Ringwoodite-out reaction.

5.3 Reaction Kinetics

Thus far, I have mostly assumed that phase transitions happen near-instantaneously, and the phase assemblages will always be the equilibrium assemblage. However, there is sufficient evidence (e.g. of metastable Olivine wedges in cold slabs (e.g. Kawakatsu and Yoshioka, 2011)). I sketched some of the potential impacts of this in section 4.4.5. King *et al.* (2015) illustrated the potential dynamic effect of kinetics for pyroxene to garnet reaction and Agrusta *et al.* (2014) also considered the impact of olivine reaction kinetics, promoting slab stagnation with the parameters selected for the pyroxene to garnet reactions having a more significant effect than the olivine-wadsleyite reactions, although this has not yet been implemented in global 3D models.

Of course, having discussed above our potentially quite poor knowledge of equilibrium phase relations, estimations of the rate of reaction are similarly poorly constrained. Given the poor fit to d410 for the current combination of geodynamics, mineral physics and seismic filtering scheme, and the possibility of a significant role for disequilibrium phase relation around d410, there is a natural extension of the workflow of chapters 3 and 4 to use the radial component of velocity to calculate the time in the wadsleyite stability field and therefore the relative proportions of olivine and wadsleyite.

5.4 Sensitivity of SS Precursors

As I have highlighted in chapter 3, the comparison of d410-d660 structure to observations using *SS* precursors requires a handling of the sensitivity of these seismic phases to a discontinuity surface that is much rougher than that recovered by studies in the real Earth. I suggest that there is a series of approximations with increasing similarity to the underlying physics. First, the spherical cap filter discussed in Chapter 3 where the sensitivity of the phase is as simplified as possible whilst still acknowledging the uneven distribution of bouncepoints within the Earth. Second, the finite frequency kernel for a horizontal reflector that I applied as a filter in Chapter 4. Whilst this captures the complex sensitivity away from the ray-theoretical bouncepoint, it doesn't allow a consideration of the complexities of the interaction of a wavefront with a rough discontinuity or a complex region of elevated reflectivity. This is a significant gap in our current understanding of the *SS*-precursor observation. Previous workers (e.g. Koroni and Trampert, 2021) have shown an accurate recovery of observed d410 and d660 structure when using a full waveform, but the recovery of a geodynamically anticipated rough discontinuity (Figure 44)

has not yet been considered.

5.5 Water and Melt

Another complication that I have not considered here is the effect of hydration and any partial melt in the mantle transition zone. Water is anticipated to be more soluble in wadsleyite and ringwoodite than the upper and lower mantle assemblage (e.g. Price *et al.*, 2019). This potentially would favour the water bearing phase, elevating and depressing d410 and d660 respectively in wet regions (e.g. Houser, 2016). Additionally, the change of solubility around d410 potentially would favour the formation of localised partial melt along d410 if local convection brought material from the MTZ to the upper mantle (Bercovici and Karato, 2003). Low velocity lenses have been reported (e.g. Revenaugh and Sipkin, 1994; Song *et al.*, 2004; Tauzin *et al.*, 2017; Wei and Shearer, 2017) on top of d410 which have been interpreted as lenses of melt, including beneath North America by Carr *et al.* (2025). Interestingly, these are in a similar location as to where Houser (2016) note deflection of d410 and d660 consistent with water controlling mantle transition zone topography. This could either affect the observation by locally cooling the mantle due to the enthalpy of melting, or by making the discontinuity in regions of partial melt appear brighter, and bias returned signal compared to regions that remain below the solidus. The role of water on the phase diagram remains contentious, with some authors (e.g. Ghosh *et al.*, 2013) claiming that the presence of water deepens the phase transformation and makes the Clapeyron slope more negative (i.e. makes the temperature-dependence more extreme), and others (e.g. Muir *et al.*, 2021) claiming the extremes of the probable concentration of water depress the ringwoodite-out transformation by ~ 8 km, but do not have any appreciable effect on the Clapeyron slope of the phase transformation. If such hydration were to be quite localised, given the results of the filtering introduced in Chapter 3, the impact on global discontinuity structure could be very limited compared to the stronger global thermal signal, though of course if the clapeyron slope of ringwoodite-out were reduced, it would be more notable. The current evidence for or against the presence of significant wt% of water in the MTZ is currently subtle and not yet entirely convincing (e.g. Houser, 2016; Wang *et al.*, 2021; Fei *et al.*, 2017). However, in balance, the roles of water and melt around the mantle transition zone are probably most interesting due to the potential impacts on geochemistry and as as a store for water over Earth history (e.g. Bercovici and Karato, 2003; Ohtani, 2021; Muir *et al.*, 2025) instead of global seismology or geodynamics.

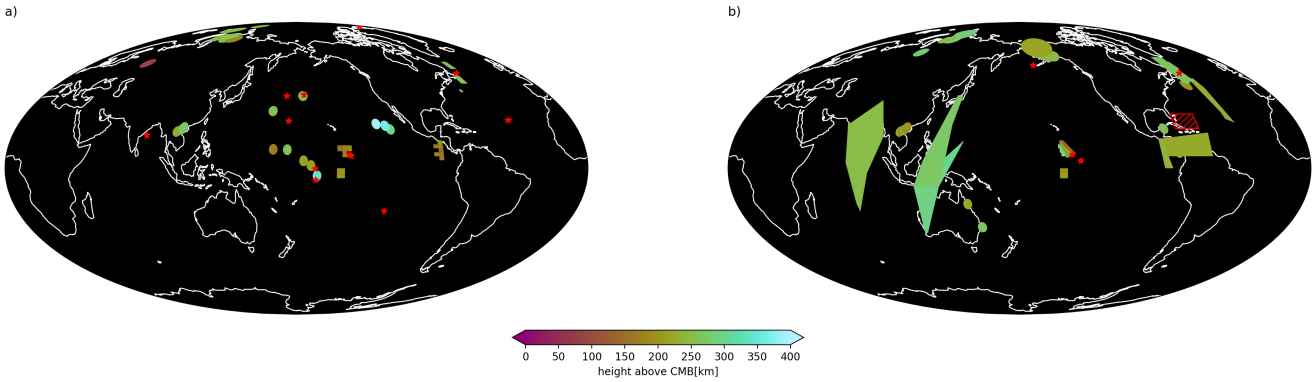

Figure 78: Height of D'' reflector above CMB *a)* observations in P-wave structure *b)* observations in S-wave structure. Red stars and hatched regions are areas where a robust null-observation has been reported. Sources are listed in Table 9 in Appendix A.

5.6 Discontinuities in the Lower Mantle

So far the focus has been fairly closely on the transitions in the mantle transition zone, but there are other seismically observed discontinuities aside from d410 and d660, namely in the lowermost mantle a precursor to *ScS* has been observed since the 1980s (e.g. Lay and Helmberger, 1983), and is usually interpreted in terms of a phase transition (Sidorin *et al.*, 1998) from bridgmanite to post-perovskite (Murakami *et al.*, 2004; Oganov and Ono, 2004), which is expected to have a large positive Clapeyron slope and possibly a lower viscosity than the overlying mantle.

ScS precursors have been reported in many regions, summarised in Figure 78, and there is an emerging picture of global topography on this boundary. This potentially represents another dataset to compare MCMs to, although this may be more complex and conditional than for the MTZ discontinuities discussed above, particularly since the observations presented together in Figure 78 were obtained by a broad suite of techniques and are not necessarily comparable to each other or a synthetic reflectivity structure.

Firstly, having highlighted the large uncertainties in the mid-mantle phase diagram above, due to the much higher pressures and temperatures, experiments to synthesise post-perovskite are more difficult than those constraining the ringwoodite-bridgmanite phase boundary, for instance, so there are fewer observations. Further, the chemical composition of the lowermost mantle is strongly debated, which does effect the stability of the post-perovskite phase. Secondly, instead of a simple reflected phase *SdS*, much of the precursor is from the refracted phase *SDS*, which samples more of the boundary region as it turns, so some of the simplifying assumptions I made in Chapters 3 and 4

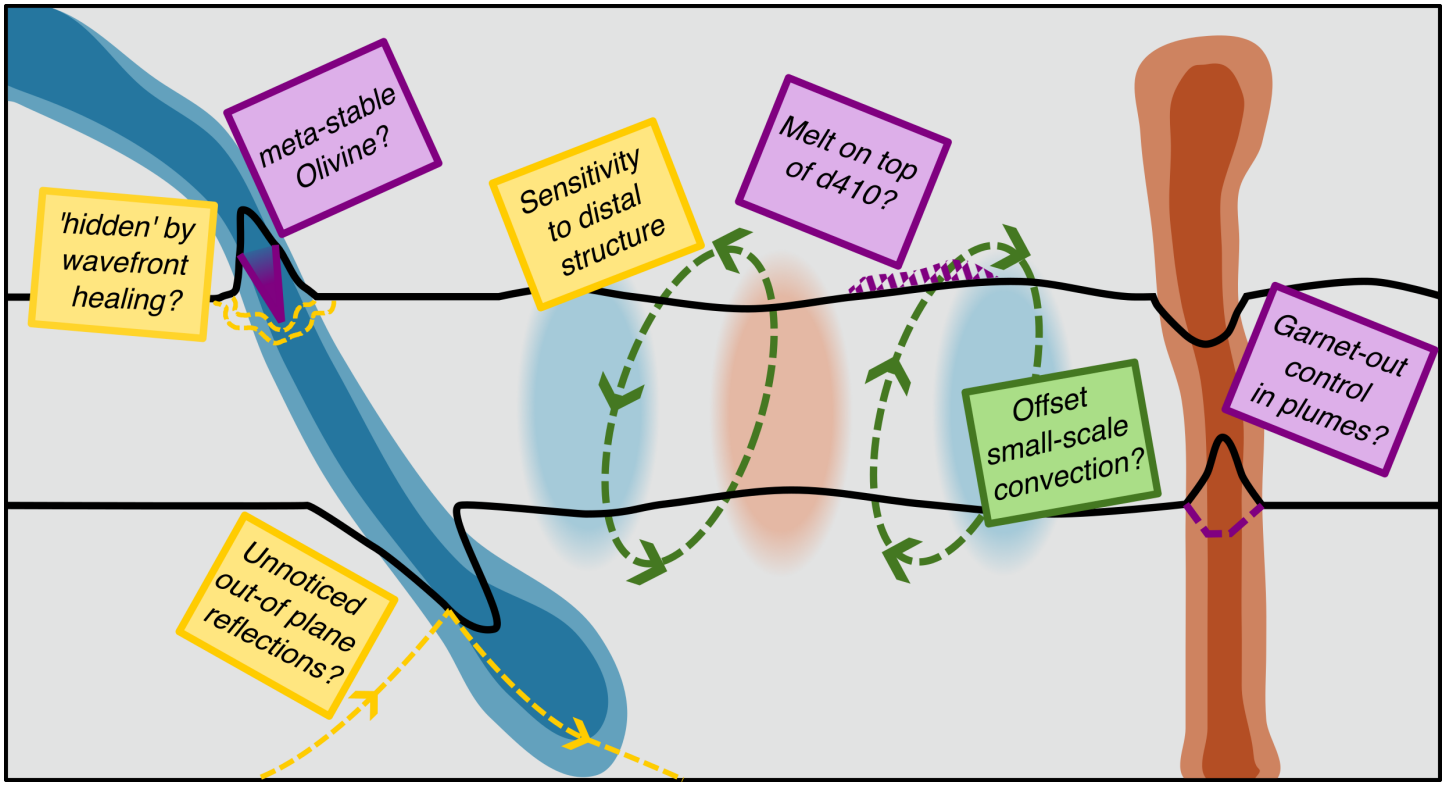

Figure 79: Cartoon of possible explanations of positive correlations of d410 and d660. Yellow 'post-it notes' and annotations are seismological, Green geodynamic, and purple mineral physical putative explanations.

may no longer apply.

However, tackling these issues would allow expected observations of the D″ discontinuity to be produced for geodynamic simulations with different assumptions about the compositional or rheological structure.

5.7 Where Does the Positive Correlation of d410 and d660 Come From?

As highlighted in Chapter 4, despite varying a broad suite of geodynamic parameters I was unable to produce correlated d410-d660 structures from well-resolved simulations. Figure 79 illustrates some potential explanations.

Structure on d410 may be more complex than that expected for a discontinuity controlled by a single reaction, either due to meta stable wedges of olivine in downgoing slabs or the formation of partial melt on d410. However, these are unlikely as complete solutions since the first would need some way of taking the positive correlation from the extremely local to the global and the second is probably quite minor as an effect.

If plume excess temperatures are sufficiently high they may deliver sufficient

basalt to the lower mantle transition zone, resulting in the deeper garnet-out reaction controlling the discontinuity depth. We saw this in several of the simulations I presented in Chapter 4, where it did not result in global correlation of d410 and d660, but like the meta-stable olivine with some method of spreading the resulting positive correlation could be important.

It is often suggested (e.g. Goes *et al.*, 2022) that the positive correlation of d410 and d660 is due to uncorrelated thermal structure between d410 and d660. Geodynamic intuition and 3D simulations (Chapter 4) suggest that for the larger circulatory flows this is unlikely. In this thesis, due to the comparatively poor resolution of the models used, I have not been able to consider smaller scale convective structure in the mantle transition zone, and it is therefore strictly possible that these could explain the d410-d660 correlation if they control the discontinuities away from the plumes and slabs.

However, before explaining the observation of positive d410-d660 correlation, we need to understand the seismological observation. The brief demonstration I gave of the finite frequency kernel filter in Chapter 4 suggests that many bouncepoints may have significant sensitivity to regions thousands of kilometres away from the ray theoretical bouncepoint. Further, due to the steep discontinuity surface, there may be complex interactions between the wavefront and the reflector that obscure elevations on d410. Finally, Rochira and Thomas (2023) showed that out-of plane arrivals of *SS*-precursors may result in energy from discontinuity reflections in the mantle transition zone being misinterpreted as deeper scatterers, which might also result in some error in the interpretation of discontinuity topography recovered from precursors.

5.8 Future Work

I have alluded to several areas where future work is required.

A fundamental shortcoming of the models presented in this thesis is the unrealistic rheologies employed in them. To draw meaningful conclusions about Earth requires realistic mantle rheologies so it would be desirable to run much higher resolution simulations which are well resolved with mid-mantle viscosities on order 10^{20} or 10^{21} Pa.s. As well as permitting simulation of the mantle at Earth-like vigour (which may in itself change the pattern of convection in the mid-mantle, and its expression in predicted discontinuity topographies), these simulations would also be more likely to efficiently segregate harzburgite and basalt in the basalt density filter due to the reduced viscosity, permit the inclusion of weak uppermost aesthenosphere (e.g. Cerpa *et al.*, 2022). As mentioned elsewhere in the thesis, the rheology employed here is simple, with a

mild temperature dependence. Employing a more realistic rheology is clearly a logical next step, and we might reasonably expect a rheology with a much stronger temperature dependence in particular to produce more Earth-like slab dynamics in the mantle transition zone, particularly the ponding of slabs (e.g. Chen *et al.*, 2022). This rheologically more complicated set of models would also ideally include grain size effects (e.g. Gülcher *et al.*, 2022) and non-linear rheology laws that more accurately approximate dislocation creep. In retrospect the suite of Chapter 4 was maybe larger than necessary, with variations of CMB temperature less impactful than I had been expecting. It may have been better to instead run fewer high vigour Earth-like MCMs instead which might have better captured the deflection of slabs in the MTZ, and the accumulation of high C-value material in the basalt density filter.

A proper quantification of the effect of different methods for handling the sensitivity of *SS*-precursors to the discontinuity topography is necessary. This would compare the bouncepoint spherical cap filter and a finite frequency sensitivity kernel filter with the topography recovered using a full waveform being propagated through either a reference 1D model modified with the geodynamically predicted discontinuity or through the synthetic seismic structure of the whole mantle transition zone. This would be focused on the sensitivity to the steep deflections around upwellings and downwellings as this is where more complex physics may be expected to bias the observations.

An improved implementation of olivine metastability could also result in some interesting results. First, a look-up table of the seismic properties of olivine would be created using the parameters used within its stability field, extended deeper into the mantle. To create a reflectivity structure then, we would require some kind of quantification of the kinetics to give proportions of the equilibrium and disequilibrium tables to mix. Initially, at least, this would be quite arbitrary, but could in principle be tuned to published models of olivine-wadsleyite kinetics. This might also help to establish in a global circulation context the potential role of the buoyant metastable wedge and if implementing it into global circulation codes is important for an accurate description of slab dynamics. Considerations of the kinetically delayed phase transition would pair well with the extension of the methods in Chapter 3 to receiver functions, which given the extensive networks in place in North America, East Asia and Europe would make an interesting comparison. The shallow dynamics implemented in global mantle circulation models are significantly simplified to those implemented and captured by 3D regional models (e.g. Jiang *et al.*, 2025), so a comparison to these would be preferable.

Extending this methodology to the D'' discontinuity would not be so very

difficult, and as discussed above would result in some point of comparison between the hot thermal boundary layer in MCMs and the D'' in Earth, which is poorly constrained. A comparison could be made either in regions where observations have been reported (Figure 78) or by considering suitable earthquakes and stations with a separation where a reflection might be visible above the noise. This would be of interest as non-observation of D'' has thermal and potentially compositional implications, but the current literature is biased towards positive observations.

Conclusions

I have explored the interaction of mineral physics, geodynamics and seismology in this thesis, particularly the interaction of geodynamics and seismology with the increasingly complex picture of mineral phase relations in mantle materials. I intended to evaluate the role of more complex phase relations (i.e. the complex patchwork of phase stability fields suggested by gibbs-free energy minimisation codes) on the dynamics and seismology of the MTZ.

In Chapter 2 I showed that branching phase boundaries (such as the ringwoodite to bridgmanite and periclase reaction *via* akimotoite) are not expected to have an effect on the global convection (since enthalpy and volume changes must be conserved at the branching point), and that therefore the simple ringwoodite to bridgmanite and periclase reaction is an acceptable approximation for the olivine-system reactions in the lower mantle transition zone. Curved phase boundaries were found to be able to exert distinct effects in cold and warm regions, but only when the phase parameters were much higher in magnitude than those suggested in the literature for post-garnet.

A method to use the thermochemical structures predicted by mantle circulation models to predict d410 and d660 was developed in Chapter 3. I demonstrated that discontinuity surfaces predicted for mantle circulation models were much rougher than those recovered by *SS*-precursor studies, even when a simple filter for the sensitivity of the *SS*-precursor is applied, but that the MCM this was tested on did not perform well when compared to the Earth.

A variety of thermochemical structures were generated in Chapter 4, and evaluated using their predicted mid-mantle discontinuity structure. Simulations with a lower viscosity around d670 were able to produce a satisfactory fit to d670, although no simulations were able to produce a good fit for d410, the thickness of the mantle transition zone, or the correlation between the discontinuities. A variety of putative explanations for the positive correlation from the literature were tested (including a kinetic delay of the olivine-out reaction, whose impact was too limited to explain correlation away from subduction zones, and the enrichment of the lower mantle transition zone in basalt, which was judged to damage the good returned fit to d660), although

none were found to produce a positive correlation between the discontinuities or a d410 structure that matches published observations.

Whilst the poor match between the geodynamic simulations and observations in Chapters 3 and 4 is disappointing, it suggests that a lot remains to be learnt about the materials that make up the mantle transition zone, how it is observed, and therefore its dynamics. Whilst a simple parametrisation of the phase transformations seemed acceptable for the geodynamic problem in Chapter 2, including the full suite of phase transformations and some of the seismology of the seismic phases used yielded interesting results. In particular, whilst it is premature to attempt to constrain mid-mantle dynamics using the observation of the discontinuities alone, the synthetic discontinuities presented here have highlighted the extreme roughness of the phase transformation surface, and illustrated some of the basic sensitivity of the discontinuity topographies to the pattern of global circulation. I failed to evaluate how important the use of the full mineral physics tables were compared to using a parameterized prediction of the discontinuities. The next frontier is a fuller integration of the advances in our knowledge of mid-mantle mineralogy and computational methods in geodynamics and seismology.

Appendix A

Compilation of Observations of D'' Discontinuity

In Figures 11 and 78 I plotted literature observations of the D'' discontinuity. These are scattered across forty years of literature, so I collate a list of citations here, along with regions and reported discontinuity heights.

Table 9: Summary of literature observations of D''. Where no height above the CMB is reported (or a more complex topography is reported), the fourth column is blank, but where there is a robust null-observation reported in a region a $\times$ mark is used.

Citation	Phase	Region	h [km]
Lay and Helmberger 1983	S	Okhotsk to North America	278
Lay and Helmberger 1983	S	Okhotsk to Europe	318
Lay and Helmberger 1983	S	Argentina to North America	251
Schlittenhardt *et al.* 1985	S	Fiji to US	$\times$
Schlittenhardt *et al.* 1985	P	Fiji to South America	$\times$
Schlittenhardt *et al.* 1985	P	Brazil to Europe	$\times$
Schlittenhardt *et al.* 1985	P	Banda Sea to Europe	$\times$
Schlittenhardt *et al.* 1985	P	Okhotsk to Central America	$\times$
Schlittenhardt *et al.* 1985	S	Sea of Japan to US	$\times$
Young and Lay 1987	S	India//Indian Ocean	280
Davis and Weber 1990	P	Northern Siberia	293
Young and Lay 1990	S	Alaska and Bearing St	243
Revenaugh and Jordan 1991*b*	S	Sumba-Philippines to GUMO	340
Revenaugh and Jordan 1991*b*	S	Sumba-Philippines to MAJO	305
Revenaugh and Jordan 1991*b*	S	Sumba-Philippines to NWAO	330
Revenaugh and Jordan 1991*b*	S	Japan-Izu	
Houard and Nataf 1992	P	Northern Siberia	300

Citation	Phase	Region	h [km]
Houard and Nataf 1992	P	North Atlantic	300
Houard and Nataf 1993	P	Siberia (S)	
Houard and Nataf 1993	P	Siberia (Coast)	270
Houard and Nataf 1993	P	Offshore Siberia	280
Weber 1993	P	Nansen Basin	279
Weber 1993	P	Kara Sea	286
Weber 1993	P	Northern Siberia A	286
Weber 1993	S	Northern Siberia A	281
Weber 1993	S	Northern Siberia B	316
Kendall and Shearer 1994	S	off Queensland	300
Kendall and Shearer 1994	S	off Philippines	
Kendall and Shearer 1994	S	North Queensland	250
Kendall and Shearer 1994	S	Arabia	
Kendall and Shearer 1994	S	Sudan-Egypt-Libya	
Kendall and Shearer 1994	S	Madagascar	
Kendall and Nangini 1996	S	North of Caribbean	×
Kendall and Nangini 1996	S	West Cuba to Yucatan	290
Kendall and Nangini 1996	S	Panama to Antilles and Venezuela	250
Olivieri *et al.* 1997	S	Bellingshausen sea	
Reasoner and Revenaugh 1999	P	Pacific Central America 1	190
Reasoner and Revenaugh 1999	P	Pacific central America 2	208
Reasoner and Revenaugh 1999	P	Pacific Central America 3	184
Reasoner and Revenaugh 1999	P	Pacific Central America 4	162
Reasoner and Revenaugh 1999	P	Pacific Central America 5	182
Reasoner and Revenaugh 1999	P	Pacific Central America 6	212
Reasoner and Revenaugh 1999	P	Pacific Central America 7	218
Reasoner and Revenaugh 1999	P	Central Pacific 1	194
Reasoner and Revenaugh 1999	P	Central Pacific 2	174
Reasoner and Revenaugh 1999	P	Central Pacific 3	200
Reasoner and Revenaugh 1999	P	Central Pacific 4	212
Russell *et al.* 2001	P	Central Pacific	230
Thomas *et al.* 2002	P	N Siberia DAWY	210
Thomas *et al.* 2002	P	N Siberia	300
Thomas *et al.* 2002	P	South Russia	91
Lay *et al.* 2004	S	Eastern Pacific	264
Wallace and Thomas 2005	S	Newfoundland	220
Wallace and Thomas 2005	S	North-MidAtlantic	260

Citation	Phase	Region	h [km]
Avants *et al.* 2006	S	Central Pacific A	189
Avants *et al.* 2006	S	Central Pacific B	323
Avants *et al.* 2006	S	Central Pacific C	172
Avants *et al.* 2006	S	Central Pacific D	339
Avants *et al.* 2006	S	Central Pacific E	239
Avants *et al.* 2006	S	Central Pacific F	156
Avants *et al.* 2006	S	Central Pacific G	401
Avants *et al.* 2006	S	Central Pacific H	199
Avants *et al.* 2006	S	Central Pacific I	181
Lay *et al.* 2006	S	Central Pacific 1	345
Lay *et al.* 2006	S	Central Pacific 2	236
Lay *et al.* 2006	S	Central Pacific 3	161
Kito *et al.* 2007	P	Cocos Plate	
van der Hilst *et al.* 2007	S	Cascadia-Northern Andes	
Chaloner *et al.* 2009	S	SE Asia	240
Chaloner *et al.* 2009	P	SE Asia	250
Chaloner *et al.* 2009	S	SE Asia	190
Chaloner *et al.* 2009	S	SE Asia	230
Chaloner *et al.* 2009	S	SE Asia	305
Chaloner *et al.* 2009	S	SE Asia	230
Chaloner *et al.* 2009	S	SE Asia	340
Chaloner *et al.* 2009	S	SE Asia	220
Chaloner *et al.* 2009	P	SE Asia	270
Chaloner *et al.* 2009	P	SE Asia	290
Chaloner *et al.* 2009	P	SE Asia	250
Chaloner *et al.* 2009	P	SE Asia	310
Chaloner *et al.* 2009	P	SE Asia	310
Thomas and Laske 2015	P	Central Pacific	×
Thomas and Laske 2015	P	Central Pacific	391
Thomas and Laske 2015	P	Central Pacific	×
Thomas and Laske 2015	P	Central Pacific	×
Thomas and Laske 2015	P	Central Pacific	291
Thomas and Laske 2015	P	Central Pacific	441
Thomas and Laske 2015	P	Central Pacific	×
Thomas and Laske 2015	P	Central Pacific	×
Thomas and Laske 2015	P	Central Pacific	291
Thomas and Laske 2015	P	Central Pacific	291
Thomas and Laske 2015	P	Central Pacific	341

Citation	Phase	Region	h [km]
Thomas and Laske 2015	P	Central Pacific	241
Thomas and Laske 2015	P	Central Pacific	411
Thomas and Laske 2015	P	Central Pacific	191
Thomas and Laske 2015	P	Central Pacific	241
Yao *et al.* 2015	S	North Atlantic	304
Durand *et al.* 2019	S	North Atlantic (S)	300
Durand *et al.* 2019	S	North Atlantic (N)	300
Durand *et al.* 2019	S	North Atlantic C	×
Durand *et al.* 2019	P	North Atlantic (S)	300
Durand *et al.* 2019	P	North Atlantic (N)	300
Durand *et al.* 2019	P	North Atlantic C	×
Pisconti *et al.* 2019	S	Mid-Atlantic	
Pisconti *et al.* 2019	P	Mid-Atlantic	
Li and Miller 2021	S	Central America	
Hiemer and Thomas 2022	P	Offshore Brazil	
Pisconti *et al.* 2022	S	Southern Mid-Atlantic 'region 1'	
Pisconti *et al.* 2022	S	Southern Atlantic 'region 0	

Bibliography

Agius, M. R., Rychert, C. A., Harmon, N., Tharimena, S., and Kendall, J. M. A thin mantle transition zone beneath the equatorial Mid-Atlantic Ridge. *Nature*, **589**(7843):562–566, 2021. doi:10.1038/s41586-020-03139-x.

Agrusta, R., Goes, S., and van Hunen, J. Subducting-slab transition-zone interaction: Stagnation, penetration and mode switches. *Earth and Planetary Science Letters*, **464**:10–23, 2017.

Agrusta, R., van Hunen, J., and Goes, S. The effect of metastable pyroxene on the slab dynamics. *Geophysical Research Letters*, **41**(24):8800–8808, 2014. doi:10.1002/2014GL062159.

Akaogi, M., Takayama, H., Kojitani, H., Kawaji, H., and Atake, T. Low-temperature heat capacities, entropies and enthalpies of Mg2SiO4 polymorphs, and α-β-γ and post-spinel phase relations at high pressure. *Physics and Chemistry of Minerals*, **34**(3):169–183, 2007. doi:10.1007/s00269-006-0137-3.

Aki, K. and Richards, P. G. *Quantitative Seismology: Theory and Methods*. WH Freeman and Company, San Francisco, 1st edition, 1980.

Allègre, C., Manhès, G., and Lewin, E. Chemical composition of the Earth and the volatility control on planetary genetics. *Earth and Planetary Science Letters*, **185**(1-2):49–69, 2001. doi:10.1016/S0012-821X(00)00359-9.

Avants, M., Lay, T., Russell, S. A., and Garnero, E. J. Shear velocity variation within the D' region beneath the central Pacific. *Journal of Geophysical Research: Solid Earth*, **111**(B5), 2006. doi:10.1029/2004JB003270.

Baker, M. B. and Beckett, J. R. The origin of abyssal peridotites: a reinterpretation of constraints based on primary bulk compositions. *Earth and Planetary Science Letters*, **171**(1):49–61, 1999. doi:10.1016/S0012-821X(99)00130-2.

Bao, X., Lithgow-Bertelloni, C. R., Jackson, M. G., and Romanowicz, B. On the relative temperatures of Earth's volcanic hotspots and mid-ocean ridges. *Science*, **375**(6576):57–61, 2022. doi:10.1126/science.abj8944.

Baumgardner, J. R. *A Three-Dimensional Finite Element Model for Mantle Convection*. University of California, Los Angeles, 1983.

Baumgardner, J. R. and Frederickson, P. O. Icosahedral Discretization of the Two-Sphere. *SIAM Journal on Numerical Analysis*, **22**(6):1107–1115, 1985. Publication Title: Source: SIAM Journal on Numerical Analysis Volume: 22 Issue: 6.

Béguelin, P., Panton, J., Andersen, M., Elliott, T., Davies, H., Rodney, J., and Plimmer, A. Comparing Geochemical and Geodynamical Models of Plume and Ridge Mantle Source Composition. *Geochemistry, Geophysics, Geosystems*, **26**(8):e2025GC012357, 2025*a*. doi:10.1029/2025GC012357.

Béguelin, P., Stracke, A., Ballmer, M. D., Huang, S., Willig, M., and Bizimis, M. Variations in Hawaiian Plume Flux Controlled by Ancient Mantle Depletion. *AGU Advances*, **6**(2):e2024AV001434, 2025*b*. doi:10.1029/2024AV001434.

Bercovici, D. and Karato, S. I. Whole-mantle convection and the transition-zone water filter. *Nature*, **425**(6953):39–44, 2003. doi:10.1038/nature01918.

Bercovici, D., Schubert, G., and Glatzmaier, G. A. Three-Dimensional Spherical Models of Convection in the Earth's Mantle. *Science*, **244**(4907):950–955, 1989. doi:10.1126/science.244.4907.950.

Bernal, J. Response to 'The structure of the Earth down to the 20° discontinuity'. In *Geophysical Discussion*, volume LIX, pages 265–269. Observatory, London, 1936.

Bina, C. R. and Helffrich, G. Geophysical Constraints on Mantle Composition. In *Treatise on Geochemistry: Second Edition*, volume 3, pages 41–65. Elsevier, 2013. doi:10.1016/B978-0-08-095975-7.00202-3.

Bina, C. R. and Liu, M. A note on the sensitivity of mantle convection models to composition-dependent phase relations. *Geophysical Research Letters*, **22**(19):2565–2568, 1995. doi:10.1029/95GL02546.

Birch, F. Elasticity and constitution of the Earth's interior. *Journal of Geophysical Research (1896-1977)*, **57**(2):227–286, 1952. doi:10.1029/JZ057i002p00227.

Bird, P. An updated digital model of plate boundaries. *Geochemistry, Geophysics, Geosystems*, **4**(3), 2003. doi:10.1029/2001GC000252.

Bissig, F., Khan, A., and Giardini, D. Evidence for basalt enrichment in the mantle transition zone from inversion of triplicated P- and S-waveforms. *Earth and Planetary Science Letters*, **580**:117387, 2022. doi:10.1016/j.epsl.2022.117387.

Boehler, R. High-pressure experiments and the phase diagram of lower mantle and core materials. *Reviews of Geophysics*, **38**(2):221–245, 2000. doi:10.1029/1998RG000053.

Bonatto, L., Schlaphorst, D., Silveira, G., Mata, J., Civiero, C., Piromallo, C., and Schimmel, M. Unveiling the Distinct Structure of the Upper Mantle Beneath the Canary and Madeira Hotspots, as Depicted by the 660, 410, and X Discontinuities. *Journal of Geophysical Research: Solid Earth*, **129**(5):e2023JB028195, 2024. doi:10.1029/2023JB028195.

Bower, D. J., Gurnis, M., and Sun, D. Dynamic origins of seismic wavespeed variation in D". *Physics of the Earth and Planetary Interiors*, **214**:74–86, 2013. doi:10.1016/j.pepi.2012.10.004.

Bull, A. J. The Convection Current Hypothesis of Mountain Building. *Geological Magazine*, **68**(11):495–498, 1931. doi:10.1017/S001675680009840X.

Bull, A. L., Domeier, M., and Torsvik, T. H. The effect of plate motion history on the longevity of deep mantle heterogeneities. *Earth and Planetary Science Letters*, **401**:172–182, 2014. doi:10.1016/j.epsl.2014.06.008.

Bunge, H., Richards, M. A., Lithgow-Bertelloni, C., Grand, S., Baumgardner, J., and Romanowicz, B. Time scales and heterogeneous structure in geodynamic earth models. *Science*, **280**:91–95, 1998.

Bunge, H.-P. and Baumgardner, J. R. Mantle convection modeling on parallel virtual machines. *Computers in Physics*, **9**(2):207, 1995. doi:10.1063/1.168525.

Bunge, H.-P. and Davies, J. H. Tomographic images of a mantle circulation model. *Geophysical Research Letters*, **28**(1):77–80, 2001. doi:10.1029/2000GL011804. _eprint: https://onlinelibrary.wiley.com/doi/pdf/10.1029/2000GL011804.

Bunge, H. P., Richards, M. A., and Baumgardner, J. R. A sensitivity study of three-dimensional spherical mantle convection at 108 Rayleigh number:

Effects of depth-dependent viscosity, heating mode, and an endothermic phase change. *Journal of Geophysical Research: Solid Earth*, **102**(6):11991–12007, 1997. doi:10.1029/96jb03806.

Bunge, H.-P., Richards, M. A., and Baumgardner, J. R. Mantle–circulation models with sequential data assimilation: inferring present–day mantle structure from plate–motion histories. *Philosophical Transactions of the Royal Society of London. Series A: Mathematical, Physical and Engineering Sciences*, **360**:2545–2567, 2002. doi:10.1098/rsta.2002.1080.

Burky, A. L., Irving, J. C., and Simons, F. J. The mantle transition zone beneath eastern North America: Receiver functions and tomographic velocity models. *Physics of the Earth and Planetary Interiors*, **340**:107035, 2023. doi:10.1016/j.pepi.2023.107035.

Byerly, P. The Montana earthquake of June 28, 1925, G.M.C.T. *Bulletin of the Seismological Society of America*, **16**(4):209–265, 1926. doi:10.1785/BSSA0160040209.

Cammarano, F., Romanowicz, B., Stixrude, L., Lithgow-Bertelloni, C., and Xu, W. Inferring the thermochemical structure of the upper mantle from seismic data. *Geophysical Journal International*, **179**(2):1169–1185, 2009. doi:10.1111/j.1365-246X.2009.04338.x.

Capitani, C. d. and Petrakakis, K. The computation of equilibrium assemblage diagrams with Theriak/Domino software. *American Mineralogist*, **95**(7):1006–1016, 2010. doi:10.2138/am.2010.3354. Publisher: De Gruyter.

Carr, S. A. B., Olugboji, T., Park, J., and Karato, S.-i. High-resolution mapping of North America suggests numerous low-velocity zones above and below the mantle transition zone. *Tectonophysics*, **908**:230775, 2025. doi:10.1016/j.tecto.2025.230775.

Cerpa, N. G., Sigloch, K., Garel, F., Heuret, A., Davies, D. R., and Mihalynuk, M. G. The Effect of a Weak Asthenospheric Layer on Surface Kinematics, Subduction Dynamics and Slab Morphology in the Lower Mantle. *Journal of Geophysical Research: Solid Earth*, **127**(8), 2022. doi:10.1029/2022JB024494.

Chaloner, J. W., Thomas, C., and Rietbrock, A. P - and S -wave reflectors in D' beneath southeast Asia. *Geophysical Journal International*, **179**(2):1080–1092, 2009. doi:10.1111/j.1365-246X.2009.04328.x.

Chambers, K., Deuss, A., and Woodhouse, J. H. Reflectivity of the 410-km discontinuity from PP and SS precursors. *Journal of Geophysical Research: Solid Earth*, **110**(B2), 2005*a*. doi:10.1029/2004JB003345.

Chambers, K., Woodhouse, J. H., and Deuss, A. Topography of the 410-km discontinuity from PP and SS precursors. *Earth and Planetary Science Letters*, **235**(3):610–622, 2005*b*. doi:10.1016/j.epsl.2005.05.014.

Chanyshev, A., Ishii, T., Bondar, D., Bhat, S., Kim, E. J., Farla, R., Nishida, K., Liu, Z., Wang, L., Nakajima, A., Yan, B., Tang, H., Chen, Z., Higo, Y., Tange, Y., and Katsura, T. Depressed 660-km discontinuity caused by akimotoite–bridgmanite transition. *Nature*, **601**(7891):69–73, 2022. doi:10.1038/s41586-021-04157-z.

Chen, F., Davies, D. R., Goes, S., Suchoy, L., and Kramer, S. C. How Slab Age and Width Combine to Dictate the Dynamics and Evolution of Subduction Systems: A 3-D Spherical Study. *Geochemistry, Geophysics, Geosystems*, **23**(11):e2022GC010597, 2022. doi:10.1029/2022GC010597.

Chen, Y.-W., Wu, J., Bunge, H.-P., Stotz, I., Robl, G., and Schuberth, B. S. A. Tomopac2: an unfolded-slab plate reconstruction validated via mantle circulation models in a closed-loop experiment. *Proceedings of the Royal Society A: Mathematical, Physical and Engineering Sciences*, **481**(2318), 2025. doi:10.1098/rspa.2024.0726.

Chevrot, S., Vinnik, L., and Montagner, J.-P. Global-scale analysis of the mantle Pds phases. *Journal of Geophysical Research: Solid Earth*, **104**(B9):20203–20219, 1999. doi:10.1029/1999JB900087.

Christensen, U. R. Dynamic phase boundary topography by latent heat effects. *Earth and Planetary Science Letters*, **154**(1):295–306, 1998. doi:10.1016/S0012-821X(97)00192-1.

Christensen, U. R. and Yuen, D. A. The Interaction of a Subducting Lithospheric Slab With a Chemical or Phase Boundary. *Journal of Geophysical Research*, **89**(B6):4389–4402, 1984. doi:10.1029/JB089iB06p04389.

Christensen, U. R. and Yuen, D. A. Layered convection induced by phase transitions. *Journal of Geophysical Research*, **90**(B12), 1985. doi:10.1029/jb090ib12p10291.

Chust, T. C., Steinle-Neumann, G., Dolejš, D., Schuberth, B. S. A., and Bunge, H.-P. MMA-EoS: A Computational Framework for Mineralogical Thermodynamics. *Journal of Geophysical Research: Solid Earth*, **122**(12):9881–9920, 2017. doi:10.1002/2017JB014501.

Čížková, H. and Bina, C. R. Linked influences on slab stagnation: Interplay between lower mantle viscosity structure, phase transitions, and plate coupling. *Earth and Planetary Science Letters*, **509**:88–99, 2019. doi:10.1016/j.epsl.2018.12.027.

Clauser, C. and Huenges, E. Thermal Conductivity of Rocks and Minerals. In *A Handbook of Physical Constants: Rock Physics and Phase Relations*, edited by Ahrens, T. J., volume 3 of *AGU Reference Shelf Series*. American Geophysical Union, 1995.

Cobden, L., Thomas, C., and Trampert, J. Seismic Detection of Post-perovskite Inside the Earth. In *The Earth's Heterogeneous Mantle*, edited by Khan, A. and Deschamps, F., pages 391–440. Springer International Publishing, Cham, 2015. doi:10.1007/978-3-319-15627-9_13.

Collier, J. D. and Helffrich, G. R. The thermal influence of the subducting slab beneath South America from 410 and 660 km discontinuity observations. *Geophysical Journal International*, **147**(2):319–329, 2001. doi:10.1046/j.1365-246X.2001.00532.x.

Connolly, J. Computation of phase equilibria by linear programming: A tool for geodynamic modeling and its application to subduction zone decarbonation. *Earth and Planetary Science Letters*, **236**(1-2):524–541, 2005. doi:10.1016/j.epsl.2005.04.033.

Connolly, J. a. D. The geodynamic equation of state: What and how. *Geochemistry, Geophysics, Geosystems*, **10**(10), 2009. doi:10.1029/2009GC002540.

Cottaar, S. and Deuss, A. Large-scale mantle discontinuity topography beneath Europe: Signature of akimotoite in subducting slabs. *Journal of Geophysical Research: Solid Earth*, **121**(1):279–292, 2016. doi:10.1002/2015JB012452.

Crameri, F., Shephard, G. E., and Heron, P. J. The misuse of colour in science communication. *Nature Communications*, **11**(1):5444, 2020. doi:10.1038/s41467-020-19160-7.

Crotwell, H. P., Owens, T. J., and Ritsema, J. The TauP Toolkit: Flexible Seismic Travel-time and Ray-path Utilities. *Seismological Research Letters*, **70**(2):154–160, 1999. doi:10.1785/gssrl.70.2.154.

Dahlen, F. A. Finite-frequency sensitivity kernels for boundary topography perturbations. *Geophysical Journal International*, **162**(2):525–540, 2005. doi:10.1111/j.1365-246X.2005.02682.x.

Dai, Y. Global imaging of the mantle transition zone from SS precursors reveals a 660 dictated by expected thermal upwellings and downwellings, while the 410 requires more complexity. In *AGU Fall 2024*. Washington, D. C., 2024.

Dannberg, J., Eilon, Z., Faul, U., Gassmöller, R., Moulik, P., and Myhill, R. The importance of grain size to mantle dynamics and seismological observations. *Geochemistry, Geophysics, Geosystems*, **18**(8):3034–3061, 2017. doi:10.1002/2017GC006944.

Dannberg, J., Gassmöller, R., Li, R., Lithgow-Bertelloni, C., and Stixrude, L. An entropy method for geodynamic modelling of phase transitions: capturing sharp and broad transitions in a multiphase assemblage. *Geophysical Journal International*, **231**(3):1833–1849, 2022. doi:10.1093/gji/ggac293.

Davies, C. J. Cooling history of Earth's core with high thermal conductivity. *Physics of the Earth and Planetary Interiors*, **247**:65–79, 2015. doi:10.1016/j.pepi.2015.03.007.

Davies, D. R., Davies, J. H., Bollada, P. C., Hassan, O., Morgan, K., and Nithiarasu, P. A hierarchical mesh refinement technique for global 3-D spherical mantle convection modelling. *Geoscientific Model Development*, **6**(4):1095–1107, 2013. doi:10.5194/gmd-6-1095-2013.

Davies, D. R., Goes, S., Davies, J. H., Schuberth, B. S., Bunge, H. P., and Ritsema, J. Reconciling dynamic and seismic models of Earth's lower mantle: The dominant role of thermal heterogeneity. *Earth and Planetary Science Letters*, **353-354**:253–269, 2012. doi:10.1016/j.epsl.2012.08.016.

Davies, D. R., Goes, S., and Lau, H. C. Thermally dominated deep mantle LLSVPs: A review. In *The Earth's Heterogeneous Mantle: A Geophysical, Geodynamical, and Geochemical Perspective*, pages 441–477. Springer International Publishing, 2015*a*. doi:10.1007/978-3-319-15627-9_14.

Davies, D. R., Goes, S., and Sambridge, M. On the relationship between volcanic hotspot locations, the reconstructed eruption sites of large igneous

provinces and deep mantle seismic structure. *Earth and Planetary Science Letters*, **411**:121–130, 2015*b*. doi:10.1016/j.epsl.2014.11.052.

Davies, G. F. *Dynamic Earth: Plates, Plumes and Mantle Convection*. Cambridge University Press, Cambridge, 1999.

Davies, G. F. Episodic layering of the early mantle by the 'basalt barrier' mechanism. *Earth and Planetary Science Letters*, **275**(3-4):382–392, 2008*a*. doi:10.1016/j.epsl.2008.08.036.

Davies, J. H., Gudmundsson, O., and Clayton, R. W. Spectra of mantle shear wave velocity structure. *Geophysical Journal International*, **108**(3):865–882, 1992. doi:10.1111/j.1365-246X.1992.tb03476.x.

Davies, J. H., Panton, J., Altoe, I., Andersen, M., Béguelin, P., Biggin, A., Davies, C., Elliott, T., Engbers, Y., Fernandes, V. M., Ferreira, A., Fowler, S., Ghelichkhan, S., Koelemeijer, P., Latallerie, F., Li, A., Morgan, G., Mason, S., Myhill, B., Nowacki, A., Récalde, N., O'Malley, C., Plimmer, A., Porcelli, D., Roberts, G., Rodney, J., Shea, J., Shorttle, O., Sturgeon, W., Walker, A., Ward, J., and Wookey, J. How to assess similarities and differences between mantle circulation models and Earth using disparate independent observations: Data and Analysis. 2024. doi:10.5281/ZENODO.13960492.

Davies, J. H., Panton, J., Altoe, I., Andersen, M., Béguelin, P., Biggin, A., Davies, C., Elliott, T., Engbers, Y. A., Fernandes, V. M., Ferreira, A. M. G., Fowler, S., Ghelichkhan, S., Heinen, B. J., Koelemeijer, P., Latallerie, F., Li, W., Morgan, G., Mason, S. J., Myhill, R., Nowacki, A., O'Malley, C. P., Plimmer, A., Porcelli, D., Récalde, N., Roberts, G. G., Rodney, J. B., Shea, J., Shorttle, O., Sturgeon, W., Walker, A. M., Ward, J., and Wookey, J. How to assess similarities and differences between mantle circulation models and Earth using disparate independent observations. *Proceedings of the Royal Society A: Mathematical, Physical and Engineering Sciences*, **481**(2315):20240827, 2025. doi:10.1098/rspa.2024.0827.

Davies, N. S., Herringshaw, L. G., and Raine, R. J. Controls on trace fossil diversity in an Early Cambrian epeiric sea: New perspectives from northwest Scotland. *Lethaia*, **42**(1):17–30, 2009. doi:10.1111/j.1502-3931.2008.00130.x.

Davies, R. *Applying Multi-Resolution Numerical Methods to Geodynamics*. Cardiff University, School of Earth, Ocean & Planetary Sciences, 2008*b*.

Davis, J. P. and Weber, M. Lower mantle velocity inhomogeneity observed at

GRF array. *Geophysical Research Letters*, **17**(2):187–190, 1990. doi:10.1029/GL017i002p00187.

Deschamps, F. and Cobden, L. Estimating core-mantle boundary temperature from seismic shear velocity and attenuation. *Frontiers in Earth Science*, **10**:1031507, 2022. doi:10.3389/feart.2022.1031507.

Desiderio, M. and Ballmer, M. D. Ancient Stratified Thermochemical Piles Due To High Intrinsic Viscosity. *Geophysical Research Letters*, **51**(14):e2024GL110006, 2024. doi:10.1029/2024GL110006.

Deuss, A., Redfern, S. A. T., Chambers, K., and Woodhouse, J. H. The Nature of the 660-Kilometer Discontinuity in Earth's Mantle from Global Seismic Observations of *PP* Precursors. *Science*, **311**(5758):198–201, 2006. doi:10.1126/science.1120020.

Dong, J., Fischer, R. A., Stixrude, L. P., Brennan, M. C., Daviau, K., Suer, T.-A., Turner, K. M., Meng, Y., and Prakapenka, V. B. Nonlinearity of the post-spinel transition and its expression in slabs and plumes worldwide. *Nature Communications*, **16**(1):1039, 2025. doi:10.1038/s41467-025-56231-z.

Doubrovine, P. V., Steinberger, B., and Torsvik, T. H. A failure to reject: Testing the correlation between large igneous provinces and deep mantle structures with EDF statistics. *Geochemistry, Geophysics, Geosystems*, **17**(3):1130–1163, 2016. doi:10.1002/2015GC006044.

Durand, S., Thomas, C., and Jackson, J. M. Constraints on D" beneath the North Atlantic region from P and S traveltimes and amplitudes. *Geophysical Journal International*, **216**:1132 – 1144, 2019. doi:10.1093/gji/ggy476.

Dziewonski, A. M. and Anderson, D. L. Preliminary reference Earth model. *Physics of Earth and Planetary Interiors*, **25**:297–356, 1981.

Dziewonski, A. M., Hager, B. H., and O'Connell, R. J. Large-scale heterogeneities in the lower mantle. *Journal of Geophysical Research*, **82**(2):239–255, 1977. doi:10.1029/jb082i002p00239.

Edgeworth, R., Dalton, B. J., and Parnell, T. The pitch drop experiment. *European Journal of Physics*, **5**(4):198–200, 1984. doi:10.1088/0143-0807/5/4/003.

Faccenda, M., VanderBeek, B. P., de Montserrat, A., Yang, J., Rappisi, F., and Ribe, N. ECOMAN: an open-source package for geodynamic and

seismological modelling of mechanical anisotropy. *Solid Earth*, **15**(10):1241–1264, 2024. doi:10.5194/se-15-1241-2024.

Fei, H., Ballmer, M. D., Faul, U., Walte, N., Cao, W., and Katsura, T. Variation in bridgmanite grain size accounts for the mid-mantle viscosity jump. *Nature*, 2023. doi:10.1038/s41586-023-06215-0.

Fei, H., Yamazaki, D., Sakurai, M., Miyajima, N., Ohfuji, H., Katsura, T., and Yamamoto, T. A nearly water-saturated mantle transition zone inferred from mineral viscosity. *Science Advances*, **3**(6):e1603024, 2017. doi:10.1126/sciadv.1603024.

Fei, Y., Van Orman, J., Li, J., van Westrenen, W., Sanloup, C., Minarik, W., Hirose, K., Komabayashi, T., Walter, M., and Funakoshi, K. Experimentally determined postspinel transformation boundary in Mg2SiO4 using MgO as an internal pressure standard and its geophysical implications. *Journal of Geophysical Research: Solid Earth*, **109**(B2), 2004. doi:10.1029/2003JB002562.

Flament, N., Bodur, Ö. F., Williams, S. E., and Merdith, A. S. Assembly of the basal mantle structure beneath Africa. *Nature*, **603**(7903):846–851, 2022. doi:10.1038/s41586-022-04538-y.

Flanagan, M. P. and Shearer, P. M. Global mapping of topography on transition zone velocity discontinuities by stacking SS precursors. *Journal of Geophysical Research: Solid Earth*, **103**(B2):2673–2692, 1998. doi:10.1029/97JB03212.

Forsyth, D. and Uyeda, S. On the Driving Forces of Plate Tectonics. *Geophysical Journal of the Royal Astronomical Society*, **43**(3):163–200, 1975. doi:10.1111/j.1365-246X.1975.tb04143.x.

Fourel, L., Limare, A., Jaupart, C., Surducan, E., Farnetani, C. G., Kaminski, E. C., Neamtu, C., and Surducan, V. The Earth's mantle in a microwave oven: thermal convection driven by a heterogeneous distribution of heat sources. *Experiments in Fluids*, **58**(8), 2017. doi:10.1007/s00348-017-2381-3.

French, S. W. and Romanowicz, B. Broad plumes rooted at the base of the Earth's mantle beneath major hotspots. *Nature*, **525**(7567):95–99, 2015. doi:10.1038/nature14876.

Garel, F., Goes, S., Davies, D. R., Davies, J. H., Kramer, S. C., and Wilson, C. R. Interaction of subducted slabs with the mantle transition-zone: A regime diagram from 2-D thermo-mechanical models with a mobile trench

and an overriding plate. *Geochemistry, Geophysics, Geosystems*, **15**(5):1739–1765, 2014. doi:10.1002/2014GC005257.

Gassmöller, R., Dannberg, J., Bangerth, W., Heister, T., and Myhill, R. On formulations of compressible mantle convection. *Geophysical Journal International*, **221**(2):1264–1280, 2020. doi:10.1093/gji/ggaa078.

Ghosh, S., Ohtani, E., Litasov, K. D., Suzuki, A., Dobson, D., and Funakoshi, K. Effect of water in depleted mantle on post-spinel transition and implication for 660 km seismic discontinuity. *Earth and Planetary Science Letters*, **371-372**:103–111, 2013. doi:10.1016/j.epsl.2013.04.011.

Gilbert, G. K. *Lake Bonneville*, volume 1 of *Monographs of the United States Geological Survey*. Government Printing Office, Washington, D. C., 1890.

Girard, J., Amulele, G., Farla, R., Mohiuddin, A., and Karato, S.-i. Shear deformation of bridgmanite and magnesiowüstite aggregates at lower mantle conditions. *Science*, **351**(6269):144–147, 2016. doi:10.1126/science.aad3113.

Glasgow, M. E., Zhang, H., Schmandt, B., Zhou, W.-Y., and Zhang, J. Global variability of the composition and temperature at the 410-km discontinuity from receiver function analysis of dense arrays. *Earth and Planetary Science Letters*, **643**:118889, 2024. doi:10.1016/j.epsl.2024.118889.

Glatzmaier, G. Numerical Simulations of Mantle Convection: Time-Dependent, Three-Dimensional, Compressible, Spherical Shell. *Geophysical & Astrophysical Fluid Dynamics*, **43**:223–264, 1988. doi:10.1080/03091928808213626.

Goes, S., Cammarano, F., and Hansen, U. Synthetic seismic signature of thermal mantle plumes. *Earth and Planetary Science Letters*, **218**(3-4):403–419, 2004. doi:10.1016/S0012-821X(03)00680-0.

Goes, S., Capitanio, F. A., and Morra, G. Evidence of lower-mantle slab penetration phases in plate motions. *Nature*, **451**(7181):981–984, 2008. doi:10.1038/nature06691.

Goes, S., Yu, C., Ballmer, M. D., Yan, J., and van der Hilst, R. D. Compositional heterogeneity in the mantle transition zone. *Nature Reviews Earth & Environment*, **3**(8):533–550, 2022. doi:10.1038/s43017-022-00312-w.

Gordon, R. B. Thermally Activated Processes in the Earth: Creep and Seismic Attenuation. *Geophysical Journal International*, **14**(1-4):33–43, 1967. doi:10.1111/j.1365-246X.1967.tb06219.x.

Gottschaldt, K.-D., Walzer, U., Hendel, R. F., Stegman, D. R., Baumgardner, J. R., and Mühlhaus, H.-B. Stirring in 3-d spherical models of convection in the Earth's mantle. *Philosophical Magazine*, **86**(21-22):3175–3204, 2006. doi:10.1080/14786430500197991.

Grand, S. P., Van Der Hilst, R. D., and Widiyantoro, S. Global seismic tomography: A snapshot of convection in the earth. *GSA Today*, **7**(4):1–7, 1997.

Gu, Y., Dziewonski, A. M., and Agee, C. B. Global de-correlation of the topography of transition zone discontinuities. *Earth and Planetary Science Letters*, **157**:57–67, 1998.

Gu, Y. J., Dziewoński, A. M., and Ekström, G. Simultaneous inversion for mantle shear velocity and topography of transition zone discontinuities. *Geophysical Journal International*, **154**(2):559–583, 2003. doi:10.1046/j.1365-246X.2003.01967.x.

Guerrero, J. M., Deschamps, F., Hsieh, W.-P., and Tackley, P. J. The combined effect of heterogeneous thermal conductivity, chemical density contrast, and heat-producing element enrichment on the stability of primordial reservoirs above the core-mantle boundary. *Earth and Planetary Science Letters*, **637**:118699, 2024. doi:10.1016/j.epsl.2024.118699.

Guerrero, J. M., Deschamps, F., Li, Y., Hsieh, W.-P., and Tackley, P. J. Influence of heterogeneous thermal conductivity on the long-term evolution of the lower-mantle thermochemical structure: implications for primordial reservoirs. *Solid Earth*, **14**(2):119–135, 2023. doi:10.5194/se-14-119-2023.

Gülcher, A. J. P., Golabek, G. J., Thielmann, M., Ballmer, M. D., and Tackley, P. J. Narrow, Fast, and "Cool" Mantle Plumes Caused by Strain-Weakening Rheology in Earth's Lower Mantle. *Geochemistry, Geophysics, Geosystems*, **23**(10):e2021GC010314, 2022. doi:10.1029/2021GC010314.

Guo, Z. and Zhou, Y. Finite-frequency imaging of the global 410-and 660-km discontinuities using SS precursors. *Geophysical Journal International*, **220**(3):1978–1994, 2020.

Gutenberg, B. Über die Konstitution des Erdinnern, erschlossen aus Erdbebenbeobachtungen. *Physikalische Zeitschrift*, **XIV**:1217–1218, 1913.

Hager, B. H., Clayton, R. W., Richards, M. A., Comer, R. P., and Dziewonski, A. M. Lower mantle heterogeneity, dynamic topography and the geoid. *Nature*, **313**(6003):541–545, 1985. doi:10.1038/313541a0.

Hart, S. R., Hauri, E. H., Oschmann, L. A., and Whitehead, J. A. Mantle Plumes and Entrainment: Isotopic Evidence. *Science*, **256**:517–520, 1992.

Haskell, N. A. The Motion of a Viscous Fluid Under a Surface Load. *Physics*, **6**(8):265–269, 1935. doi:10.1063/1.1745329.

Heister, T., Dannberg, J., Gassmöller, R., and Bangerth, W. High accuracy mantle convection simulation through modern numerical methods - II: Realistic models and problems. *Geophysical Journal International*, **210**(2):833–851, 2017. doi:10.1093/gji/ggx195. ArXiv: 1702.05075.

Hernández, E. R., Brodholt, J., and Alfè, D. Structural, vibrational and thermodynamic properties of Mg2SiO4 and MgSiO3 minerals from first-principles simulations. *Physics of the Earth and Planetary Interiors*, **240**:1–24, 2015. doi:10.1016/j.pepi.2014.10.007.

Herring, C. Diffusional Viscosity of a Polycrystalline Solid. *Journal of Applied Physics*, **21**(5):437–445, 1950. doi:10.1063/1.1699681.

Hess, H. Mid-oceanic ridges and tectonics of the sea-floor. *Deep Sea Research and Oceanographic Abstracts*, **13**(5):1080, 1966. doi:10.1016/0011-7471(76)91230-4.

Hiemer, V. and Thomas, C. Generation of Reflections and PKP Precursors From a Scattering Layer in D". *Geophysical Research Letters*, **49**(4):e2021GL096900, 2022. doi:10.1029/2021GL096900.

van der Hilst, R. D., de Hoop, M. V., Wang, P., Shim, S.-H., Ma, P., and Tenorio, L. Seismostratigraphy and Thermal Structure of Earth's Core-Mantle Boundary Region. *Science*, **315**(5820):1813–1817, 2007. doi:10.1126/science.1137867.

Hirose, K. Phase transitions in pyrolitic mantle around 670-km depth: Implications for upwelling of plumes from the lower mantle. *Journal of Geophysical Research: Solid Earth*, **107**(B4):ECV 3–1–ECV 3–13, 2002. doi:10.1029/2001JB000597.

Hoffman, A. W. and Hart, S. R. An assessment of local and regional isotopic equilibrium in the mantle. *Earth and Planetary Science Letters*, **38**(1):44–62, 1978. doi:10.1016/0012-821X(78)90125-5.

Hofmann, A. Sampling Mantle Heterogeneity through Oceanic Basalts: Isotopes and Trace Elements. In *Treatise on Geochemistry*, pages 67–101. Elsevier, 2014. doi:10.1016/B978-0-08-095975-7.00203-5.

Hofmann, A. W. Mantle geochemistry: the message from oceanic magmatism. *Nature*, **385**:219–229, 1997.

Holmes, A. Radioactivitity and Earth Movements. *Transactions of the Geological Society of Glasgow*, **18**:559–606, 1931.

Hosseini, K., Matthews, K. J., Sigloch, K., Shephard, G. E., Domeier, M., and Tsekhmistrenko, M. SubMachine: Web-Based Tools for Exploring Seismic Tomography and Other Models of Earth's Deep Interior. *Geochemistry, Geophysics, Geosystems*, **19**(5):1464–1483, 2018. doi:10.1029/2018GC007431.

Houard, S. and Nataf, H.-C. Further evidence for the 'Lay discontinuity' beneath northern Siberia and the North Atlantic from short-period P-waves recorded in France. *Physics of the Earth and Planetary Interiors*, **72**(3):264–275, 1992. doi:10.1016/0031-9201(92)90206-B.

Houard, S. and Nataf, H.-C. Laterally varying reflector at the top of *D'* beneath northern Siberia. *Geophysical Journal International*, **115**(1):168–182, 1993. doi:10.1111/j.1365-246X.1993.tb05597.x.

Houser, C. Global seismic data reveal little water in the mantle transition zone mantle phase transitions. *Earth and Planetary Science Letters*, **448**:94–101, 2016.

Houser, C., Masters, G., Flanagan, M., and Shearer, P. Determination and analysis of long-wavelength transition zone structure using SS precursors. *Geophysical Journal International*, **174**(1):178–194, 2008. doi:10.1111/j.1365-246X.2008.03719.x.

Houser, C. and Williams, Q. Reconciling Pacific 410 and 660km discontinuity topography, transition zone shear velocity patterns, and mantle phase transitions. *Earth and Planetary Science Letters*, **296**(3-4):255–266, 2010. doi:10.1016/j.epsl.2010.05.006.

Hu, M. and Gurnis, M. Edges of thermochemical structures in the lower mantle. *Physics of the Earth and Planetary Interiors*, page 107381, 2025. doi:10.1016/j.pepi.2025.107381.

Huang, M., Li, Y., and Zhao, L. Effects of thermal, compositional and rheological properties on the long-term evolution of large thermochemical piles of primordial material in the deep mantle. *Science China Earth Sciences*, **65**(12):2405–2416, 2022. doi:10.1007/s11430-021-9950-7.

Huang, Q., Schmerr, N., Waszek, L., and Beghein, C. Constraints on Seismic Anisotropy in the Mantle Transition Zone From Long-Period SS Precursors. *Journal of Geophysical Research: Solid Earth*, **124**(7):6779–6800, 2019. doi:10.1029/2019JB017307.

Huang, R., Thomson, A. R., Brodholt, J. P., Crichton, W. A., Rosenthal, A., Druzhbin, D., Backhouse, N., Taschimowitz, I., Bessas, D., Yaroslavtsev, S., and Wang, B. Sound velocity measurements of γ-(Mg0.91Fe0.09)2SiO4 show that the ringwoodite to bridgmanite and ferropericlase phase transformation does not produce the seismically observed 660 km discontinuity. *Earth and Planetary Science Letters*, **663**:119416, 2025. doi:10.1016/j.epsl.2025.119416.

Irifune, T., Nishiyama, N., Kuroda, K., Inoue, T., Isshiki, M., Utsumi, W., Funakoshi, K.-i., Urakawa, S., Uchida, T., Katsura, T., and Ohtaka, O. The Postspinel Phase Boundary in Mg_2 SiO_4 Determined by in Situ X-ray Diffraction. *Science*, **279**(5357):1698–1700, 1998. doi:10.1126/science.279.5357.1698.

Ishii, T., Frost, D. J., Kim, E. J., Chanyshev, A., Nishida, K., Wang, B., Ban, R., Xu, J., Liu, J., Su, X., Higo, Y., Tange, Y., Mao, H.-k., and Katsura, T. Buoyancy of slabs and plumes enhanced by curved post-garnet phase boundary. *Nature Geoscience*, pages 1–5, 2023. doi:10.1038/s41561-023-01244-w.

Ishii, T., Kojitani, H., and Akaogi, M. Post-spinel transitions in pyrolite and Mg2SiO4 and akimotoite–perovskite transition in MgSiO3: Precise comparison by high-pressure high-temperature experiments with multi-sample cell technique. *Earth and Planetary Science Letters*, **309**(3-4):185–197, 2011. doi:10.1016/j.epsl.2011.06.023.

Ita, J. and King, S. D. Sensitivity of convection with an endothermic phase change to the form of governing equations, initial conditions, boundary conditions, and equation of state. *Journal of Geophysical Research: Solid Earth*, **99**(B8):15919–15938, 1994. doi:10.1029/94JB00852.

Ito, E., Akaogi, M., Topor, L., and Navrotsky, A. Negative Pressure-Temperature Slopes for Reactions Forming MgSiO3 Perovskite from Calorimetry. *Science*, **249**(4974):1275–1278, 1990. doi:10.1126/science.249.4974.1275.

Ito, E. and Takahashi, E. Postspinel transformations in the system Mg2SiO4-Fe2SiO4 and some geophysical implications. *Journal of Geophysical*

Research: Solid Earth, **94**(B8):10637–10646, 1989. doi:10.1029/JB094iB08p10637.

Ito, E., Takahashi, E., and Matsui, Y. The mineralogy and chemistry of the lower mantle" an implication of the ultrahigh-pressure phase relations in the system MgO-FeO-SiO 2. *Earth and Planetary Science Letters*, **67**:238–248, 1984.

Jackson, J. M. and Thomas, C. Seismic and Mineral Physics Constraints on the D" Layer. In *Geophysical Monograph Series*, edited by Marquardt, H., Ballmer, M., Cottaar, S., and Konter, J., pages 193–227. Wiley, 1st edition, 2021. doi:10.1002/9781119528609.ch8.

Jacobs, M. H., Van Den Berg, A. P., and De Jong, B. H. The derivation of thermo-physical properties and phase equilibria of silicate materials from lattice vibrations: Application to convection in the Earth's mantle. *Calphad*, **30**(2):131–146, 2006. doi:10.1016/j.calphad.2005.10.001.

Javaheri, P., Lowman, J. P., and Tackley, P. J. Spherical geometry convection in a fluid with an Arrhenius thermal viscosity dependence: The impact of core size and surface temperature on the scaling of stagnant-lid thickness and internal temperature. *Physics of the Earth and Planetary Interiors*, **349**:107157, 2024. doi:10.1016/j.pepi.2024.107157.

Jeffreys, H. The Rigidity of the Earth's Central Core. *Geophysical Journal International*, **1**:371–383, 1926. doi:10.1111/j.1365-246X.1926.tb05385.x.

Jeffreys, H. and Bullen, K. E. Seismological Tables. Technical report, British Association Seismological Committee, London, 1940.

Jenkins, J., Cottaar, S., White, R. S., and Deuss, A. Depressed mantle discontinuities beneath Iceland: Evidence of a garnet controlled 660 km discontinuity? *Earth and Planetary Science Letters*, **433**:159–168, 2016. doi:10.1016/j.epsl.2015.10.053.

Jiang, S., Duvernay, T., Hoggard, M. J., Hawkins, R., Campbell, I. H., and Davies, D. R. Investigating the Lid Effect on the Generation of Ocean Island Basalts: 2. Geodynamical Simulations. *Geochemistry, Geophysics, Geosystems*, **26**(4):e2024GC012123, 2025. doi:10.1029/2024GC012123.

Jones, R. B. Diffusion Creep in Polycrystalline Magnesium. *Nature*, **207**(4992):70–70, 1965. doi:10.1038/207070a0.

Jones, T. D., Sime, N., and van Keken, P. E. Burying Earth's Primitive Mantle in the Slab Graveyard. *Geochemistry, Geophysics, Geosystems*, **22**(3), 2021. doi:10.1029/2020GC009396.

Jordan, T. H., Puster, P., Glatzmaier, G. A., and Tackley, P. J. Comparisons Between Seismic Earth Structures and Mantle Flow Models Based on Radial. *Science*, **261**:1427–1431, 1993.

Judd, E. J., Tierney, J. E., Lunt, D. J., Montañez, I. P., Huber, B. T., Wing, S. L., and Valdes, P. J. A 485-million-year history of Earth's surface temperature. *Science*, **385**(6715):eadk3705, 2024. doi:10.1126/science.adk3705.

Karato, S.-i., Zhang, S., and Wenk, H.-R. Superplasticity in Earth's Lower Mantle: Evidence from Seismic Anisotropy and Rock Physics. *Science*, **270**(5235):458–461, 1995.

Katsura, T. and Ito, E. The system Mg2SiO4-Fe2SiO4 at high pressures and temperatures: Precise determination of stabilities of olivine, modified spinel, and spinel. *Journal of Geophysical Research: Solid Earth*, **94**(B11):15663–15670, 1989. doi:10.1029/JB094iB11p15663.

Katsura, T., Yamada, H., Nishikawa, O., Song, M., Kubo, A., Shinmei, T., Yokoshi, S., Aizawa, Y., Yoshino, T., Walter, M. J., Ito, E., and Funakoshi, K.-i. Olivine-wadsleyite transition in the system (Mg,Fe)2SiO4. *Journal of Geophysical Research: Solid Earth*, **109**(B2), 2004. doi:10.1029/2003JB002438.

Katsura, T., Yamada, H., Shinmei, T., Kubo, A., Ono, S., Kanzaki, M., Yoneda, A., Walter, M. J., Ito, E., Urakawa, S., Funakoshi, K., and Utsumi, W. Post-spinel transition in Mg2SiO4 determined by high P–T in situ X-ray diffractometry. *Physics of the Earth and Planetary Interiors*, **136**(1-2):11–24, 2003. doi:10.1016/S0031-9201(03)00019-0.

Kawakatsu, H. and Yoshioka, S. Metastable olivine wedge and deep dry cold slab beneath southwest Japan. *Earth and Planetary Science Letters*, **303**(1-2):1–10, 2011. doi:10.1016/j.epsl.2011.01.008.

Keifer, I. and Dueker, K. Testing the hypothesis that temperature modulates 410 and 660 discontinuity topography beneath the eastern United States. *Earth and Planetary Science Letters*, **524**, 2019. doi:10.1016/j.epsl.2019.115723.

Kendall, J. M. and Nangini, C. Lateral variations in D' below the Caribbean. *Geophysical Research Letters*, **23**(4):399–402, 1996. doi:10.1029/95GL02659.

Kendall, J.-M. and Shearer, P. M. Lateral variations in D' thickness from long-period shear wave data. *Journal of Geophysical Research: Solid Earth*, **99**(B6):11575–11590, 1994. doi:10.1029/94JB00236.

Kennett, B. and Bunge, H. P. *Geophysical Continua*. Cambridge University Press, Cambridge, 1st edition, 2008.

Kennett, B. L., Engdahl, E. R., and Buland, R. Constraints on seismic velocities in the Earth from traveltimes. *Geophysical Journal International*, **122**(1):108–124, 1995. doi:10.1111/j.1365-246X.1995.tb03540.x.

Kennett, B. L. N. and Engdahl, E. R. Traveltimes for global earthquake location and phase identification. *Geophysics Journal International*, **105**:429–465, 1991.

Khan, A., Boschi, L., and Connolly, J. a. D. On mantle chemical and thermal heterogeneities and anisotropy as mapped by inversion of global surface wave data. *Journal of Geophysical Research: Solid Earth*, **114**(B9), 2009. doi:10.1029/2009JB006399.

King, S. D. On topography and geoid from 2-D stagnant lid convection calculations. *Geochemistry, Geophysics, Geosystems*, **10**(3):2008GC002250, 2009. doi:10.1029/2008GC002250.

King, S. D. Reconciling laboratory and observational models of mantle rheology in geodynamic modelling. *Journal of Geodynamics*, **100**:33–50, 2016. doi:10.1016/j.jog.2016.03.005.

King, S. D., Frost, D. J., and Rubie, D. C. Why cold slabs stagnate in the transition zone. *Geology*, **43**(3):231–234, 2015. doi:10.1130/G36320.1.

King, S. D. and Ita, J. Effect of slab rheology on mass transport across a phase transition boundary. *Journal of Geophysical Research: Solid Earth*, **100**(B10):20211–20222, 1995. doi:10.1029/95JB01964.

Kito, T., Rost, S., Thomas, C., and Garnero, E. J. New insights into the P - and S -wave velocity structure of the D' discontinuity beneath the Cocos plate. *Geophysical Journal International*, **169**(2):631–645, 2007. doi:10.1111/j.1365-246X.2007.03350.x.

Kojitani, H., Inoue, T., and Akaogi, M. Precise measurements of enthalpy of postspinel transition in Mg2SiO4 and application to the phase boundary calculation. *Journal of Geophysical Research: Solid Earth*, **121**(2):729–742, 2016. doi:10.1002/2015JB012211.

Kojitani, H., Yamazaki, M., Tsunekawa, Y., Katsuragi, S., Noda, M., Inoue, T., Inaguma, Y., and Akaogi, M. Enthalpy, heat capacity and thermal expansivity measurements of MgSiO3 akimotoite: Reassessment of its self-consistent thermodynamic data set. *Physics of the Earth and Planetary Interiors*, **333**:106937, 2022. doi:10.1016/j.pepi.2022.106937.

Kong, F., Gao, S. S., Liu, K. H., Fang, Y., Zhu, H., Stern, R. J., and Li, J. Metastable olivine within oceanic lithosphere in the uppermost lower mantle beneath the eastern United States. *Geology*, 2022. doi:10.1130/G49879.1.

Koroni, M., Bozdağ, E., Paulssen, H., and Trampert, J. Sensitivity analysis of seismic waveforms to upper-mantle discontinuities using the adjoint method. *Geophysical Journal International*, **210**(3):1965–1980, 2017. doi:10.1093/gji/ggx286.

Koroni, M. and Trampert, J. Imaging global mantle discontinuities: a test using full-waveforms and adjoint kernels. *Geophysical Journal International*, **226**(3):1498–1516, 2021. doi:10.1093/gji/ggab119.

Krauss, H. and McNamara, A. Superpiles: The Impact of Mantle Cooling on Large Low Velocity Provinces. 2025. doi:10.21203/rs.3.rs-7060145/v1.

Kreielkamp, P., Stein, C., and Hansen, U. LLSVPs of primordial origin: Implications for the evolution of plate tectonics. *Earth and Planetary Science Letters*, **579**, 2022. doi:10.1016/j.epsl.2021.117357.

Krischer, L., Megies, T., Barsch, R., Beyreuther, M., Lecocq, T., Caudron, C., and Wassermann, J. ObsPy: a bridge for seismology into the scientific Python ecosystem. *Computational Science & Discovery*, **8**(1):014003, 2015. doi:10.1088/1749-4699/8/1/014003.

Kronbichler, M., Heister, T., and Bangerth, W. High accuracy mantle convection simulation through modern numerical methods: High accuracy mantle convection simulation. *Geophysical Journal International*, **191**(1):12–29, 2012. doi:10.1111/j.1365-246X.2012.05609.x.

Kuwayama, Y., Hirose, K., Cobden, L., Kusakabe, M., Tateno, S., and Ohishi, Y. Post-Perovskite Phase Transition in the Pyrolitic Lowermost Mantle:

Implications for Ubiquitous Occurrence of Post-Perovskite Above CMB. *Geophysical Research Letters*, **49**(1), 2022. doi:10.1029/2021GL096219.

Laske, G., Masters, G., Ma, Z., and Pasyanos, M. CRUST1.0: An Updated Global Model of Earth's Crust. In *Geophysical Research Abstracts*, volume 14, pages EGU2012–3743–1. EGU, Vienna, Austria, 2012.

Lawrence, J. F. and Shearer, P. M. Imaging mantle transition zone thickness with *SdS* - *SS* finite-frequency sensitivity kernels. *Geophysical Journal International*, **174**(1):143–158, 2008. doi:10.1111/j.1365-246X.2007.03673.x.

Lay, T., Garnero, E. J., and Russell, S. A. Lateral variation of the D' discontinuity beneath the Cocos Plate. *Geophysical Research Letters*, **31**(15), 2004. doi:10.1029/2004GL020300.

Lay, T. and Helmberger, D. V. A lower mantle S-wave triplication and the shear velocity structure of D". *Geophysical Journal of the Royal Astronomical Society*, **75**(3):799–837, 1983. doi:10.1111/j.1365-246X.1983.tb05010.x.

Lay, T., Hernlund, J., and Buffett, B. A. Core-Mantle boundary heat flow. *Nature Geoscience*, **1**:25–32, 2008. doi:10.1038/ngeo.2007.44.

Lay, T., Hernlund, J., Garnero, E. J., and Thorne, M. S. A Post-Perovskite Lens and *D"* Heat Flux Beneath the Central Pacific. *Science*, **314**(5803):1272–1276, 2006. doi:10.1126/science.1133280.

Lebedev, S., Chevrot, S., and Van Der Hilst, R. Correlation between the shear-speed structure and thickness of the mantle transition zone. *Physics of the Earth and Planetary Interiors*, **136**(1-2):25–40, 2003. doi:10.1016/S0031-9201(03)00020-7.

Lee, S.-H., Rhie, J., Park, Y., and Kim, K.-H. Topography of the 410 and 660 km discontinuities beneath the Korean Peninsula and southwestern Japan using teleseismic receiver functions. *Journal of Geophysical Research: Solid Earth*, **119**(9):7245–7257, 2014. doi:10.1002/2014JB011149.

Lehmann, I. P'. *Publications du Bureau central séismologique internationale. Série A: Travaux scientifiques*, **14**:87–115, 1936.

Li, R., Dannberg, J., Gassmoeller, R., Lithgow-Bertelloni, C., and Stixrude, L. How Phase Transitions Impact Changes in Mantle Convection Style Throughout Earth's History: From Stalled Plumes to Surface Dynamics. 2024. doi:10.22541/essoar.171291881.13670109/v1.

Li, W.-R., Shorttle, O., Maclennan, J., Matthews, S., Zhang, Y., Namur, O., Soderman, C. R., and Geist, D. Taking the Temperature of Ocean Islands: A Petrological Approach. *Journal of Petrology*, **66**(5):egaf033, 2025. doi:10.1093/petrology/egaf033.

Li, Y., Deschamps, F., and Tackley, P. J. Effects of low-viscosity post-perovskite on the stability and structure of primordial reservoirs in the lower mantle. *Geophysical Research Letters*, **41**(20):7089–7097, 2014. doi:10.1002/2014GL061362.

Li, Y. and Miller, M. S. Seismic Evidence for Thermal and Chemical Heterogeneities in D“ Region Beneath Central America From Grid Search Modeling. *Geophysical Research Letters*, **48**(14):e2021GL092493, 2021. doi:10.1029/2021GL092493.

Lidaka, T. and Suetsugu, D. Seismological evidence for metastable olivine inside a subducting slab. *Nature*, **356**(6370):593–595, 1992. doi:10.1038/356593a0.

Litasov, K., Ohtani, E., Sano, A., Suzuki, A., and Funakoshi, K. In situ X-ray diffraction study of post-spinel transformation in a peridotite mantle: Implication for the 660-km discontinuity. *Earth and Planetary Science Letters*, **238**(3):311–328, 2005. doi:10.1016/j.epsl.2005.08.001.

Liu, H., Wang, W., Jia, X., Leng, W., Wu, Z., and Sun, D. The combined effects of post-spinel and post-garnet phase transitions on mantle plume dynamics. *Earth and Planetary Science Letters*, **496**:80–88, 2018. doi:10.1016/j.epsl.2018.05.031.

Liu, J., Topor, L., Zhang, J., Navrotsky, A., and Liebermann, R. C. Calorimetric study of the coesite-stishovite transformation and calculation of the phase boundary. *Physics and Chemistry of Minerals*, **23**(1), 1996. doi:10.1007/BF00202988.

Liu, L.-g. Silicate perovskite from phase transformations of pyrope-garnet at high pressure and temperature. *Geophysical Research Letters*, **1**(6):277–280, 1974. doi:10.1029/GL001i006p00277.

Liu, Z., Li, J., and Kong, F. Topographic variations of mantle transition zone discontinuities in the Java subduction zone and adjacent regions from receiver function analyses. *Tectonophysics*, **849**:229723, 2023. doi:10.1016/j.tecto.2023.229723.

Maguire, R., Ritsema, J., and Goes, S. Evidence of Subduction-Related Thermal and Compositional Heterogeneity Below the United States From Transition Zone Receiver Functions. *Geophysical Research Letters*, **45**(17):8913–8922, 2018. doi:10.1029/2018GL078378.

Maguire, R., Ritsema, J., Van Keken, P. E., Fichtner, A., and Goes, S. P - and S -wave delays caused by thermal plumes. *Geophysical Journal International*, **206**(2):1169–1178, 2016. doi:10.1093/gji/ggw187.

Mao, W. and Zhong, S. Slab stagnation due to a reduced viscosity layer beneath the mantle transition zone. *Nature Geoscience*, **11**(11):876–881, 2018. doi:10.1038/s41561-018-0225-2.

Mao, W. and Zhong, S. Controls on Global Mantle Convective Structures and Their Comparison With Seismic Models. *Journal of Geophysical Research: Solid Earth*, **124**(8):9345–9372, 2019. doi:10.1029/2019JB017918.

McKenzie, D. and Parker, R. L. The North Pacific · an Example of Tectonics on a Sphere. *Nature*, **216**:1276–1280, 1967.

Met Office. Cartopy: a cartographic python library with a Matplotlib interface. 2010. Https://doi.org/10.5281/zenodo.1182735.

Mitrovica, J. X. Haskell [1935] revisited. *Journal of Geophysical Research: Solid Earth*, **101**(B1):555–569, 1996. doi:10.1029/95JB03208.

Mitrovica, J. X. and Forte, A. M. A new inference of mantle viscosity based upon joint inversion of convection and glacial isostatic adjustment data. *Earth and Planetary Science Letters*, **225**(1-2):177–189, 2004. doi:10.1016/j.epsl.2004.06.005.

Mohorovicic, A. Earthquake of 8 October 1909 (English trans. by Skoko Dragutin). *Geofizika*, **9**:3–56, 1992.

Morgan, G. T., Davies, J. H., Myhill, R., and Panton, J. On the global geodynamic consequences of different phase boundary morphologies. *Solid Earth*, **16**(4/5):297–314, 2025*a*. doi:10.5194/se-16-297-2025.

Morgan, G. T., Davies, J. H., Myhill, R., Wookey, J., and Panton, J. A method for the prediction of seismic discontinuity topography from thermochemical mantle circulation models. *Geophysical Journal International*, **243**(2):ggaf344, 2025*b*. doi:10.1093/gji/ggaf344.

Morgan, W. J. Convection Plumes in the Lower Mantle. *Nature*, **230**:42–43, 1971.

Morishima, H., Kato, T., Suto, M., Ohtani, E., Urakawa, S., Utsumi, W., Shimomura, O., and Kikegawa, T. The Phase Boundary Between α- and β-Mg_2 SiO_4 Determined by in Situ X-ray Observation. *Science*, **265**(5176):1202–1203, 1994. doi:10.1126/science.265.5176.1202.

Mosenfelder, J. L., Marton, F. C., Ross, C. R., Kerschhofer, L., and Rubie, D. C. Experimental constraints on the depth of olivine metastability in subducting lithosphere. *Physics of the Earth and Planetary Interiors*, **127**(1-4):165–180, 2001. doi:10.1016/S0031-9201(01)00226-6.

Muir, J. M. R., Zhang, F., and Brodholt, J. P. The effect of water on the post-spinel transition and evidence for extreme water contents at the bottom of the transition zone. *Earth and Planetary Science Letters*, **565**:116909, 2021. doi:10.1016/j.epsl.2021.116909.

Muir, J. M. R., Zheng, X., and Zhang, F. Gradually Hydrating Upper Mantle and a Moderately Wet Mantle Transition Zone Determined From Wadsleyite-Olivine Phase Relations. *Journal of Geophysical Research: Solid Earth*, **130**(11):e2025JB031482, 2025. doi:10.1029/2025JB031482.

Müller, R. D., Cannon, J., Qin, X., Watson, R. J., Gurnis, M., Williams, S., Pfaffelmoser, T., Seton, M., Russell, S. H. J., and Zahirovic, S. GPlates: Building a Virtual Earth Through Deep Time. *Geochemistry, Geophysics, Geosystems*, **19**(7):2243–2261, 2018. doi:10.1029/2018GC007584.

Müller, R. D., Flament, N., Cannon, J., Tetley, M. G., Williams, S. E., Cao, X., Bodur, Ö., Zahirovic, S., and Merdith, A. A tectonic-rules-based mantle reference frame since 1 billion years ago - implications for supercontinent cycles and plate–mantle system evolution. *Solid Earth*, **13**(7):1127–1159, 2022. doi:10.5194/se-13-1127-2022.

Munch, F. D., Khan, A., Tauzin, B., Van Driel, M., and Giardini, D. Seismological evidence for thermo-chemical heterogeneity in Earth's continental mantle. *Earth and Planetary Science Letters*, **539**:116240, 2020. doi:10.1016/j.epsl.2020.116240.

Munch, F. D., Romanowicz, B., Mukhopadhyay, S., and Rudolph, M. L. Deep mantle plumes feeding periodic alignments of asthenospheric fingers beneath the central and southern Atlantic Ocean. *Proceedings of the National Academy of Sciences*, **121**(46):e2407543121, 2024. doi:10.1073/pnas.2407543121.

Murakami, M., Hirose, K., Kawamura, K., Sata, N., and Ohishi, Y. Post-Perovskite Phase Transition in MgSiO $_3$. *Science*, **304**(5672):855–858, 2004. doi:10.1126/science.1095932.

Nakagawa, T. and Tackley, P. J. Effects of a perovskite-post perovskite phase change near core-mantle boundary in compressible mantle convection. *Geophysical Research Letters*, **31**(16), 2004. doi:10.1029/2004GL020648.

Nakagawa, T., Tackley, P. J., Deschamps, F., and Connolly, J. A. Incorporating self-consistently calculated mineral physics into thermochemical mantle convection simulations in a 3-D spherical shell and its influence on seismic anomalies in Earth's mantle. *Geochemistry, Geophysics, Geosystems*, **10**(3), 2009. doi:10.1029/2008GC002280.

Neele, F., Regt, H., and Decar, J. Gross errors in upper-mantle discontinuity topography from underside reflection data. *Geophysical Journal International*, **129**(1):194–204, 1997. doi:10.1111/j.1365-246X.1997.tb00949.x.

Neele, F. and Regt, H. D. Imaging upper-mantle discontinuity topography usingunderside-reflection data. *Geophysical Journal International*, **137**(1):91–106, 1999. doi:10.1046/j.1365-246x.1999.00768.x.

Nerlich, R., Colli, L., Ghelichkhan, S., Schuberth, B., and Bunge, H.-P. Constraining central Neo-Tethys Ocean reconstructions with mantle convection models. *Geophysical Research Letters*, **43**(18):9595–9603, 2016. doi:10.1002/2016GL070524.

Ni, S., Tan, E., Gurnis, M., and Helmberger, D. Sharp Sides to the African Superplume. *Science*, **296**, 2002.

Oganov, A. R. and Ono, S. Theoretical and experimental evidence for a post-perovskite phase of MgSiO3 in Earth's D" layer. *Nature*, **430**(6998):445–448, 2004. doi:10.1038/nature02701.

Ohtani, E. Hydration and Dehydration in Earth's Interior. *Annual Review of Earth and Planetary Sciences*, **49**(1):253–78, 2021. doi:10.1146/annurev-earth-080320-062509.

Olivieri, M., Pino, N. A., and Morelli, A. Evidence for an S-velocity discontinuity in the lowermost mantle beneath the South Eastern Pacific Basin. *Geophysical Research Letters*, **24**(21):2617–2620, 1997. doi:10.1029/97GL52742.

Ono, S., Ito, E., and Katsura, T. Mineralogy of subducted basaltic crust (MORB) from 25 to 37 GPa, and chemical heterogeneity of the lower mantle. *Earth and Planetary Science Letters*, **190**:57–63, 2001.

Ottonello, G., Civalleri, B., Ganguly, J., Vetuschi Zuccolini, M., and Noel, Y. Thermophysical properties of the α–β–γ polymorphs of Mg2SiO4: a computational study. *Physics and Chemistry of Minerals*, **36**(2):87–106, 2009. doi:10.1007/s00269-008-0260-4.

Panasyuk, S. V. and Hager, B. H. Inversion for mantle viscosity profiles constrained by dynamic topography and the geoid, and their estimated errors. *Geophysical Journal International*, **143**:821–836, 2000.

Panton, J. *Advances in using three-dimensional mantle convection models to address global geochemical cycles.* Ph.D. thesis, Prifysgol Caerdydd Cardiff University, 2020.

Panton, J., Davies, J. H., Elliott, T., Andersen, M., Porcelli, D., and Price, M. G. Investigating Influences on the Pb Pseudo-Isochron Using Three-Dimensional Mantle Convection Models With a Continental Reservoir. *Geochemistry, Geophysics, Geosystems*, **23**(8):e2021GC010309, 2022. doi:10.1029/2021GC010309.

Panton, J., Davies, J. H., Koelemeijer, P., Myhill, R., and Ritsema, J. Unique composition and evolutionary histories of large low velocity provinces. *Scientific Reports*, **15**(1):4466, 2025. doi:10.1038/s41598-025-88931-3.

Papanagnou, I., Schuberth, B. S. A., and Thomas, C. Geodynamic predictions of seismic structure and discontinuity topography of the mantle transition zone. *Geophysical Journal International*, **234**(1):355–378, 2023. doi:10.1093/gji/ggac478.

Pasyanos, M. E., Masters, T. G., Laske, G., and Ma, Z. LITHO1.0: An updated crust and lithospheric model of the Earth. *Journal of Geophysical Research: Solid Earth*, **119**(3):2153–2173, 2014. doi:10.1002/2013JB010626.

Patterson, C. Age of meteorites and the earth. *Geochimica et Cosmochimica Acta*, **10**(4):230–237, 1956. doi:10.1016/0016-7037(56)90036-9.

Paulson, A. and Richards, M. A. On the resolution of radial viscosity structure in modelling long-wavelength postglacial rebound data. *Geophysical Journal International*, **179**(3):1516–1526, 2009. doi:10.1111/j.1365-246X.2009.04362.x.

Pisconti, A., Creasy, N., Wookey, J., Long, M. D., and Thomas, C. Mineralogy, fabric and deformation domains in D" across the southwestern border of the African LLSVP. *Geophysical Journal International*, **232**(1):705–724, 2022. doi:10.1093/gji/ggac359.

Pisconti, A., Thomas, C., and Wookey, J. Discriminating Between Causes of D' Anisotropy Using Reflections and Splitting Measurements for a Single Path. *Journal of Geophysical Research: Solid Earth*, **124**(5):4811–4830, 2019. doi:10.1029/2018JB016993.

Plimmer, A., Davies, J. H., and Panton, J. Investigating the Effect of Lithosphere Thickness and Viscosity on Mantle Dynamics Throughout the Supercontinent Cycle. *Geochemistry, Geophysics, Geosystems*, **25**(11):e2024GC011688, 2024. doi:10.1029/2024GC011688.

Poirier, J.-P. *Introduction to the Physics of the Earth's Interior*. Cambridge University Press, 2nd edition, 2000.

Pons, M., Sobolev, S. V., Liu, S., and Neuharth, D. Hindered Trench Migration Due To Slab Steepening Controls the Formation of the Central Andes. *Journal of Geophysical Research: Solid Earth*, **127**(12):e2022JB025229, 2022. doi:10.1029/2022JB025229.

Powell, R. and Holland, T. An internally consistent dataset with uncertainties and correlations: 3. Applications to geobarometry, worked examples and a computer program. *Journal of Metamorphic Geology*, **6**(2):173–204, 1988. doi:10.1111/j.1525-1314.1988.tb00415.x.

Price, M. G., Davies, J. H., and Panton, J. Controls on the Deep-Water Cycle Within Three-Dimensional Mantle Convection Models. *Geochemistry, Geophysics, Geosystems*, **20**(5):2199–2213, 2019. doi:10.1029/2018GC008158.

Rao, B. P., Kumar, M. R., and Saikia, D. Seismic Evidence for a Hot Mantle Transition Zone Beneath the Indian Ocean Geoid Low. *Geochemistry, Geophysics, Geosystems*, **21**(7):e2020GC009079, 2020. doi:10.1029/2020GC009079.

Reasoner, C. and Revenaugh, J. Short-period P wave constraints on D' reflectivity. *Journal of Geophysical Research: Solid Earth*, **104**(B1):955–961, 1999. doi:10.1029/1998JB900053.

Rebeur-Paschwitz, E. The Earthquake of Tokio, April 18, 1889. *Nature*, **40**:294–295, 1889. doi:https://doi.org/10.1038/040294e0.

Revenaugh, J. and Jordan, T. H. Mantle layering from ScS reverberations: 2. The transition zone. *Journal of Geophysical Research: Solid Earth*, **96**(B12):19763–19780, 1991*a*. doi:10.1029/91JB01486.

Revenaugh, J. and Jordan, T. H. Mantle layering from *ScS* reverberations: 4. The lower mantle and core-mantle boundary. *Journal of Geophysical Research: Solid Earth*, **96**(B12):19811–19824, 1991*b*. doi:10.1029/91JB02163.

Revenaugh, J. and Sipkin, S. A. Seismic evidence for silicate melt atop the 410-km mantle discontinuity. *Nature*, **369**(6480):474–476, 1994. doi:10.1038/369474a0.

Ribe, N. M., Stutzmann, E., Ren, Y., and van der Hilst, R. Buckling instabilities of subducted lithosphere beneath the transition zone. *Earth and Planetary Science Letters*, **254**(1-2):173–179, 2007. doi:10.1016/j.epsl.2006.11.028.

Ricard, Y. Physics of Mantle Convection. In *Treatise on Geophyiscs , volume 7: Mantle Dynamics*, edited by Bercovici, D. and Schubert, G., pages 31–87. Elsevier, Amsterdam, 2007.

Ringwood, A. and Major, A. The system Mg2SiO4-Fe2SiO4 at high pressures and temperatures. *Physics of the Earth and Planetary Interiors*, **3**:89–108, 1970. doi:10.1016/0031-9201(70)90046-4.

Ringwood, A. E. Mineralogical constitution of the deep mantle. *Journal of Geophysical Research (1896-1977)*, **67**(10):4005–4010, 1962*a*. doi:10.1029/JZ067i010p04005.

Ringwood, A. E. A model for the upper mantle. *Journal of Geophysical Research (1896-1977)*, **67**(2):857–867, 1962*b*. doi:10.1029/JZ067i002p00857.

Ritsema, J., McNamara, A. K., and Bull, A. L. Tomographic filtering of geodynamic models: Implications for model interpretation and large-scale mantle structure. *Journal of Geophysical Research: Solid Earth*, **112**(B1), 2007. doi:10.1029/2006JB004566.

Ritsema, J., Xu, W., Stixrude, L., and Lithgow-Bertelloni, C. Estimates of the transition zone temperature in a mechanically mixed upper mantle. *Earth and Planetary Science Letters*, **277**(1):244–252, 2009. doi:10.1016/j.epsl.2008.10.024.

Robl, G., Schuberth, B. S. A., Papanagnou, I., and Thomas, C. From seismic models to mantle temperatures: Uncertainties related to mineralogical

complexities and limited tomographic resolution. *Geophysical Journal International*, **241**(3):2003–2027, 2025. doi:10.1093/gji/ggaf141.

Rochira, F. and Thomas, C. On the Importance of Using Directional Information in the Search for Lower Mantle Reflectors. *The Seismic Record*, **3**(2):96–104, 2023. doi:10.1785/0320220038.

Rost, S. and Thomas, C. Improving Seismic Resolution Through Array Processing Techniques. *Surveys in Geophysics*, **30**(4-5):271–299, 2009. doi:10.1007/s10712-009-9070-6.

Rudolph, M. L., Lekić, V., and Lithgow-Bertelloni, C. Viscosity Jump in Earth's mid-mantle. *Science*, **350**(6266):1349–1352, 2015. doi:10.1126/science.aad4972.

Russell, S. A., Reasoner, C., Lay, T., and Revenaugh, J. Coexisting shear- and compressional-wave seismic velocity discontinuities beneath the central Pacific. *Geophysical Research Letters*, **28**(11):2281–2284, 2001. doi:10.1029/2000GL012553.

Rychert, C. A. and Shearer, P. M. A Global View of the Lithosphere-Asthenosphere Boundary. *Science*, **324**(5926):495–498, 2009. doi:10.1126/science.1169754.

Saki, M., Wirp, S. A., Billen, M., and Thomas, C. Seismic evidence for possible entrainment of rising plumes by subducting slab induced flow in three subduction zones surrounding the Caribbean Plate. *Physics of the Earth and Planetary Interiors*, **352**:107212, 2024. doi:10.1016/j.pepi.2024.107212.

Schellart, W. P., Stegman, D. R., and Freeman, J. Global trench migration velocities and slab migration induced upper mantle volume fluxes: Constraints to find an Earth reference frame based on minimizing viscous dissipation. *Earth-Science Reviews*, **88**(1):118–144, 2008. doi:10.1016/j.earscirev.2008.01.005.

Schlittenhardt, J., Schweitzer, J., and Muller, G. Evidence against a discontinuity at the top of D'. *Geophysical Journal International*, **81**(1):295–306, 1985. doi:10.1111/j.1365-246X.1985.tb01364.x.

Schubert, G., Turcotte, D. L., and Olsen, P. *Mantle Convection in the Earth and Planets*. Cambridge University Press, Cambridge, 2009.

Schubert, G., Yuen, D. A., and Turcotte, D. L. Role of Phase Transitions in a Dynamic Mantle. *Geophysical Journal of the Royal Astronomical Society*, **42**:705–735, 1975.

Schuberth, B. S., Bunge, H. P., and Ritsema, J. Tomographic filtering of high-resolution mantle circulation models: Can seismic heterogeneity be explained by temperature alone? *Geochemistry, Geophysics, Geosystems*, **10**(5), 2009*a*. doi:10.1029/2009GC002401.

Schuberth, B. S., Bunge, H. P., Steinle-Neumann, G., Moder, C., and Oeser, J. Thermal versus elastic heterogeneity in high-resolution mantle circulation models with pyrolite composition: High plume excess temperatures in the lowermost mantle. *Geochemistry, Geophysics, Geosystems*, **10**(1), 2009*b*. doi:10.1029/2008GC002235.

Shearer, P. M. *Introduction to Seismology*. Cambridge University Press, Cambridge, 2nd edition, 2009.

Shearer, P. M. *Introduction to Seismology*. Cambridge University Press, Cambridge, 3rd edition, 2019.

Shearer, P. M. and Masters, T. G. Global mapping of topography on the 660-km discontinuity. *Nature*, **335**:791–796, 1992.

Shephard, G. E., Matthews, K. J., Hosseini, K., and Domeier, M. On the consistency of seismically imaged lower mantle slabs. *Scientific Reports*, **7**(1):1–17, 2017. doi:10.1038/s41598-017-11039-w.

Shi, Z., Mitchell, R. N., Li, Y., Wan, B., Chen, L., Peng, P., Zhao, L., Liu, L., and Zhu, R. Sluggish thermochemical basal mantle structures support their long-lived stability. *Nature Communications*, **15**(1):10000, 2024. doi:10.1038/s41467-024-54416-6.

Sidorin, I., Gurnis, M., and Helmberger, D. V. Evidence for a Ubiquitous Seismic Discontinuity at the Base of the Mantle. *Science*, **286**:1326–1331, 1999.

Sidorin, I., Gurnis, M., Helmberger, D. V., and Ding, X. Interpreting D" seismic structure using synthetic waveforms computed from dynamic models. *Earth and Planetary Science Letters*, **163**(1-4):31–41, 1998. doi:10.1016/S0012-821X(98)00172-1.

Song, T.-R. A., Helmberger, D. V., and Grand, S. P. Low-velocity zone atop the 410-km seismic discontinuity in the northwestern United States. *Nature*, **427**(6974):530–533, 2004. doi:10.1038/nature02231.

Stegman, D. R. *Thermochemical evolution of terrestrial planets: Earth, Mars, and the Moon*. Ph.D., University of California, Berkeley, United States – California, 2003. ISBN: 9780496690626.

Stein, S. and Wysession, M. *An Introduction to Seismology, Earthquakes, and Earth Structure*. Blackwell Publishing, Malden, MA, 1st edition, 2003.

Steinberger, B. Effects of latent heat release at phase boundaries on flow in the Earth's mantle, phase boundary topography and dynamic topography at the Earth's surface. *Physics of the Earth and Planetary Interiors*, **164**(1):2–20, 2007. doi:10.1016/j.pepi.2007.04.021.

Steinberger, B. and Calderwood, A. R. Models of large-scale viscous flow in the Earth's mantle with constraints from mineral physics and surface observations. *Geophysical Journal International*, **167**(3):1461–1481, 2006. doi:10.1111/j.1365-246X.2006.03131.x.

Steinberger, B., Roy, P., Pons, M., and Jopke, M. P. Why Are Plume Excess Temperatures Much Less Than the Temperature Drop Across the Lowermost-Mantle Thermal Boundary Layer? *Journal of Geophysical Research: Solid Earth*, **130**(4):e2024JB030111, 2025. doi:10.1029/2024JB030111.

Steinberger, B. and Torsvik, T. H. A geodynamic model of plumes from the margins of Large Low Shear Velocity Provinces. *Geochemistry, Geophysics, Geosystems*, **13**(1), 2012. doi:10.1029/2011GC003808.

Stixrude, L. and Lithgow-Bertelloni, C. Thermodynamics of mantle minerals - I. Physical properties. *Geophysical Journal International*, **162**(2):610–632, 2005. doi:10.1111/j.1365-246X.2005.02642.x.

Stixrude, L. and Lithgow-Bertelloni, C. Thermodynamics of mantle minerals - II. Phase equilibria. *Geophysical Journal International*, **184**(3):1180–1213, 2011. doi:10.1111/j.1365-246X.2010.04890.x.

Stixrude, L. and Lithgow-Bertelloni, C. Thermal expansivity, heat capacity and bulk modulus of the mantle. *Geophysical Journal International*, **228**(2):1119–1149, 2022. doi:10.1093/gji/ggab394.

Stixrude, L. and Lithgow-Bertelloni, C. Thermodynamics of mantle minerals – III: the role of iron. *Geophysical Journal International*, **237**(3):1699–1733, 2024. doi:10.1093/gji/ggae126.

Styles, E., Davies, D. R., and Goes, S. Mapping spherical seismic into physical structure: biases from 3-D phase-transition and thermal boundary-layer heterogeneity: 3-D biases in 1-D seismic velocities. *Geophysical Journal International*, **184**(3):1371–1378, 2011*a*. doi:10.1111/j.1365-246X.2010.04914.x.

Styles, E., Goes, S., van Keken, P. E., Ritsema, J., and Smith, H. Synthetic images of dynamically predicted plumes and comparison with a global tomographic model. *Earth and Planetary Science Letters*, **311**(3):351–363, 2011*b*. doi:10.1016/j.epsl.2011.09.012.

Su, C., Liu, Y., Fan, D., Song, W., Jiang, J., Sun, Z., and Yang, G. Thermodynamic Properties of Fe-Bearing Wadsleyite and Determination of the Olivine-Wadsleyite Phase Transition Boundary in (Mg,Fe)2SiO4 System. *Frontiers in Earth Science*, **10**, 2022. doi:10.3389/feart.2022.879678.

Tackley, P. Mantle Geochemical Geodynamics. In *Treatise on Geophyiscs , volume 7: Mantle Dynamics*, edited by Bercovici, D. and Schubert, G., pages 325–370. Elsevier, Amsterdam, 2007.

Tackley, P. J., Stevenson, D. J., Glatzmaier, G. A., and Schubert, G. Effects of an endothermic phase transition at 670 km depth in a spherical model of convection in the Earth's mantle. *Nature*, **361**(6414):699–704, 1993. doi:10.1038/361699a0.

Tackley, P. J., Stevenson, D. J., Glatzmaier, G. A., and Schubert, G. Effects of multiple phase transitions in a three-dimensional spherical model of convection in Earth's mantle. *Journal of Geophysical Research*, **99**(B8), 1994. doi:10.1029/94jb00853.

Tackley, P. J. and Xie, S. The thermochemical structure and evolution of Earth's mantle: Constraints and numerical models. *Philosophical Transactions of the Royal Society A: Mathematical, Physical and Engineering Sciences*, **360**:2593–2609, 2002. doi:10.1098/rsta.2002.1082.

Tan, E. and Gurnis, M. Metastable superplumes and mantle compressibility. *Geophysical Research Letters*, **32**(20):1–4, 2005. doi:10.1029/2005GL024190.

Tauzin, B., Kim, S., and Kennett, B. L. N. Pervasive seismic low-velocity zones within stagnant plates in the mantle transition zone: Thermal or compositional origin? *Earth and Planetary Science Letters*, **477**:1–13, 2017. doi:10.1016/j.epsl.2017.08.006.

Tauzin, B., Waszek, L., Ballmer, M. D., Afonso, J. C., and Bodin, T. Basaltic reservoirs in the Earth's mantle transition zone. *Proceedings of the National Academy of Sciences*, **119**(48):e2209399119, 2022. doi:10.1073/pnas.2209399119.

Thielmann, M., Golabek, G. J., and Marquardt, H. Ferropericlase Control of Lower Mantle Rheology: Impact of Phase Morphology. *Geochemistry, Geophysics, Geosystems*, **21**(2), 2020. doi:10.1029/2019GC008688.

Thomas, C., Kendall, J.-M., and Weber, M. The lowermost mantle beneath northern Asia-I. Multi-azimuth studies of a D' heterogeneity. *Geophysical Journal International*, **151**(1):279–295, 2002. doi:10.1046/j.1365-246X.2002.01759.x.

Thomas, C. and Laske, G. D' observations in the Pacific from PLUME ocean bottom seismometer recordings. *Geophysical Journal International*, **200**(2):851–862, 2015. doi:10.1093/gji/ggu441.

Thompson, D. A., Helffrich, G., Bastow, I. D., Kendall, J. M., Wookey, J., Eaton, D. W., and Snyder, D. B. Implications of a simple mantle transition zone beneath cratonic North America. *Earth and Planetary Science Letters*, **312**(1-2):28–36, 2011. doi:10.1016/j.epsl.2011.09.037.

Torsvik, T. H., Smethurst, M. A., Burke, K., and Steinberger, B. Large igneous provinces generated from the margins of the large low-velocity provinces in the deep mantle. *Geophysical Journal International*, **167**(3):1447–1460, 2006. doi:10.1111/j.1365-246X.2006.03158.x.

Tromp, J., Tape, C., and Liu, Q. Seismic tomography, adjoint methods, time reversal and banana-doughnut kernels: Seismic tomography, adjoint methods, time reversal and banana-doughnut kernels. *Geophysical Journal International*, **160**(1):195–216, 2004. doi:10.1111/j.1365-246X.2004.02453.x.

Tsuchida, M. and Kameyama, M. 2-D Numerical Simulations on Formation and Descent of Stagnant Slabs: Important Roles of Trench Migration and Its Temporal Change. *Frontiers in Earth Science*, **8**, 2020. doi:10.3389/feart.2020.00117.

Turcotte, D. and Schubert, G. *Geodynamics*. Cambridge University Press, Cambridge, 3rd edition, 2014.

Van Heck, H. J., Davies, J. H., Elliott, T., and Porcelli, D. Global-scale modelling of melting and isotopic evolution of Earth's mantle: Melting modules for TERRA. *Geoscientific Model Development*, **9**(4):1399–1411, 2016. doi:10.5194/gmd-9-1399-2016.

Vasilos, T., Mitchell, J. B., and Spriggs, R. M. Creep of Polycrystalline Magnesia. *Journal of the American Ceramic Society*, **47**(4):203–204, 1964. doi:10.1111/j.1151-2916.1964.tb14395.x.

Verhoogen, J. Phase changes and convection in the Earth's mantle. *Philosophical Transactions of the Royal Society A: Mathematical, Physical and Engineering Sciences*, **258**(1088):276–283, 1965. doi:10.1098/rsta.1965.0040.

Vinnik, L. Detection of waves converted from P to SV in the mantle. *Physics of the Earth and Planetary Interiors*, **15**(1):39–45, 1977. doi:10.1016/0031-9201(77)90008-5.

Wallace, M. and Thomas, C. Investigating D" structure beneath the North Atlantic. *Physics of the Earth and Planetary Interiors*, **151**(1):115–127, 2005. doi:10.1016/j.pepi.2005.02.001.

Walter, M. J. 2.08 Melt Extraction and Compositional Variability in Mantle Lithosphere. In *Treatise on Geochemistry*, volume 2, pages 363– 394. Elsevier, 2003.

Wang, W., Zhang, H., Brodholt, J. P., and Wu, Z. Elasticity of hydrous ringwoodite at mantle conditions: Implication for water distribution in the lowermost mantle transition zone. *Earth and Planetary Science Letters*, **554**:116626, 2021. doi:10.1016/j.epsl.2020.116626.

Wang, Z. R., Stotz, I. L., Bunge, H.-P., Vilacís, B., Hayek, J. N., Ghelichkhan, S., and Lebedev, S. Cenozoic upper mantle flow history of the Atlantic realm based on Couette/Poiseuille models: Towards paleo-mantle-flowgraphy. *Physics of the Earth and Planetary Interiors*, **340**:107045, 2023. doi:10.1016/j.pepi.2023.107045.

Ward, J., Walker, A. M., Nowacki, A., Panton, J., and Davies, J. H. The sensitivity of lowermost mantle anisotropy to past mantle convection. *Physics of the Earth and Planetary Interiors*, **356**:107264, 2024. doi:10.1016/j.pepi.2024.107264.

Waszek, L., Anandawansha, R., Sexton, J., and Tauzin, B. Thermochemistry of the Mantle Transition Zone Beneath the Western Pacific. *Geophysical Research Letters*, **51**(18):e2024GL110852, 2024. doi:10.1029/2024GL110852.

Waszek, L., Schmerr, N. C., and Ballmer, M. D. Global observations of reflectors in the mid-mantle with implications for mantle structure and dynamics. *Nature Communications*, **9**(1):1–13, 2018. doi:10.1038/s41467-017-02709-4.

Waszek, L., Tauzin, B., Schmerr, N. C., Ballmer, M. D., and Afonso, J. C. A poorly mixed mantle transition zone and its thermal state inferred from seismic waves. *Nature Geoscience*, **14**(12):949–955, 2021. doi:10.1038/s41561-021-00850-w.

Weber, M. P- and S-wave reflections from anomalies in the lowermost mantle. *Geophysical Journal International*, **115**(1):183–210, 1993. doi:10.1111/j.1365-246X.1993.tb05598.x.

Wei, S. S. and Shearer, P. M. A sporadic low-velocity layer atop the 410 km discontinuity beneath the Pacific Ocean. *Journal of Geophysical Research: Solid Earth*, **122**(7):5144–5159, 2017. doi:10.1002/2017JB014100.

White, W. and Klein, E. Composition of the Oceanic Crust. In *Treatise on Geochemistry*, volume 4, pages 457–496. Elsevier, 2014. doi:10.1016/B978-0-08-095975-7.00315-6.

Whittaker, J. M., Afonso, J. C., Masterton, S., Müller, R. D., Wessel, P., Williams, S. E., and Seton, M. Long-term interaction between mid-ocean ridges and mantle plumes. *Nature Geoscience*, **8**(6):479–483, 2015. doi:10.1038/ngeo2437.

Whittaker, S., Thorne, M. S., Schmerr, N. C., and Miyagi, L. Seismic array constraints on the D" discontinuity beneath Central America. *Journal of Geophysical Research: Solid Earth*, **121**(1):152–169, 2016. doi:10.1002/2015JB012392.

Wieczorek, M. A. and Meschede, M. SHTools: Tools for Working with Spherical Harmonics. *Geochemistry, Geophysics, Geosystems*, **19**(8):2574–2592, 2018. doi:10.1029/2018GC007529.

Wilson, J. T. Evidence from ocean islands suggesting movement in the Earth. *Philosophical Transactions of the Royal Society A: Mathematical, Physical and Engineering Sciences*, **258**(1088):145–167, 1965. doi:10.1098/rsta.1965.0029.

Wolf, J., Becker, T. W., Garnero, E., Liu, K. H., and West, J. D. Comprehensive global data set of uniformly processed shear-wave splitting measurements. *Geophysical Journal International*, **241**(2):863–875, 2025. doi:10.1093/gji/ggaf076.

Wolstencroft, M. *Understanding the Thermal Evolution of Earth*. Ph.D. thesis, Cardiff University | Prifysgol Caerdydd, Cardiff, 2008.

Wolstencroft, M. and Davies, J. H. Influence of the Ringwoodite-Perovskite transition on mantle convection in spherical geometry as a function of Clapeyron slope and Rayleigh number. *Solid Earth*, **2**(2):315–326, 2011. doi:10.5194/se-2-315-2011.

Wysession, M., Lay, T., Revenaugh, J., Williams, Q., Garnero, E., and Jeanloz, R. The D" discontinuity and its implications. *The Core–Mantle Boundary Region, Geodyn. Ser.*, **28**:273–297, 1998.

Xu, W., Lithgow-Bertelloni, C., Stixrude, L., and Ritsema, J. The effect of bulk composition and temperature on mantle seismic structure. *Earth and Planetary Science Letters*, **275**(1-2):70–79, 2008. doi:10.1016/j.epsl.2008.08.012.

Yan, J., Ballmer, M. D., and Tackley, P. J. The evolution and distribution of recycled oceanic crust in the Earth's mantle: Insight from geodynamic models. *Earth and Planetary Science Letters*, **537**, 2020. doi:10.1016/j.epsl.2020.116171.

Yanagisawa, T., Yamagishi, Y., Hamano, Y., and Stegman, D. R. Mechanism for generating stagnant slabs in 3-D spherical mantle convection models at Earth-like conditions. *Physics of the Earth and Planetary Interiors*, **183**(1):341–352, 2010. doi:10.1016/j.pepi.2010.02.005.

Yang, W.-S. *Variable viscosity thermal convection at infinite Prandtl number in a thick spherical shell*. University of Illinois at Urbana-Champaign, 1997.

Yao, Y., Whittaker, S., and Thorne, M. S. D' discontinuity structure beneath the North Atlantic from Scd observations. *Geophysical Research Letters*, **42**(10):3793–3801, 2015. doi:10.1002/2015GL063989.

Ye, Y., Gu, C., Shim, S.-H., Meng, Y., and Prakapenka, V. The postspinel boundary in pyrolitic compositions determined in the laser-heated diamond anvil cell. *Geophysical Research Letters*, **41**(11):3833–3841, 2014. doi:10.1002/2014GL060060.

Young, C. J. and Lay, T. Evidence for a shear velocity discontinuity in the lower mantle beneath India and the Indian Ocean. *Physics of the Earth and Planetary Interiors*, **49**:37–53, 1987.

Young, C. J. and Lay, T. Multiple phase analysis of the shear velocity structure in the D' region beneath Alaska. *Journal of Geophysical Research: Solid Earth*, **95**(B11):17385–17402, 1990. doi:10.1029/JB095iB11p17385.

Yu, C., Day, E. A., de Hoop, M. V., Campillo, M., and van der Hilst, R. D. Mapping Mantle Transition Zone Discontinuities Beneath the Central Pacific With Array Processing of SS Precursors. *Journal of Geophysical Research: Solid Earth*, **122**(12):10,364–10,378, 2017. doi:10.1002/2017JB014327.

Yu, C., Goes, S., Day, E. A., and Van Der Hilst, R. D. Seismic evidence for global basalt accumulation in the mantle transition zone. *Science Advances*, **9**(22), 2023. doi:10.1126/sciadv.adg0095.

Yu, Y., Gao, S. S., and Liu, K. H. Topography of the 410 and 660 km Discontinuities Beneath the Cenozoic Okavango Rift Zone and Adjacent Precambrian Provinces. *Journal of Geophysical Research: Solid Earth*, **125**(9), 2020. doi:10.1029/2019JB019290.

Yu, Y. G., Wentzcovitch, R. M., Vinograd, V. L., and Angel, R. J. Thermodynamic properties of MgSiO3 majorite and phase transitions near 660 km depth in MgSiO3 and Mg2SiO 4: A first principles study. *Journal of Geophysical Research: Solid Earth*, **116**(2), 2011. doi:10.1029/2010JB007912.

Yu, Y. G., Wu, Z., and Wentzcovitch, R. M. alpha-beta-gama transformations in Mg2SiO4 in Earth's transition zone. *Earth and Planetary Science Letters*, **273**(1-2):115–122, 2008. doi:10.1016/j.epsl.2008.06.023.

Yuan, Q. and Li, M. Instability of the African large low-shear-wave-velocity province due to its low intrinsic density. *Nature Geoscience*, **15**(4):334–339, 2022. doi:10.1038/s41561-022-00908-3.

van Zelst, I., Crameri, F., Pusok, A., Glerum, A., Dannberg, J., and Thieulot, C. 101 Geodynamic modelling: How to design, carry out, and interpret numerical studies. *Solid Earth Discussions*, pages 1–80, 2021. doi:10.5194/se-2021-14.

Zhao, L. and Chevrot, S. SS-wave sensitivity to upper mantle structure: Implications for the mapping of transition zone discontinuity topographies. *Geophysical Research Letters*, **30**(11), 2003. doi:10.1029/2003GL017223.

Zhong, S. and Gurnis, M. Role of plates and temperature-dependent viscosity in phase change dynamics. *Journal of Geophysical Research: Solid Earth*, **99**(B8):15903–15917, 1994. doi:10.1029/94JB00545.

Zhong, S., Yuen, D. A., and Moresi, L. Numerical Methods for Mantle Convection. In *Treatise on Geophyiscs , volume 7: Mantle Dynamics*, edited by Bercovici, D. and Schubert, G., pages 227–252. Elsevier, Amsterdam, 2007.